

Advanced Instrumentation and Measurements for Early Nondestructive Evaluation of Damage and Defects in Aerostructures and Aging Aircraft

Final Report

Air Force University Research Initiative in Materials Degradation
and Fatigue in Aerospace Structures

AFOSR Contract No. F49620-93-1-0268
Vanderbilt University, John P. Wikswo, Principal Investigator

August 11, 2000

20000908 037

REPORT DOCUMENTATION PAGE

AFRL-SR-BL-TR-00-

Public reporting burden for this collection of information is estimated to average 1 hour per response, including gathering and maintaining the data needed, and completing and reviewing the collection of information. Send comments regarding this burden estimate or any other aspect of this collection of information, including suggestions for reducing this burden, to Washington Headquarters Service, Paperwork Project Team, Paperwork Reduction Project (1218-0187), Washington, DC 20503.

sources,
ct of this
Jefferson
is

0391

1. AGENCY USE ONLY (Leave blank)		2. REPORT DATE	3. REPORT TYPE AND DATES COVERED 01 Apr 93 to 31 Dec 98 Final	
4. TITLE AND SUBTITLE ADVANCED INSTRUMENTATION AND MEASUREMENTS FOR EARLY NONDESTRUCTIVE EVALUATION OF DAMAGE AND DEFECTS IN AEROSTRUCTURES AND AGING AIRCRAFT			5. FUNDING NUMBERS 61102F 2305/GS	
6. AUTHOR(S) Dr Wikswo				
7. PERFORMING ORGANIZATION NAME(S) AND ADDRESS(ES) Vanderbilt Univ 512 kirkland hall Nashville TN 37240			8. PERFORMING ORGANIZATION REPORT NUMBER	
9. SPONSORING/MONITORING AGENCY NAME(S) AND ADDRESS(ES) AFOSR/NE 801 North Randolph Street Rm 732 Arlington, VA 22203-1977			10. SPONSORING/MONITORING AGENCY REPORT NUMBER F4962093-1-0268	
11. SUPPLEMENTARY NOTES				
12a. DISTRIBUTION AVAILABILITY STATEMENT APPROVAL FOR PUBLIC RELEASED; DISTRIBUTION UNLIMITED			12b. DISTRIBUTION CODE	
13. ABSTRACT (Maximum 200 words) The project is divided into eight tasks, which range from the development of NDE instrumentation, theoretical measurement models and experimental techniques, to more basic studies of the initiation and development of fatigue cracks and the magnetic measurement of the electrical currents that are generated during corrosion in aluminum structures. Key aspects of this work have already been transitioned to the Air Force, and a regular program of corrosion measurements in ongoing to support maintenance of the KC-135.				
14. SUBJECT TERMS			15. NUMBER OF PAGES	
			16. PRICE CODE	
17. SECURITY CLASSIFICATION OF REPORT UNCLASSIFIED		18. SECURITY CLASSIFICATION OF THIS PAGE UNCLASSIFIED	19. SECURITY CLASSIFICATION OF ABSTRACT UNCLASSIFIED	20. LIMITATION OF ABSTRACT UL

THIS QUANTITY IS REQUIRED 4

Standard Form 298 (Rev. 2-89) (EG)
Prescribed by ANSI Std. Z39.18
Designed using Perform Pro, WHS/DIOR, Oct 94

Advanced Instrumentation and Measurements for Early Nondestructive Evaluation of Damage and Defects in Aerostructures and Aging Aircraft

Final Report

Air Force University Research Initiative in Materials Degradation
and Fatigue in Aerospace Structures

AFOSR Contract No. F49620-93-1-0268
Vanderbilt University, John P. Wikswo, Principal Investigator

August 11, 2000

TABLE OF CONTENTS

INTRODUCTION.....	ii
TASK 1. NDE INSTRUMENTATION DEVELOPMENT	1/1
Task 1.1 NDE Instrumentation (Vanderbilt)	1/1
TASK 2. NDE THEORY AND TECHNIQUES	2/1
Tasks 2.1.1/2.2.1-4 SQUID Measurements and Models (Vanderbilt)	2/1
TASK 3. IMAGE PROCESSING	3/1
TASK 5. FATIGUE DAMAGE CHARACTERIZATION	5/1
TASK 6. CORROSION	6/1
TASK 7. EVALUATION OF NDE CAPABILITIES	7/1
APPENDIX 1. DEPTH-SELECTIVE EDDY CURRENT ANALYSIS	A1/1
APPENDIX 2. THEORETICAL MODEL I	A2/1
APPENDIX 3. THEORETICAL MODEL II	A3/1
APPENDIX 4. THEORETICAL MODEL III	A4/1

INTRODUCTION

This University Research Initiative (URI) project was directed towards the development of advanced instrumentation and measurement techniques suitable for detection and analysis of cracking and corrosion in aging aircraft. The project is divided into eight tasks, which range from the development of NDE instrumentation, theoretical measurement models and experimental techniques, to more basic studies of the initiation and development of fatigue cracks and the magnetic measurement of the electrical currents that are generated during corrosion in aluminum structures. The measurement techniques that were explored in great detail include SQUID magnetometry, laser interferometry, ultrasonics, and advanced deconvolution/image processing. In all aspects of this effort, we developed collaborations with Air Force Laboratories and Air Logistics Centers, manufacturers of military and civilian aircraft, and other industrial organizations with an active interest in aircraft NDE. The research was conducted at both Northwestern University and Vanderbilt University; this report describes the Vanderbilt effort.

Superconducting QUantum Interference Device (SQUID) magnetometers offer promise as multi-mode instruments capable of high resolution images of extremely low-frequency eddy currents, and they can be configured to image the magnetic susceptibility of titanium, aluminum and non-metallic composites. Vanderbilt University has applied the expertise gained with its SQUID Magnetic Imaging Facility towards the development of NDE instrumentation and techniques applicable to the aging aircraft problem, particularly obtaining high resolution images of flaws and corrosion deep inside second and third layer structures. Key aspects of this work have already been transitioned to the Air Force, and a regular program of corrosion measurements is ongoing to support maintenance of the KC-135. The sheet-inducer eddy-current NDE techniques are presently being implemented for NASA.

TASK 1. NDE INSTRUMENTATION DEVELOPMENT

Task 1.1 NDE Instrumentation (Vanderbilt)

TASK 1 NDE INSTRUMENTATION DEVELOPMENT

1. Objective

The objective is to adapt existing SQUID instrumentation and facilities for the development and evaluation of SQUID NDE techniques.

2. Accomplishments

A. SQUID Imaging System

Over the past years, a well-equipped facility has been developed for SQUID NDE, which includes the various SQUID magnetometers, a small magnetic shield, and a large magnetically-shielded room. This includes a high-speed, non-magnetic x-y stage located inside the small magnetic shield. An additional x-y stage has been recently added, located outside of the small shield, which operates via a diving board assembly (see Fig. 1.1). New, user-friendly software has been developed to control the x-y stage and provide a real-time view of data as it is acquired. The SQUID hardware is essentially complete and represents a stable, state-of-the-art laboratory system for NDE research.

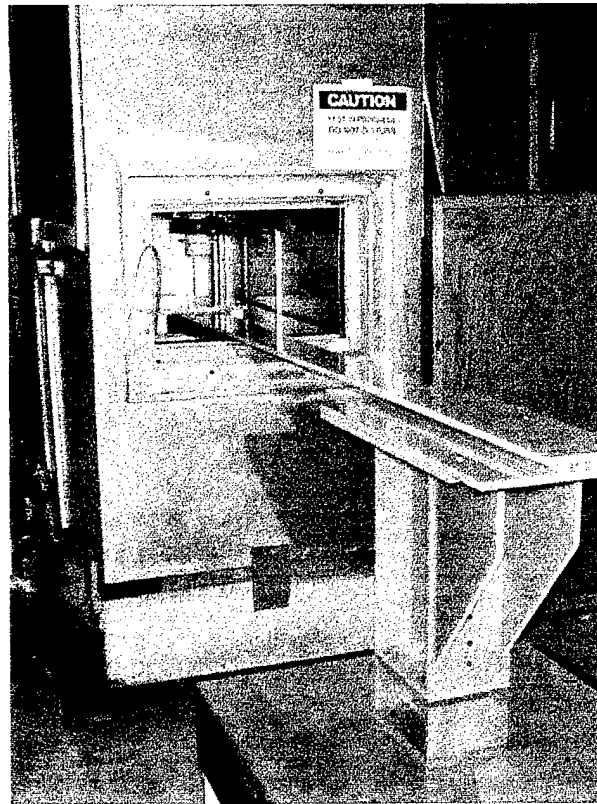


Figure 1.1 SQUID NDE system at Vanderbilt University.

B. Orthogonal Eddy current Inducer

An orthogonal inducer has been designed for inducing the eddy current in an arbitrary direction for enhancing the sensitivity of crack detection. Instead of a small multi-wire sheet inducer that is rigidly attached to the SQUID, the orthogonal inducer with two identical multi-wire sheets has been built and tested. The orthogonal inducer has been optimized for inducing the eddy current in different test objects. This inducer technology has also been successfully applied to a HTS SQUID (KFA). The sheet current inducer represents a major step towards the practical realization of SQUID NDE on aging aircraft.

The optimized orthogonal inducer will be presented in detail under Task 2.

3. Personnel Supported:

John P. Wikswo, Professor of Physics
Yu Pei Ma, Research Assistant Professor of Physics
William G. Jenks, Research Associate of Physics
Eduardo Parente Ribiero, Visiting Graduate Student

4. Publications and related items

Journal Articles

"Techniques for Depth-Selective, Low-Frequency Eddy Current Analysis for SQUID-Based Non Destructive Testing," Y.P. Ma and J.P. Wikswo, Jr., J. Nondestr. Eval., 14(3): 149-167 (1995).

"A New, Finite Element Approach to Reconstruct a Bounded and Discontinuous Two-Dimensional Current Image from a Magnetic Field Map," S. Tan, N.G. Sepulveda, and J.P. Wikswo, Jr., J. Computational Physics, 122: 150-164 (1995).

"A Numerical Study of the Use of SQUID Magnetometers to Detect Hidden Flaws in Conducting Objects," N.G. Sepulveda and J.P. Wikswo, Jr., J. Appl. Phys., 79(4): 2122-2135 (1996).

Conference Proceedings:

"SQUID Magnetometers Applied to Aging Aircraft NDE," J.P. Wikswo, Jr., Proc. of the Joint USAF/NASA/FAA Aging Aircraft NDI Workshop Covering Research of Enhanced Conventional NDI Technologies, Ames, IA, November 1994.

"SQUID Eddy Current Techniques for Detection of Second Layer Flaws," Y.P. Ma and J.P. Wikswo, Jr., Review of Progress in QNDE, 13: 303-309 (1994).

"SQUID Magnetometers for NDE in the Power Industry," W.G. Jenks, Y.P. Ma, and J.P. Wikswo, Jr., EPRI Topical Workshop: Electromagnetic NDE Applications in the Electric Power Industry, Session Three, August 21-23, 1995.

"Depth-Selective SQUID Eddy Current Techniques for Second Layer Flaw Detection," Y.P. Ma and J.P. Wikswo, Jr., Review of Progress in QNDE, 15: 401-408 (1996).

"Conductivity Imaging in Plates Using Magnetic Imaging Current Tomography," D.J. Staton and J.P. Wikswo, Jr., Review of Progress in QNDE, 15: 845-851 (1996).

"SQUID Magnetometers for Nondestructive Testing and Biomagnetism," Y.P. Ma and J.P. Wikswo, Jr., Proceedings of 1996 Chinese American Academic and Professional Convention (CAAPCON), pp. 4.14.1-4.17.4 (1996).

Book Chapters and Invited Review Articles:

"SQUID Magnetometers for Biomagnetism and Non-Destructive Testing: Important Questions and Initial Answers," J.P. Wikswo, Jr., IEEE Transactions on Applied Superconductivity, 5(2): 74-120 (1995) (Plenary Lecture).

"High-Resolution Magnetic Imaging: Cellular Action Currents and Other Applications," J.P. Wikswo, Jr., NATO ASI on SQUID Sensors: Fundamentals, Fabrication and Applications, H. Weinstock, Ed., Kluwer Academic Publishers, The Netherlands, pp. 307-360 (1996).

"The Magnetic Inverse Problem for NDE," J.P. Wikswo, Jr., NATO ASI on SQUID Sensors: Fundamentals, Fabrication and Applications, H. Weinstock, Ed., Kluwer Academic Publishers, The Netherlands, pp. 629-695 (1996).

"SQUIDs," W.G. Jenks, I.M. Thomas, and J.P. Wikswo, Jr., Encyclopedia of Applied Physics, G.L. Trigg, E.S. Vera, and W. Greulich, Eds., VCH Publishers, Inc., New York, NY, vol. 19, pp. 457-468 (1997).

"Scanning SQUID Microscopy," J.R. Kirtley and J.P. Wikswo, Jr., Annu. Rev. Mater. Sci., 29: 117-148 (1999).

5. Interactions/Transitions:

a. Participation/presentations

"Advanced Instrumentation and Measurements for Early Nondestructive Evaluation of Damage and Defects in Aerostructures and Aging Aircraft," Second USAF Aging Aircraft Conference, Oklahoma City, OK, May 1994.

"Applications of Superconducting Magnetometry to Aircraft Corrosion," Tri-Service Conference on Corrosion, Orlando, FL, June 1994.

"SQUID Magnetometers for Biomagnetism and Non-Destructive Testing: Important Questions and Initial Answers," J.P. Wikswo, Jr., Plenary Lecture, Applied Superconductivity Conference, Boston, MA, October 1994.

"SQUID Magnetometers Applied to Aging Aircraft NDE," J.P. Wikswo, Jr., FAA/USAF/NASA Aging Aircraft Inspection Workshop on Enhanced Conventional Technologies, Ames, IA, November 1994.

"Recent Developments in 5K Cryocoolers - An Outsider's View," Closing Summary, 5K Cryocooler Workshop, Elmsford, NY, July 1995.

"Imaging of Electric and Magnetic Sources," NATO Advanced Study Institute on SQUID Sensors: Fundamentals, Fabrication and Applications, Villa del mare, Maretea, Italy, June 1995.

"The Two-Dimensional Magnetic Inverse Problem," NATO Advanced Study Institute on SQUID Sensors: Fundamentals, Fabrication and Applications, Villa del mare, Maretea, Italy, June 1995.

"Advanced Instrumentation and Measurements for Early Nondestructive Evaluation of Damage and Defects in Aerostructures and Aging Aircraft," J.P. Wikswo, Jr., Air Force 3rd Aging Aircraft Conference, Wright-Patterson AFB, OH, September 1995.

"NDE with SQUIDs," Alcoa Technical Center, Alcoa Center, PA, October 1995.

"Biomagnetism and Non-Destructive Testing: Shared Problems and Solutions," Plenary Lecture, 1996 Biomagnetism Conference, Sante Fe, NM, February 1996.

John Wikswo attended the AFOSR/NDE Program Review Meeting at Warner Robins, Air Force Base, GA on April 2, 1996.

John Wikswo attended the QNDE Conference held on July 28 - August 2, 1996 in Brunswick, Maine.

b. Consultative and advisory functions

Professor Wikswo is a member of the Scientific Advisory Board of Hypres Inc., meeting involve discussions about digital SQUID magnetometers and cryocoolers.

John Wikswo met with NCI Information Systems and staff from Warner Robins Air Logistics Center on March 5 - 6, 1996 and August 5 - 6, 1996 to discuss corrosion and the Air Force aging aircraft problem.

c. Transitions

Discussions with and demonstrations to numerous visitors to our labs.

6. New discoveries, inventions, or patent disclosures:

Two related patents, not funded by the Air Force, were issued.

"Apparatus and Method for Imaging the Structure of Diamagnetic and Paramagnetic Objects," J.P. Wikswo, Jr. and A. Lauder, United States Patent 5,408,178 (April 8, 1995); Mexican Patent 17845 (June 28, 1995).

"Magnetometer and Method of Measuring a Magnetic Field," J.P. Wikswo, Jr. W.C. Black, Jr., E.C. Hirschhoff, J.R. Marsden, and D.N. Paulson, United States Patent 5,444,372 (August 22, 1995).

7. Honors/Awards:

John P. Wikswo, Plenary Lecturer, Applied Superconductivity Conference, Boston, October 1994.

TASK 2. NDE THEORY AND TECHNIQUES

Task 2.1.1 / 2.2.1-4 SQUID Measurements and Models (Vanderbilt)

TASK 2 NDE THEORY AND TECHNIQUES

1. Objective

The objective is to refine eddy current techniques for SQUID detection of second layer corrosion and fatigue cracks in simulated aluminum aircraft skins.

2. Accomplishments

A. Three Theoretical Models

We have developed improved models for calculating the magnetic and electric fields being mapped during dc and ac SQUID current imaging measurements. A goal is to assess the effects of flaw shape on the magnetic signal; initially we have concentrated our efforts towards shapes that are amenable to an analytical solution, such as a spheroidal inclusions [Appendix 2], an elliptical flaw [Appendix 3], and a flat-bottomed hole [Appendix 4]. The potential distribution due to the presence of the flaw/inhomogeneity is found and then the magnetic field originating from the presence of the flaw/inhomogeneity in the uniform field is calculated.

The results of the analysis have shown that the presence of a spheroidal inclusion affects the potential distribution due to the surface of the conductor only in the close proximity of the inclusion. The analysis has also shown that the qualitative behavior of the magnetic field does not change appreciably for more elongated or rounded spheroidal inclusions (different eccentricities) which are deep beneath the surface and the results indicate that the magnetic field might be interpreted as being generated by a "dipole-like" source for both axial and transverse excitations and little information on the actual shape of the source is provided by this result. However, the dipole moment contains information about the volume of the inclusion, and the shape of the signal provides the depth of the inclusion, hence the measurement of the magnetic signal could be used for quantitative characterization of inclusion volume.

The analysis of the magnetic signal from a flat-bottom hole shows that the bottom of the hole does not affect the magnetic field significantly. The importance of this finding is that the hole with a finite length may be treated as a through hole for which the solutions are less complicated. The calculations for an elliptical hole have shown that the signal strength is not only the dimension of the ellipse, but also a function of its orientation relative to the current. The results for a crack-like flaw are derived from the solution for an elliptical hole, which has been used for both quantitative and qualitative purpose.

B. Depth-selective and Self-referencing Techniques Using Sheet Inducers

Current injection into a conductor has been used successfully to detect subsurface flaws by measuring the magnetic field normal to the surface [5]. But, in circumstances when an insulation layer (e.g., paint on an aircraft) covers the conductor, induced eddy currents

provide the ability to examine these flaws without any contact. The use of induced eddy currents for SQUID NDE has been the focus of this project.

The inducers used for excitation current, can be a single coil, double coil, or a current sheet. Primarily, eddy current inducer development has been towards the use of SQUID systems that measure only the vertical component of the magnetic field. For these systems, the vertical eddy current does not contribute to the magnetic signal, then we need consider only the horizontal components of the current in the test sample. By using a sheet inducer, which can apply an ac magnetic field parallel to the test surface, to induce a large extended eddy current in a desired orientation, cracks or material loss inside conductors can be imaged.

The induced eddy current distribution inside a conductive plate depends on the frequency, thickness, and conductivity of the plate. The detailed calculations for the eddy current distribution is presented in Appendix 1 [6]. Both the magnitude and the phase of the eddy current are well-defined functions of depth. At certain phase angles, the current density below the surface is much larger than that at the surface. We can take advantage of this dependence since the magnetic signal measured by the SQUID is due to the eddy current being disturbed by a flaw in the plate. The magnetic signal from the eddy current at any desired phase relative to the excitation current provides information about the current distribution at a certain depth below the surface. By choosing an appropriate frequency and phase angle, the magnetic signal due to the surface structures can be minimized and the signal due to the flaw at desired depth can be relatively enhanced. The optimum frequency and the optimum phase depend on the conductivity and the thickness of the material, and the location of the flaw of interest. These parameters can be found experimentally.

One specific application has been in the development of a flight-line capable instrument used in aging aircraft NDE. Along with the development of the eddy current inducer itself, we have developed a self-referencing technique to minimize the signal from an axial symmetric structure such as a fastener so that the signal from the fatigue crack emanating from the fastener can be isolated. With the ability to steer the orientation of the induced eddy current, the signal amplitude dependence provides information about the geometry of the flaw as well.

By combining both the depth and orientation dependence of the signal amplitude, location and shape information of flaws can be determined using these induced eddy current techniques. Specific applications, such as the detection of fatigue cracks beneath the rivets in lap-joints, can greatly benefit from this development. This paper will present the theoretical background of the techniques, experimental verification and a few of their applications.

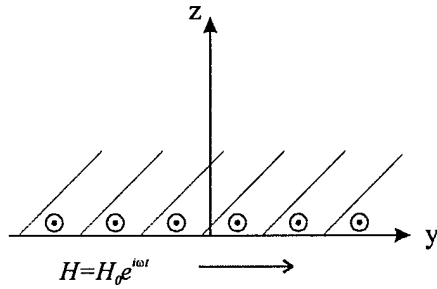
I. Theoretical Background

1. Depth and Phase Sensitivity

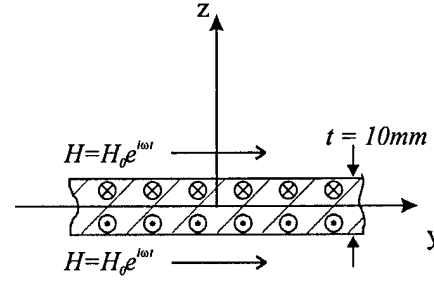
The theoretical calculations for depth-selective eddy current technique using a sheet inducer has been published elsewhere [6]. A conductor, with magnetic permeability μ and electric

conductivity σ , that is of infinite extent in the x - y direction, is placed in a time-varying magnetic field. The field, with angular frequency $\omega = 2\pi f$, is uniform and parallel to the boundary surface, *i.e.*, in the y direction, then the induced eddy current is in the x direction only (see Fig. 2.1a and 2.1b). Both the magnetic field and eddy current are uniform in the plane parallel to the surface of the plate,

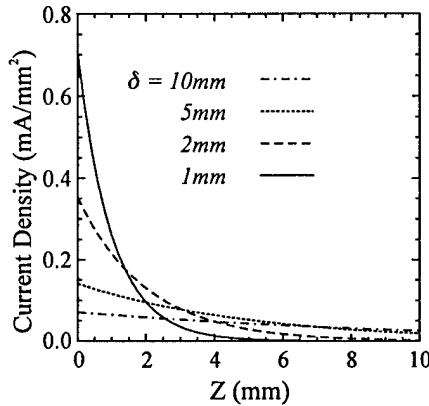
a) Half space



b) Plate with thickness t



c)



d)

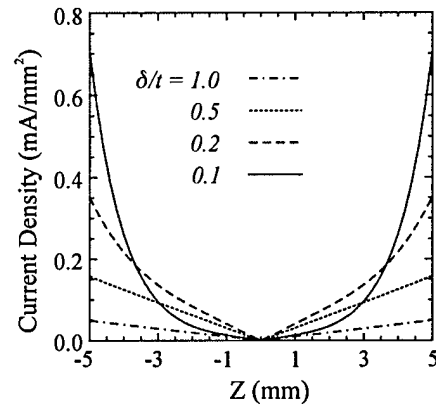


Figure 2.1. (a) The coordinate system for a semi-infinite extended conductor. (b) The coordinate system for an infinite extended conducting plate. (c) The magnitude of the induced eddy current for a semi-infinite extended conductor. (d) The magnitude of the induced eddy current density distribution inside a 10 mm thick conducting plate.

There are two cases:

(1) The conductor is of infinite extent in the positive z direction, as shown in Fig. 2.1a, the eddy current decreases exponentially with (z/δ) , as shown as in Fig. 2.1c, where z is depth and

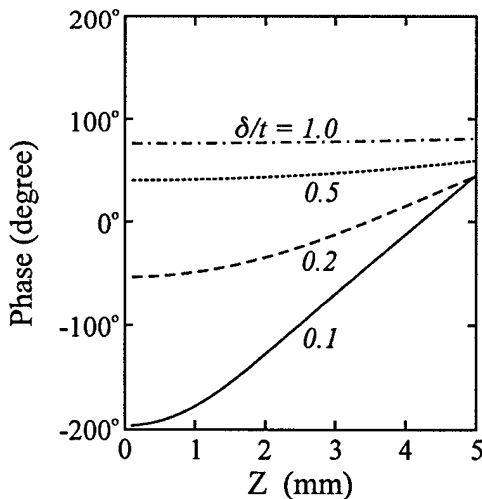
$$\delta = \sqrt{\frac{2}{\omega\mu\sigma}} \quad (1)$$

is termed the skin depth or penetration depth, which is well known [8].

(2). The conductor is a plate with finite thickness, as shown as in Fig. 2.1b, the induced current becomes zero at the center of the plate, and its distribution is asymmetric about the center plane of the plate. Figures 2.1d show the magnitude of the induced eddy current densities for a conducting plate ($t = 10 \text{ mm}$), as a function of z , calculated for $\delta/t = 0.1, 0.2, 0.5, 1.0$. At the center of the plate, the current density vanishes. At higher frequencies, where $\delta \leq 0.1 t$, the current density reduce with depth exponentially within δ (see the solid line in Fig. 2.1d). At lower frequencies, where $\delta \geq 0.5 t$, the induced eddy current density reduces linearly with depth. In this case, the actual penetration depth is no longer the same as δ given by Eq. (1). In fact, increasing δ/t , i.e., reducing the frequency below this point, would not increase the actual penetration of the induced current into the plate.

The phase of the eddy current, which is defined as the difference from the phase of the applied magnetic field and is a well defined function of depth (z/δ), plays an important role in the application. Figure 2.2a is the phase of the eddy current as a function of depth, calculated for $\delta/t = 0.1, 0.2, 0.5, 1.0$. The horizontal axis is the depth for half plate. The phase changes more rapidly at higher frequency. Figure 2.2b is an example of the distribution of the real (solid line) and image (dotted line) component of the eddy current for $\delta/t = 0.1$ through the plate, where the real (or in-phase) component has a phase angle $\phi = 0^\circ$, and the image (or quadrature) component has a phase angle $\phi = 90^\circ$.

a) Phase of eddy current



b) Density of eddy current, $\delta=1\text{mm}$

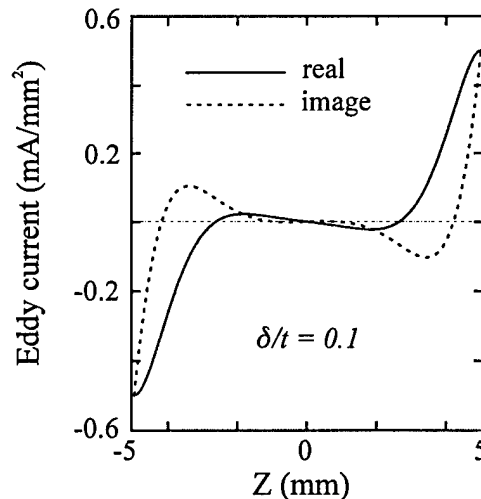


Figure 2.2. (a) The phase of the eddy current as a function of depth, calculated for $\delta/t = 0.1, 0.2, 0.5, 1.0$ within half plate. (b) The eddy current distribution through the plate thickness at phase $\phi = 0^\circ$ (solid line) and $\phi = 90^\circ$ (dotted line) for $\delta/t = 0.1$.

Different from the magnitude of the current in Fig. 2.1, the real (or image) component of the current does not decay monotonically with depth (see Fig. 2.2b). Beneath the surface the polarity of the current changes several times with local nulls. At a particular phase angle, the current on the surface may be even much smaller than that below the surface.

In this research project, the magnetic signal we are interested in is the z component of the field only. Ideally, a uniformly distributed current in x-y plane does not produce magnetic signal. The perturbation of the uniform current would produce a magnetic signal, which amplitude depends on the lift-off distance and the amount of the current disturbed. The phase of the magnetic signal is related to the phase of the current disturbed. The ability to control the depth at which the current density becomes relatively larger is a potentially useful means to adjust depth sensitivity and to search preferentially for non-surface breaking flaws.

Figure 2.3 is a demonstration for depth-selection. Figure 2.3a and 2.3b are the calculated eddy current distribution through a 12.6 mm aluminum plate at phase 45° and 135° . The spaces between the nearest dashed lines are 1 mm. The three shaded areas indicate the current density at the surface, 1 mm below the surface and 2 mm below the surface (with 1 mm vertical extension). At phase 45° the surface current is largest, while at 135° , the current is largest at 2 mm below the surface. Figure 2.3c is a sketch three slots located at the surface, 1 mm and 2 mm below the surface. The amplitudes of the calculated magnetic signals produced by the flaws in Fig. 2.3c are shown in Fig. 2.3d. The surface flaw produces the largest signal at phase 45° , while it produces the smallest signal at phase 135° . The shaded area in Fig. 2.3d indicates the phases, at which the signal from the sub-surface flaw can be enhanced relative to the surface flaw.

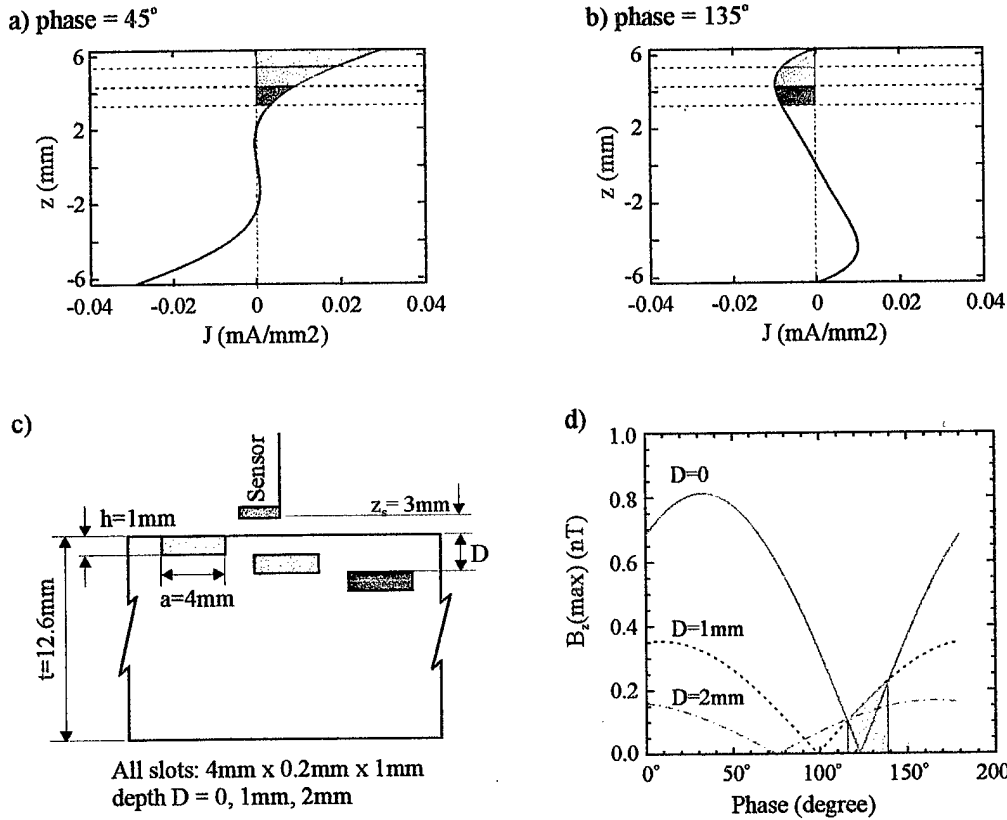


Figure 2.3. The principal for depth-selection. (a) and (b) The calculated eddy current through a 12.6 mm conducting plate at phase 45° and 135° , respectively. The shaded areas indicate the current density within 1mm region from the surface (green), 1mm (red) and 2mm (blue) below the surface. (c) The sketch of the location of the flaw. (d) The amplitude of the magnetic signal, produced by the flaws in (c), as a function of the phase and the depth. The shaded region indicates the phases, at which the surface flaw produces the smallest signal.

2. Magnetic field from orthogonal current

At low frequency, a first order approach to simulate the magnetic signal produced by a flaw is to treat the induced eddy current around the flaw as a perturbation of a uniform current density. The magnetic field may then be calculated by the law of Biot and Savart, just as was done in the case of an injected dc current source [9]:

$$\vec{B}(\vec{r}) = \int_{V'} \frac{\nabla' \times \vec{J}(\vec{r}')}{|\vec{r} - \vec{r}'|} dv' + \frac{\mu_0}{4\pi} \int_{S'} \frac{\vec{J}(\vec{r}') \times \vec{n}}{|\vec{r} - \vec{r}'|} ds', \quad (2)$$

where $\mu_0 = 4\pi \times 10^{-7}$ H/m and \vec{n} is a unit vector normal to the bounding surface and in the outward direction from the region occupied by the current density.

The fields discussed below are all the normal component of the magnetic field. In our previous work, we have calculated and measured the magnetic fields due to uniform dc current disturbed by flaws inside the conductor [A-1,10,11]. Different from the dc current, the eddy current density varies with the depth, and thus the expressions for dc current have to be modified. At high frequency, the amplitude of the magnetic signal due to a subsurface structure may be reduced, and its phase may be shifted due to shielding effect.

Since the strength of the signal depends upon the cross section of the flaw in the direction of the current [A-2] for a fixed lift-off distance, changing the orientation of the eddy current may optimize the sensitivity of detection.

For an axial symmetric flaw or structure, such as a hole, the magnetic signal is independent of the orientation of the current, while for an axial asymmetric flaw, such as a slot, the amplitude of the signal is orientation dependent. The relative variation of the amplitude provides the information about the geometry of the flaw, that is useful for eliminating the signal from the symmetric structure. For example, extracting the signal due to a crack from a rivet. For such application one measurement requires a series of data with different current orientations.

The vector current density J in Eq. 2 can be decomposed as two independent orthogonal currents, J_x and J_y ,

$$\vec{J}(\vec{r}') = \vec{J}_x(\vec{r}') + \vec{J}_y(\vec{r}'),$$

then the magnetic field

$$\vec{B}(\vec{r}) = \vec{B}_x(\vec{r}) + \vec{B}_y(\vec{r}),$$

where B_x and B_y are corresponding to J_x and J_y , respectively. If both J_x and J_y are constant through the x - y plane, the resultant current has a well-defined direction. This provides us with a method to produce a magnetic image corresponding to the current with a desired orientation from two separate images that are corresponding to two independent orthogonal currents mathematically.

Figure 2.4 shows two configurations for composition:

a) Both currents with frequency ω in-phase. The magnitudes of each current, J_x and J_y , are determined by the desired angle α of the resultant current, $J_y/J_x = \tan\alpha$, as shown in Fig. 2.4a. The resultant current is also sinusoidal and has the same phase as each current, but is oriented at a fixed angle α with respect to the current in the x -direction.

b) Both currents with frequency ω and magnitude I_0 but with a phase difference of 90° , as shown in Fig. 2.4b. The resultant current $J(t)$ has a magnitude J_0 that is time-independent, but with an orientation angle that rotates with time, $\alpha = \omega t$, with a frequency the same as the frequency of the ac current. The in-phase ($\alpha = \omega t = 0^\circ$) and the quadrature ($\alpha = 90^\circ$) components are one set of orthogonal currents. The magnetic field image corresponding to the current with an angle α can be obtained by the in-phase and quadrature components.

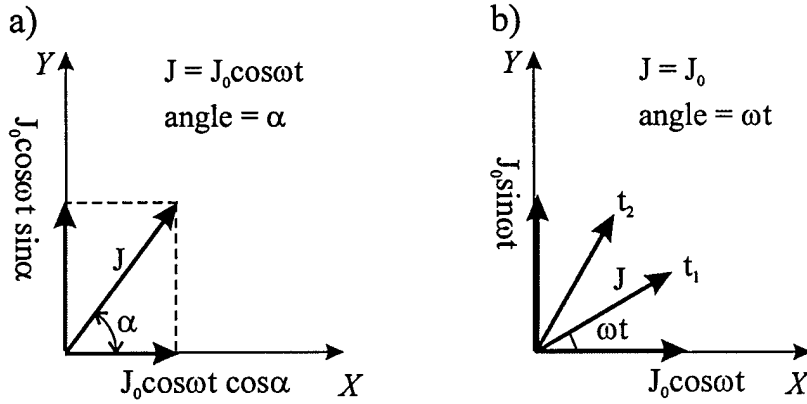


Figure 2.4. The sketch of the current composing. (a) The resultant current is sinusoidal, but has a fixed angle with respect to I_x . (b) The resultant current has a constant magnitude, but rotates its orientation with a frequency ω .

The configuration (a) is a better choice for the application of depth-selection because its phases provide the depth information. If B_x and B_y are the magnetic images due to the current J_x (oriented at 0°) and J_y (oriented at 90°), respectively, and

$$J_x = J_y = J_0,$$

the magnetic field B_α corresponding the current J_0 oriented at an angle α can be obtained mathematically

$$B_\alpha(\vec{r}) = B_x(r) \cos \alpha + B_y(r) \sin \alpha.$$

The superposition of the two images, obtained from two separate measurements when the corresponding currents are orthogonal, is equivalent to the image obtained from one measurement with the current angle, $\tan^{-1}(J_y/J_x)$. We have verified this experimentally.

There are two major effects when the angle of the current changes: both the orientation of the dipolar signal and its amplitude change. The orientation of the dipole implies the orientation of the current that is disturbed. Fig. 2.5 shows the amplitude of the dipole for the hole does not change but rotates with the current angle. It is important to note that the behavior is opposite for the slot. The orientation of the dipole due to the slot does not rotate but merely changes in amplitude as the current direction is changed. The amplitude for the slot is almost zero at 90° (parallel current). This is expected because the thin slot does not disturb the current significantly in the direction parallel to the slot. This different dependence on current angle provides us with a method to distinguish the signal due to the slot from the signal due to the hole, which is termed self-referencing. The detail of the self-referencing method will be discussed in Part III.

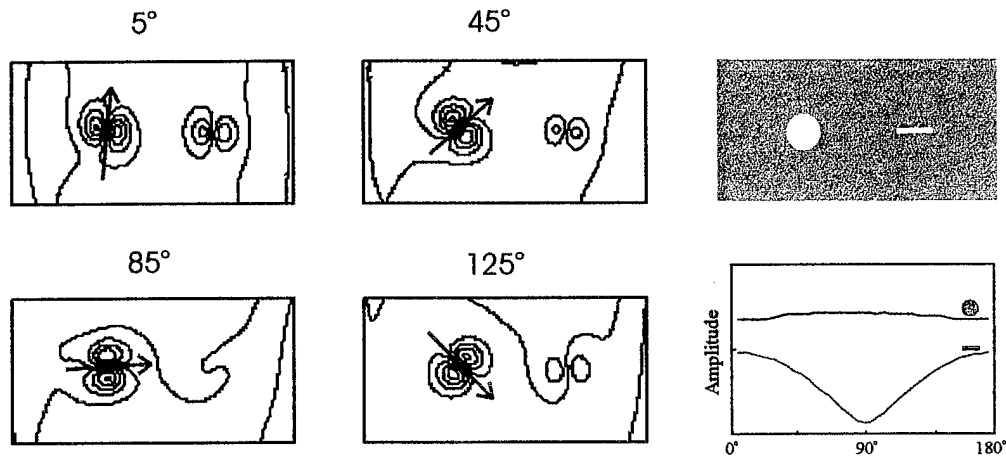


Figure 2.5. The field maps of the magnetic signal due to a 0.5-inch diameter circular hole and a 0.5-inch long thin slot as a function of eddy current direction. The plot shows the amplitude of the dipole signal for the hole and the slot. Ideally, it should be a constant for a perfect hole.

II. Sheet Inducer

In principle, a current sheet of infinite extent produces a spatially uniform magnetic field, which may induce an eddy current with a well-defined direction inside a conducting plate parallel to the current sheet. As shown in Fig. 2.6, a current sheet along the x direction produces a magnetic field along the y direction. The magnitude of the field is $H_0 = I_e / 2$, where I_e is the excitation current per unit width.

The eddy current sheet inducer has gone through a progression of design improvements over the past several years. However, the basic design remains the same and the changes reflect modifications in sheet inducer fabrication and incorporation of new techniques, such as inducing eddy currents in orthogonal directions. The basic design of the inducer is a sheet of conducting strips or wires that will induce planar, unidirectional eddy currents in a planar sample located above or below it.

Figure 6 shows the inducer placed below the sample. In this case, the inducer should be larger than the dimension of the sample to reduce the affect of the edge field of the inducer itself. This requires the use of a large-sized inducer for large test specimens. A better approach is to rigidly attach the sheet inducer beneath the SQUID sensor above the sample. With the inducer centrally fixed beneath the sensor coil, the inducer is basically silent, and does not require a sample dependent geometry. The dimension of the sheet inducer here should be larger than both the lift-off distance (the distance between the sensor and the test sample), and the diameter of the pick-up coil. Figure 7 shows a rule-of-thumb that can be used for designing the width of the inducer as a function of lift-off and pick-up coil radius.

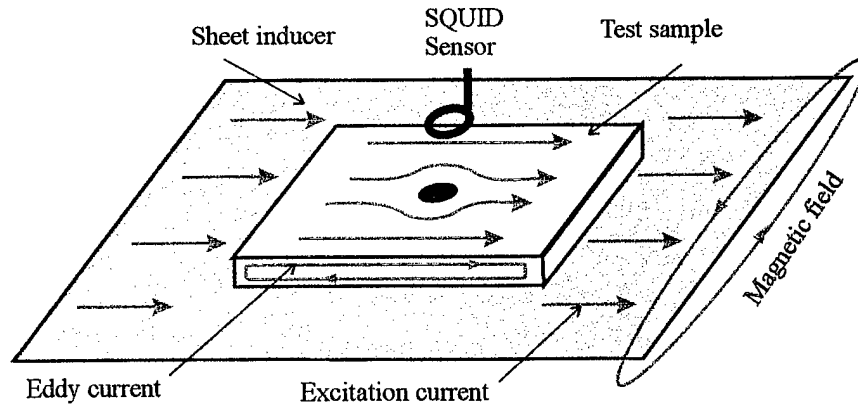


Figure 2.6 The sheet inducer, carrying excitation current along the x direction, creates a magnetic field tangential to the plane.. The induced eddy currents in the test sample are disturbed by the flaw and produces a magnetic signal which is detected by the SQUID magnetometer located above the sample..

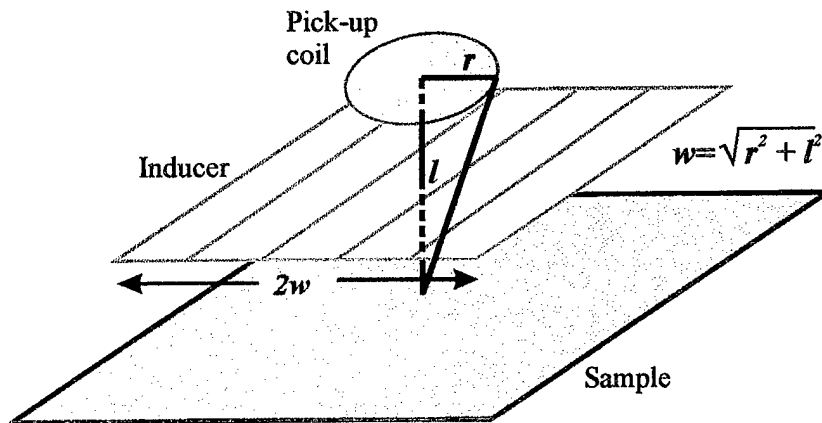


Figure 2.7 The rule-of-thumb used for inducer designing.

The schematics shown in Fig. 2.8 show the progression of the design development of the eddy current sheet inducer.

The first was a 300- μm thick copper sheet that had been divided into a set of 2-cm wide parallel strips which were serially connected with a low frequency ac voltage source to minimize distortion of the inducer current distribution by the sample (see Fig. 2.8a). In these earlier uses, the inducer was located under the test sample and moved along with the sample on the scanning stage. This required large inducers to avoid unwanted signal from the inducer edges.

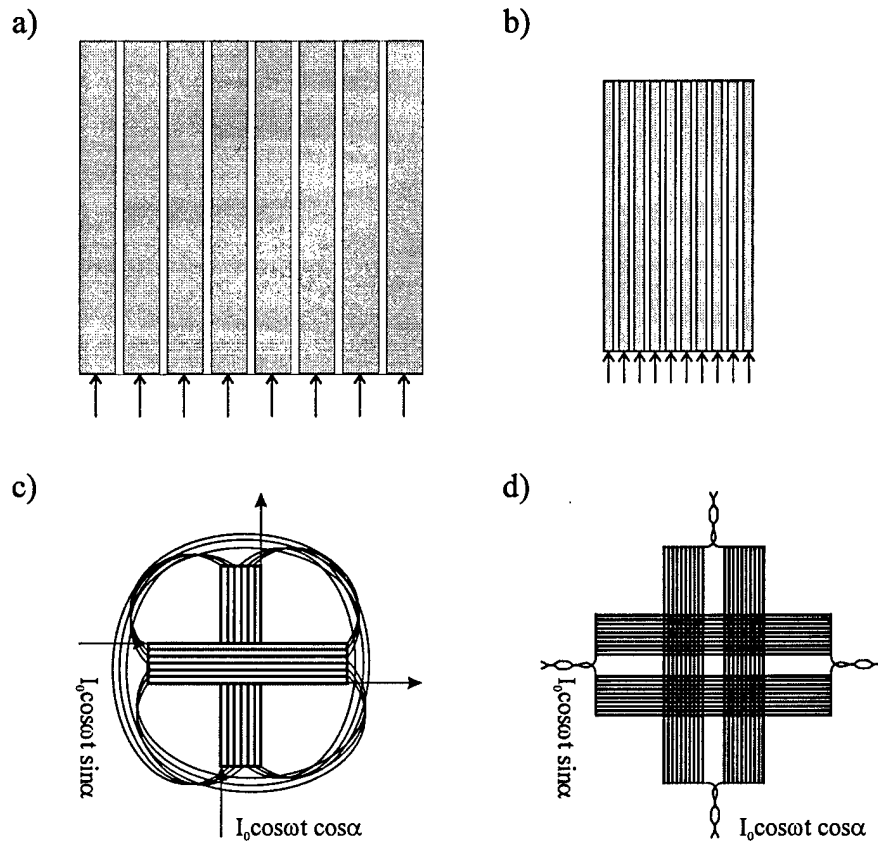


Figure 2.8 Design progression of eddy-current sheet inducers a) Copper sheet with wide strips, b) Single flexible flat cable, c) Orthogonal flexible flat cables, and d) Double sided printed-circuit board.

To provide a more uniform induced current to a large sample over the scanned area without large inducer size, a small 16-wire flexible flat cable replaced the large striped sheet inducer (see Fig. 2.8b). This was rigidly attached to the sensor between the sensor and the sample. This kept the inducer fixed with respect to the sensor and minimize the background due to the inducer, and ideally for the sample without the access to the bottom. This inducer could be physically rotated 90° in order to measure orthogonal information.

Figure 2.8c shows the next modification which was to overlap two of these flat cables at 90° to one another in order to obtain measurements for both orthogonal current directions simultaneously. This eliminated the need to physically rotate the inducer. The magnetic image for a certain current orientation may be obtained either mathematically or by adjusting the ratio of the current between the two orthogonal current sheets.

The most recent design change was to replace the two orthogonal flexible flat cables with a 0.010-inch thick double-sided printed circuit board (see Fig. 2.8d). Each wire strip is 1.5

mm wide and separated by 0.5 mm. The 4 wires at the center were not connected to the source. Using printed circuit board masking techniques allows for more flexibility in inducer design, insures precise orthogonality of the two current directions, and transfers easily to commercial production.

Note that the orthogonal inducer creates a current with a well-defined orientation only at the region where the two inducers are overlapping.

III. Depth-selective and Self-referencing Technique

1. Optimization

As discussed in section I, the depth-selective technique can be used to enhance the signal from a subsurface flaw by maximizing the phase shift between the current density at the surface and the desired depth. The maximum phase shift depends on the thickness and the conductivity of the test object and the frequency. For a given sample, the optimum frequency may be found experimentally.

For demonstration purposes, we have examined a sample comprised of two layers of 1.6-mm thick aluminum plate containing simulated flaws (see Fig. 2.9). The simulated lap-joint contained a separate hole and slot in the top layer while the bottom layer contained a connected hole and slot.

To improve the detection of second layer slot, the self-referencing technique can be used in conjunction with the capability to measure as a function of depth. At a particular phase angle, the eddy current at the surface becomes zero, while the eddy current below the surface becomes relatively larger. Since the magnitude of the magnetic signal due to a slot depends on the current disturbed by the slot, when the signal due to the surface structures is minimized, and the signal due to the subsurface slot is enhanced at this particular phase angle.

Figure 2.9 shows the magnetic images for the frequencies of 230 Hz, 1.1 kHz, and 5.4 kHz, respectively. The in-phase images (phase = 0°) show that the first-layer flaws are the largest contributors to the magnetic signal, especially at the higher frequencies. The quadrature images (phase = 90°) show where the second layer signal has a much larger signal ($f = 1100$ Hz) relative to the first layer signals and tells us the operating conditions to optimize detection of this particular flaw.

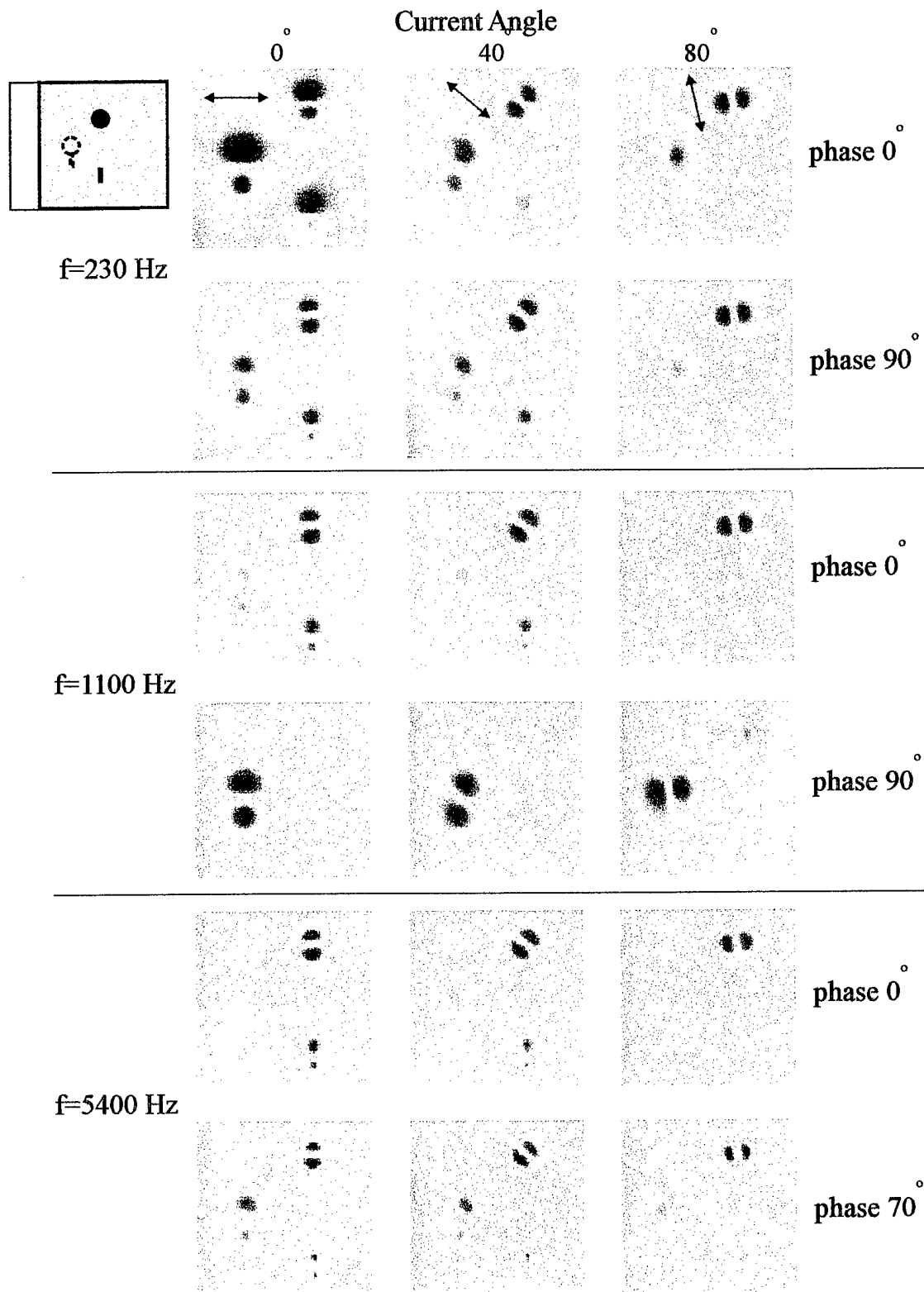


Figure 2.9. Magnetic maps for simulated flaws as a function of inducer frequency, phase angle and current direction.

To determine optimal phase and current angle for maximizing the signal from the second layer flaw at different frequencies, the relative signal amplitudes for the hole, slot and the hole/slot combination as a function of phase and current angle are plotted in Fig. 2.10. This gives us a more quantitative approach over direct visual examination of the magnetic maps shown previously. At a low frequency (230 Hz), the signal from the second layer hole/slot combination (dashed blue line) is comparable with the signal from the first layer flaws, which means that the eddy-currents penetrate both layers. Because of this, the phase shift between the second layer and the first layer is small making it difficult to separate the second layer signal from the first layer signal. At the high frequency (5.4 kHz), the second layer signal is too small to distinguish from the first layer signal no matter how large the phase shift is. Of the three frequencies tested, the mid-range frequency (1.1 kHz) produced the largest phase shift ($\sim 50^\circ$) and the second layer signal was easily distinguished from the first layer signals for current angles ranging from 70° to 110° (shown as shaded).

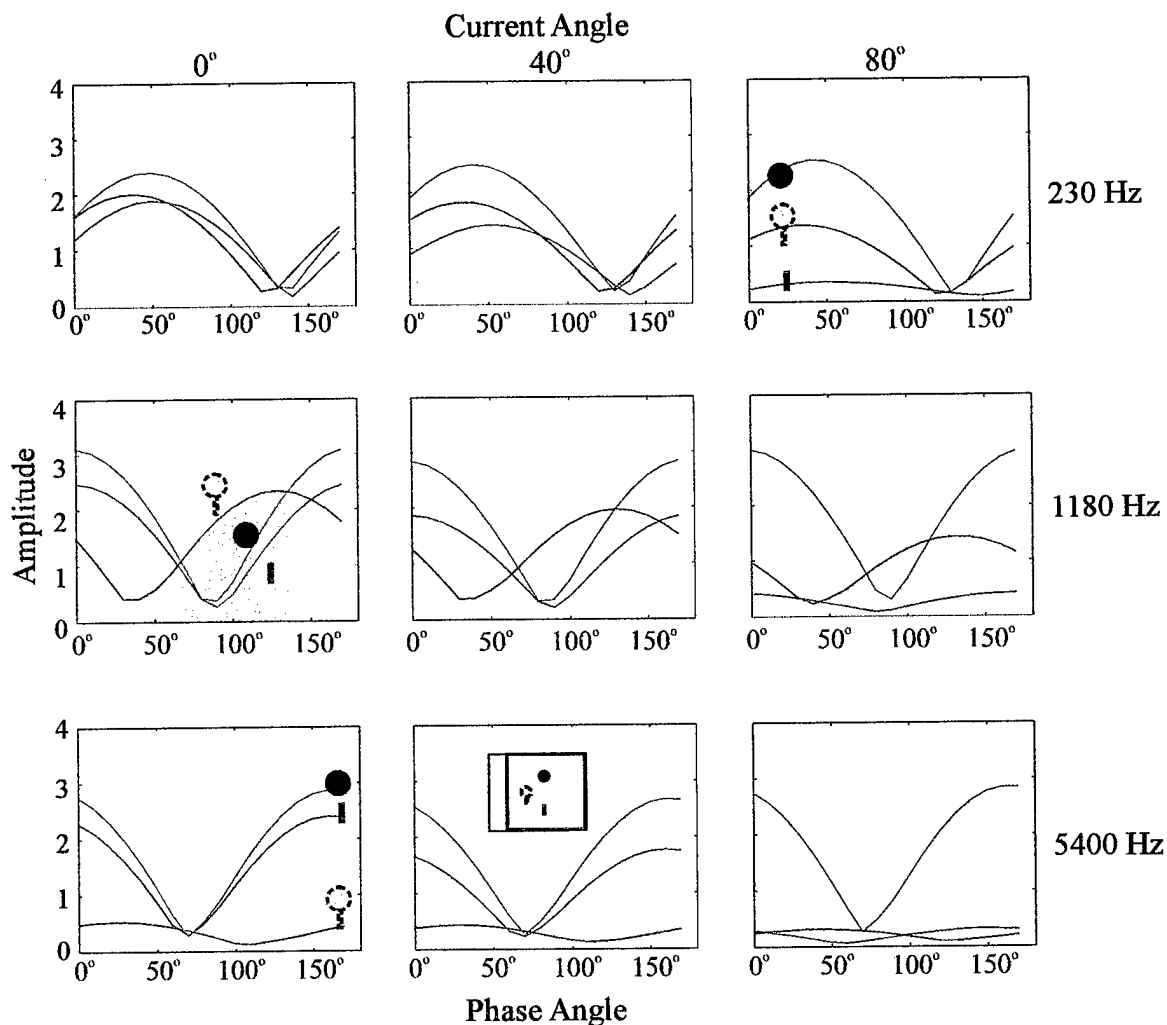


Figure 2.10 Signal amplitude as a function of phase angle for fixed current angles. The shaded area represents the optimal operating range of phase angles to detect the second layer hole/slot combination.

2. Self-referencing

The self-referencing method takes advantage of signal asymmetries associated with particular flaws. For a uniformly distributed induced current, a hole produces signals with constant amplitude independent of the current direction. An asymmetric factor, which is a measure of non-roundness, can be defined as

$$A = \frac{S_{\max} - S_{\min}}{S_{\max} + S_{\min}},$$

where S_{\max} is the maximum and S_{\min} is the minimum signal amplitude. A perfectly round flaw would have $A=0$ and a very narrow slot would have $A \rightarrow 1$.

The self-referencing can be applied by varying the induced current orientation at that fixed phase angle. Using the data taken for the sample in Fig. 2.9, we demonstrate how this technique works. Figure 2.11 shows signal amplitude as a function of current angle for fixed phase angles for the hole, slot, and hole/slot combination. The first layer hole (green line) shows little asymmetry as expected. The amplitude dip for the hole at 45° and 135° is caused by the inhomogeneous inducer used, shown in Fig. 2.8d. The first layer slot (red line) shows a large signal at a current direction of 0° (perpendicular to the slot) and almost zero signal at 90° (parallel to the slot) corresponding to large asymmetry. The blue dashed line is for the hole/slot combination at the second layer and also shows some dependence (asymmetry) on current direction.

From this, the calculated asymmetry value for the hole/slot combination will then be the best measure of the crack; the larger the asymmetry, the larger the crack. If no asymmetry is present, then either no crack is present or the minimum detection limit of the system has been reached.

Figure 2.12c is a representative plot of asymmetric factor A corresponding to the data in Fig. 2.11 showing that the asymmetric factor is highest for the slot and lowest for the hole. This can be used for setting flaw detection thresholds in situations where the flaw is located near a rivet head.

The asymmetry factor can be affected by the proximity of the flaw to an edge or to another flaw since this disturbs the eddy current distribution, especially at lower frequencies. Because of this, a round hole close to an edge or to another flaw may produce a signal that is dependent on the current orientation and $A \neq 0$.

If a crack adjacent to a rivet at second layer is the object for detection, the combination of the depth-selective and self-referencing technique can be summarized in the following steps:

- 1) Acquire in-phase and quadrature data using orthogonal inducers for several frequencies. Frequency determination can be done experimentally or estimated using the standard skin depth formula.

2) Plot signal amplitude as a function of phase angle using both the in-phase and quadrature data. This should be done for incremented current angles to determine where the signal from the second-layer flaw is most distinguishable from the first-layer flaws.

3) Once the signal separation has been optimized as a function of frequency, current angle, and phase angle, determines the signal asymmetry by plotting the signal amplitude as a function of current angle at the optimized frequency and phase angle. The amount of signal asymmetry will then reflect the size of the second-layer flaw when calibrated against unflawed signals.

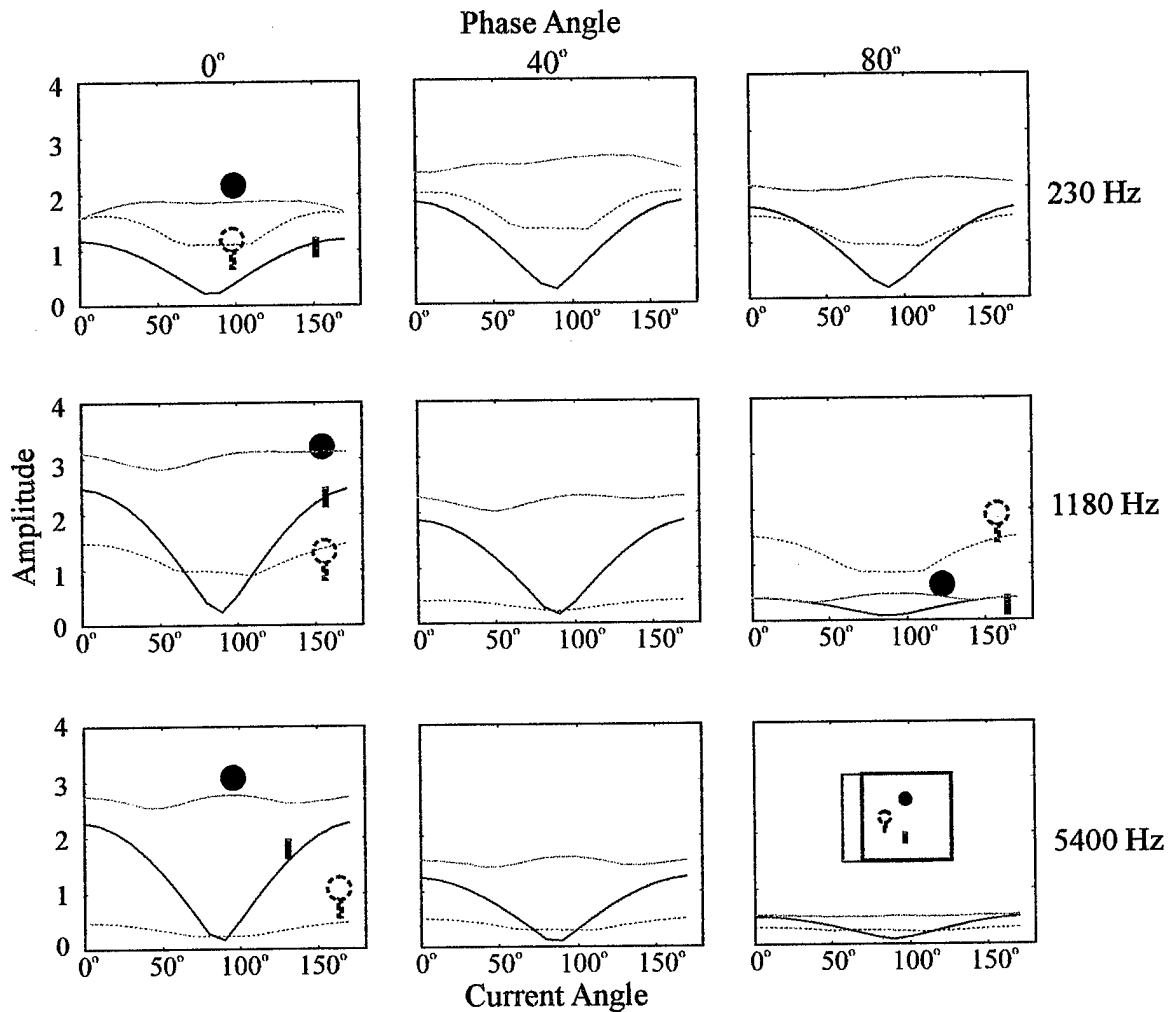


Figure 2.11. Signal amplitude as a function of current angle for fixed phase angles.

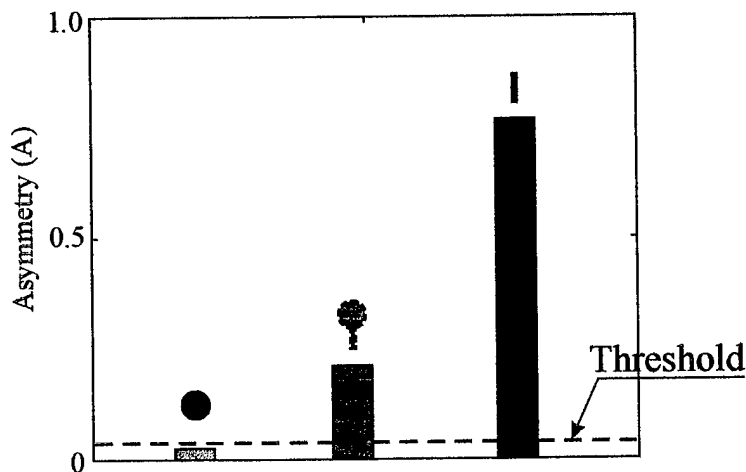


Figure 2.12 Representative asymmetry factors displayed for one frame of Fig. 2.11 (phase=40°, f=230 Hz)

IV. Applications

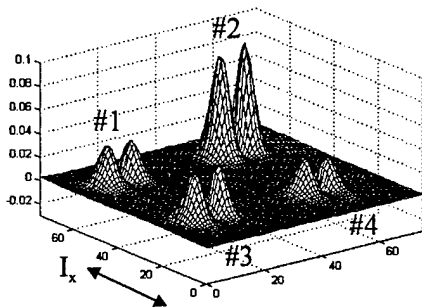
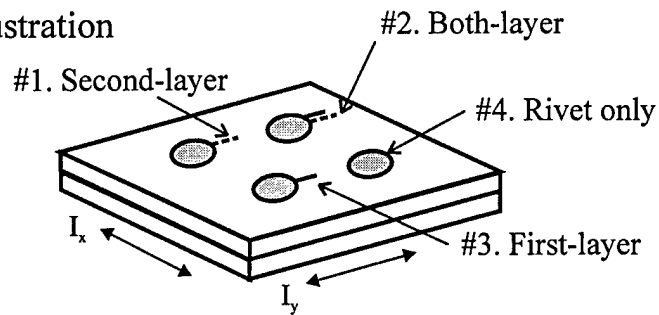
1. Detection of Slots in a Lap-Joint

This technique has been tested with a sample provided by Lockheed, as shown in Fig. 2.13a. The test sample is made of two 0.125-inch thick 7075-T6 aluminum plates bolted together by four 0.25-inch diameter flat-head aluminum fasteners that simulate the rivets. The crack defects beneath the rivet are simulated by 0.25-inch long EDM slots. As shown in Fig. 2.13a, adjacent to rivet #1 there is a 0.25 inch slot at the second layer, adjacent to rivet #2 there are two slots in both the first and second layers. Beneath rivet #3 is a slot in the first layer, and rivet #4 without any slots is used for reference.

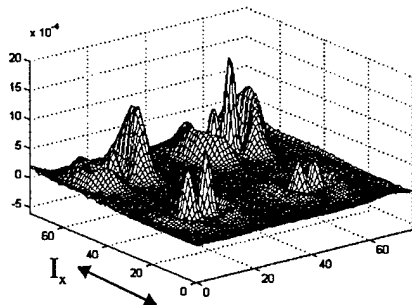
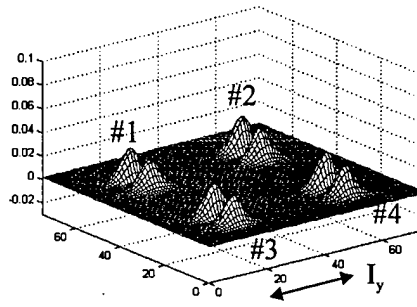
The magnetic field maps shown in Fig. 2.13 are the results from two separate scans using two orthogonal currents I_x and I_y . For each scan, both the in-phase and quadrature signals are recorded. Then the field maps corresponding to a particular phase are obtained mathematically.

The left column is for the current across the slots. At phase 0°, the amplitude of rivet with the second layer slot (#1) is smaller than that of rivet with first layer slot (#2), and larger than that of the reference rivet (#4). This indicates that both the first and second layers contribute to the signal, however, the first layer dominates. At phase 85° (Fig. 2.13c) the quadrupole signals appear, where the sharper peaks are related to the first layer and the broader peaks are related to the second layer. At phase 95° (Fig. 2.13d), the sharper peaks disappear and the second layer dominates. The amplitude of the rivet with second layer slot (#1) becomes as large as that of the rivet with slots in both layers, While the signal from the rivet with the first layer slot (#3) is same as that from the reference rivet.

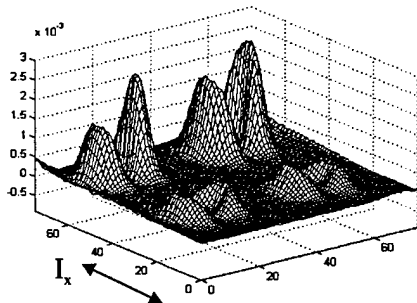
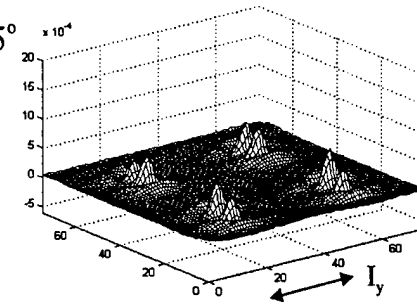
a) Sample illustration



b) Phase 0°



c) Phase 85°



d) Phase 95°

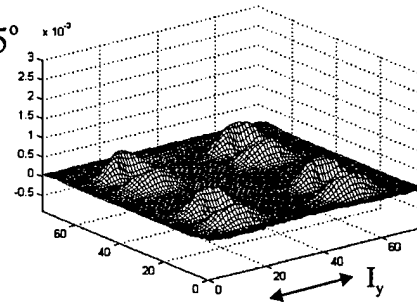


Figure 2.13 Magnetic field maps obtained by an orthogonal inducer. a) The sketch of the Lockheed test sample. b), c) and d) The field maps at phases 10° , 85° , and 95° for currents in both orthogonal directions

The right column is for the current parallel to the slots. The signals from the four rivets are similar to the signals from the reference rivet in left column.

Figure 2.14 shows the asymmetry factors obtained by combining the depth-selective technique with the self-referencing method. For phases of 10° and 95° , the amplitude of the signals are taken from the field maps corresponding to current angles ranging from 0° to 180° , as shown in Figs. 2.14a and 2.14b. The asymmetry factors F_{as} at phase 10° and 95° are shown in Fig. 2.14c and 2.14d, respectively. The minimum F_{as} , obtained in the phase from 0° to 180° for the reference rivet #4, is 10% and is chosen as a threshold indicated by the dashed line. The asymmetry factor of rivet with the second layer slot (#1) is below the threshold at phase 10° (see Fig. 2.14c), however, it is well above the threshold at phase 95° (Fig. 2.14d). The non-zero asymmetry factor of the reference rivet #4 is believed to be due to the misalignment of the rivet.

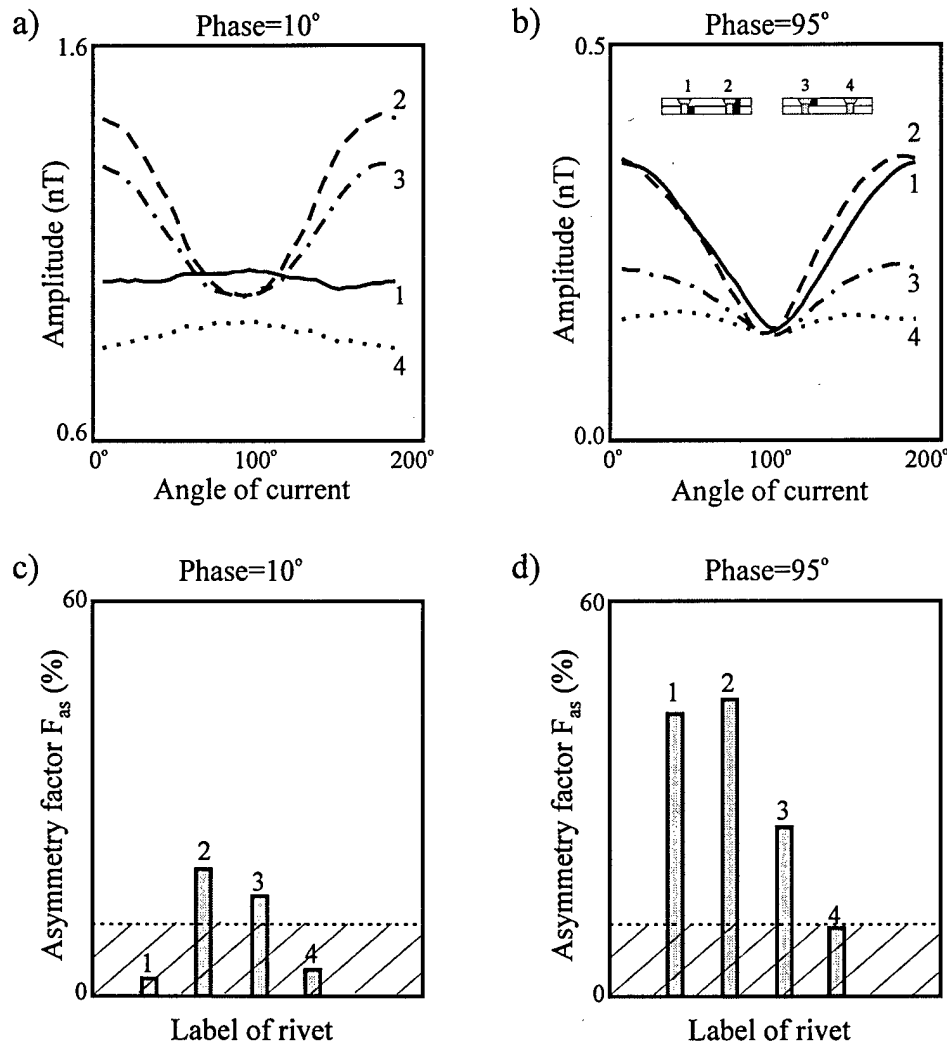


Figure 2.14. Depth-selective, self-referencing method using an orthogonal sheet inducer. (a) The amplitude at phase 10° . (b) The amplitude at phase 95° . (c) The asymmetry factor at phase 10° . (d) The asymmetry factor at phase 95° . The dashed lines indicate the threshold for slot detection.

2. Real Fatigue Cracks in a Lap-Joint

To examine more realistic fatigue cracks, a sample, which provided by Task 5, was used. It had been mechanically stress cycled causing fatigue cracking along one rivet row (#1 - #3) while the other rivet row (#4 - #6) is used for reference purposes (see Fig. 2.15a). Figure 2.15b shows the resulting surface maps of both the in-phase and quadrature signals for longitudinally induced currents. Similarly, Fig. 2.15c shows the maps for transversely induced currents. Due to the proximity of certain rivets to edges and the affect this has on the induced eddy currents, signal comparison is best done between rivets with similar edge conditions (e.g., #1 and #4).

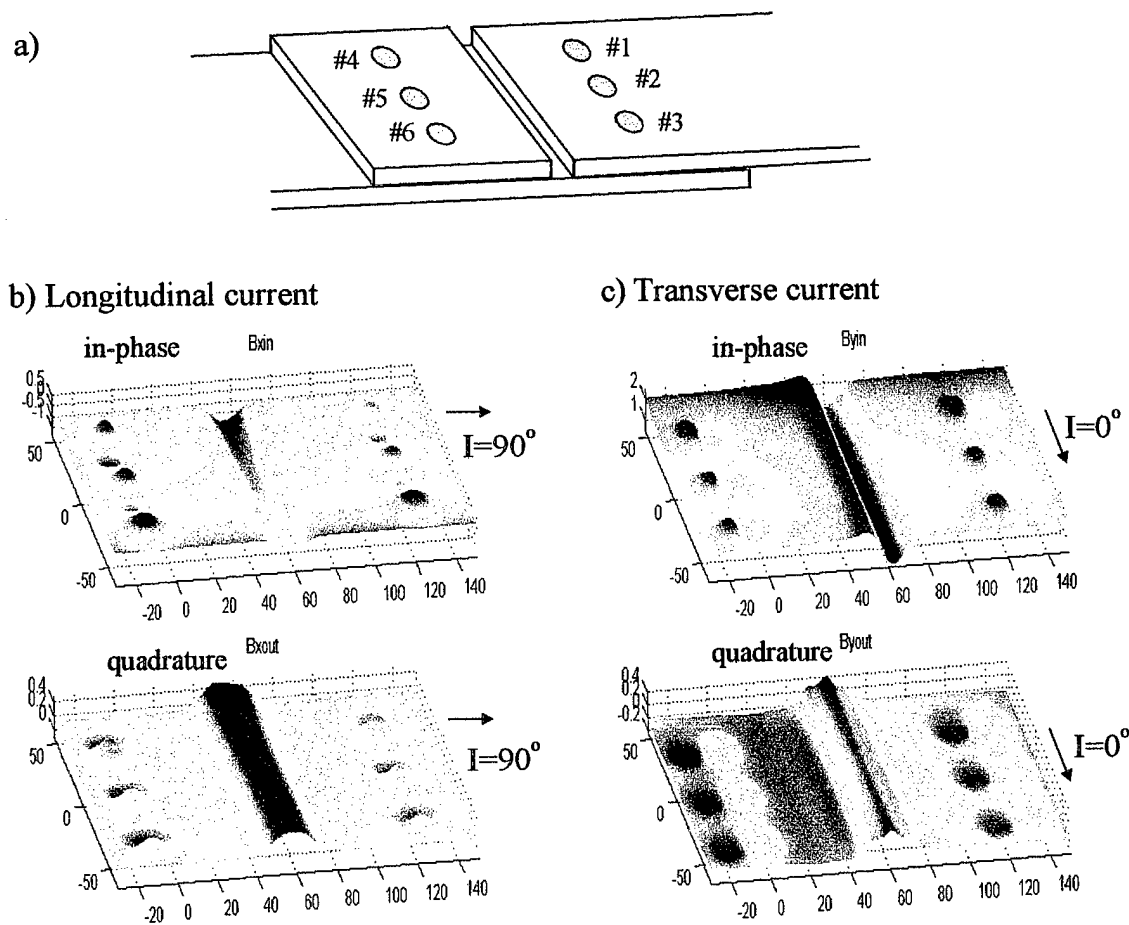


Figure 2.15 Mechanically stress-cycled sample. a) schematic showing a row of stressed rivets (#1-3) and row of reference rivets (#4-6). b) Magnetic field maps showing in-phase and quadrature signals for induced longitudinal currents. c) Images showing in-phase and quadrature signals for induced transverse currents.

Figure 2.16 shows the change in signal amplitude (Δ) versus current orientation, referenced to 0° , for similar-rivet pairs. A large difference between the red lines and the blue lines indicate evidence of cracks. The maximum Δ occurs at 90° , which is consistent with the expected direction of the fatigue cracks being along the rivet row (maximum signal when current is transverse to crack). Ideally, the reference rivets (blue) should be flat, but edges and imperfections cause deviations from this. The small dip in all curves around 45° is due to the inducer design. The largest difference of the three pairs is between #3 and #6 suggesting that #3 had a larger crack with #1 having the next larger size crack. The data is consistent with the measured total lengths of the fatigue cracks: #1 – 4.41 mm, #2 – 3.53 mm, and #3 – 4.66 mm, shown in Table 5.7.

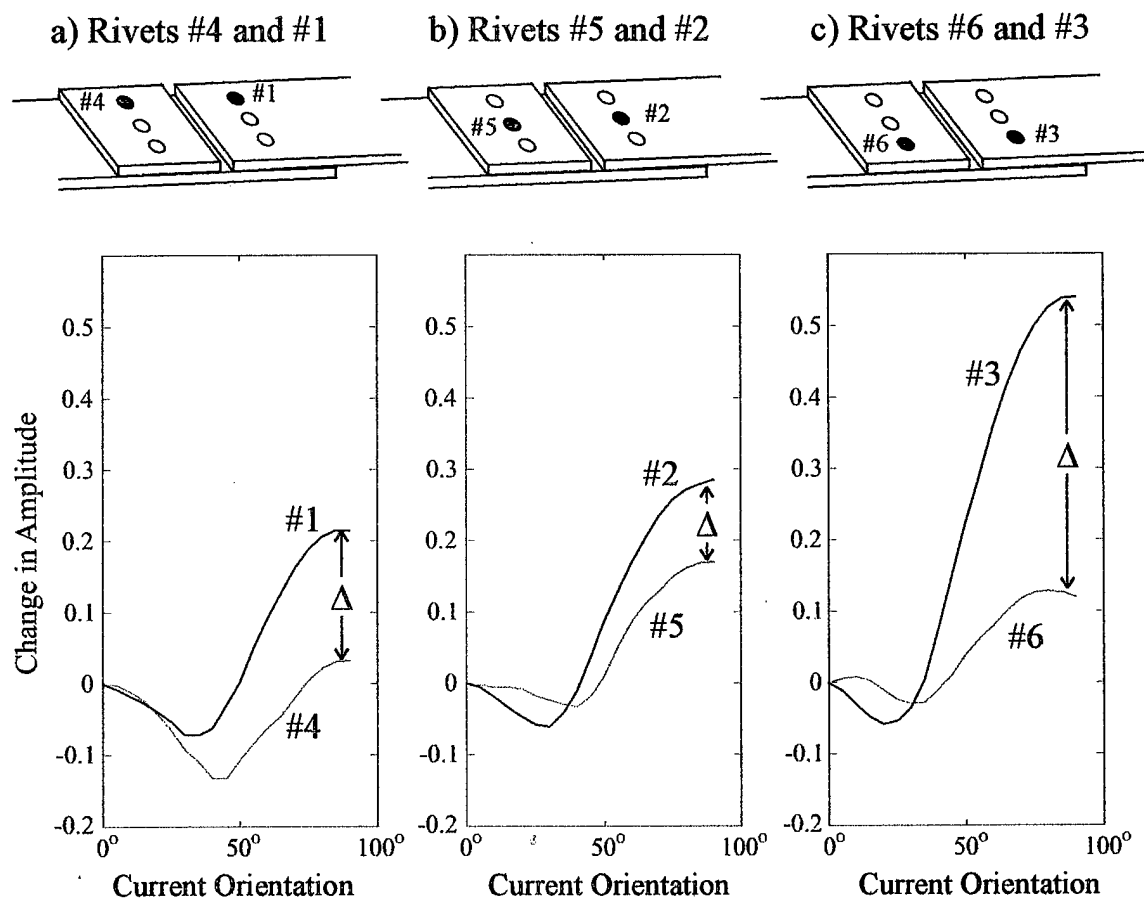


Figure 2.16. Change in peak-to-peak signal amplitude as a function of current angle (asymmetric factor) for the 3 rivet pairs. The difference Δ between the red (fatigued) and blue (reference) lines indicates cracks.

3. Homogeneity of Material

The test samples were provided by ALCOA. The aluminum alloy samples are 225 x 300 mm plates 18 mm thick.. Sample #1 is 7075-T6 and #2 is A356 (Fig. 2.17a). Six 1.2-mm diameter flat bottom holes with varying depth are open at one surface. The distance between the bottom of the holes and the other surface is 2 mm, 5 mm, 8 mm, 10 mm, 13 mm and 16 mm. Figure 2.17b is sample #6, which is 18-mm thick 7075-T6 plate, with two 1.2 mm diameter holes open at one surface and the distance between the bottom of the holes and the other surface is 2 mm. A 14.8 mm long, 1.2 mm diameter cylinder, which is made of same aluminum alloy, is inserted into one hole in such way that the 1.2 mm at the bottom of the hole remains unplugged (see Fig. 2.17d).

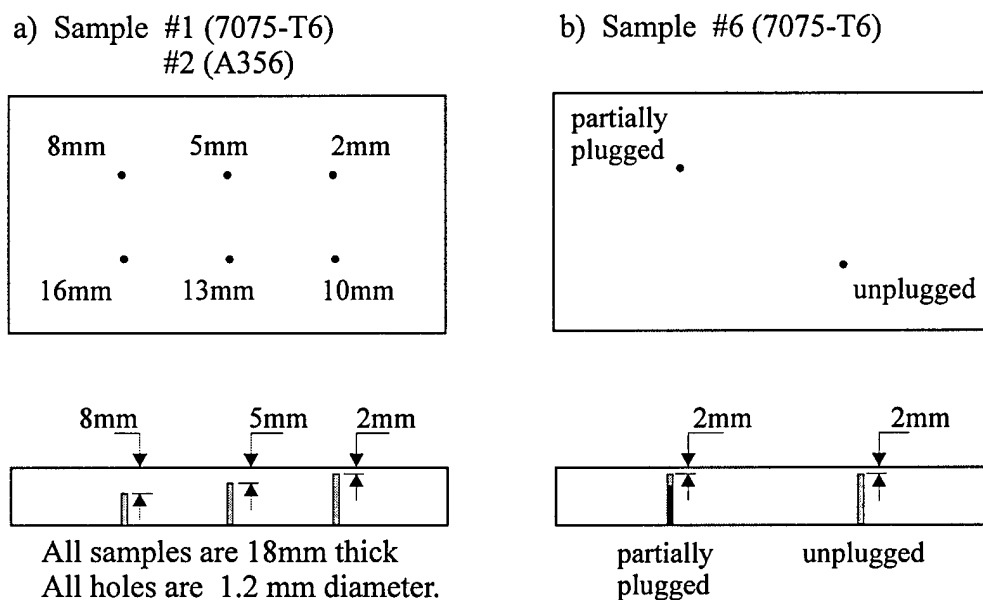


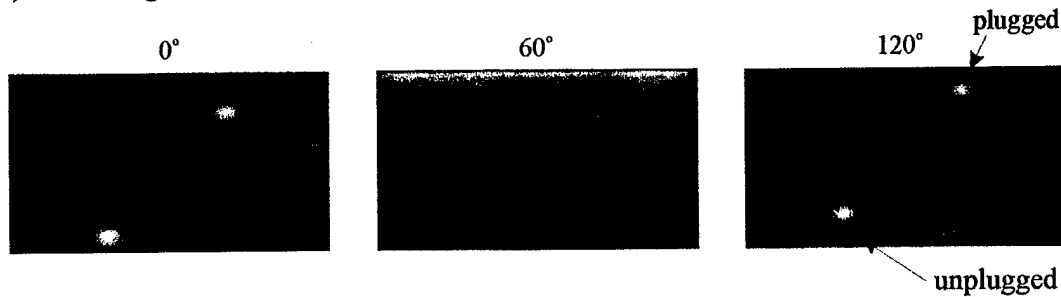
Figure 2.17 ALCOA aluminum alloy plates. a) Flat-bottomed holes of varying depth
b) Plugged vs. unplugged flat-bottomed holes.

We have tested samples at frequencies from 35 Hz to 750 Hz. The results presented are recorded at 250 Hz. For each sample, both surfaces were scanned with two orthogonal current inducers.

Sample #6 is a 18mm thick 7075-T6 aluminum plate with two holes, one of which is partially plugged with an aluminum cylinder. The images after digital processing are shown in Fig. 2.18a and 2.18b, for the surface with holes and the surface without holes, respectively. In Fig. 2.18a, the unplugged hole (lower left) produces a larger signal than that of the plugged hole. When the surface is reversed, the signal from the unplugged hole (upper left) is smaller than that from the plugged hole. This result is in agreement with the

prediction made by theoretical calculation. The eddy current induced by a sheet inducer is flowing in the opposite direction between the upper half and lower half of a plate. If the hole is extended through more than half of the plate, the signal from the top half may be partially canceled by the signal due to the lower half.

a) The image of surface with open holes



b) The image of surface without holes

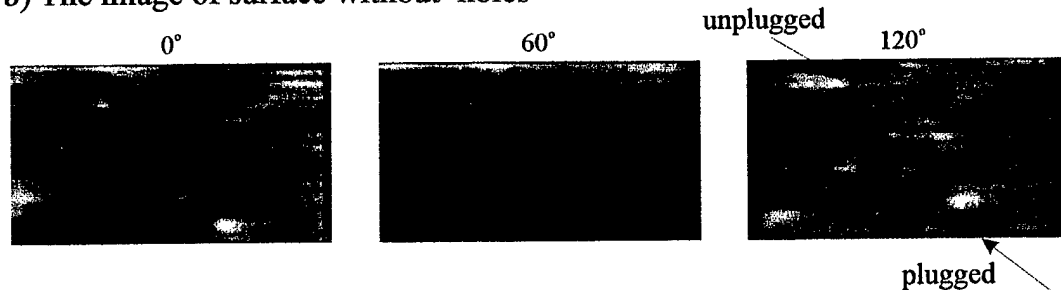
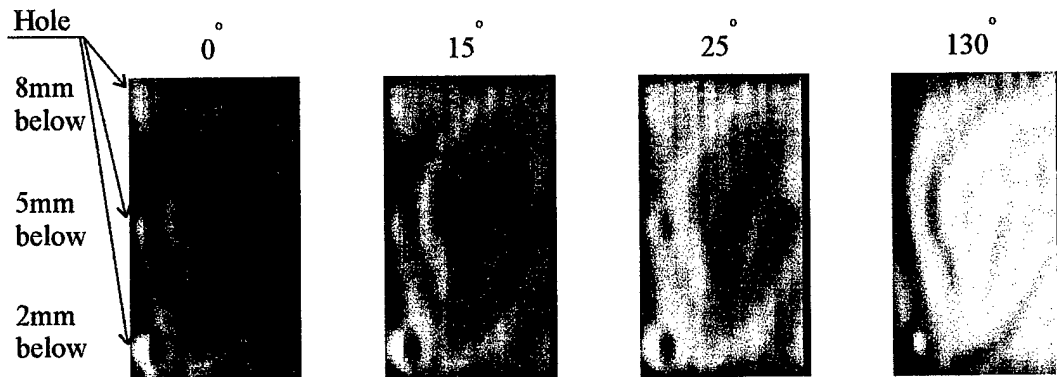


Figure 2.18 The images for an 18mm thick 7075-T6 aluminum plate with two 1.2 mm diameter holes at 2 mm below the surface(see Fig. 2.17b). (a) The surface with open holes. (b) The surface without open holes.

Figure 2.19 are the images at four different phases for sample #1, an 18mm thick 7075-T6 aluminum plate with six 1.2mm diameter holes beneath the surface. There are three dipolar signals due to the holes at 2 mm, 5 mm and 8 mm below the surface, as indicated by the arrows. The images for the current in the longitudinal direction are shown in Fig. 2.19a. Besides the dipole signals due to the holes, there is a large irregular signal over the entire sample, of which the origin is unknown. Because of this large background signal, the other holes can not be observed.

Additional measurements were made to verify that the large background signal was not an artifact of this one measurement. Figure 2.19b shows images for current in the transverse direction using a different inducer and frequency. The orientation of the dipole signals associated with the holes rotate 90° as expected. The irregular background signal is similar to that shown in Fig. 2.19a showing that it was not an artifact of the first measurement.

a) Longitudinal current, $f=170\text{Hz}$



b) Transverse current, $f=250\text{Hz}$

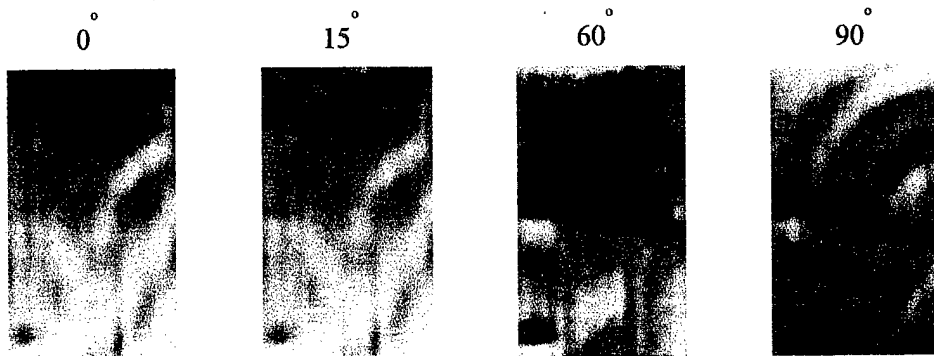


Figure 2.19 The images at four different phases for an 18-mm thick 7075-T6 aluminum plate with six 12 mm diameter holes beneath the surface (a) using a narrow inducer oriented in the longitudinal direction (up-down). The arrows indicate the dipolar signals due to the holes at 2 mm, 5 mm, and 8 mm beneath the surface. (b) using a wider inducer oriented in the transverse direction (left-right). Only two dipolar signals, 2 mm and 5 mm below the surface, are observed. Both measurements show the similar large extended background signals.

Figure 2.20 shows the 3-D surface maps for phases 130° and 15° of the Fig. 2.19a. At a phase of 130° , the amplitude of the extended background is as large as that of the hole 2 mm below the surface. The holes at 5 mm and 8 mm below the surface can not be seen. However, at a phase of 15° , all three holes are evident, and the background signal has been reduced. This indicates that the extended feature is primarily located within the first 5 mm of the surface.

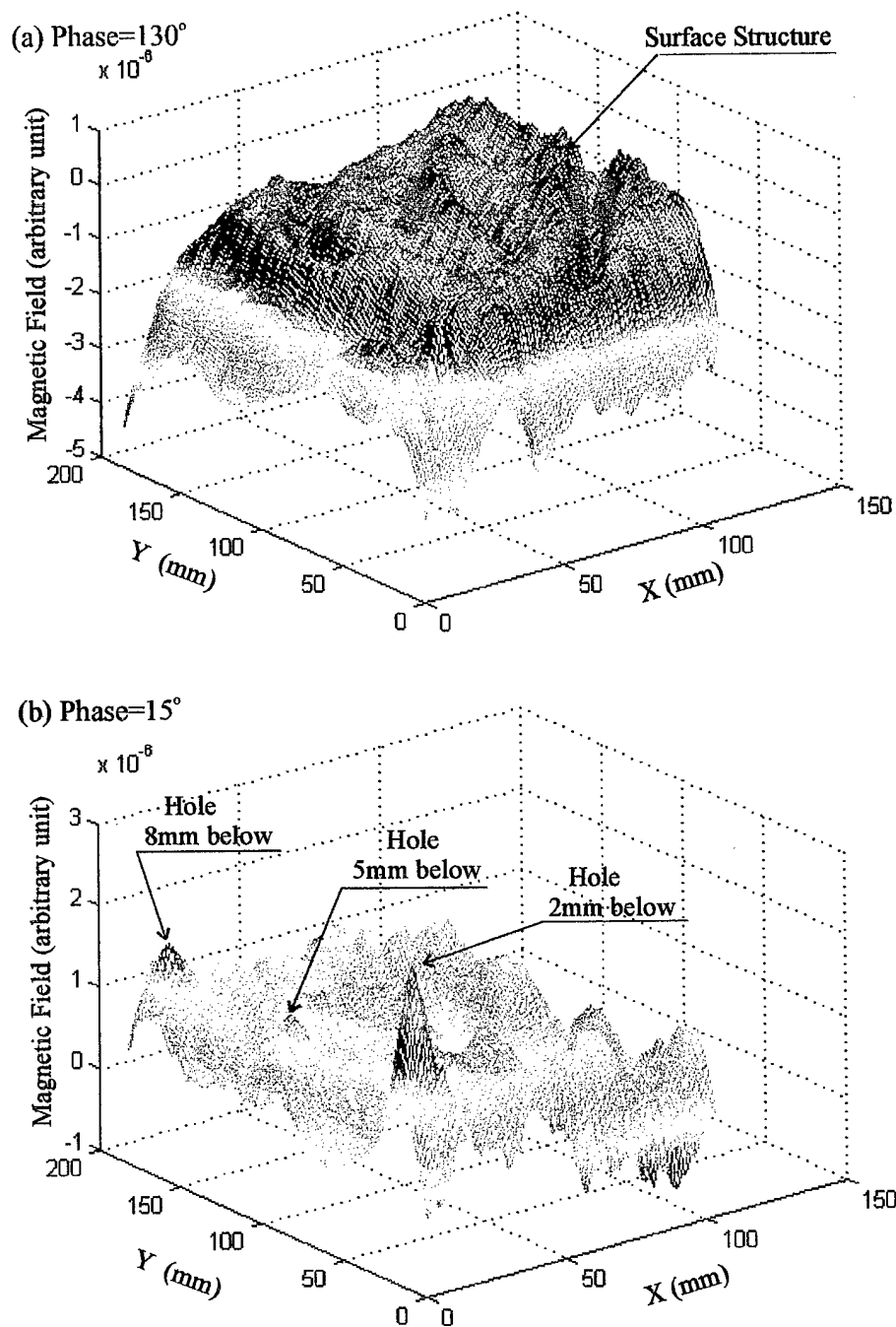
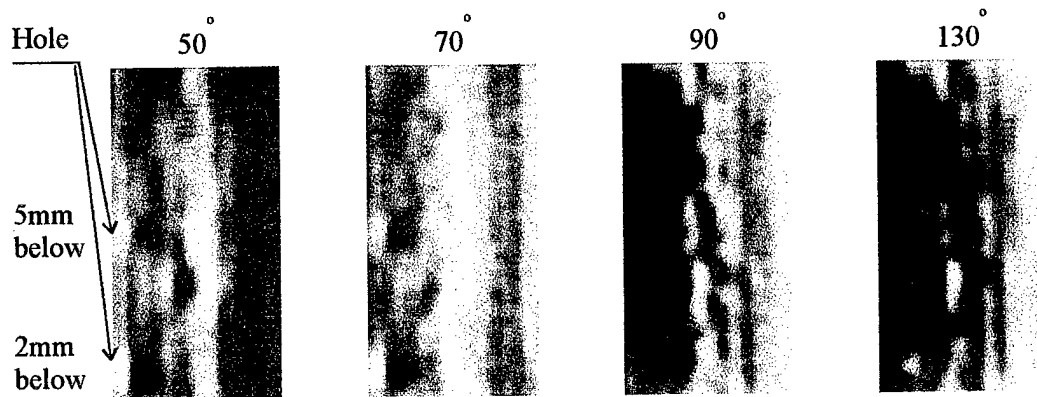


Figure 2.20. The 3-D surface maps of the image in Fig. 2.19a. (a) The large extended feature appears at phase 130°, where the holes are not observed. (b) Three holes appear at phase 15° where the amplitude of the extended feature has been reduced.

Measurements have also been made on sample #2, an 18-mm thick aluminum A356 plate (see Fig. 2.16a). Figure 2.21 shows the images for the surface without holes. The current is induced in the longitudinal (2.21a) and transverse (2.21b) directions. Two dipolar signals due to the holes at 2 mm and 5 mm below the surface are indicated by the arrows. There are a number of strong dipolar signals at the middle of the sample that reflect the localized source, such as inclusions, inside the sample. Figure 2.22 are the 3-D surface maps for the images in Figure 2.21a corresponding to phases of 130° and 50° .

a) Longitudinal current, $f=250\text{Hz}$



b) Transverse current, $f=250\text{Hz}$

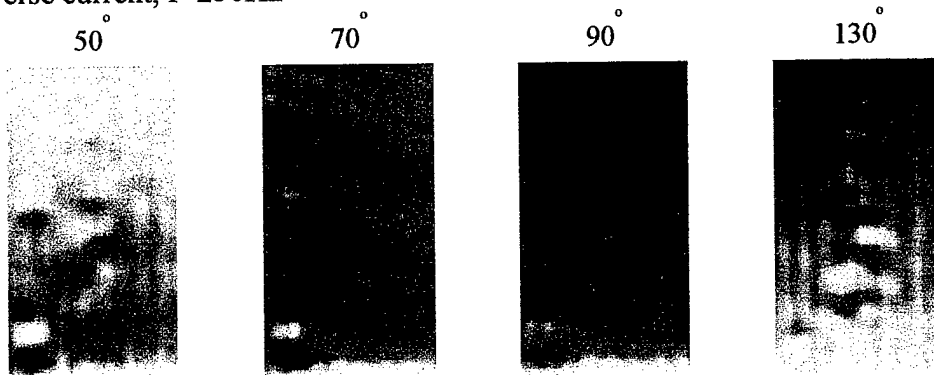


Figure 2.21 The images at four phases for an 18-mm thick A356 aluminum plate with 1.2-mm diameter holes beneath the surface. At 250 Hz, two holes (2 mm and 5 mm below the surface) can be seen and are indicated by the arrows. Note the large dipolar features throughout the sample.

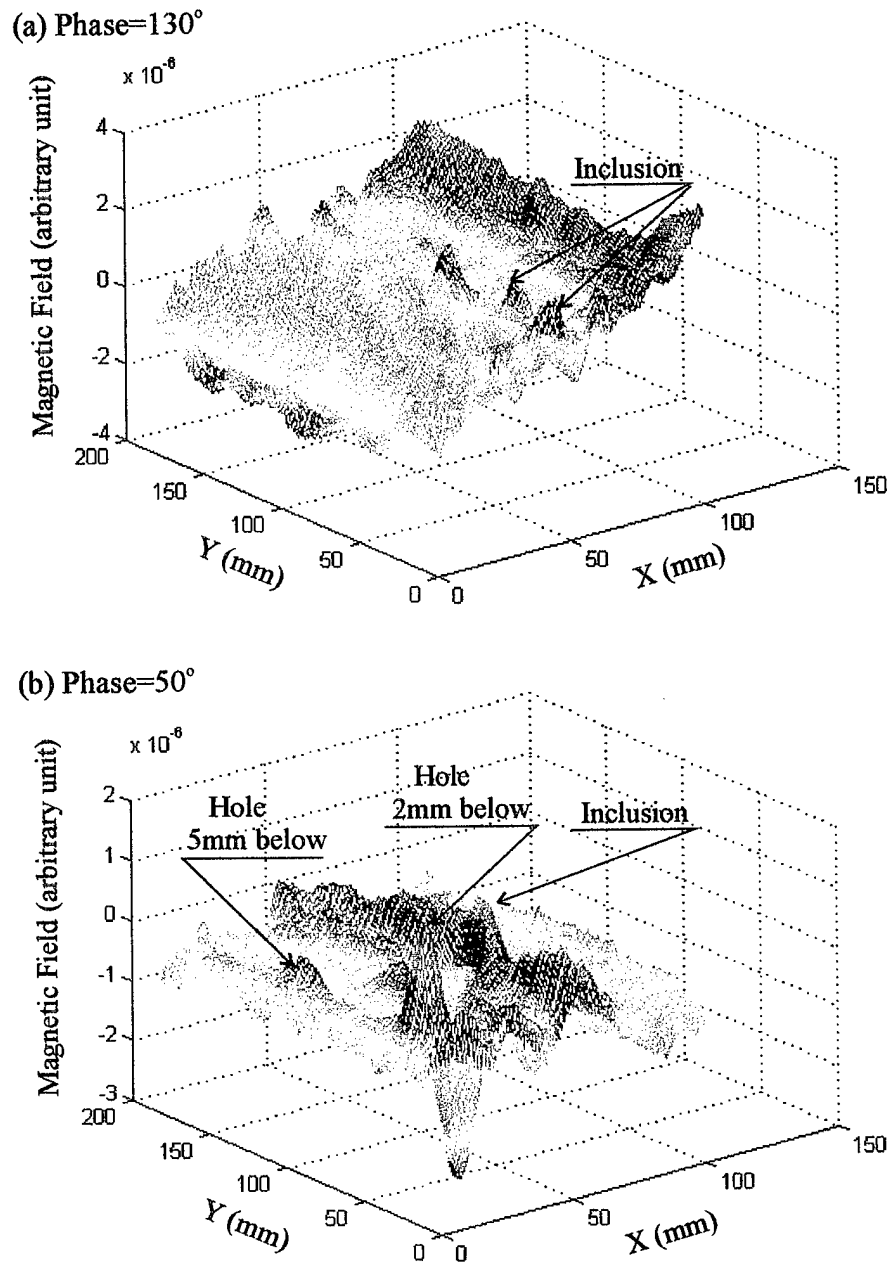


Figure 2.22 The 3-D surface map of the image in Fig. 2.20a at phase (a) 130° and (b) 50°. The signals from the holes are indicated by the arrows. The dipolar signals at the middle of the sample are large compared with that due to the holes in both phases.

V. Conclusions

SQUID eddy current systems has been developed and used for aging aircraft NDE. The sheet inducers have been successfully used for detection of second layer corrossions and cracks. Figure 2.23 and 2.24 are two examples for such application. Fig. 2.23 shows the images of second layer corrossions, and the 3-D images in Fig. 2.24 demonstrate the deep source signal extraction using phase-selective techniques.

Because of the linear relation between the magnetic field and the current source, the superposition of the magnetic fields corresponding to two independent current sources is equivalent to the magnetic field due to the superposition of the two current source. This linearity allow us to obtain the magnetic image at any phase angle from the in-phase and quadrature field map, and obtain the field map for any desired current orientation from the two field maps produced by two independent orthogonal currents mathematically.

The depth-selective techniques allow us to select the optimum frequency and the optimum phase for a particular test object with a source at a desired location. This technique is useful for two situations.

1. Maximize the signal from a deep source only. The frequency should not be lower than that, below which the penetration depth would not increase.
2. Extract the signal from a deeper souse from the signal due to the surface structure. Select the frequency, at which the phases for the current at those two location has largest difference. It should not be too low that the phases of the current from the two source are almost same, and it should not be too high that the strength of the field due to the deeper source become too small.

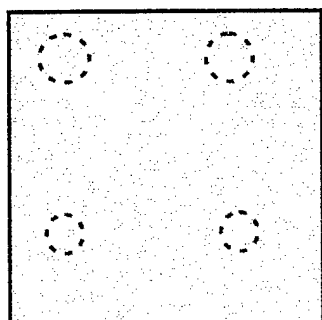
The self-referencing method repulses the signal due to the axial symmetric structure, such as rivet or hole, and extracts the signal from the asymmetric sources, such as crack adjacent to the rivet. It is able to set a threshold due to the imperfect hole or rivet, above which the crack exists. This method may be useful for automatic inspection.

SAMPLE WITH HIDDEN CORROSION (7075-T6)

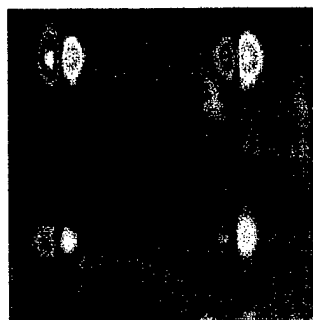
(Two 0.125 inch thick aluminum plates with four sites of corrosion in the second layer)

$f = 210 \text{ Hz}$, Phase = 130°

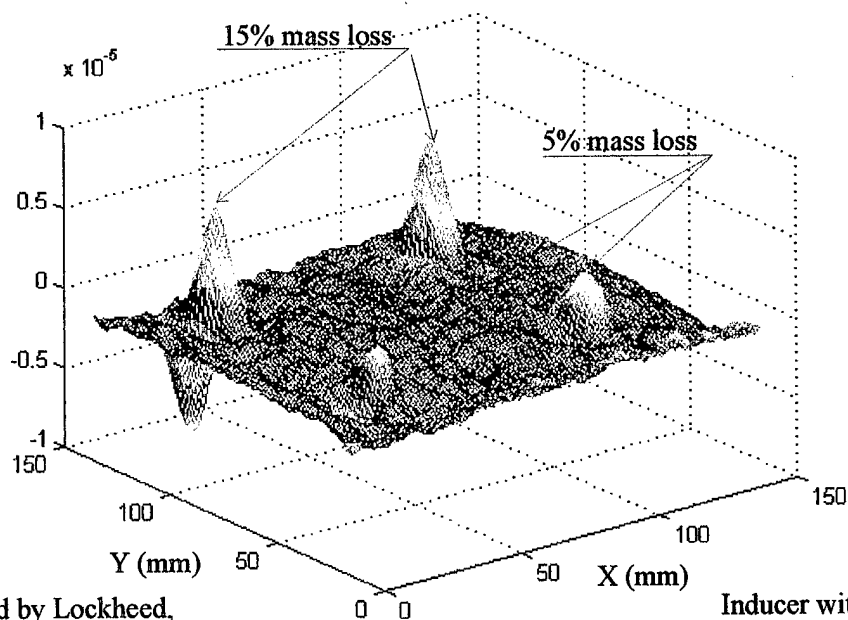
a)



b)



c)



Sample provided by Lockheed,

Inducer with 4 wires

Figure 2.23. Images of second layer corrosions.

MAGNETIC IMAGE OF CRACKS ADJACENT TO RIVETS

(Using Depth-Selective Technique)

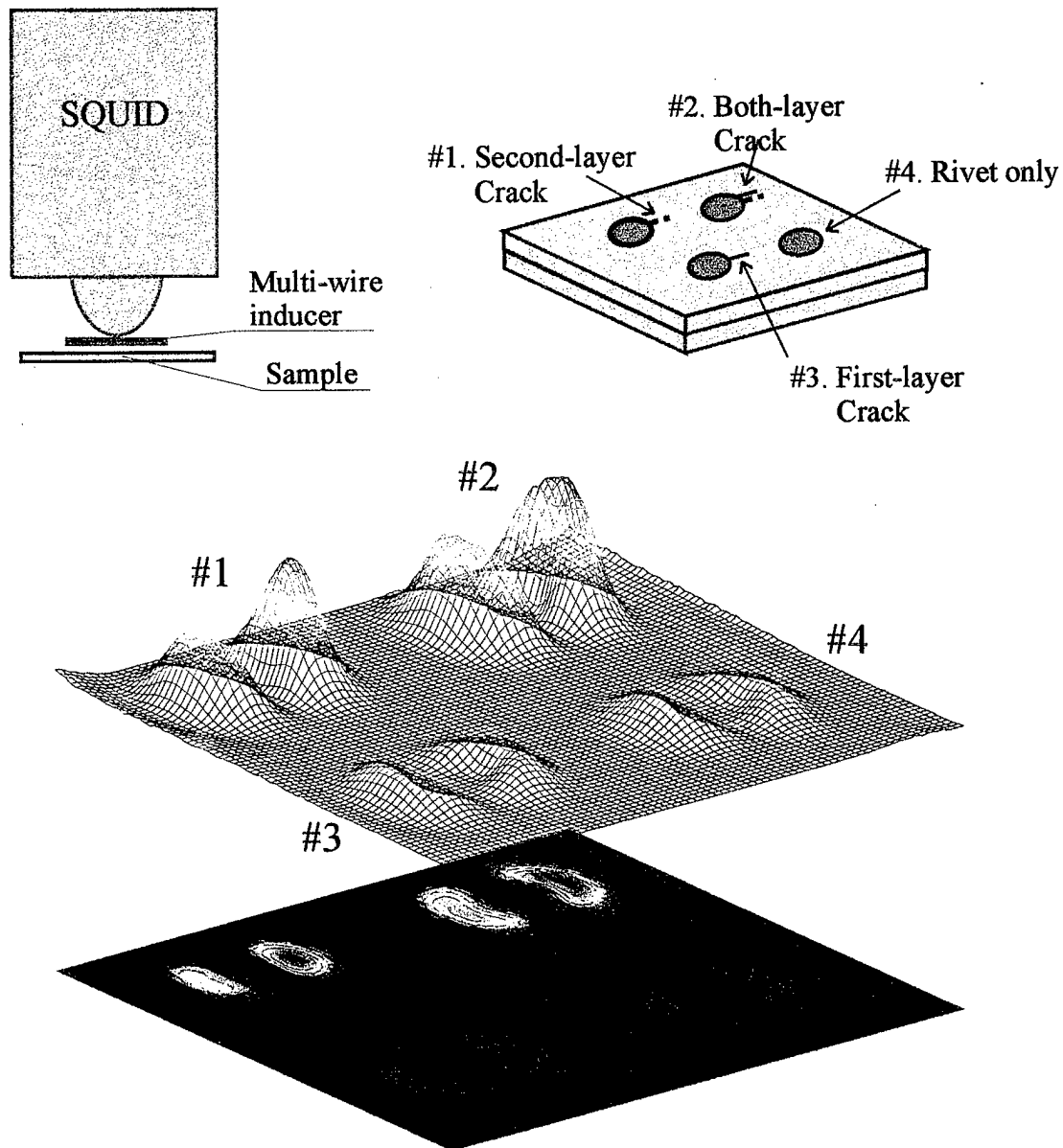


Figure 2.24. An example for deep-source signal detection using depth-selective techniques.

3. Personnel Supported:

John P. Wikswo, Professor of Physics

Yu Pei Ma, Research Assistant Professor of Physics

Nestor G. Sepulveda, Research Assistant Professor of Physics

William G. Jenks, Research Associate of Physics

4. Publications and Related Items

Journal Articles:

"Techniques for Depth-Selective, Low-Frequency Eddy Current Analysis for SQUID-Based Non-Destructive Testing," Y.P. Ma and J.P. Wikswo, Jr., J. Nondestr. Eval., 14(3): 149-167 (1995).

"Line Follower for Finite Element Post-Processing and Current Imaging," N.G. Sepulveda and J.P. Wikswo, Jr., Communications in Numerical Methods and Engineering, 11: 1025-1032 (1995).

Conference Proceedings:

"SQUID Eddy Current Techniques for Detection of Second Layer Flaws," Y.P. Ma and J.P. Wikswo, Jr., Review of Progress in QNDE, 13: 303-309 (1994).

"SQUID Magnetometers for NDE in the Power Industry," W.G. Jenks, Y.P. Ma, and J.P. Wikswo, Jr., EPRI Topical Workshop: Electromagnetic NDE Applications in the Electric Power Industry, Session Three, August 21-23, 1995.

"Depth-Selective SQUID Eddy Current Techniques for Second Layer Flaw Detection," Y.P. Ma and J.P. Wikswo, Jr., Review of Progress in QNDE, 15: 401-408 (1996).

"SQUID Magnetometers for Nondestructive Testing and Biomagnetism," Y.P. Ma and J.P. Wikswo, Jr., Proceedings of 1996 Chinese American Academic and Professional Convention (CAAPCON), pp. 4.17.1-4.17.4 (1996).

Book Chapters and Invited Review Articles:

"The Magnetic Inverse Problem for NDE," J.P. Wikswo, Jr., NATO ASI on SQUID Sensors: Fundamentals, Fabrication and Applications, H. Weinstock, Ed., Kluwer Academic Publishers, The Netherlands, pp. 629-695 (1996).

"SQUIDS for Non-Destructive Evaluation," W.G. Jenks, S.S.H. Sadeghi, and J.P. Wikswo, Jr., J. of Physics D: Applied Physics, 30(3): 293-323 (1997).

"SQUIDS," W.G. Jenks, I.M. Thomas, and J.P. Wikswo, Jr., Encyclopedia of Applied Physics, G.L. Trigg, E.S. Vera, and W. Greulich, Eds., VCH Publishers, Inc., New York, NY, vol. 19, pp. 457-468 (1997).

"Applications of SQUID Magnetometers to Biomagnetism and Nondestructive Evaluation," J.P. Wikswo, Applications of Superconductivity, H. Weinstock, Ed., (Kluwer Academic Publishers, The Netherlands), pp. 139-228 (2000).

Patents

"Method and Apparatus for Detecting Flaws Below the Surface of an Electrically Conductive Object," Y.P. Ma and J.P. Wikswo, Jr., United States Patent 5,610,517 (March 11, 1997).

5. Interactions/Transitions:

a. Participation/presentations

Y.P. Ma attended the 1996 Chinese American Academic and Professional Convention (CAAPCON) which was held on June 29 - July 2, 1996 in Ottawa, Ontario, Canada.

Y.P. Ma attended the QNDE Conference which was held on July 28 - August 2, 1996 in Brunswick, Maine.

John Wikswo attended the AFOSR/NDE Program Review Meeting at Warner Robins, Air Force Base, GA on April 2, 1996.

John Wikswo attended the QNDE Conference held on July 28 - August 2, 1996 in Brunswick, Maine.

John Wikswo attended the Corrosion '97 Conference held on March 9 - 14 1997 in New Orleans, LA.

John Wikswo attended the NASPE '97 Conference held on May 7 - 10, 1997 in New Orleans, LA.

John Wikswo attended the NATO ASI Conference held on June 1 - 20, 1997 in Loen, Norway.

John Wikswo and Yu Pei Ma attended the QNDE Conference held on July 27 - August 1, 1997 in San Diego, California.

b. Consultative and advisory functions

John Wikswo met with NCI Information Systems and staff from Warner Robins Air Logistics Center on March 5 - 6, 1996 and August 5 - 6, 1996 to discuss corrosion and the Air Force aging aircraft problem.

See Task 6 (Corrosion) for discussion of transfer of the SQUID technology to NCI, Inc. at WR-ALC.

c. Transitions

Discussions with and demonstrations to numerous visitors to our labs.

We have established a collaboration with a German SQUID NDE consortium that involves KFA, Lufthansa, Rohmann GmbH, Airbus, and others. We are testing their high T_c SQUID magnetometers and showing them how to incorporate our sheet inducers and flaw extraction algorithms into their instrument.

6. New discoveries, inventions, or patent disclosures:

"Method and Apparatus for Detecting Flaws Below the Surface of an Electrically Conductive Object," Y.P. Ma and J.P. Wikswo, Jr., United States Patent 5,610,517 (March 11, 1997).

7. Honors/Awards:

None

REFERENCE

1. J.P. Wikswo, Jr., J.M. van Egeraat, Y.P. Ma, N.G. Sepulveda, D.J. Staton, S. Tan, and R.S. Wijesinghe, "Instrumentation and techniques for high-resolution magnetic imaging," in *Digital Image Synthesis and Inverse Optics*, vol. 1351, A.F. Gmitro, P.S. Idell, and I.J. LaHaie, Eds., SPIE Proceedings, pp. 438-470, 1990.
2. Y.P. Ma, D.J. Staton, N.G. Sepulveda, and J.P. Wikswo, Jr., "Imaging flaws with a SQUID magnetometer array," in *Review of Progress in QNDE*, vol. 10A, D.O. Thompson and D.E. Chimenti, Eds., New York: Plenum Press, pp. 979-986, 1991.
3. D.J. Staton, Y.P. Ma, N.G. Sepulveda, and J.P. Wikswo, Jr., "High resolution magnetic mapping using a SQUID magnetometer array," *IEEE Trans. Mag.*, vol. 27, no. 2, pp. 3237-3240, 1991.
4. J.P. Wikswo, Jr., D.B. Crum, W.P. Henry, Y.P. Ma, N.G. Sepulveda, and D.J. Staton, "An improved method for magnetic identification and localization of cracks in conductors," *Journal of Nondestructive Evaluation*, vol. 12, no. 2, pp. 109-119, 1993.

5. Y.P. Ma and J.P. Wikswo, Jr., "Detection of deep flaw inside a conductor using a SQUID magnetometer," in *Review of Progress in QNDE*, vol. 11A, D.O. Thompson and D.E. Chimenti, Eds., New York: Plenum Press, pp. 1153-1159, 1992
6. Y.P. Ma and J.P. Wikswo, Jr., "Techniques for Depth-Selective, Low-Frequency Eddy Current Analysis for SQUID-Based Non-Destructive Testing," *J. of Nondestructive Evaluation*, Vol.14, No.3, 149-167 (1995).
7. Y.P. Ma and J. P. Wikswo, Jr., in *Review of Progress in QNDE*, Vol. 15, D.O. Thompson and D.E. Chimenti, Eds., New York: Plenum Press, pp. 401-408, (1996).
8. W.R. Smythe, *Static and dynamic electricity*, pp. 309, McGraw-Hill, New York, 1950.
10. Appendix 4
11. Y.P. Ma, D.J. Staton, N.G. Sepulveda, and J.P. Wikswo Jr., "Imaging flaws with a SQUID magnetometer array", *Rev. of Progress in Quantitative Nondestructive Evaluation*, D.O. Thompson and D.E. Chimenti, Eds., Vol. 10A, pp. 979-986, Plenum, New York, 1991
12. Appendix 3

TASK 3. IMAGE PROCESSING

TASK 3 IMAGE PROCESSING

1. Objectives

The primary task is that of developing high resolution image restoration algorithms for detecting high resolution images of material failures. These restoration algorithms are to enhance signals obtained from SQUID measurements of the electromagnetic fields generated by passing current through the material being analyzed for failures. Due to the measurement process, these electromagnetic field recordings are low in detail and must be enhanced to provide high detail information

2. Accomplishments

A. Blind Deconvolution

In a standard signal processing application, it is necessary to monitor a phenomenon of interest in order to gain an understanding of its behavior. Unfortunately, it often happens that a signal(s) of interest is not directly measurable, but, a linear transformed version of the signal is available. This linear operation may serve to represent instrumentation dynamics and (or) distortions introduced by the medium in which the measurements are conducted. Whatever the case, it is assumed that the measured data is obtained by a linear convolution of the signal of interest with the linear operator's unit-impulse response (point spread function). The classical deconvolution problem is concerned with recovering the signal of interest from the measured signal when knowledge of the convolving system's unit-impulse response is available. The deconvolution operation therefore seeks to undo the effect of the convolution operation. Various solutions to this classical problem have been advanced which are often dependent on the measurement system being minimum phase.

Blind deconvolution is applied when recovery of the excitation signal is to be achieved without knowledge of the convolution operator's dynamics. It should be clear that unless additional information concerning the signal being recovered is given, the blind deconvolution problem is intractable. A commonly invoked assumption is that the signal being recovered is white in nature. For this work we shall impose a less restrictive requirement on the excitation and also not require that the convolving operator be minimum phase.

A solution to the blind deconvolution problem is dependent on the kurtosis associated with the deconvolving operator's response. One of the more practical uses of kurtosis is that of providing a measure of the "spikeness" of a unimodal random variable relative to a Gaussian random variable with the same variance. If a unimodal random variable's kurtosis is positive then it is said to be "heavier tailed" than a Gaussian random variable whose kurtosis is zero and its distribution is more "spiky" than the equivalent Gaussian distribution. If the kurtosis is negative then the random variable is "lighter tailed" and possesses a smoother behavior relative to that of a Gaussian random variable

Since no knowledge concerning the convolution operator's dynamics are presumed, it is necessary to impose restrictive conditions on the excitation signal in order to make a solution feasible. One of the more commonly invoked requirements is that the excitation be composed of statistically independent samples of an underlying random variable. A time

series of the nature is commonly referred to a *white noise*. For the purposes of this work, this restriction is eased to that of requiring that the excitation signal be uncorrelated of order two and four.

The primary problem is concerned with using these magnetic field measurements for inverting the relationship existent between the underlying current density in a material and the resultant magnetic field. This relationship is a Fredholm equation of the first kind and its inversion (deconvolution) is extremely ill-posed. As a consequence, it is necessary to use sophisticated approaches in recovering the underlying current density behavior.

The use of two-dimensional blind deconvolution methods for non-evasively detecting material failure in aging aircraft using SQUID continued. This approach seeks to undue the smoothing effects caused by the measurement mechanism which transforms the injected (or induced) current into a magnetic field recorded by SQUID instrumentation. This transformation is mathematically represented as a linear two-dimensional convolution in which the injected (or induced) current serves as the input signal and the corresponding magnetic field as the output (observed) signal. This effort is providing increasingly improved current reconstruction images.

A number of two-dimensional blind deconvolution methods for non-evasively detecting material failure in aging aircraft using SQUID were developed. The ability of these approaches to extract useful images of high resolution quality for detect material failures has proven encouraging. This demanding task requires the reversal of the smoothing operation resulting from the measurement process that transforms the injected (or induced) current into a low resolution magnetic field recorded by SQUID instrumentation. This process corresponds to a two-dimensional convolution operation in which the injected (or induced) current serves as the input signal and the corresponding magnetic field as the output (observed) signal. The algorithms developed have been based on norm cumulant deconvolution, and, contemporary signal enhancement.

An example of the algorithm's performance can be seen in Fig. 3.1 where the magnetic field measured by the SQUID magnetometer has been successfully deconvolved to produce the original current density distribution in the shape of the letters VU. Another example is shown in Fig. 3.2 where the image from the sample described previously in Task 2 has been deconvolved to reveal the simulated flaws located at the 12 o'clock positions above the fasteners.

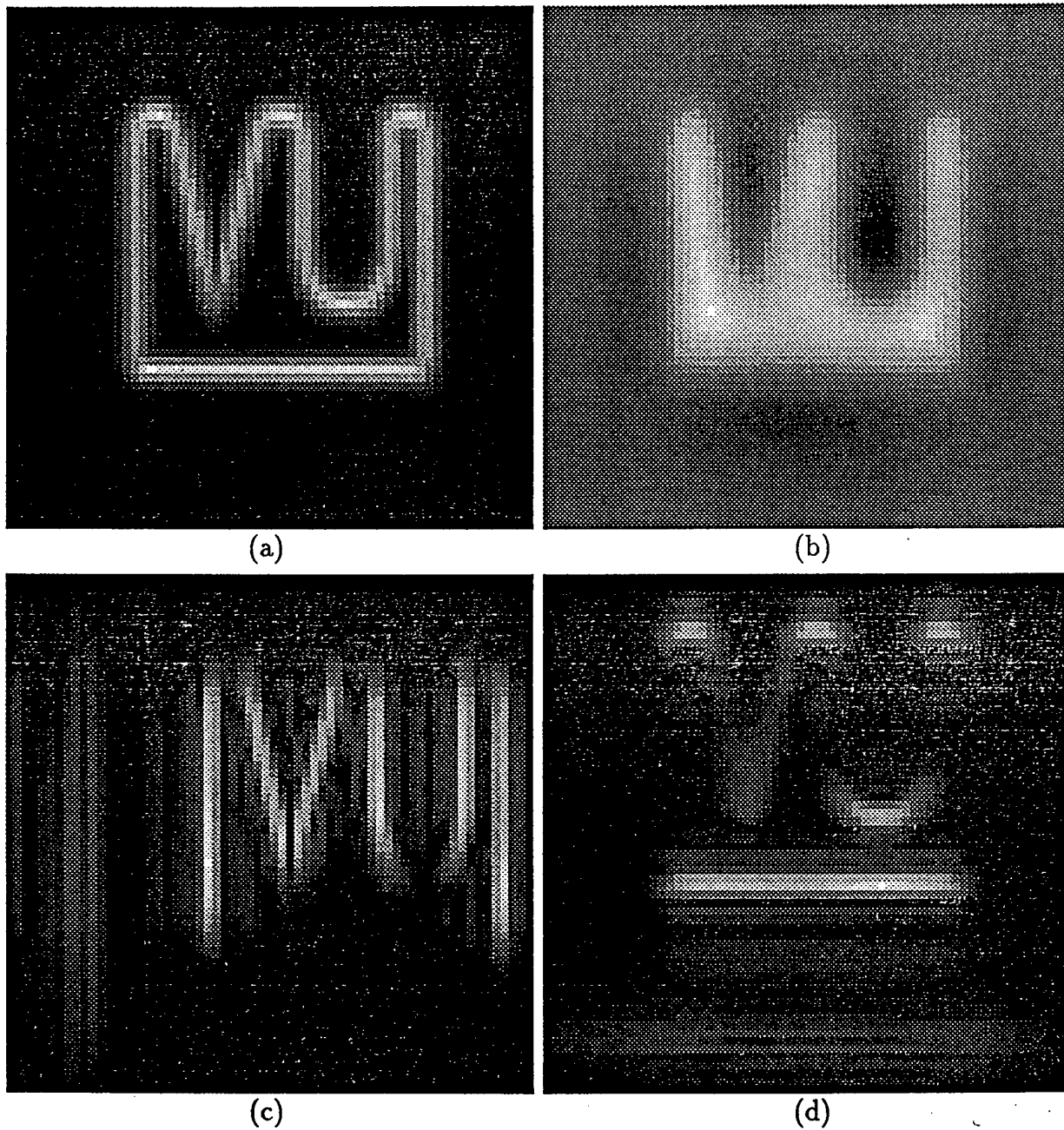
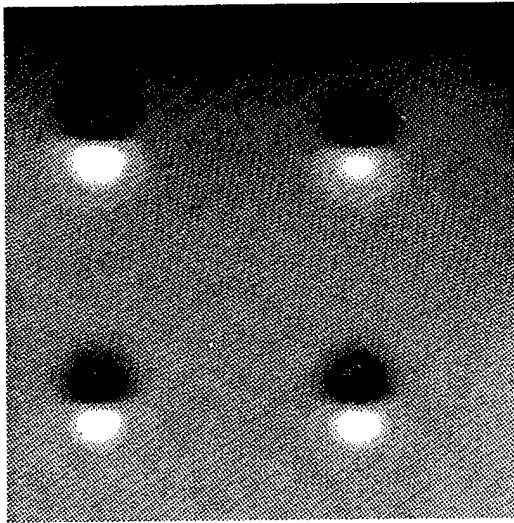
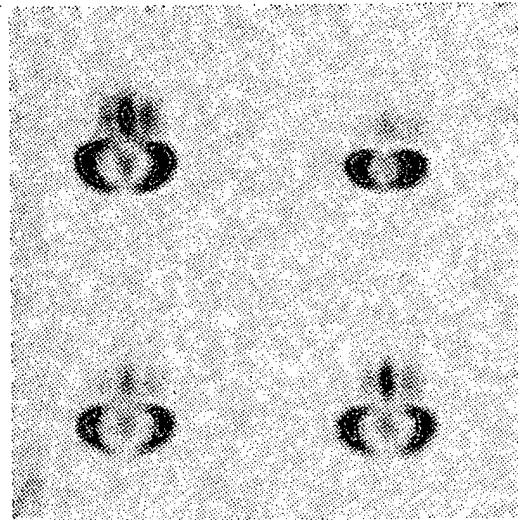


Figure 3.1. Blind deconvolution on a current carrying wire in the shape of VU;
 (a) Original current source density, (b) the z-component of the induced magnetic field, (c) recovered magnitude along the y-direction using blind deconvolution, (d) recovered magnitude along the x-direction using blind deconvolution.

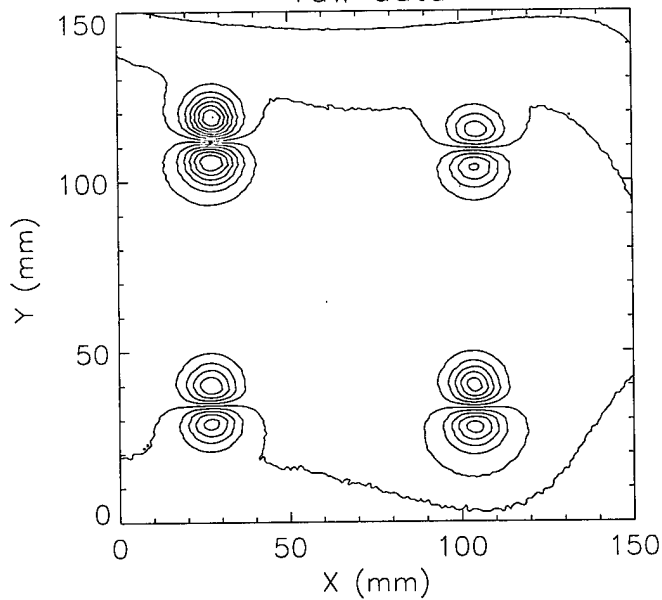
a) raw data



b) blind deconvolution



c) raw data



d) blind deconvolution

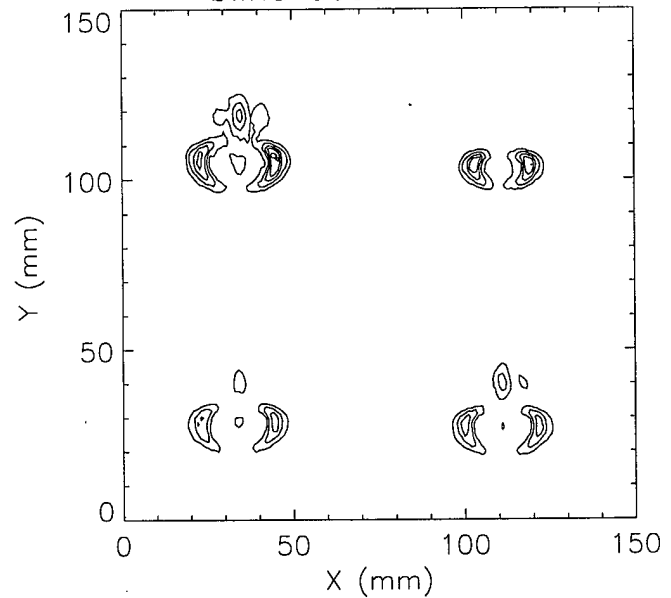


Figure 3.2. Application of blind deconvolution to magnetic image from EDM simulated flaws in panels of 7075-T6 aluminum with 0.25 inch fasteners. See Figure 2.13a for details of sample. (a) magnetic field raw data, (b) blind deconvolution yielding field source (J_y only), (c) contour plot of raw data, (d) contour plot of field source.

B. Signal Enhancement

A number of signal enhancements algorithms have been coded, tested and are available. One of the more recent approaches entails a symmetric image detection approach. This later approach makes fewer assumptions on the underlying physics and therefore should be more robust in behavior. It is currently occupying most of the signal processing group's effort.

Our group has introduced a new family of cumulant extrema algorithms that show great promise. Professor Cadzow has proven that under suitable conditions met in many applications, the extremum of the deconvolved response cumulant magnitude will theoretically result in perfect deconvolution. This algorithm has been coded for one-dimensional synthetic data and is presently being implemented for application to the two-dimensional SQUID generated data. The specific cumulant extrema algorithms identified as $k(4,2)$ and $k(6,2)$ have provided excellent results on both synthetic one-dimensional data and on real world one-dimensional satellite observations made on lightening discharges. It is anticipated that they will provide similar results on the two-dimensional SQUID data.

C. Symmetric Image Detection

More recently, the image processing group has been developing symmetric image detection methods for producing the desired high resolution current images. This approach is predicted on the fact that the magnetic image produced by point failures results in a distinctly anti-symmetric magnetic field about that point. The symmetric image detection algorithms then seeks to find the most compatible anti-symmetric component in the recorded magnetic field. Preliminary tests of this class of algorithms on actual magnetic data obtained using magnetic recording made on laboratory prepared material species are very encouraging.

D. Automated Flaw Extraction

We have implemented twenty-five different spatial filters in a user-friendly software environment that allows us to apply all of these filters to a SQUID image with several key strokes. A typical example is shown in Fig. 3.3 in which the raw data is in the upper left-hand corner and the other panels show the outputs of the various image processing procedures. Here a small flaw at the center of the image is invisible in the raw data, but is revealed by several of the filters.

The image processing software has now been switched completely from PV WaveTM to MathlabTM, which is providing us with lower costs and greater flexibility and conformity within our research group and that of other groups. As discussed in greater detail under Task 2, we have been developing automated flaw extraction procedures, based on orthogonal imaging and image rotation, that allow us to discriminate between circular holes, holes with cracks, and cracks alone. These routines are now transferred to Matlab and are in regular use in our laboratory and at KFA. There is an ongoing effort to develop other filtering and image improvement techniques on a case-by-case basis.

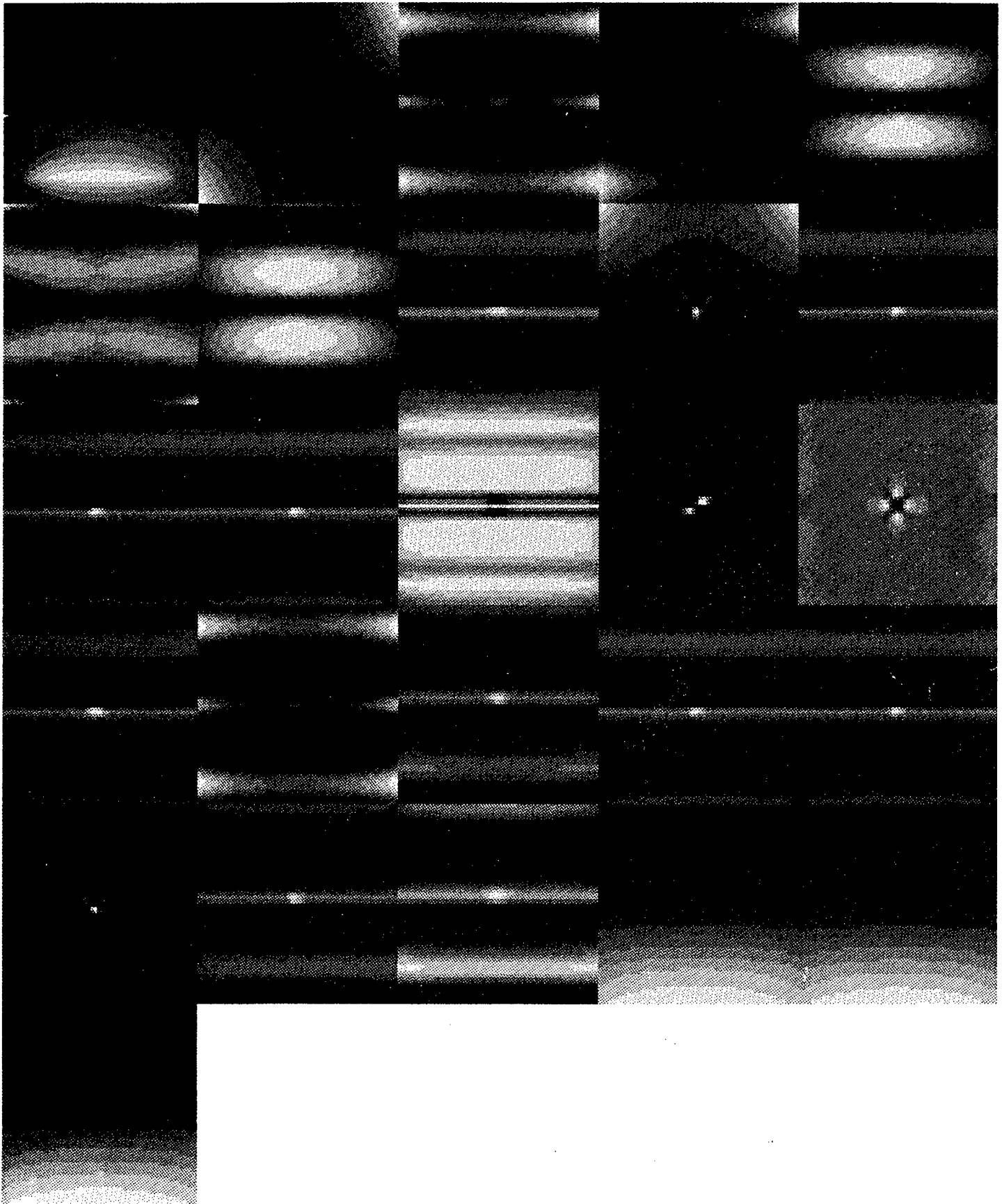


Figure 3.3 Example of image processing capability using multiple filters.

3. Personnel Supported:

James A. Cadzow, Professor of Electrical & Computer Engineering
Xingkang Li, Research Associate
Brian Ball, Graduate Student
Nestor G. Sepulveda, Research Assistant Professor of Physics

4. Publications and Related Items

"Blind Deconvolution," J.A. Cadzow and X. Li, Digital Signal Processing, 5(1): 3-20 (1995).

"Blind Deconvolution via Cumulant Extrema," IEEE Signal Processing Magazine, Special Issue on Blind Deconvolution, 13(3): 24-42 (1996).

"Estimation of Phase for Noisy Linear Phase Signals," R. Kakarala and J.A. Cadzow, IEEE Trans. Signal Processing, 44(10): 2483-2497 (1996).

"Linear Recursive Operator's Response Using the Discrete Fourier Transform," J.A. Cadzow, IEEE Signal Processing Magazine, 16(2), 100-110, March (1999).

5. Interactions/Transitions:

a. Participation/presentations at meetings, conferences, seminars, etc.

Professor Cadzow spent six weeks visiting colleagues at Sandia National Laboratory, the University of New Mexico, and Los Alamos National Laboratory to discuss SQUID image processing.

b. Consultative and advisory functions to other laboratories and agencies

None

c. Transitions.

None

6. New discoveries, inventions, or patent disclosures:

Development of a new class of image symmetry detection algorithms.

7. Honors/Awards:

None

TASK 5. FATIGUE DAMAGE CHARACTERIZATION

TASK 5. FATIGUE DAMAGE CHARACTERIZATION

1. Objectives

One aim of Task 5 is to create an inventory of fatigue-damaged structural elements that can be used to test the sensitivity and reliability of the NDE methods developed here. The other is to generate basic information about the distribution, location and character of fatigue damage, information useful for defining the prospects of early nondestructive detection. Evaluate the mechanical parameters that govern wear and crack initiation in the locale of a rivet hole. The mechanical parameters are the local bulk stresses, contact stresses and slip amplitudes, and derivatives of these basic variables. The parameters seek to link the physically observed form of damage and damage mechanisms, i.e.; fretting and fatigue. The effects of rivet and joint geometry, friction, interference and clamping are also being sought for single-row and double-row riveted lap joints. To accomplish this, 2D and 3D finite element models will be devised. The cyclic plastic constitutive relations for 2024-T3 and 7075-T6, which must be incorporated into the finite element models, will be measured.

2. Accomplishments

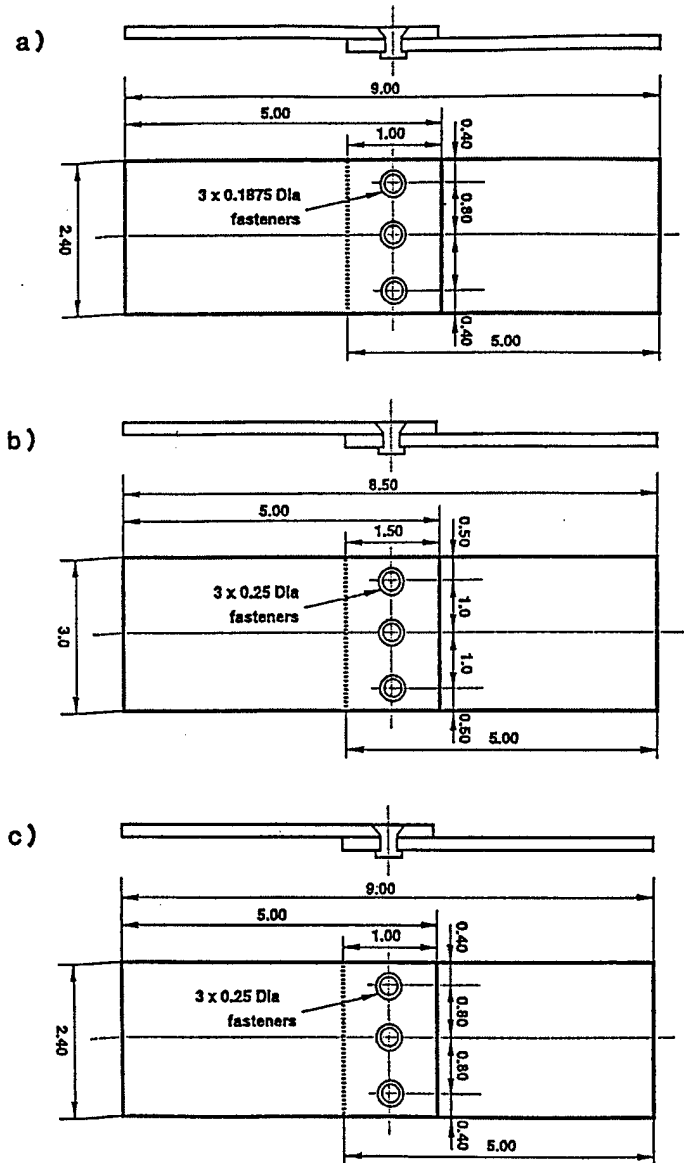
A. Inventory of Fatigue-damaged Samples

We have prepared a set of 39 riveted lap joints fastened by a single row of 3 rivets (108 rivet holes in all). Three panel thickness are represented: 0.060 in, 0.080 in and 0.100 in. as shown in Figure 5.1. A fraction of the 39 samples were subjected to cyclic loading to produce a number of small, fatigue cracks which initiated in the countersunk region of the panel adjacent to the interior panel surface. After cyclically loading, the rivets were removed and the interior surfaces of the panels were examined under a microscope and photographed to establish the size and location of the cracks. Examples of the cracks as viewed on the interior surface of the countersunk panel are shown in Figure 5.2. There are more than 20 cracks but fewer than 80 contained in the sample set. The length of the cracks ranges from 0.178 mm to 6.16 mm. Some of the samples possess cracks at several of the 3 rivet locations and some locations display multiple cracks. Many of the cracks are not visible on the exterior surface. In some cases, the cyclic loading also produced prominent fretting damage around the rivet hole. After microscopic examination, the samples were reassembled and riveted. The cracked samples are randomly dispersed among the crack-free samples. Each sample is identified by a number, 1 - 39, which appears on a label (protected by scotch tape) located at the edge of the sample¹. A document identifying the cracked samples has been made.

¹ The non-permanent character of the sample identification label will make it possible to "reshuffle" the samples and renumber them. Consequently, they could be used over and over again by the same NDE investigators.

A riveted lap joint fastened by a single row of 3 countersunk rivets was prepared. The thickness of each panel is 2.15 mm, with the countersink extending to a depth of about 1.65 mm. Figure 5.3 describes other details of the geometry. The joint was subjected to 10,000 cycles of cyclic loading defined by $\sigma_{\max} = 25.4$ MPa, $R = 0.1$ and $f = 1$ Hz. Upon completion of the load cycles, the rivets were removed and the interior surfaces of the panels were examined under a microscope and photographed to establish the size and location of the cracks. Figures 5.4 to 5.7 are typical examples. Two dominant cracks emanated from each countersunk hole, one on each side (near 4 o'clock and 8 o'clock). Each crack extended along the bottom surface of the upper panel and along the top, countersunk hole surface. No cracks were found near the straight holes in the lower panels. Table 5.1 is a record of the 6 crack lengths, along the two surfaces for each crack. The length of the cracks ranged from 1.61 mm to 2.56 mm. Cyclic loading also resulted in prominent fretting damage. Each hole showed this form of damage in the two typical locations described in the previous section, i.e.; on the surface of the countersunk hole and on the underside of the upper panel towards the loaded end. This sample was provided to test the sensitivity of the nondestructive crack detection methods.

The characterized samples were used by Northwestern and Vanderbilt investigators to evaluate the sensitivity of NDI methods



Figurer 5.1 Schematics showing dimensions of aluminum lap joints: (a) thickness = 0.060 inch. (b) thickness = 0.08 inch. (c) thickness = 0.1 inch.

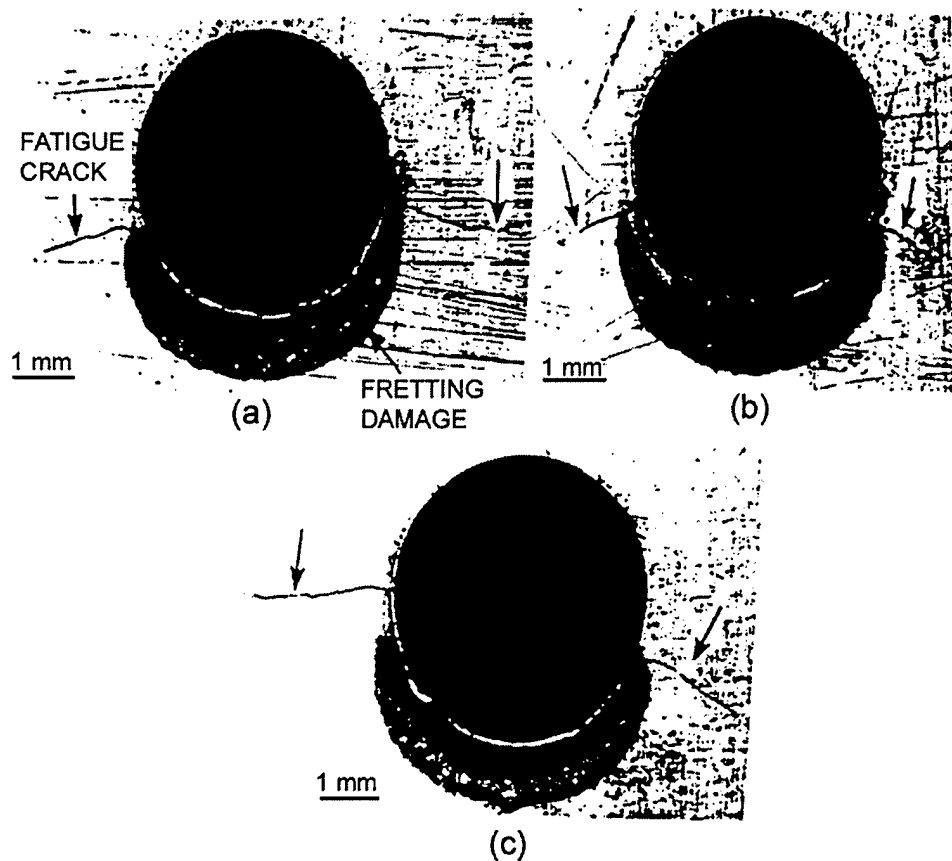


Figure 5.2 Examples of fatigue cracks observed on the interior panel surface in the locale of three countersunk rivet holes of a test sample subjected to a cyclic stress range of $\Delta\sigma = 106$ Mpa. Note: the dark, half moon-shaped regions below the holes are the result of intense fretting wear. The cracks range in length from 1.76 mm to 4.32 mm. Magnification: 8X.

Table 5.1

	Hole # 1		Hole # 2		Hole # 3	
Countersunk hole radius, mm	4.41		4.43		4.4	
Straight hole radius, mm	2.46		2.46		2.47	
Lengths and locations of cracks at rivet holes in countersunk panel, a (mm)						
	Hole # 1		Hole # 2		Hole # 3	
	Left Side	Right Side	Left Side	Right Side	Left Side	Right Side
Exterior panel surface	1.77	1.75	1.78	1.68	1.97	2.08
Interior panel surface	2.15	2.26	1.61	1.92	2.56	2.1

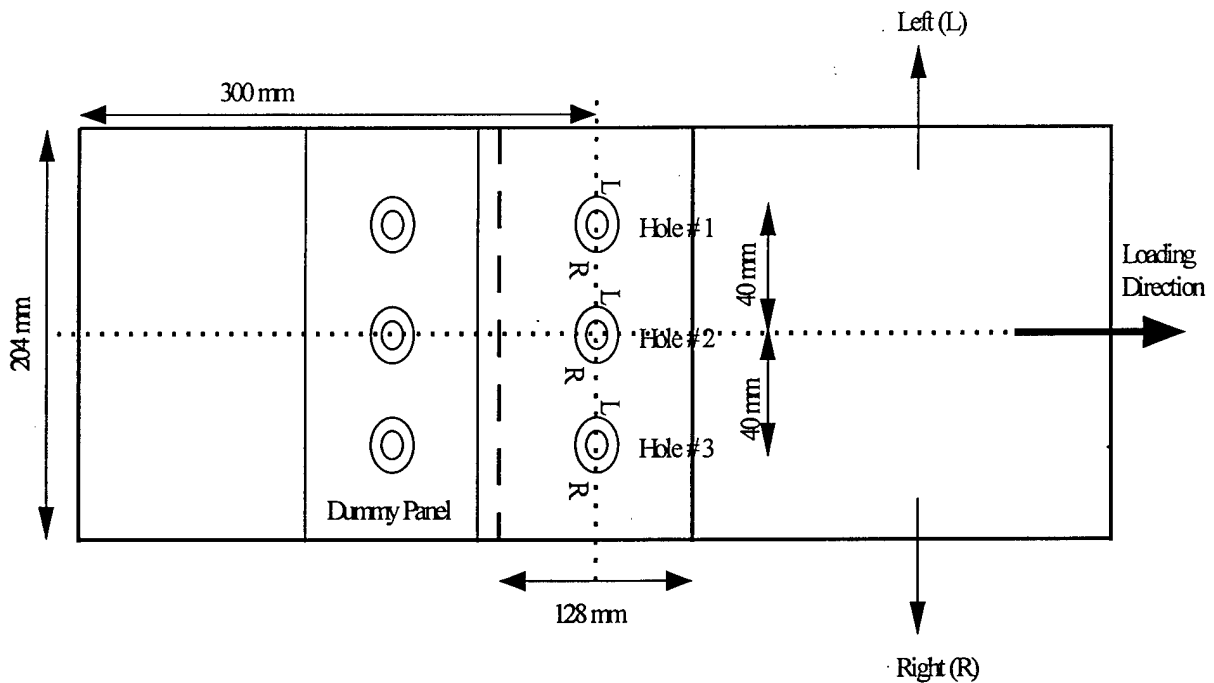


Figure 5.3. Schematic showing dimensions of the aluminum lap joint.



Figure 5.4. Crack present on the left side and exterior panel (countersunk) surface of Hole # 3 (10X). Patches of black debris identify fretted areas.



Figure 5.5. Crack present on the right side and exterior (countersunk) surface of Hole # 3 (10X). Patches of black debris identify fretted areas.

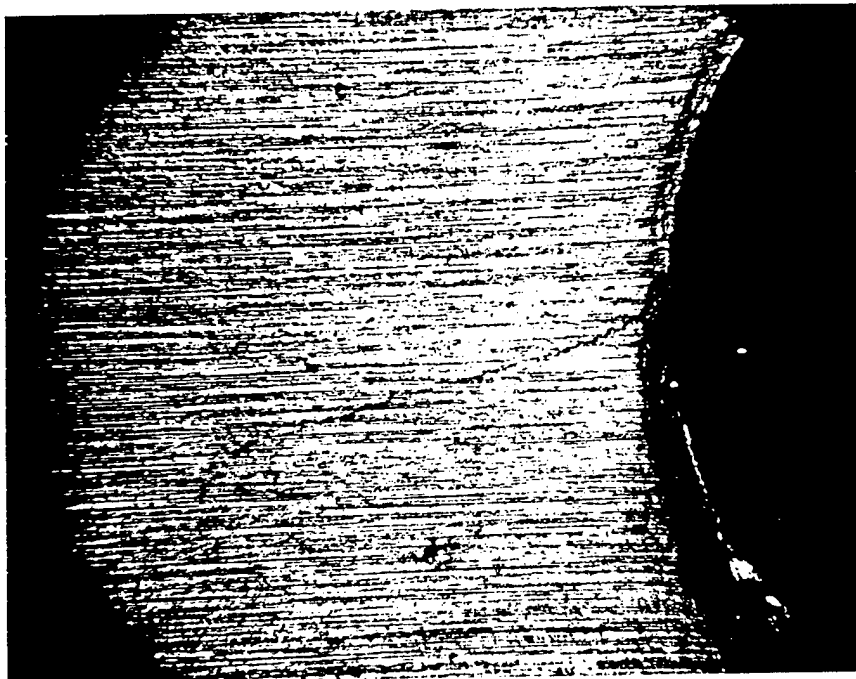


Figure 5.6. Crack present on the left side and interior panel surface of Hole # 3 (24X). Patches of black debris identify fretted areas.

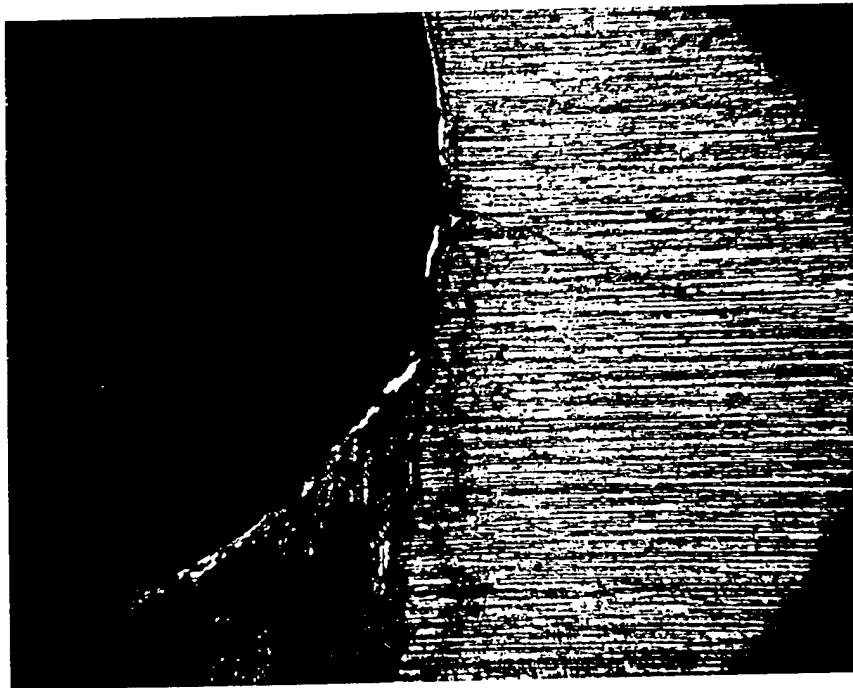


Figure 5.7. Crack present on the right side and interior panel surface of Hole # 3 (24X). Patches of black debris identify fretted areas.

B. Finite Element Analysis of Fatigue Damage at Rivet Holes

1. Introduction

The cyclic, stress-strain constitutive relations are a prerequisite for finite element modeling of cyclic loading. The modeling envisioned here involves riveted sheet connections subjected to cyclic loading with a large mean stress, e.g. $R = 0.1$. Kumar, Hahn and Rubin [1] have measured the cyclic constitutive relations of 7075-T6 for fully reversed ($R = -1$, mean stress $\sigma_M = 0$), axial, push pull loading.

This Task uses finite element methods to evaluate the cyclic stresses and strains in the locale of the fastener hole. The aim is to locate the cyclically deformed regions and determine the extent of damage, e.g., plastic deformation, crack nucleation and growth, and to use the information to assist in defining the prospects of early nondestructive detection. Furuya and Shimada [2] have proposed an average local-strain accumulation parameter, which integrates the local strain history as the load cycle progresses, in an effort to relate microcrack initiation to service life. They found an inverse relation exists between the local-strain accumulation and the number of cycles to initiate a crack. Yang and Wang [3] have established that the fatigue life under the action of a positive mean stress depends on combined effects of cyclic creep and cyclic plastic strain. Lai, Oh and Nee [4] find that the compressive residual stresses produced by an interference fit markedly reduce the stress intensity factor at the tip of a crack emanating from a hole. The stresses become increasingly tensile with radial distance from the rivet-hole interface, and the effect trails off.

The fastened (riveted or bolted) sheet is a complex, three dimensional problem involving transverse forces, interference, and friction. Three, progressively more sophisticated, finite element models were designed:

1. 2-D, In-Plane Model. An idealized, 2-dimensional, pinned connection in which the pin axis remains normal to the sheet is shown in Fig. 5-8 (a-b). Results obtained for this model are presented in the following sections.
2. 2-D, Out-of-Plane Model. A 2-dimensional model of a lap joint with a "continuous" rivet. Work on this model, which is illustrated in Fig. 5-8c, is under way. This model can account for lateral forces and provides access to the out-of-plane displacements.
3. 3-D Models. Three-dimensional models of a lap joint which can treat both the in-plane and out of plane displacements and the shape of the rivet.

The feasibility of performing detailed, 3D, finite element analyses of riveted connections that identify the critical sites and local conditions for conventional fatigue, fretting fatigue and fretting wear has been demonstrated. The results of the analyses show the specific locations in the connection where advanced NDI procedures can find early indications of fatigue and fretting damage. The analyses make it possible to evaluate the effects of rivet and joint geometry, to optimize rivet design, interference and lateral clamping. The study points to ways of improving both the performance of the riveted connection and NDI procedures for detecting damage.

2. Finite Element Models

The dimensions of the sheet and hole are shown in Fig. 5-8a. The finite element mesh for the model is shown in Fig. 5-8b. The mesh density was higher in the area adjoining the interface since most deformation is expected to be concentrated in that region, as shown in Fig. 5-8c. The length of the sheet is 5.5 times its width so that the effect of a far-field loading on the hole-sheet interface may be examined.

Three pin diameters were modeled, with pin-sheet interference of 0%, 1% and 2%. The material properties ascribed to the pin corresponded to those of steel and aluminum. The pin was modeled as a purely elastic body. Based on several trial models, it was established that the pin showed no plastic deformation except at its constrained center. Hence such an approximation did not sacrifice any accuracy. Apart from fixing the pin at the center, the long sides of the sheet were constrained in the x-direction, in keeping with the conditions found in a multi-riveted sheet. A cyclically varying load was applied at the top surface of the sheet, ranging from a peak stress of 125 MPa to a minimum of 13 MPa. Thus the sheet was subjected to a tensile mean stress.

The sheet was considered to be in plane stress and its thickness was 1.53 mm. The pin was considered to be in plane strain. Aluminum sheet was treated as isotropic elastic-plastic with the following properties:

$$E = 70.00 \text{ GPa}, \sigma_0 = 530.75 \text{ MPa and } M = 0.7 \text{ GPa}$$

The elastic modulus used for steel was 207 GPa. Calculations were performed for two values of the coefficient of friction at the pin-sheet interface, 0.2 and 0.5.

Contours showing the Mises equivalent stress contours and the equivalent plastic strains in a 1.5 mm-wide circular region enveloping the pin-sheet interface were obtained for each of the cases described above. The results for 2 cases:

- (i) 0% interference/0.2 friction/Al-pin
- (ii) 1% interference/0.2 friction/Al-pin

are reproduced in Figs. 5-9, 5-10, 5-11. The results for 0% interference/0.2 friction/Al-pin case show that under the nominal applied stress ($\sigma = 125 \text{ MPa}$), the (Mises) yield stress ($\sigma_0 = 530.7 \text{ MPa}$) is exceeded in a relatively broad region below the pin (Figure 5-9a). The peak Mises stress, $\sigma = 533 \text{ MPa}$ reflects a (Mises) stress concentration of $K = 4.9$. The peak (equivalent) plastic strains of $\epsilon_p = 0.031$ are obtained close to the interface at $\theta = 150^\circ$ and $\theta = 210^\circ$. In the "unloaded" condition (nominal stress $\sigma = 13 \text{ MPa}$), the Mises stresses (for plastic deformation in the opposite sense) are well below yielding. Consistent with this, the plastic strain distribution after unloading is identical with the fully loaded strains. In other words, there is no reverse deformation during unloading and no cyclic deformation during repeated loading.

The results for the connection with 1% interference/0.2 friction/Al-pin case are shown in Figs. 5-10 and 5-11. Figures 5-10a and 5-10b show the Mises stress and equivalent strain contours after the installation of the pin with interference. These show that the yield condition is exceeded in an

annular region about 1 mm (0.040 in.) wide with peak strains $\sigma_p = 0.009$. The Mises field after the application of the $\sigma = 125$ MPa nominal stress is similar to the one obtained in the absence of interference (see Fig. 5-5a) but peak strain, $\sigma_p = 0.023$ is smaller; the plastic strain produced by loading is about half the value generated in the absence of interference. Unloading to $\sigma = 13$ MPa does not alter the plastic strains (compare Figs. 5-10d and 5-11d).

Results for 5 other cases are summarized and compared with the ones described above:

- (iii) 2% interference/0.2 friction/Al-pin
- (iv) 0% interference/0.5 friction/Al-pin
- (v) 1% interference/0.5 friction/Al-pin
- (vi) 2% interference/0.5 friction/Al-pin
- (vii) 1% interference/0.2 friction/steel-pin

These results show that increasing the interference to 2% produces more plastic deformation around the hole but has hardly any effect on the plastic deformation produced by subsequent cyclic loading. With the higher coefficient of friction the plastic strains produced by loading are reduced by about 10% to 20%. The results for the steel pin are essentially identical to those for the aluminum pin. Finally, in no case did the unloading produce further plasticity. Figure 5-12 illustrates that there is fully reversed slip (relative motion between the pin and the contacting sheet) of $\sim 5\mu\text{m}$ in the range $+30^\circ$ to -60° and -120° to 150° (where 0° and $\pm 180^\circ$ correspond with 3 o'clock and 6 o'clock).

It appears that the cyclic stress range examined here (13 MPa to 125 MPa) produces shakedown after the first cycle for isotropic elastic-plastic behavior. In the absence of continuing cyclic plasticity, there is no fatigue damage that can be nondestructively detected. Such damage may be obtained with higher stress amplitudes. The calculations do show that there is fully reversed slip at the pin-hole interface, and this may be capable of producing fretting and fretting fatigue. This damage would be confined to a relatively thin, $\sim 10\ \mu$ -layer adjacent to the hole. The local conditions for fretting are being evaluated as part of a separate project.

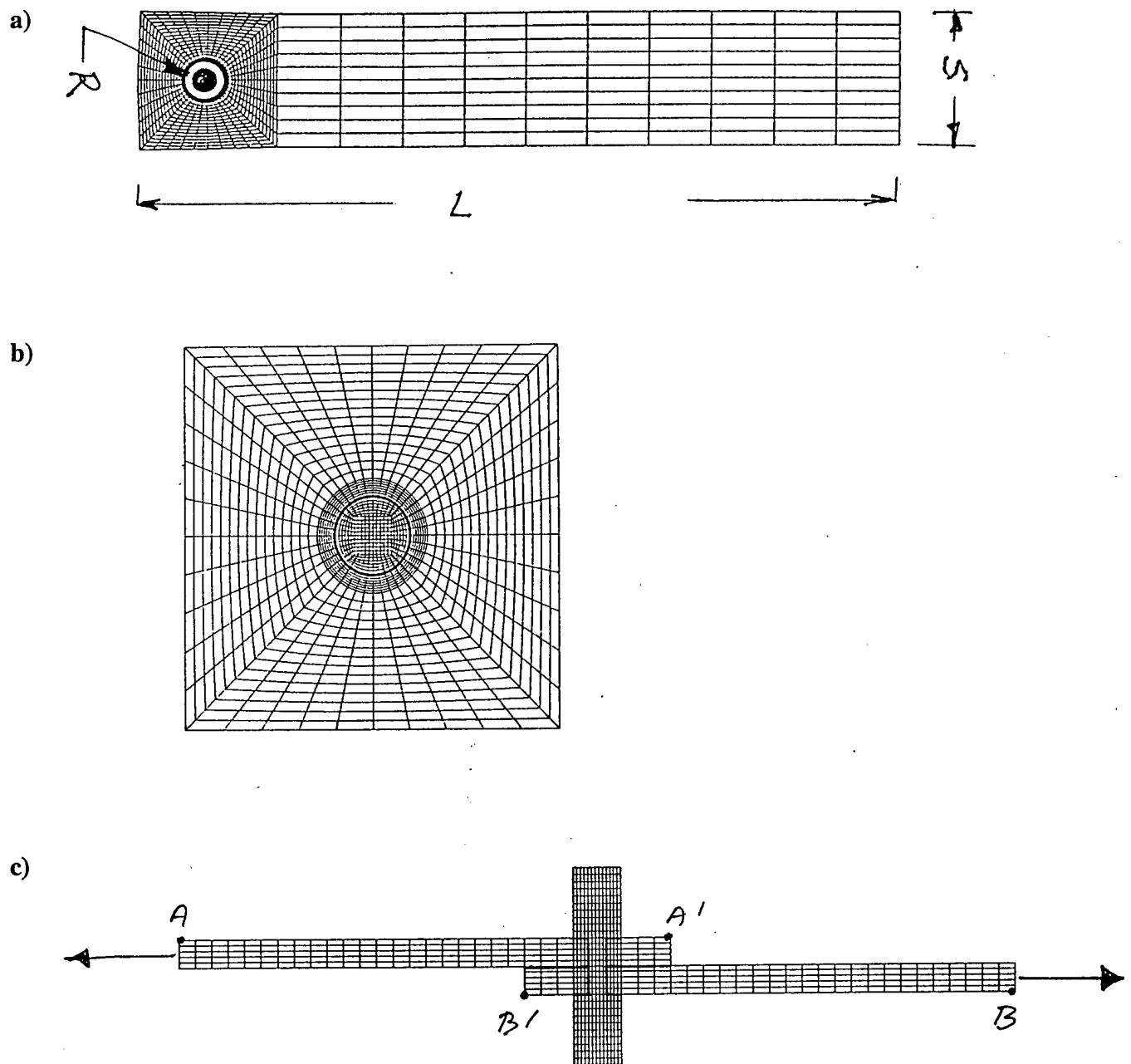


Figure 5.8. Finite element mesh for the 2-D in-plane model: (a) sheet element, and (b) detail showing pin and sheet (the dark circle identifies the location of the pin-sheet interface). The dimensions of the sheet element are: $S=30.6$ mm, $L=168.3$ mm, $R=3.06$ mm, and $t=1.53$ mm. (c) Finite element mesh of a 2-D out-of-plane model of a lap joint.

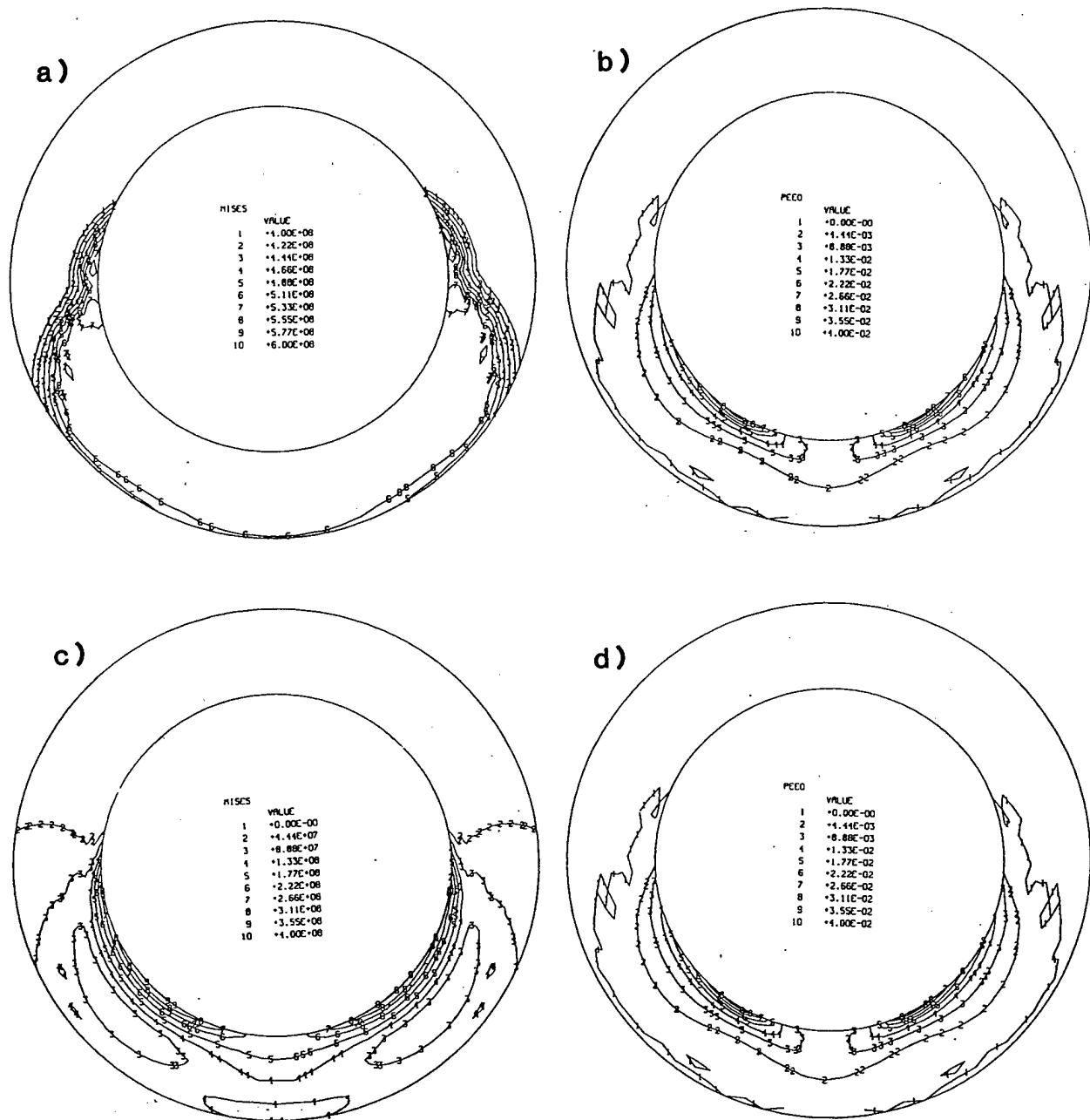


Figure 5.9 Mises stress contours and equivalent plastic strain contours obtained from 2-D in-plane finite element model for 7075-T6 sheet fastened with an aluminum pin: (a) & (b) 0% interference, coef. of friction at hole-pin interface, $\mu=0.2$, and an applied nominal stress of 125 MPa, (c) & (d) 0% interference, coef. of friction at hole-pin interface, $\mu=0.2$, after an applied nominal stress of 125 MPa and unloading to 13 MPa.

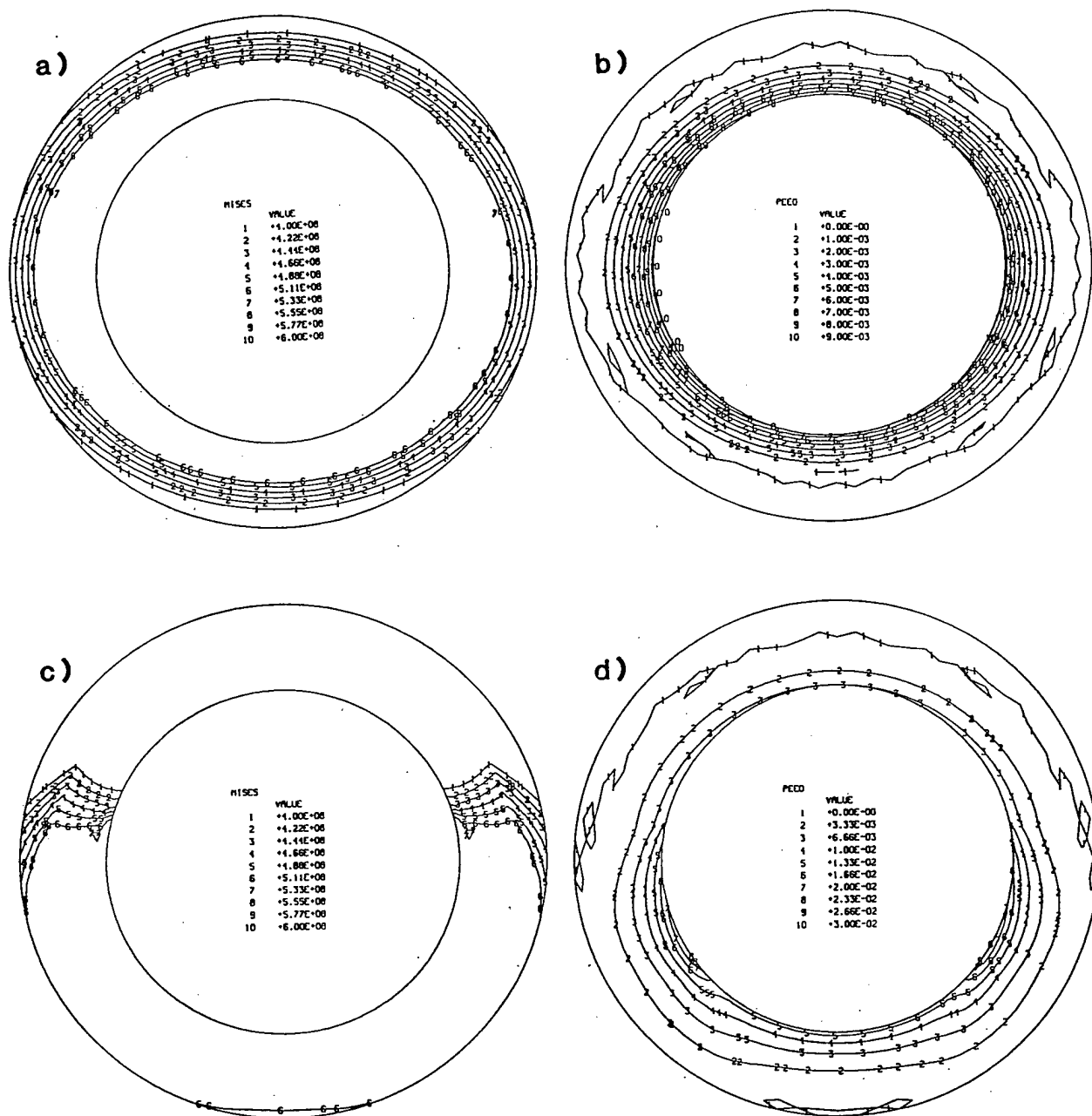


Figure 5.10. Mises stress contours and equivalent plastic strain contours obtained from 2-D in-plane finite element model for 7075-T6 sheet fastened with an aluminum pin: (a) & (b) 1% interference, coef. of friction at hole-pin interface, $\mu=0.2$, after installing the pin, (c) & (d) 1% interference, coef. of friction at hole-pin interface, $\mu=0.2$, after an applied nominal stress of 125 MPa.

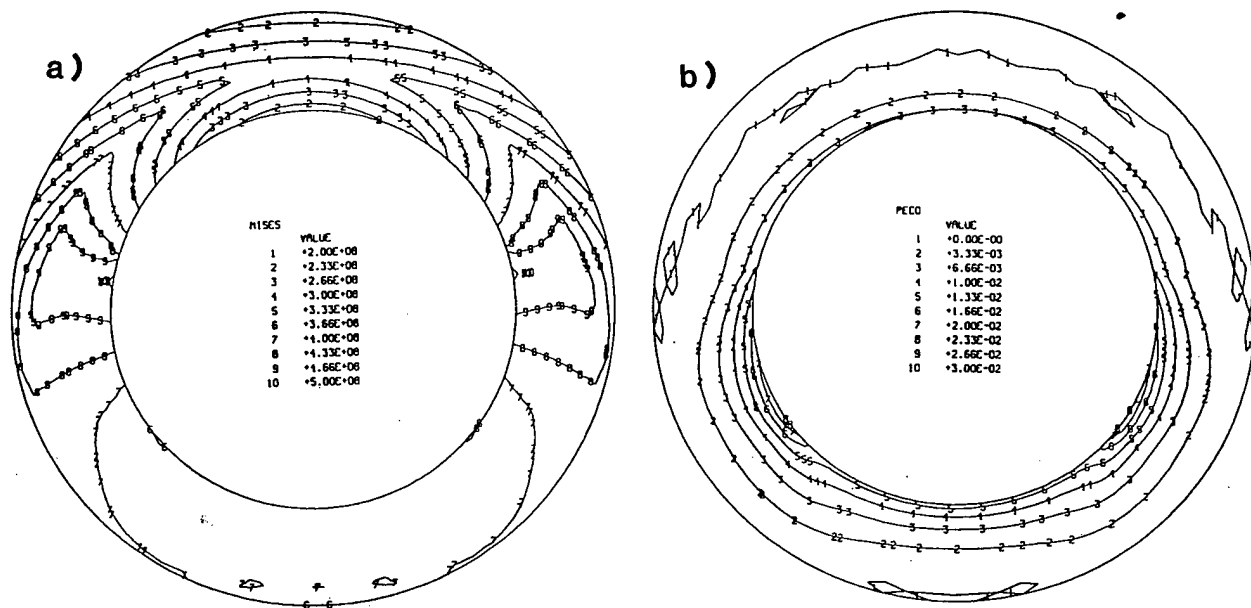


Figure 5.11. Mises stress contours and equivalent plastic strain contours obtained from 2-D in-plane finite element model for 7075-T6 sheet fastened with an aluminum pin: (a) & (b) 1% interference, coef. of friction at hole-pin interface, $\mu=0.2$, after an applied nominal stress of 125 MPa and unloading to 13 MPa.

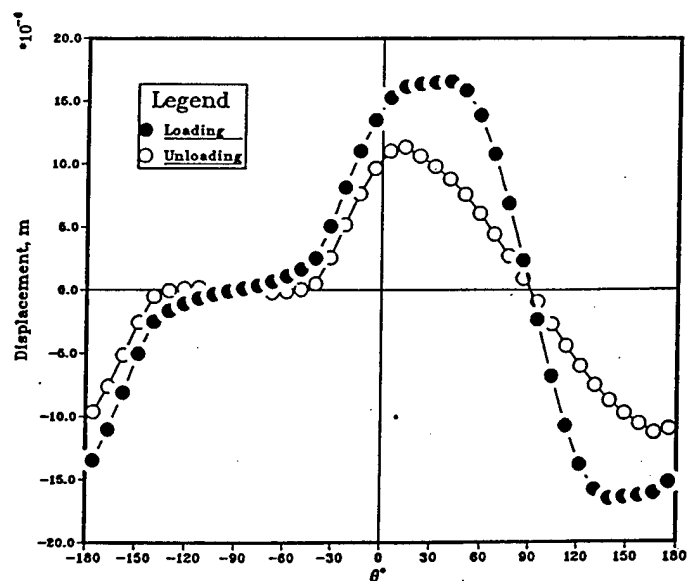


Figure 5.12 Relative tangential displacements (slip) at the pin-hole interface during loading and unloading as a function of angular position (0° and $\pm 180^\circ$ correspond with 3 o'clock and 9 o'clock, respectively).

Constitutive Relations

In order to produce large stress amplitudes with push-pull loading and avoid conventional yielding, the stress cycles include compression as well as tension but avoid buckling of the sheet coupons. This was accomplished with relatively squat samples, well supported at their ends. An example of the stress-strain hysteresis loop is shown in Figure 5.13.

The loops were modeled by the 3-parameter, bilinear, elastic-linear-kinematic hardening-plastic (ELKP) representation described in Figure 5.14. The parameters are the elastic modulus, E , the kinematic yield strength, σ_K , and the linear slope of the plastic regime, M . Since aluminum appears to be elastically stiffer in compression than in tension, the tensile and compression portions of the cycle must be treated independently as shown, in exaggerated form, in Figure 5.14 (a). The cyclic behavior was then approximated using the average value of E as shown in Figure 5.14 (b). The values of the ELKP-parameters for 7075-T6 sheet are summarized in Table 5.2 and are close to values measured previously for bar stock.

2-D Finite Element Model.

A finite element analysis of a relatively simple, 2-D model of a pinned connection was presented in the last annual report. The model consists of a strip with a hole in one end in which a pin is inserted. The center of the pin is held stationary and the pin is not permitted to tilt or bend while a load is applied to the panel. The displacements of this idealized and highly stiff arrangement are confined to the plane of the sheet. The model employs the ELKP- constitutive relations described above and has been analyzed for different values of interface friction, pin-hole interference and nominal stress.

Mechanical parameters that affect fatigue have been evaluated at the panel hole circumference. These include the plastic strain amplitude, the circumferential tensile stress, and the fretting wear and fretting fatigue parameters, F_1 and F_2 ². Examples of the variations of these parameters with angular position are shown in Figures 5.15 - 5.17. These reveal that the values of F_1 , F_2 , circumferential stress and plastic strain amplitude increase with friction and decrease with interference. Stress concentrations at the edge of the hole are as high as 6.4 for the pinned connections, compared to 3 for the stressed hole. The angular positions of the peak values of F_1 , F_2 and circumferential stress are summarized in Table 5.3. These may be compared with the observed positions listed in Table 5.4 for fatigue crack origins in countersunk, riveted lap joints of the type shown in Figure 5.1. The observed positions appear to be more consistent with the peak value of F_2 , the fretting fatigue parameter than the conjunction of peak circumferential stress and plastic strain amplitude which promote conventional fatigue. While this suggests that fretting contributed to the nucleation of the fatigue cracks, it must be recognized that the 2D-model is a less than satisfying representation of a countersunk rivet.

² $F_1 = \mu p \delta$, where μ is the coefficient of friction, p is the contact pressure and δ is the cyclic slip amplitude; $F_2 = \sigma \mu p \delta$, where σ is the circumferential stress at the panel hole interface.

Table 5.2 Summary of ELKP parameters of 7075-T6 sheet alloy.

Test no.	$\Delta\sigma$ (MPa)	σ_m (MPa)	σ_K (MPa)	$\Delta\epsilon^p$ (%)	σ_e (MPa)	$\sigma_{(e,c)}$ (MPa)	σ_a (MPa)	M (GPa)	U' (MJ/m ³)
1.	775	87.5	357	0.0275	444.4	444.5	357.1	58.3	0.196
2.	825	62.5	362.5	0.0285	424.9	425.0	362.6	59.0	0.206
3.	875	37.5	362.5	0.0465	399.8	399.9	362.7	60.2	0.337
4.	950	0	380	0.12	379.8	379.9	380.2	54.8	0.456
5.	1020	0	387.5	0.19	387.2	387.3	387.8	55.1	0.736
Avg.			369.9					57.5	

Table 5.3 Angular locations of peaks in F1, F2 and tensile stress.

Interference and Friction	0% 0.0	0% 0.2	0% 0.3	0% 0.5	0% 0.2,HL*	0.5% 0.2	0.5% 0.2,HL*
F1	-13.5°	-22.5°	-13.5° to -22.5°	-13.5°	-22.5°	-4.5°	-13.5
F2	-13.5°	-13.5°	-13.5°	-13.5°	-13.5°	+4.5° to -4.5°	-4.5
Tensile Stress	-4.5°	-4.5°	-4.5°	-4.5°	-4.5°	+22.5°	+4.5

0° corresponds to 3 PM; counterclockwise rotation produces a positive angle.

* HL refers to Higher Load (+200 MPa). The default loading is +125 MPa and the unloading magnitude is 10% of the loading magnitude.

Table 5.4 Angular location of subsurface fatigue cracks.

$\Delta\sigma$ (MPa)	HOLE #1		HOLE #2		HOLE #3	
	Right	Left	Right	Left	Right	Left
106	-2.5°	-2.5°	-20°	-7°,-20°	-	-
65	-	-	-20°	-28°	-	-
65	-	-	-	-	-	-50°
65	-	-35°	-12°	-21°	-	-7°
65	-5°	-3°	-13°	-7°	-7°	-11°
106	-28°	-7.5°	-17.5°	-28°	+2.5°	-25°
65	-12°	-4°	-3°	-4°	-17°	-21°
106	-21°	-13°	-16°	-7°	-21°	-20.5°
65	-25°	-42.5°	-10°	-12.5°	-10°	-20°
Sum of Last 5 Entries	-91°	-70°	-59.5°	-58.5°	-52.5°	-97.5°
Average of Last 5 Entries	-18.2°	-14.0°	-11.9°	-11.7°	-10.5°	-19.5°

0° corresponds to 3 PM; counterclockwise rotation produces a positive angle.

Figure 5.13 (95 5.3)

Figure 5.14 (95 5.4)

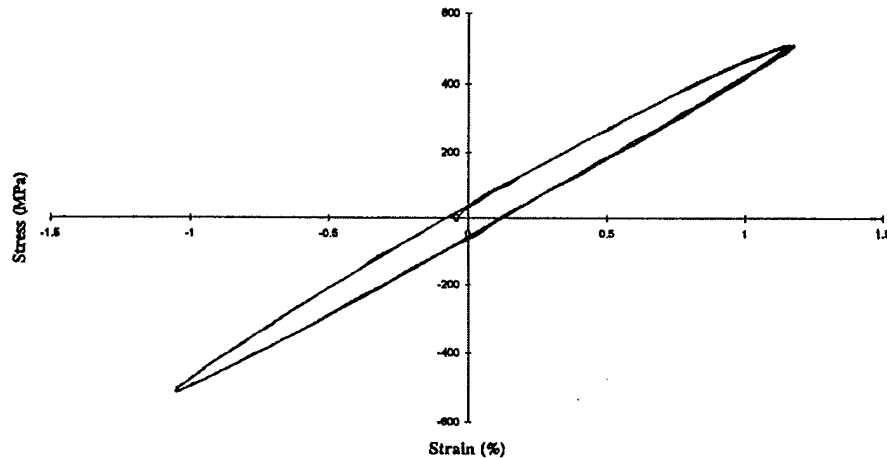


Figure 5.13 Example of cyclic, stress-strain hysteresis loop for 7075-T6. Note: 4 separate cycles are recorded.

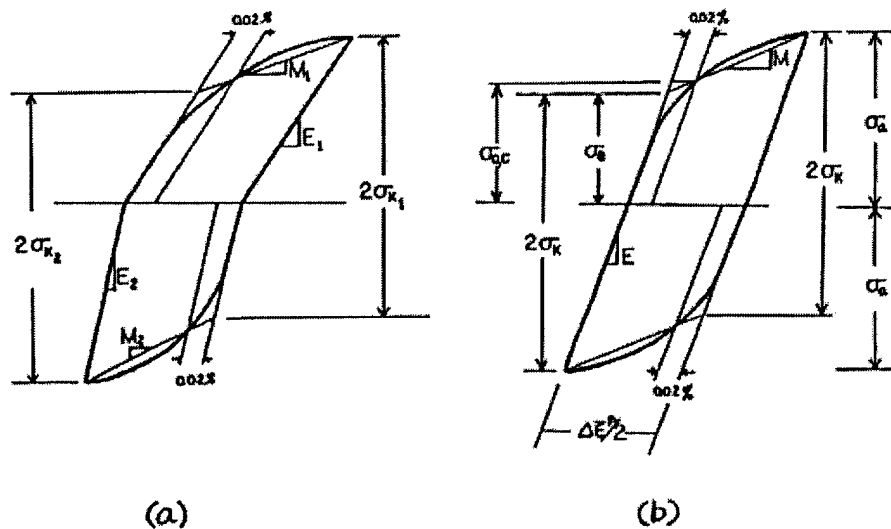


Figure 5.14 Idealized bilinear representation of material behavior defining the elastic Linear Kinematic-hardening Plastic (ELKP) parameters. The parameters E , M , and σ_k are separately obtained for the tension and compression halves of the loop, using the definition shown in (a). Three values are then averaged to obtain the symmetric ELKP loop shown in (b).

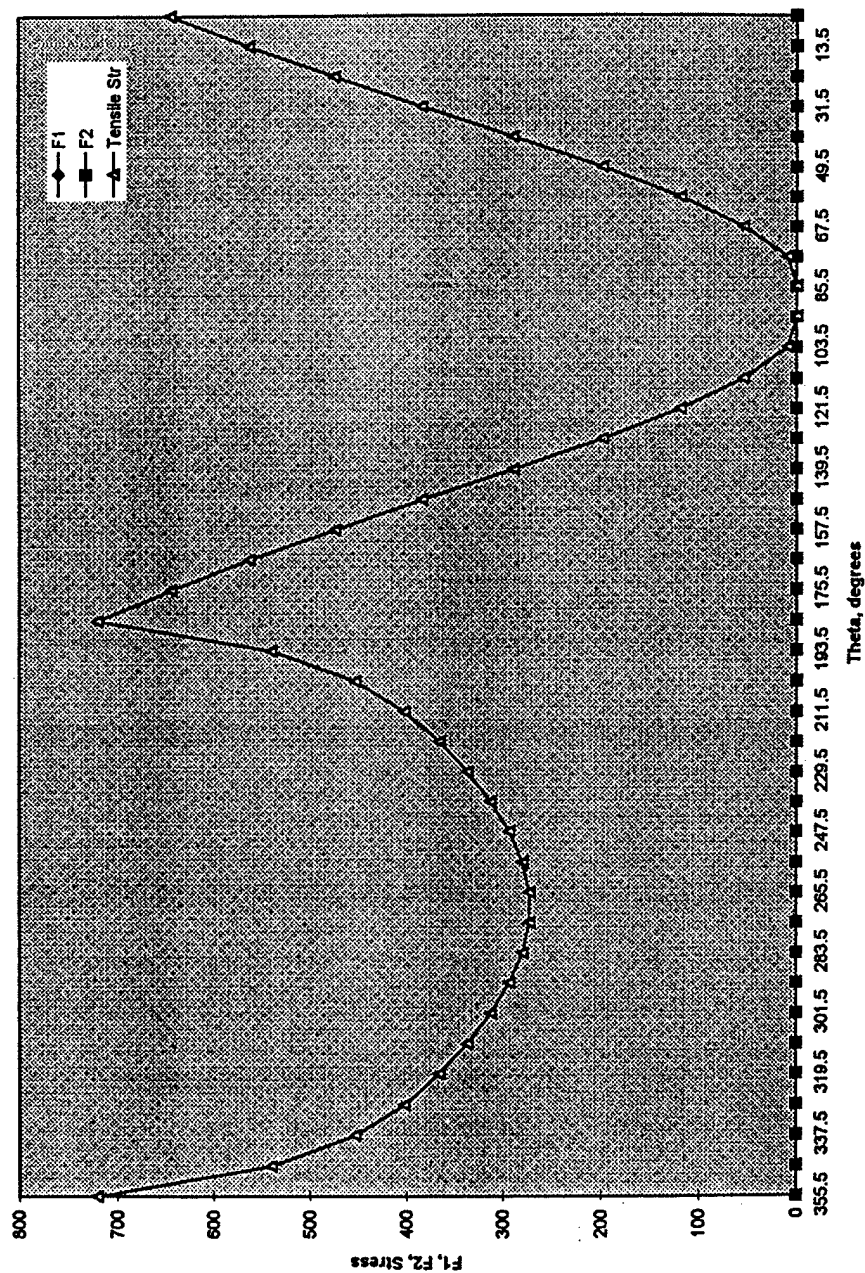
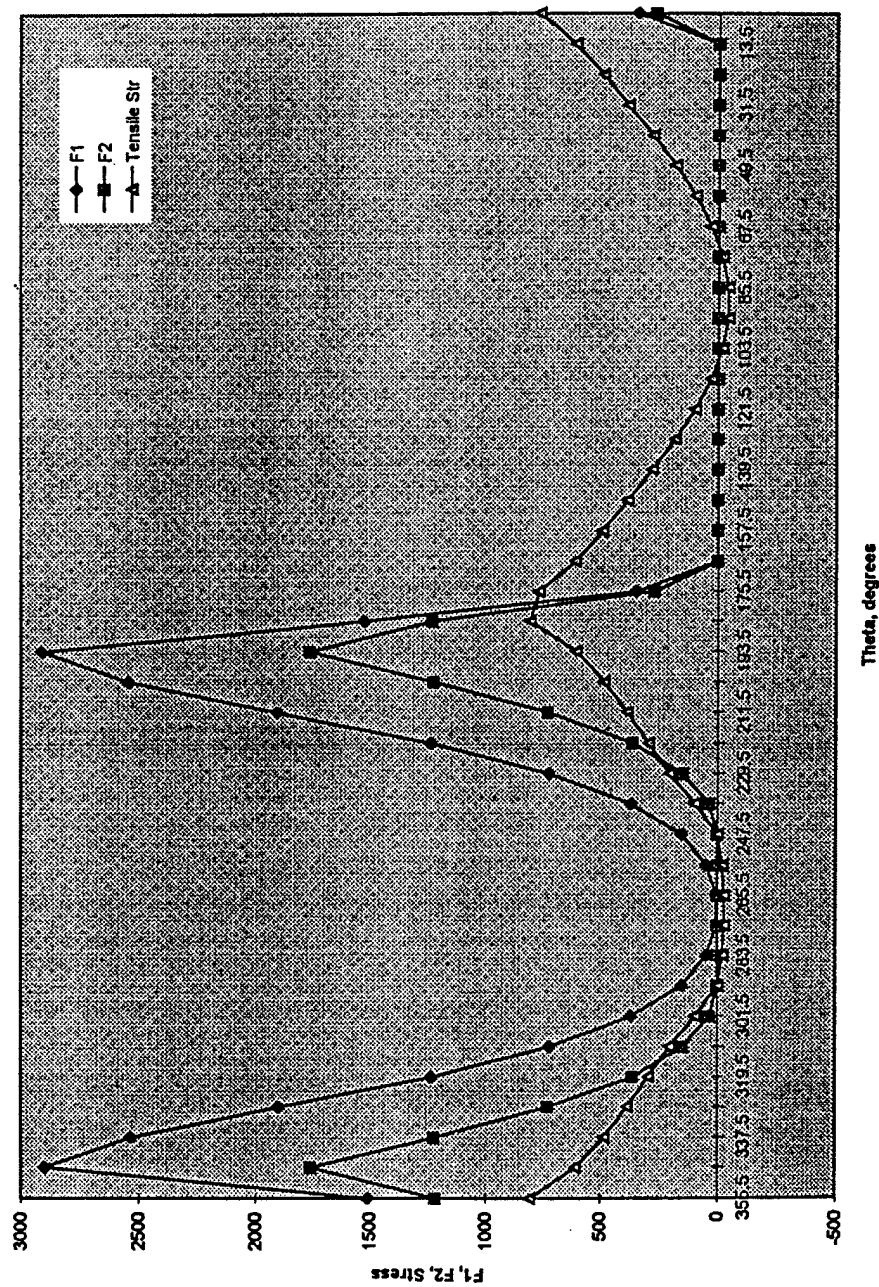


Figure 5.15 Results of the 2D, finite element analysis of a cyclically loaded, pinned connection showing the variation with angular position of the circumferential tensile stress and the parameters F_1 and F_2 at the panel hole for the case of a friction coefficient of $\mu = 0$ and with 0% interference for an applied stress range of $\Delta\sigma = 125$ MPa. Units: F_1 [Pa-m], F_2 [Mpa-kPa-m], Stress [MPa].



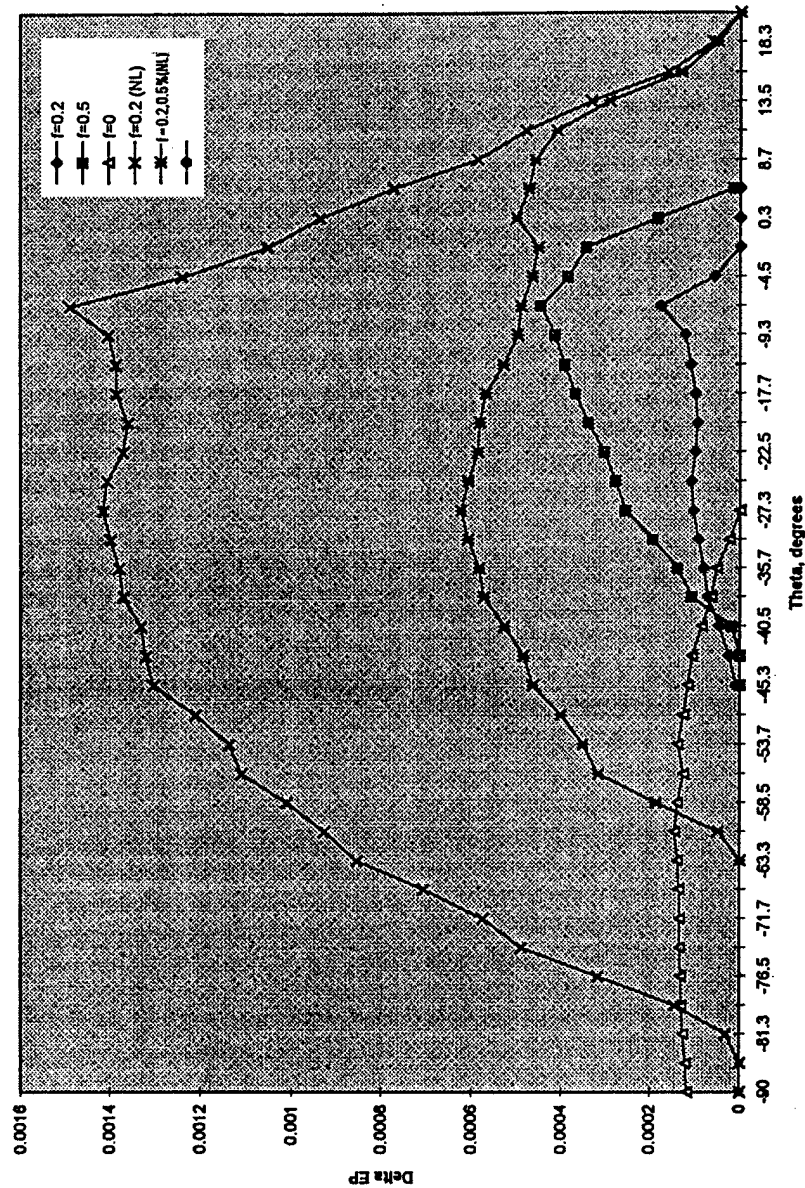


Figure 5.17 Results of the 2D, finite element analysis of a cyclically loaded, pinned connection showing the variation with angular position of the alternating, per cycle (equivalent) plastic strain for the following cases: (a) friction coefficient of $\mu = 0$ and with 0% interference for an applied stress range of $\Delta\sigma = 125$ MPa, (b) friction coefficient of $\mu = 0.2$ and with 0% interference for an applied stress range of $\Delta\sigma = 125$ MPa, (c) friction coefficient of $\mu = 0.5$ and with 0% interference for an applied stress range of $\Delta\sigma = 125$ MPa, (d) friction coefficient of $\mu = 0.2$ and with 0% interference for an applied stress range of $\Delta\sigma = 165$ MPa, and (e) friction coefficient of $\mu = 0.2$ and with 0.5% interference for an applied stress range of $\Delta\sigma = 165$ MPa. Units: F1 [Pa-m], F2 [Mpa-kPa-m], Stress [MPa].

3-D Finite Element Model (I).

The relatively primitive, 3-D finite element model of a riveted lap joint, shown in Figure 5.18, was devised to obtain both a better grasp of the 3-D-modeling requirements and insights into the joint distortion with the expenditure of minimal computation time resources. It consists of two (upper and lower), 1.53 mm- (0.60 in-) thick panels and a 6.12 mm- (0.241 in-) diameter (shank) rivet. The edges of the panels are constrained in the x-direction to simulate the behavior of a wide panel with many rivets. Further, the lower edges of each of these faces are fixed in the z direction to prevent unrestrained rotation of the body in space. All nodes lying on the symmetry faces are fixed in the y-direction (the symmetry axis). The two panels and rivet are modeled as independent bodies capable of interacting with each other. Sliding contact between the panels and at the rivet panel interfaces has been modeled using a small sliding approximation which provides for small amounts of slip and arbitrary rotations. Because of the coarseness of the mesh and the nature of the contact elements, the contacting surfaces may not provide an accurate description of the local behavior and may cause a false asymmetry in the results. A discrete collection of tangential, faceted planes is used to approximate the rivet surface and each node on the surfaces of the holes in the sheets is restricted to sliding within a facet. A cyclic load is applied at the non-lapping end face of the upper panel, while the corresponding end of the lower panel is fixed along the x-axis, as shown in Figure 5.18.

Eight variants of the model are described in Table 5.5. These include 5 different model geometries: A1 - E1; 2 levels of interface friction: $\mu = 0.2$ and $\mu = 0.5$; and 2 types of material behavior: linear elastic, and elastic-linear-kinematic hardening-plastic (ELKP) with the parameters described above and appropriate for 7075-T6 aluminum sheet. The mesh of Model A consists of 495, 8-noded, linear brick elements and 480 user defined nodes. In additions to the displacement degrees of freedom, incompatible deformation modes are added to internal elements. Primarily, these enable shearing of the elements without locking, allowing an appropriate kinematic response to bending. Further, these modes allow for a non-linear stress variation perpendicular to the bending direction, thus preventing an overestimation of the stiffness. The total number of variables is 2217. The meshes of the other models were similar. These models require substantial amounts of CPU time, e.g. 1400 seconds and 10,000 seconds for a linear elastic and elastic-plastic (ELKP) calculation, respectively, on a Power Challenge Array supercomputer. The models offer useful qualitative insights into the distortion of the joint under repeated cyclic loading, but may require further refinements to provide quantitatively reliable descriptions of local stresses and contact conditions.

Results of the 3-D-finite element calculations for a nominal applied cyclic stress range of $\Delta\sigma=125$ MPa are summarized in Figures 5.18-5.21 and in Tables 5.6 and 5.7 (see also Figure 5.23). Table 5.8 compares the calculated values of a compliance and a lateral displacement with actual measurements of these quantities. The agreements are encouraging. The models illustrate the noticeable tilting of the rivet and the accompanying, local bending of the panels which is very distinct and highly visible in the actual tests of the single row, riveted connection. As a result of the panel bending, the peak tensile stresses in the panels adjacent to the rivet hole are expected to be higher at the interior panel surfaces than at the exterior surfaces. This is confirmed by the tensile stress acting in the exterior (e.g., element f, Figure 5.23) and interior (e.g., element f', Figure 5.23) panel elements listed in Tables 5.6 and 5.7. The bending is partly obscured by the relative coarse

meshes employed. The tilting contributes to the joint compliance. As shown in Tables 5.6 and 5.7, there is a direct relation between the tilt angle and the joint compliance. Larger tilt angles and compliance values reflect larger slips at the rivet-panel and panel-panel interfaces as well as larger amounts of panel bending with attending, higher local cyclic stresses. The tilting of the rivet has a yet another undesirable effect. It forces one side of the rivet head against the panel near the edge of the rivet hole, e.g., at location A in Figure 5.22. This edge of the hole in the panel is displaced by the slip at the panel interface subjected to local bending and pushed against the adjacent panel along a circular zone a small distance from the rivet hole (location B, Figure 5.22). Fretting damage arising from the contact pressure and slip amplitude generated at B is visible in Figure 5.12, just below each of the rivet holes. However, the present 3-D models show that the panels are not in contact at location A, again because the mesh elements are too coarse and cannot reproduce the local bending at the hole. The distorted meshes indicate that the tilting of the rivet is facilitated by the countersunk head which, unlike a regular rivet head, is only supported by the panel on one side. In the absence of the countersunk head (Model E), the rivet tilt angle and compliance are reduced by $\sim 2\times$ (see Tables 5.6 and 5.7). An increase in the coefficient of friction from $\mu = 0.2$ to $\mu = 0.5$ also reduces the distortion of the joint, the slip and the tilting of the rivet. These findings illustrate that there are many connections between joint design details and the propensity for fatigue and fretting damage.

The insertion of ELKP behavior in place of linear elastic behavior has dramatic results. Comparisons of results for B3 with B1, and C5 with C2 (see Table 5.7) show that plasticity increases the rivet tilt by $\sim 2.5\times$ and the local slips by $\sim 10\times$. The comparison of Figure 5.19a (elastic behavior) and Figure 5.19b (elastic-plastic behavior) reveals the large increase in the amount of distortion and the absence of support for the countersunk rivet brought on by the onset of plastic deformation. The plastic component of slip is, largely, not recovered during unloading. For this reason, total slips calculated for linear elastic behavior serve to approximate the slip range for ELKP behavior. However, the effect of plasticity on local stresses and strains cannot be neglected for the present applied nominal stress of 125 MPa. The insertion of ELKP behavior also leads to the plastic buckling of the countersunk head (see Figure 5.21). Consistent with this finding, noticeable buckling is observed in the rivets of the one-row test panels subjected to a nominal cyclic tensile stress, $\sigma = 117$ MPa, which is less than the value, $\sigma = 125$ MPa, employed in the calculations.

In general, these findings show that 3-D finite element analyses offer new and important insights into the origins of fatigue and fretting damage of riveted connections that will be useful both from the viewpoints of joint design and damage detection.

Table 5.5 The 3-D finite element models.

Model	Rivet heads	Coefficient of Friction, μ	Material Behavior
A1	1 standard 1 countersunk (to 2 panel thickness)	0.2	elastic
B1	1 standard 1 countersunk (to full panel thickness)	0.2	elastic
B3	1 standard 1 countersunk (to full panel thickness)	0.2	ELKP
B4	1 standard 1 countersunk (to full panel thickness)	0.5	elastic
C1	2 standard	0.2	elastic
C5	2 standard	0.2	ELKP
D1	1 headless 1 countersunk (to 2 panel thickness)	0.2	elastic
E1	1 headless 1 countersunk (to full panel thickness)	0.2	elastic

Table 5.6 Summary of Results for 3d Finite Element Models of Riveted Lap Joints with Linear Elastic Material Behavior

MODEL		A1	B1	B4	C1	C2	D1	E1
Feature	Location*							
Rivet Tilt, degrees	—	3.2	3.3	3.0	2.6	1.7	3.5	3.7
Joint Compliance ($\mu\text{m}/\text{kN}$)	—	87.5	79.6	71.6	72.1	68.9	90.3	83.5
Tensile stress in elements adjacent to rivet hole (MPa)	e	413.2	351.9	311.8	357.3	219.1	436.7	359.2
	e'	270.6	344.7	295.9	189.3	167.2	269.1	318.6
	e''	459.7	400.9	394.5	467.3	658.8	528.4	544.6
	f	117.3	166.1	111.3	142.8	133.4	97.9	132.8
	f'	469.4	470.0	419.2	293.7	146.4	485.2	469.5
	f''	291.8	241.8	170.4	287.3	622.9	364.1	227.0
Contact Pressure (MPa)	h	0	0	0	0	0	0	0

*Location identified in Fig.5.23.

Table 5.7 Summary of results for 3-D finite element models B and C comparing linear elastic behavior (B1 and C2) with elastic-plastic behavior (B3 and C5) for both loading and unloading.

MODEL		B1	B3			C2	C5		
Feature	Location*	Load Value (L)	Load Value (L)	Unload Value (U)	L-U	Load Value (L)	Load Value (L)	Unload Value (U)	L-U
Rivet Tilt, degrees	---	3.3	7.33	3.33	4.0	1.7	4.17	1.33	2.84
Joint Compliance ($\mu\text{m/kN}$)	---	79.6	232.3	1549.4	---	68.9	115.3	514.5	---
Peak stress in elements adjacent to rivet hole (MPa)	e	351.9	43.8	-166.9	--	219.1	233.6	-54.1	--
	e'	344.7	210.3	-190.6	--	167.2	180.4	-34.5	--
	e''	400.9	352.3	-143.9	--	658.8	355.9	-225.75	--
	f	166.1	107.8	-21.6	--	133.4	193.8	7.2	--
	f'	470.0	277.9	-206.2	--	146.4	134.1	-83.7	--
	f''	241.8	133.8	-110.8	--	622.9	325.9	-265.96	--
Contact Pressure (MPa)	h	0	0	0	0	0	0	0	0

*Location identified in Fig.5.23.

Table 5.8 Comparison of calculated values and measurements of a compliance and an out-of-plane displacement.

	Rivet Tilt, degrees	Joint Compliance ($\mu\text{m}/\text{kN}$)
Model A1	3.2	87.5
Model B1	3.3	79.6
Model B3	7.33	232.3
Model B4	3.0	71.6
Model C1	2.6	72.1
Model C2	1.7	68.9
Model C5	4.17	115.3
Model D1	3.5	90.3
Model E1	3.7	83.5
Experimental Measurement	3.1	103.3

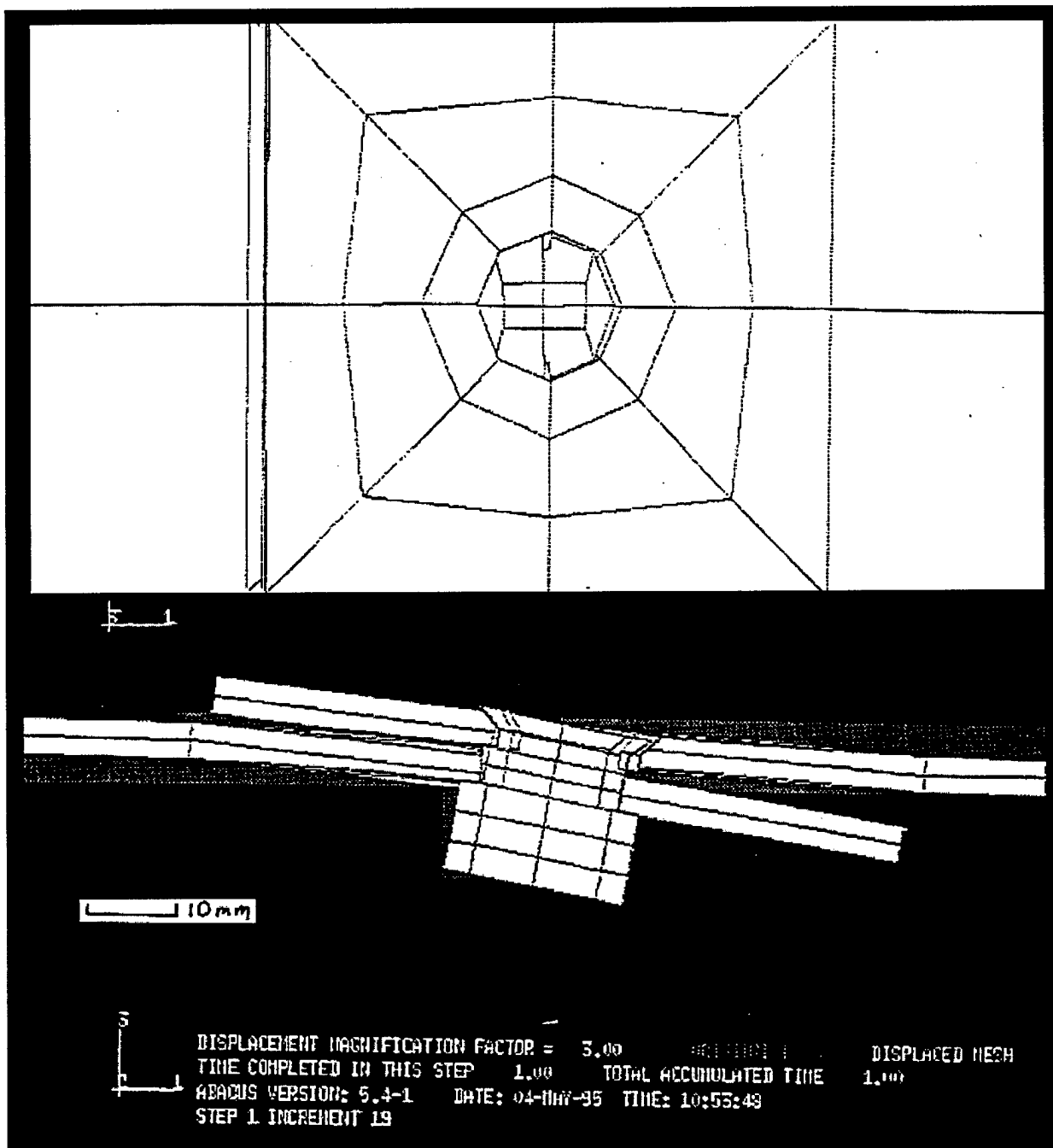


Figure 5.18 The displaced, 3D-finite element mesh for model A1 (see Table 5.5) at a nominal applied stress of $\Delta\sigma = 125$ MPa: (a) plan view and (b) side view through center of rivet. Each panel is 168.3 mm- (6.63 in-) long and 30.6 mm- (1.20 in-) wide. The rivet hole and rivet shank are 6.12 mm- (0.24 in-) in diameter. Displacements are magnified 3x.

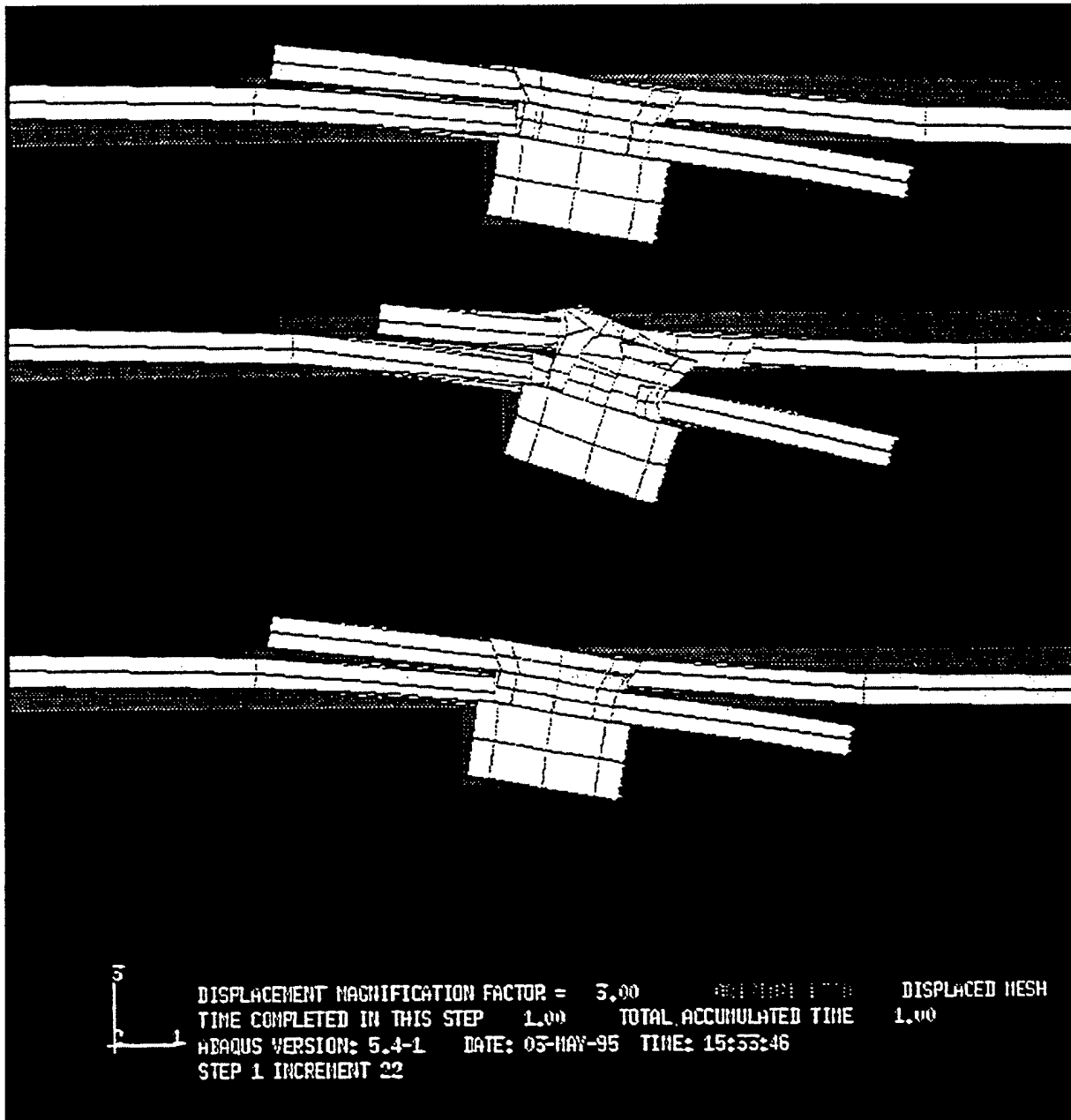


Figure 5.19 The displaced, 3D-finite element meshes for: (a) Model B1, (b) Model B3, and (c) Model B4 at a nominal applied stress of $\Delta\sigma = 125$ MPa. These are side views through center of rivet. Each panel is 168.3 mm- (6.63 in-) long and 30.6 mm- (1.20 in-) wide. The rivet hole and rivet shank are 6.12 mm- (0.24 in-) in diameter. Displacements are magnified 3x. Note the distortions of Model B3, which accounts for plastic deformation, are much larger than those of the linear elastic Model B1.

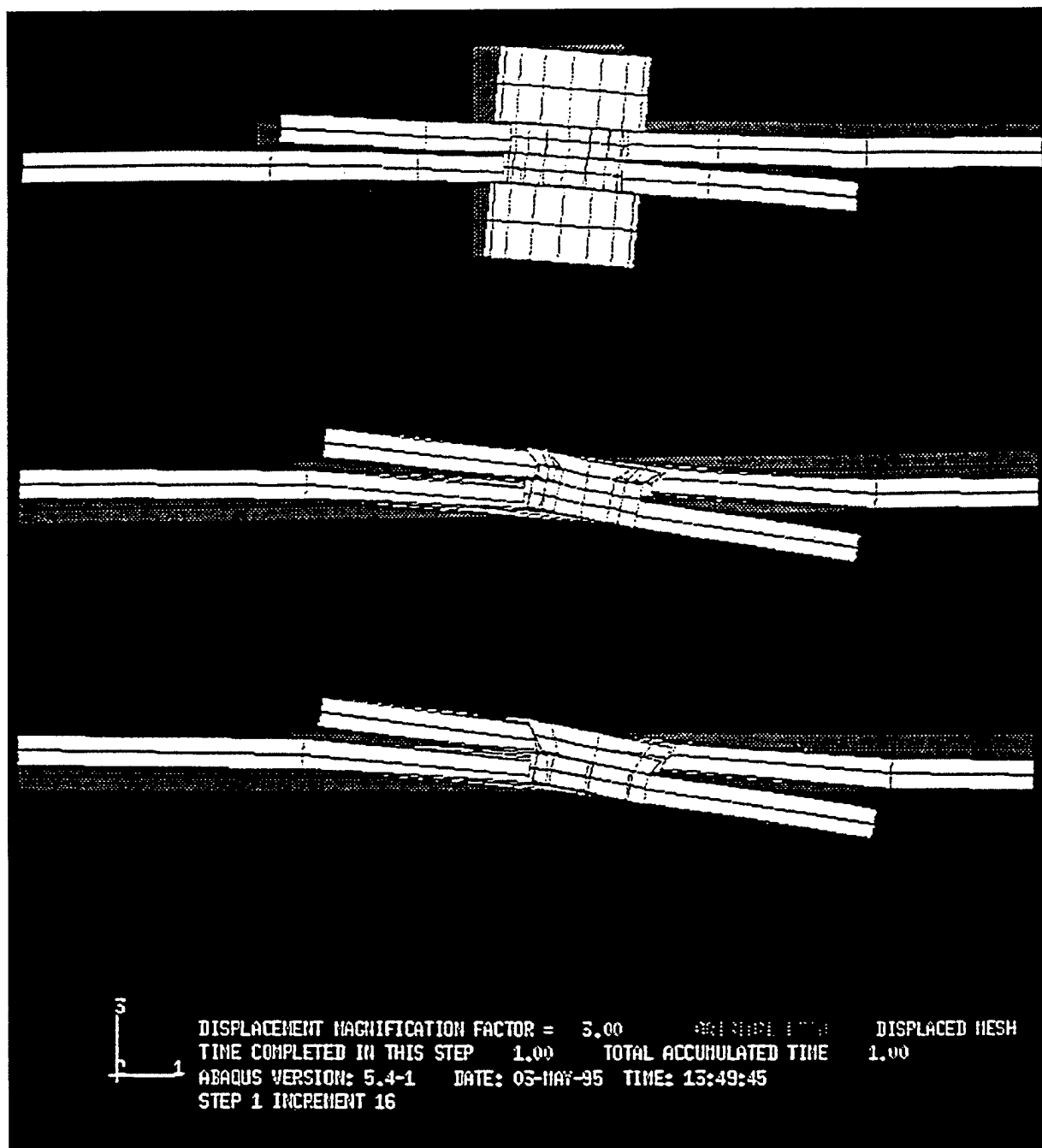


Figure 5.20 The displaced, 3D-finite element meshes for: (a) Model C1, (b) Model D1, and (c) Model E1 at a nominal applied stress of $\Delta\sigma = 125$ MPa. These are side views through center of rivet. Each panel is 168.3 mm- (6.63 in-) long and 30.6 mm- (1.20 in-) wide. The rivet hole and rivet shank are 6.12 mm- (0.24 in-) in diameter. Displacements are magnified 3x.

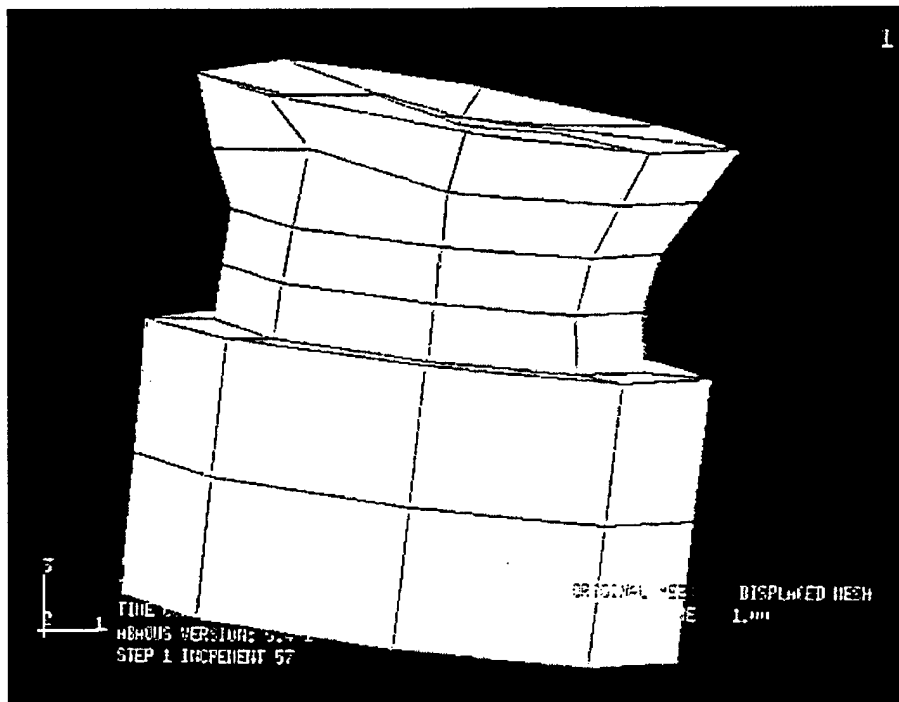


Figure 5.21 Deformed mesh of plastically deformed rivet of Model B3.

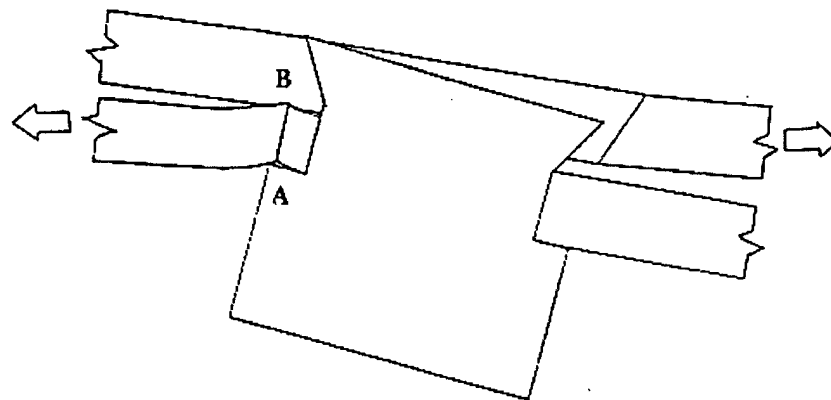


Figure 5.22 Schematic representation of a riveted lap joint under tensile load. The head of the tilted rivet presses against the lower panel at A, this forces the sharp, lower panel-hole edge against the displaced upper panel at B, producing fretting damage at that location.

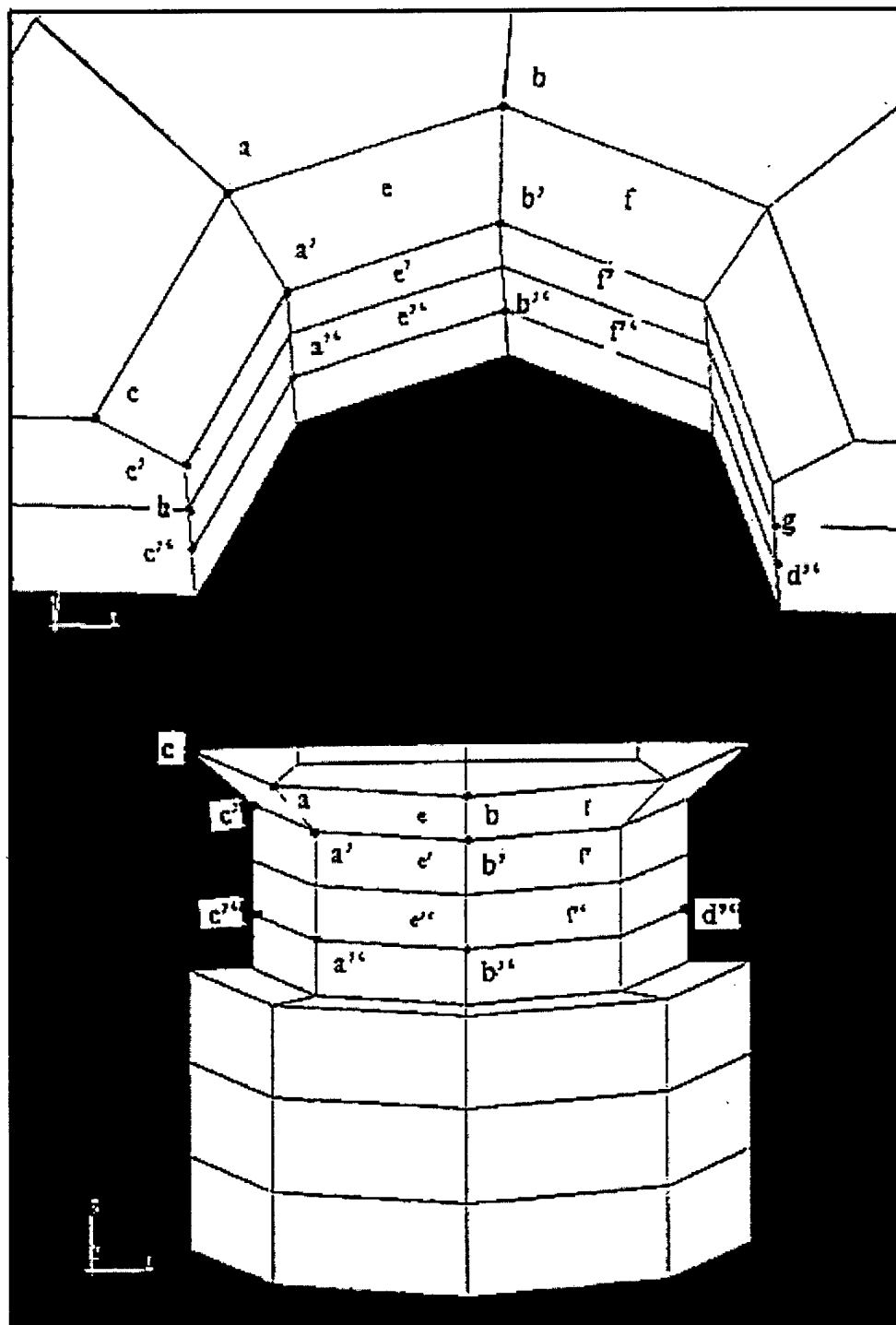


Figure 5.23 Location of mesh points, elements and other features of the 3-D model referred to in Tables 5.6 and 5.7.

3-D Finite Element Model (II).

Advanced models which capture small wavelength features of the deformation have been developed. For the sake of continuity, the basic features of the geometry and models are described at first.

The model geometry consists of two (upper and lower) sheets and a rivet. The dimensions of the model lap joint are shown in Fig. 5.24. Two different rivet geometries were considered, as shown in Fig. 5.25: (1) Model I in which the rivet has one standard head at its lower end and one head countersunk to a depth of the thickness of a single sheet, and (2) Model II in which a double-headed rivet with no countersinking is treated.

A cyclic load with $\sigma_{\max} = 125$ MPa and $R = 0.1$ is applied at the non-overlapping end face of the upper sheet while the corresponding face belonging to the lower sheet is fixed along the x-axis. In addition, the edges A and B are fixed in the z-direction to prevent unrestrained rotation of the geometry in space. The geometry shown in Fig. 5.24 represents one unit of a multi-riveted, single-row, long panel extending in the positive and negative y-directions. Lines CD and EF represent the symmetry planes and are constrained against motion in the y-direction. Purely elastic material response has been considered with $\sigma_E = 70$ GPa, $\mu = 0.2$ and $\nu = 0.25$.

In the relatively primitive models discussed previously, first-order incompatible brick elements were used to represent the bulks of the rivet and two sheets. These were chosen for three reasons: (1) they are first-order elements, which are preferred in formulating contact problems, (2) they include additional internal deformation modes that allow them to perform almost as well as normal second-order elements in bending-dominated analyses while being more economical, and (3) the version of the finite element software ABAQUS available at that time was incapable of providing an accurate solution for a half-symmetry model consisting of second-order elements. While these models served to capture the gross features of the deformation of a riveted lap joint, the first-order element were found to perform poorly when their shape deviated from rectangularity. This deviation is unavoidable in modeling the countersunk hole and rivet. This finding forced a consideration of second-order elements and a necessary improvement in the software capabilities.

The advanced models, the results of which are discussed in the following sections, consist of 27 noded (second-order) brick elements. These elements capture variations in stresses and displacements more effectively and are very effective in bending-dominated problems. However, since first-order elements remain preferred in modeling the three-body contact, the advancement may not be described as unqualified.

Model I is composed of 152 user defined elements, 1971 user defined nodes and 821 internally generated elements for contact. The total number of variables is 8376. The cpu time consumed for an elastic load (125 MPa)/unload (13 MPa) calculation was 4447.5 seconds on the SGI Power Challenge Array at NCSA. Model II consists of 172 user defined elements, 2163 user defined nodes, 909 internally generated ISS3DF elements for contact. The total number of variables is 9216. The cpu time consumed for an elastic load/unload calculation was 6460 seconds.

Results from the relatively sophisticated calculations are summarized in Table 5.9 (see also Fig. 5.25). In order to assess the degree of improvement in results, earlier results from the relatively primitive models are included (designated as "coarse"). The use of second-order elements has enabled the bending of the panels to be represented more accurately. The resulting increase in the rivet tilt is accompanied by a decrease in the displacement of the loading end. This is indicated by the compliance calculations. The lap joint compliance is defined as $C = C' - C''$. $C' = \delta/P$ is the compliance of the model joint, P is the applied load and δ is the total displacement. $C'' = L/(EA) = 93.4 \text{ m/GN}$, is the compliance of a continuous panel having the same length, L , as the model (length of two panels minus overlap) and the same cross-sectional area, A , and elastic modulus, E , as the separate panels.

Fig. 5.26 shows the displaced meshes for the two rivet geometries. The bending of the panels and tilting of the rivets produce stress and strain gradients in the thickness direction. Panel bending near the fastener increases the stress concentration while panel bending away from the fastener serves to relax stresses. As shown in Fig. 5.27, tensile stresses are higher near the inside panel surfaces, consistent with panel bending. For the countersunk panel, this coincides with the thinned section. The peak stresses vary directly with tilt and bending. The peak stress concentrations driving conventional fatigue damage are: 9.5, between $+8^\circ$ and -22° in the upper panel, and 14 at 6 o'clock in the lower panel in Model I, and, 6.0 between $+10^\circ$ and -11° in the upper panel, and 9.3 at 6 o'clock in the lower panel in Model II. As shown in Table 5.9, tilting contributes to the joint compliance. Larger tilt angles and compliance values reflect larger slips at the rivet-panel and panel-panel interfaces as well as larger amounts of panel bending with attending, higher local cyclic stresses. Countersinking results in greater tilt, panel bending, in-plane slip amplitudes and peak stresses.

Actual tests of single-row riveted connections show fretting damage in two regions. Figure 5.28 shows the typical fretting damage observed on the surface of countersunk holes. Another typical region is located on the underside of the upper panel. The edge B, shown in Fig. 5.27, is displaced by the slip at the panel interface and subjected to local bending; it is then pushed against the upper panel along a crescent shaped zone a small distance from the rivet hole (Fig. 5.29). Primary parameters that affect the extent of fretting damage are the contact stresses and slip amplitudes. These have been evaluated, shown in Table 5.9 and Fig. 5.30-5.34. Briefly, peak contact pressures of about 650 MPa are generated due to countersunk-rivet tilting. These pressures are found in the straight-hole portion. The contact pressure for the countersunk-hole contact varies between 250 MPa and 325 MPa. Peaks in the range of 375-450 MPa are generated for straight-hole contact in the absence of any countersinking. In-plane slip amplitudes range from near sticking conditions to 100 μm in Model I, and up to 48 μm in Model II.

The parameter $F1$ is a measure of the work expended in frictional rubbing between the rivet and two panels at their interfaces. It is to be noted that the spatial variation of the fretting damage shown in Fig. 5.28 corresponds very well with the calculated spatial variation of $F1$ for a countersunk rivet/hole, shown in Fig. 5.30. A direct correlation between the peaks in the variations of $F1$ and peaks in the variations of contact pressures is observed in the straight holes. In other words, the $F1$ variations and contact pressure variations peak at the same depth in a given panel in straight holes. Countersinking increases the wear damage, as indicated by $F1$ and results in lower contact pressures. It may help in pushing the depth at which the contact pressure peaks, out of phase with

respect to the corresponding depth for F1. This is suggested by the observation that only in the countersunk hole (Fig. 5.30) is there significant contact at $z = 0$ without a corresponding peak in F1 at the same depth. This can conceivably slow crack propagation rates compared to the situation where the peaks reinforce each other. It also seems that the presence of the countersink pushes the depth at which maximum wear is observed closer to $z = 0$. If this is indeed the case, the peak stresses and damage areas will also be out of phase. Panel bending affects the through-the-thickness contact locations between the rivet and hole. At $z = 0$ and $z = 2t$ (where compression due to bending is maximum), the contact pressures peak at 6 o'clock and 12 o'clock respectively. However, at the four other depths, higher peaks are found at locations short of the above angular positions, i.e.; towards 3 o'clock. The contact pressure peaks at different depths are at different angular locations and, for a straight hole, the pressure itself is proportional to the tensile stress produced by panel bending.

In conclusion, fatigue cracks may initiate at the bottom edge and/or middle layer of the hole in the upper, countersunk panel in model I. This is possible due to the coupling of peak tensile stresses with peak fretting damage. Further coupling between the in-plane and "crescent" fretting damages, occurring near 4 o'clock, would make this locale optimal for crack initiation. The fretting wear parameter, F1, shows promise as a reliable pointer to fretting damage in riveted lap joints.

Table 5.9

MODEL		Model I (coarse)	Model II (coarse)	Model I	Model II
Feature	Location*				
Joint Compliance (m/ GN)	—	34.2	27.7	30.9	24.5
Rivet Tilt, degrees	—	4.2	3.0	4.3	3.67
Total in-plane slip at rivet-panel interface (μm)	a	29.1	25.0	18.53	8.25
	a'	31.9	18.2	20.18	19.73
	a''	-67.9	-67.2	-25.88	-33.61
	b	64.7	48.0	38.2	30.7
	b'	75.7	52.0	54.3	48.4
	b''	-68.1	-73.0	-28.6	-36.6
Total in-plane slip at panel-panel interface (μm)	g	176.4	120.7	145.6	90.4
	h	166.7	135.8	14.3	34.3
Total out-of-plane slip (μm)	c	-33.3	-5.4	-8.52	-8.9
	c'	-32.1	0.0	-9.18	0.3
	c''	10.2	7.0	-19.21	-18.6
	d''	0.3	-2.0	0.9	2.0
Peak tensile stress in elements adjacent to rivet hole (MPa)	e	392.5	447.7	1187.5	746.1
	e'	591.1	414.4	1187.5	746.1
	e''	528.1	505.1	360.3	454.7
	f	236.9	341.6	942.6	719.0
	f'	697.9	434.6	942.6	719.0
	f''	408.4	440.2	404.5	483.6
Peak Contact Pressure (MPa)	panel-panel	-111.5	-115	-650	-730
	panel-rivet head	-117	-74.9	-100	-115 to -300

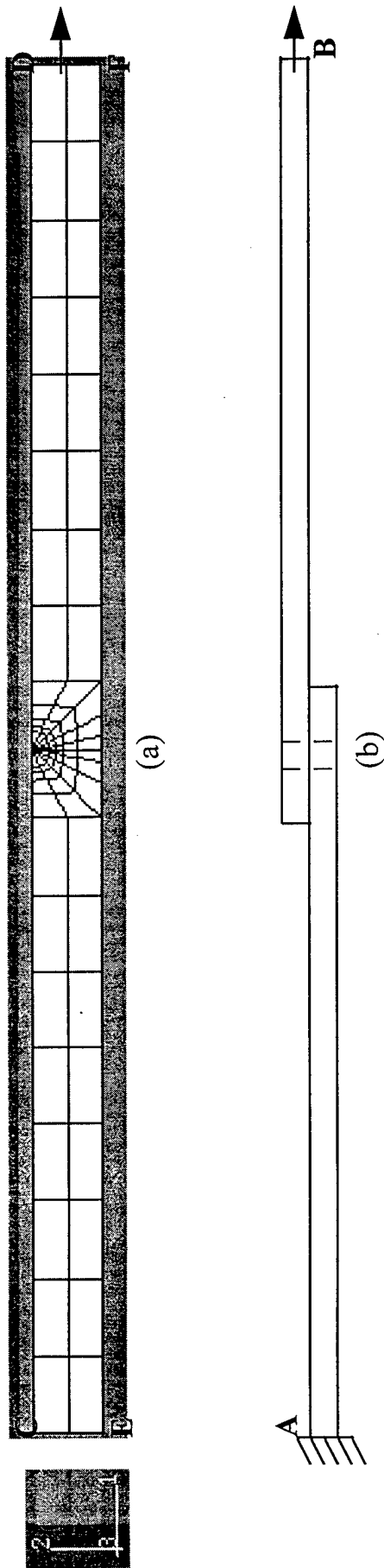


Figure 5.24. 3-D finite element model of a single rivet-row lap joint: (a) plan view of half-symmetry mesh (b) schematic of model profile. The overall length of the model is 306 mm; the length of the overlap is 30.6 mm; the half-width of each sheet is 15.3 mm, which is half the repeat distance; the thickness of each sheet is 1.53 mm; the rivet shank diameter is 6.12 mm; the rivet head diameter and height are 9.792 mm and 3.83 mm respectively.

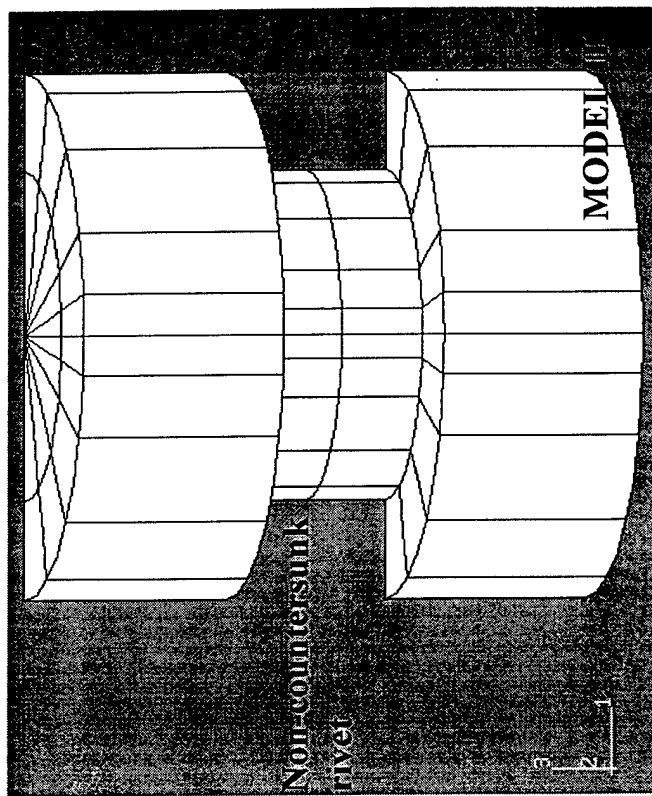
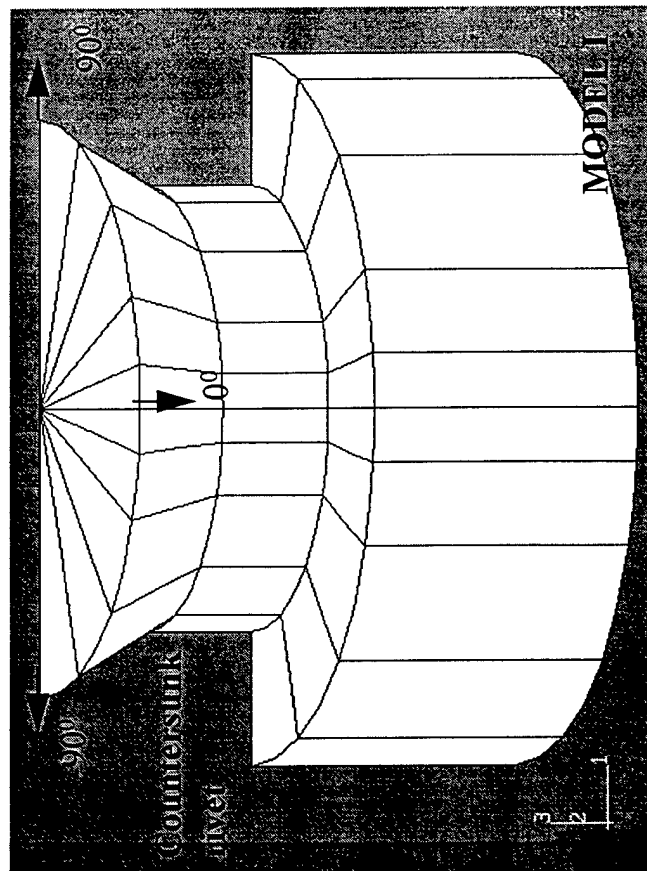
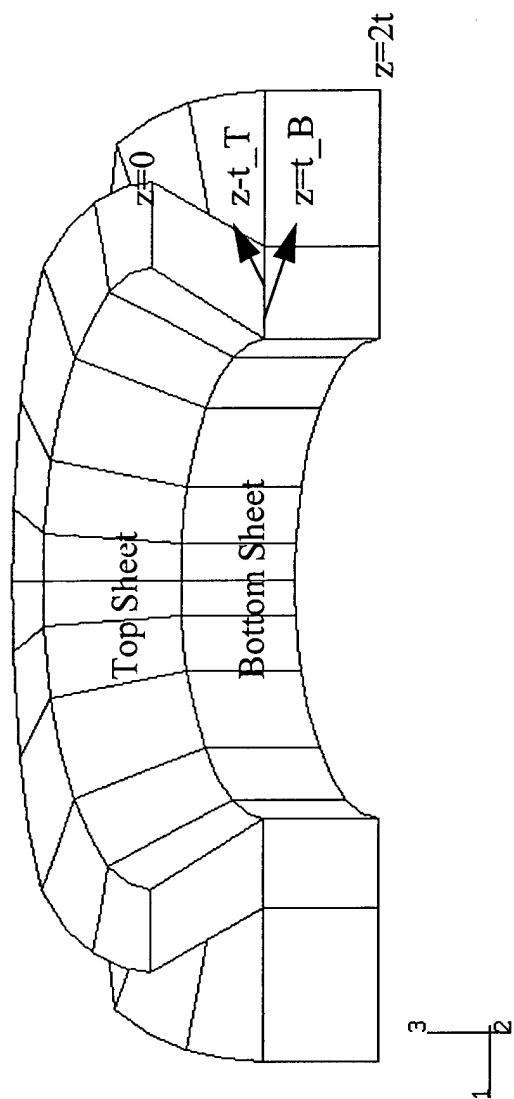


Figure 5.25. Locations of nodes and elements of 3-D models. Two rivet geometries considered are shown and the included Angle due to countersinking in Model I is 60° .

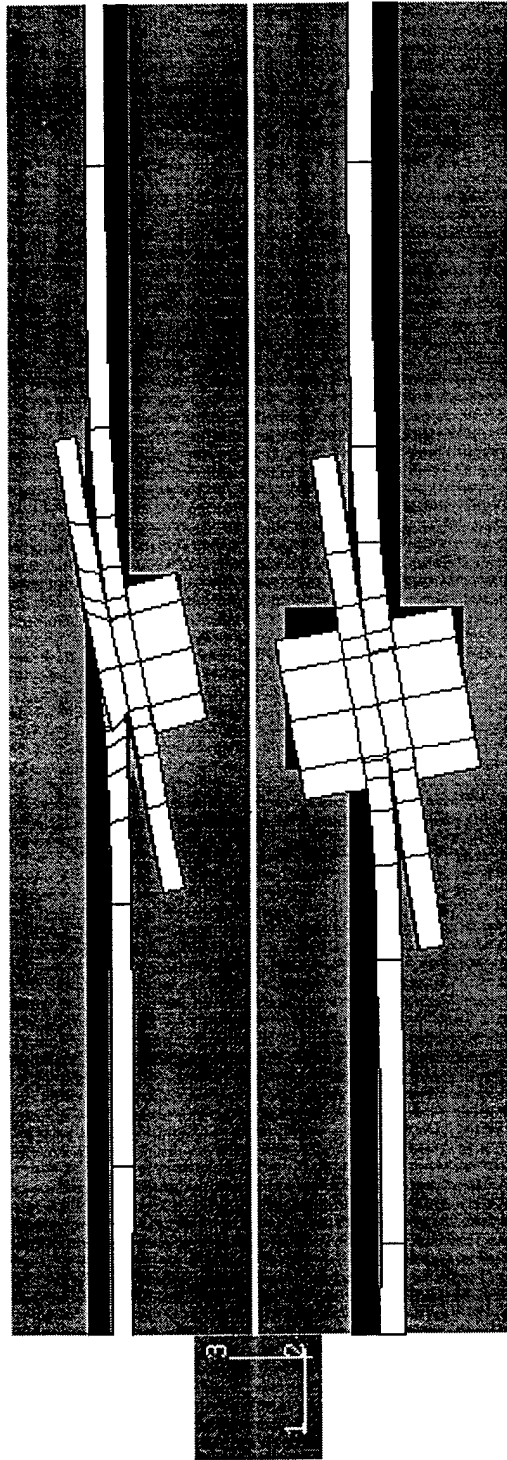
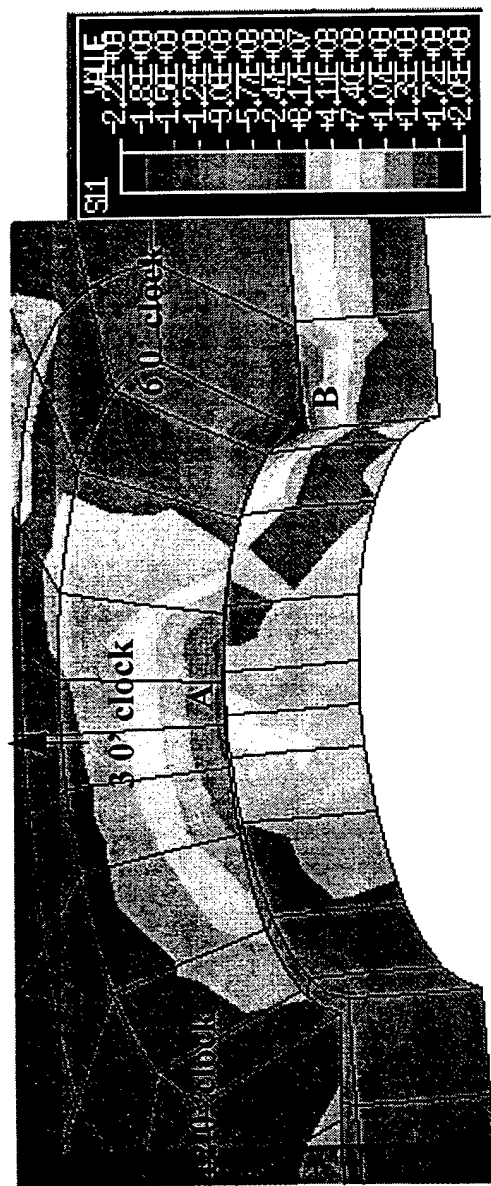


Figure 5.26. The displaced, 3-D finite element meshes for: (a) Model I (b) Model II, at a nominal applied stress of $\sigma_{\max}=125\text{MPa}$ and $R=0.1$. Displacements are magnified 3X.

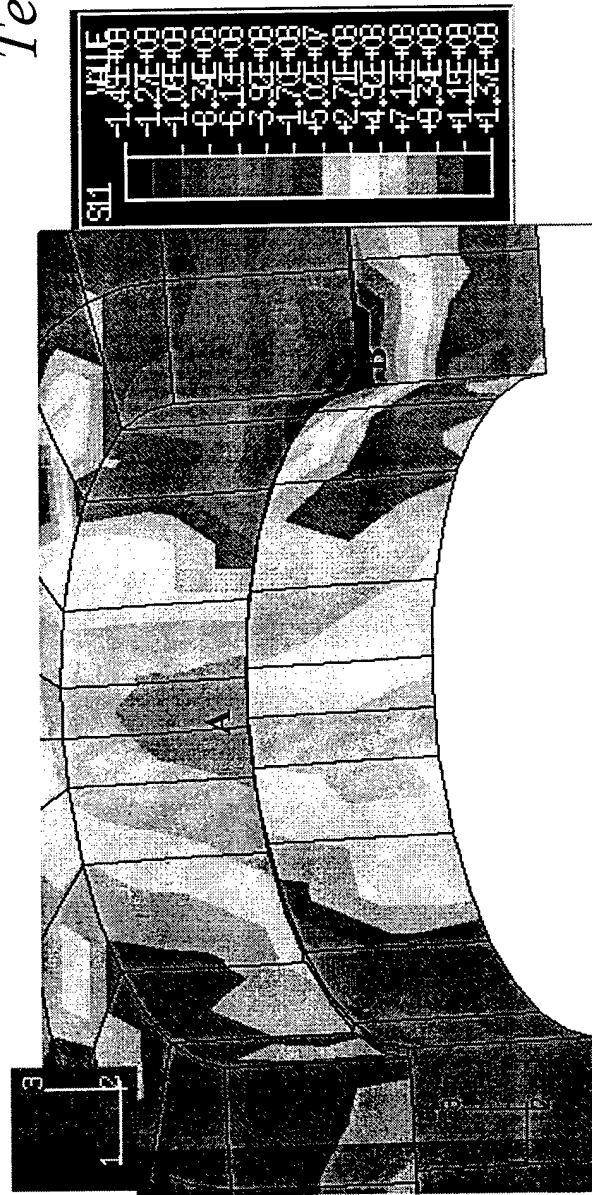


MODEL I

SCF at A = 9.5

SCF at B = 14

Tensile Stress Contours



MODEL II

SCF at A = 6.0

SCF at B = 9.3

Figure 5.27. The distribution of tensile stresses adjacent to the rivet hole is shown for each rivet/hole geometry. The steep stress gradients in the thickness direction apparent in the upper panels at 3 O'clock and are in the lower panels at 6 O'clock are a consequence of panel bending. The fatigue cracks illustrated in Figure 5.9 and 5.29 originate in the upper panel close to A because the location of the peak stress concentration is modified by highly localized and superimposing stresses arising from the lateral fretting. Fatigue cracks may originate in the lower panel close to B. In this case the stress concentration is shifted away from the rivet hole by lateral clamping forces produced by the steel fastener.

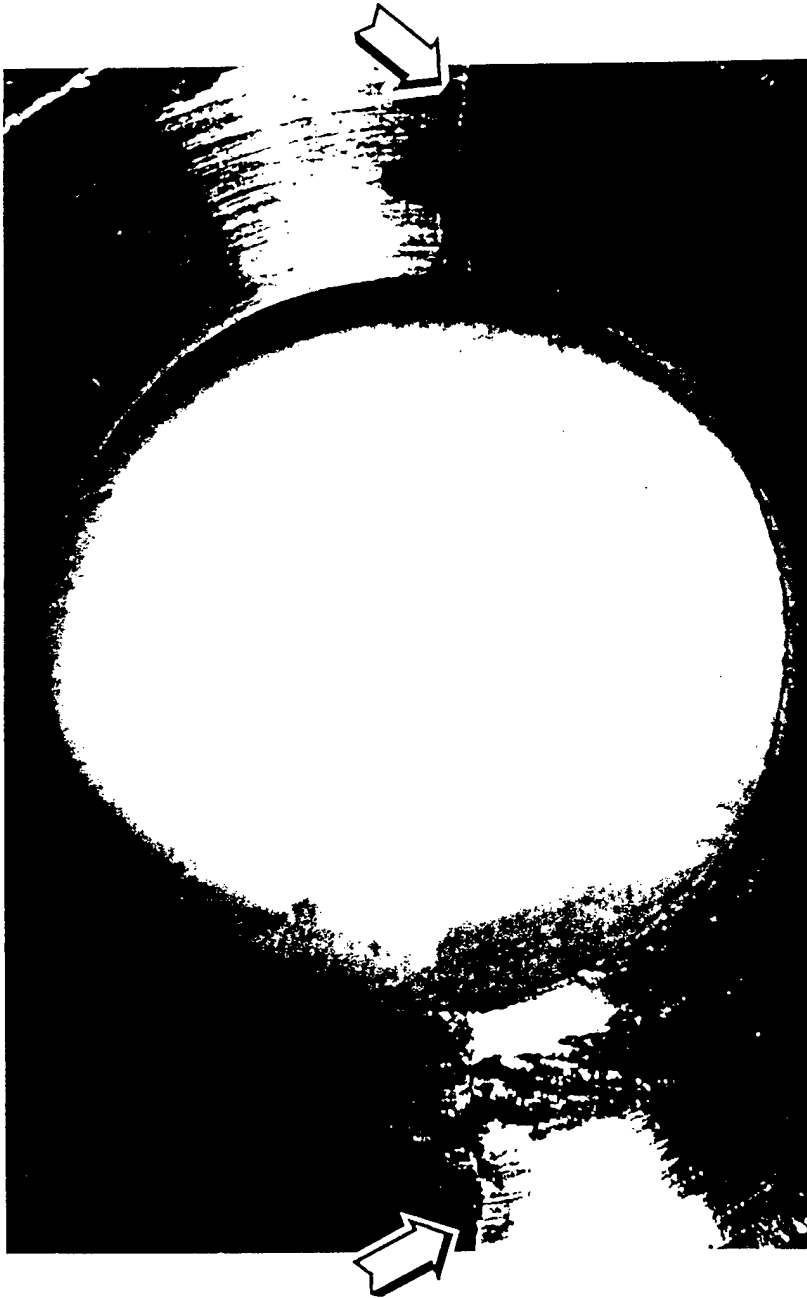


Figure 5.28 Example of fretting damage inside a countersunk hole after 10,000 cycles with a stress range of 23 Mpa and $R=0.1$. The locations of fatigue cracks associated with fretting damage are identified by arrows. Note that the distribution of fretting wear corresponds with the spatial variation of the fretting wear parameter $F1$, Shown in Figure 5.30.

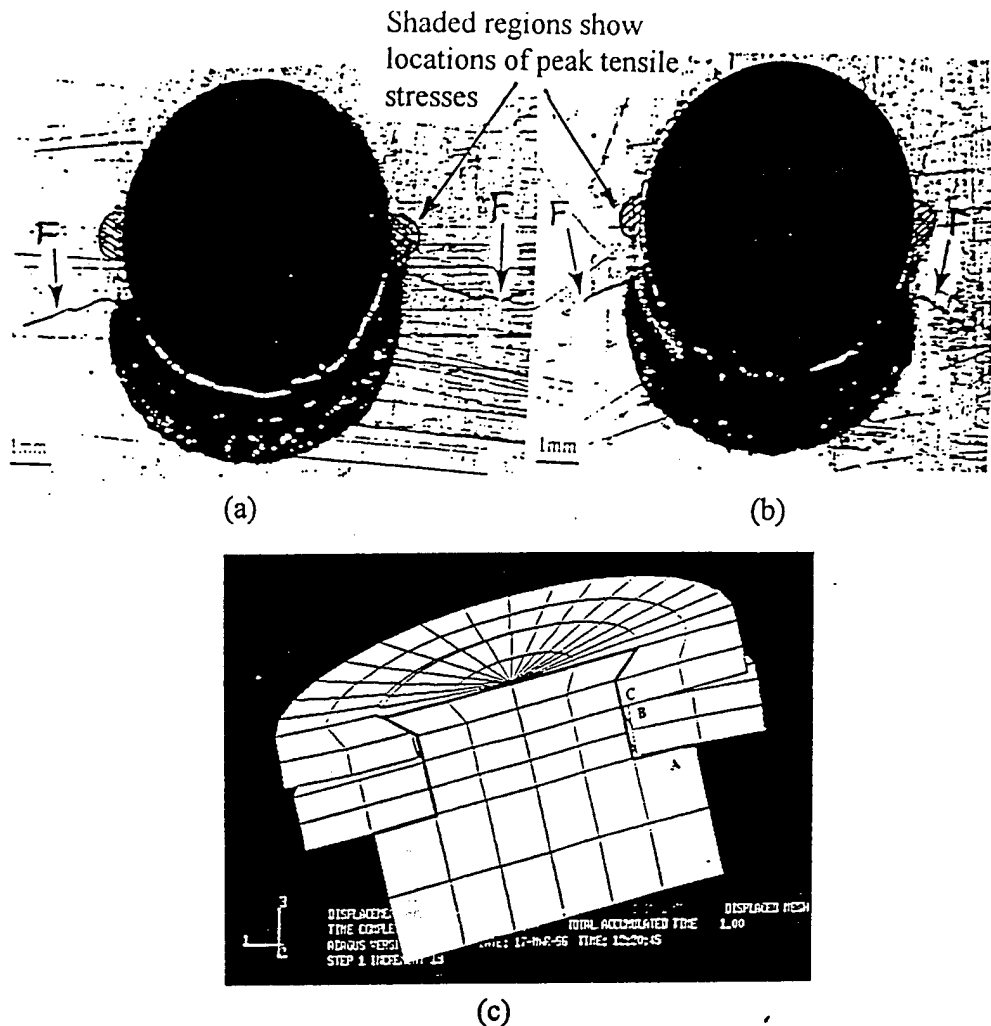


Figure 5.29. Examples of fretting damage and fatigue cracks produced in a 7075-T6, 3-rivet, 1-rivet-row lap joint. The test sample was subjected to 3261 load cycles at a nominal stress range of 106 MPa and $R=0.1$. (a) and (b) are micrographs of adjacent rivet holes viewed on the inner surface of the countersunk panel which show the location of the fatigue cracks and the "crescent" shaped (dark) regions of fretting damage. (c) shows a displaced finite element mesh in the vicinity of the tilted rivet which accounts for the fretting damage. The tilted rivet at (A) presses against the lower panel hole edge (B) against the upper panel (at C) while the two panels slip relative to each other. This produces the "crescent" fretting damage. The fatigue cracks (F) initiate at the conjunction of high bulk stresses and fretting damage rather than at the location of the peak tensile stresses (shaded).

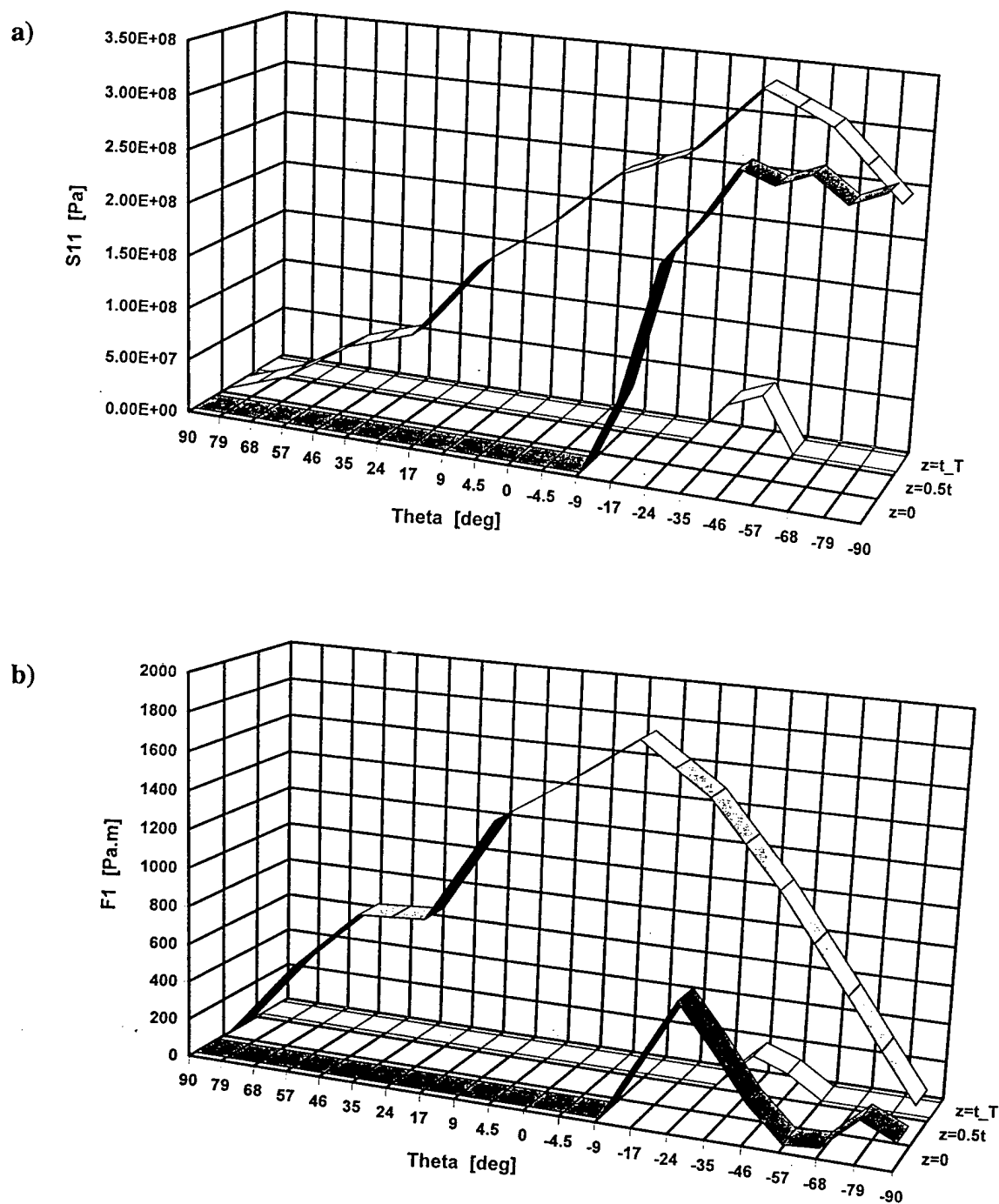
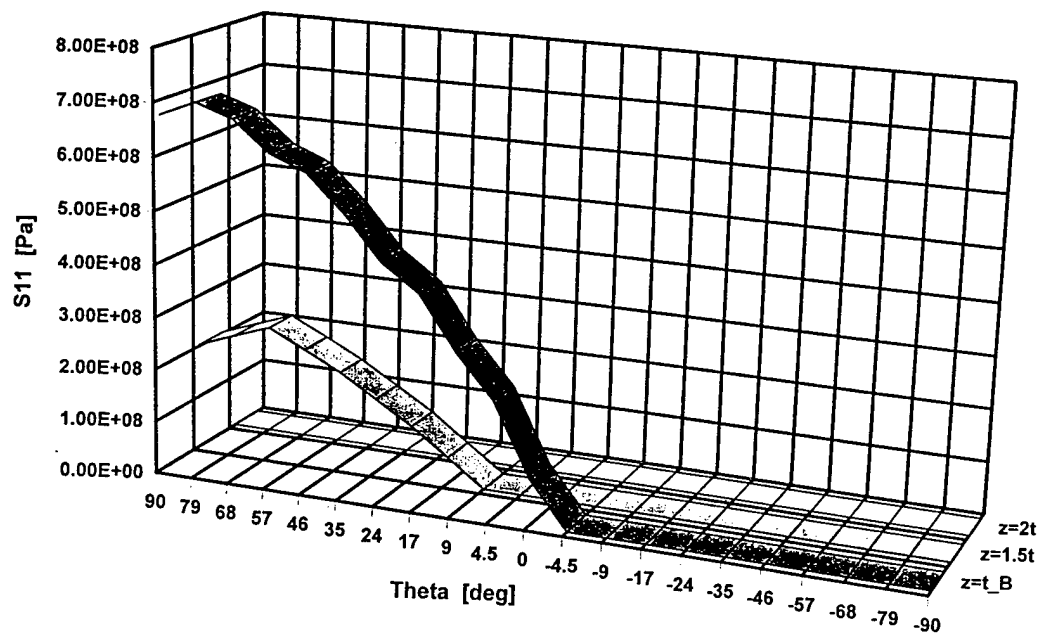


Figure 5.30. Computed, circumferential variation of: (a) contact pressure and (b) the fretting wear parameter $F1$, at the rivet-panel interface of the lower panel with the straight hole (MODEL I). Note that the spatial variation of $F1$ corresponds with the location of fretting damage in Figure 5.28.

a)



b)

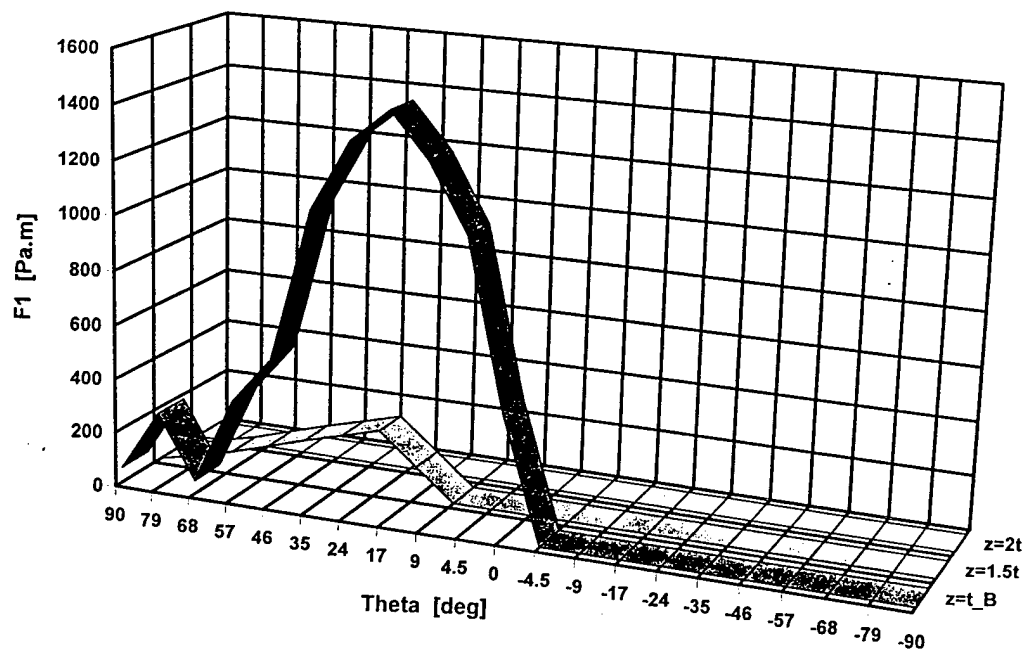


Figure 5.31. Computed, circumferential variation of: (a) contact pressure and (b) the fretting wear parameter $F1$, at the rivet-panel interface of the lower panel with the straight hole (MODEL I).

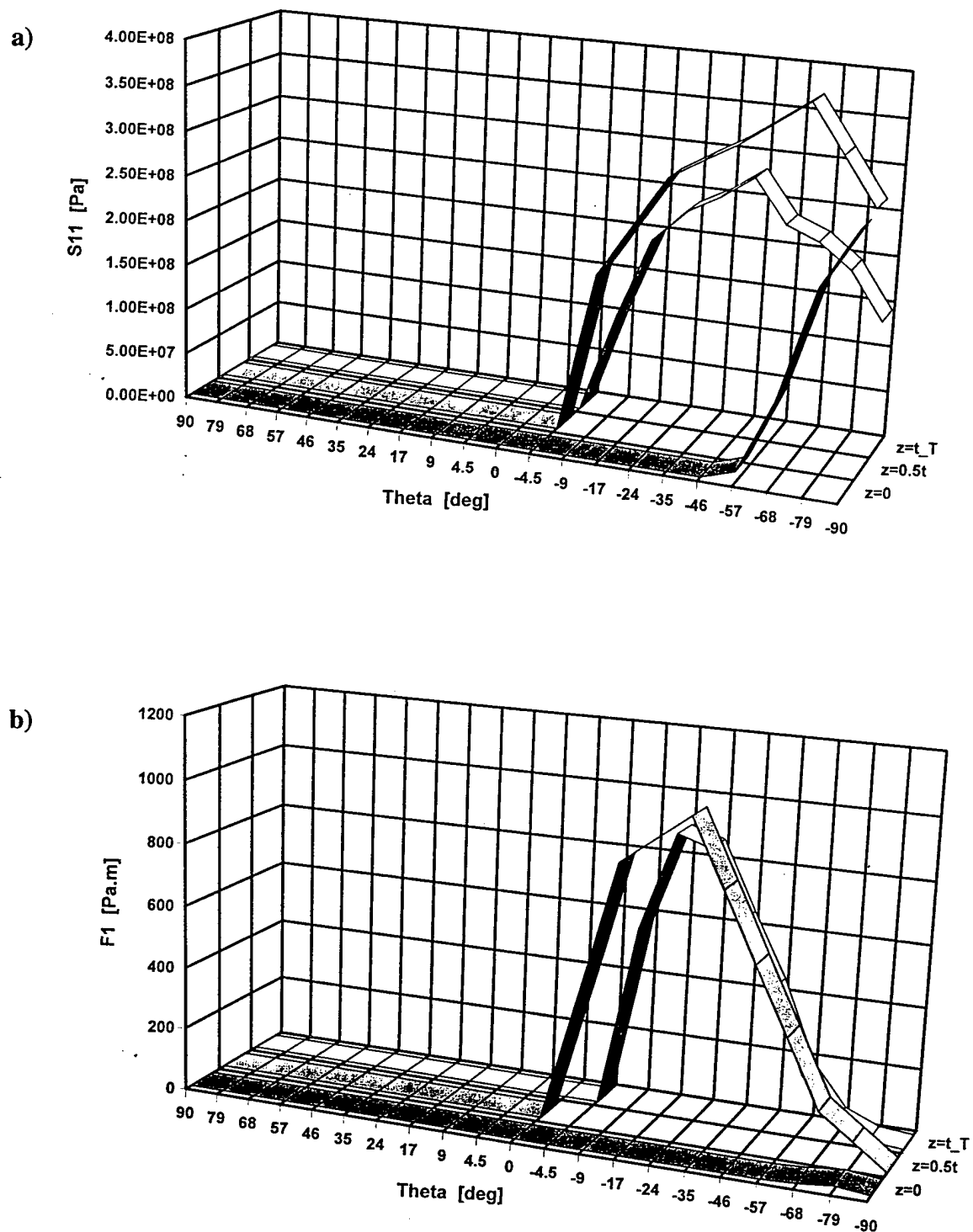
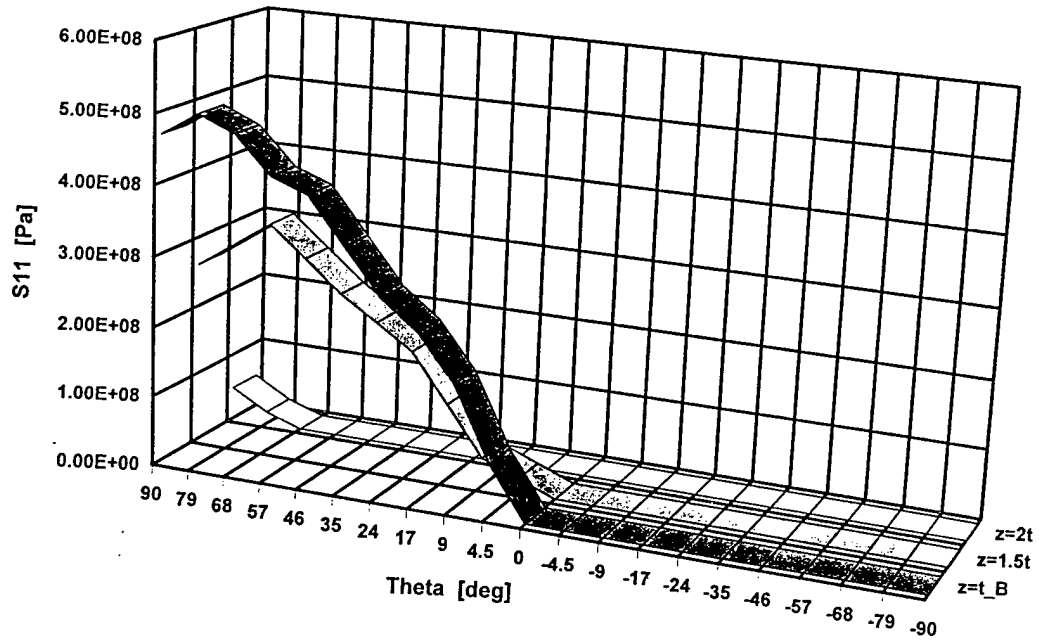


Figure 5.32. Computed, circumferential variation of: (a) contact pressure and (b) the fretting wear parameter F1, at the rivet-panel interface of the lower panel with the straight hole (MODEL II).

a)



b)

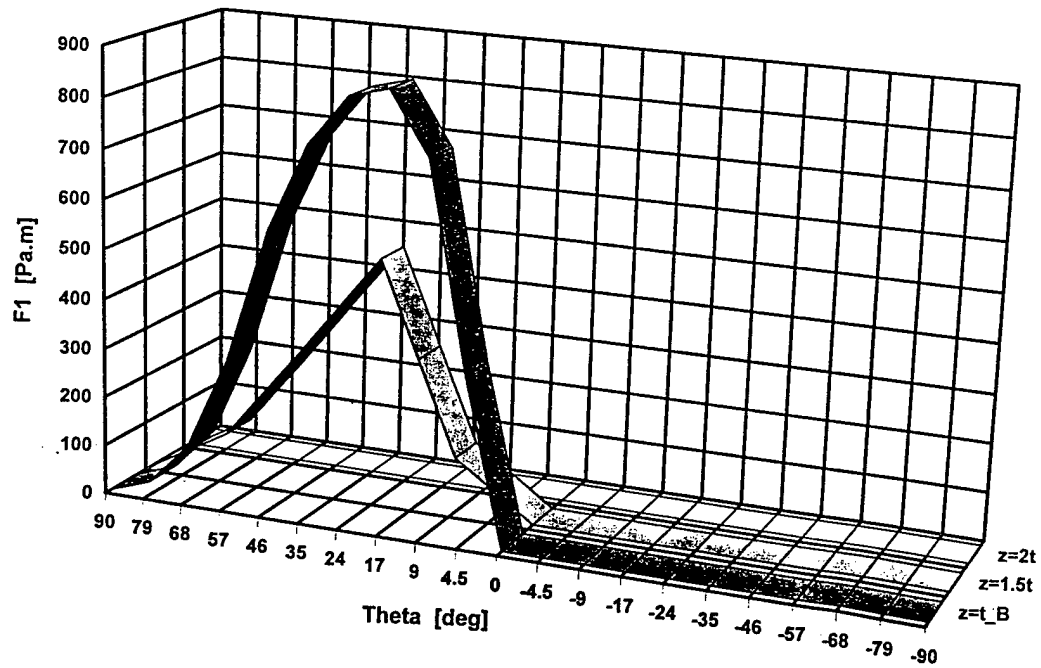


Figure 5.33. Computed, circumferential variation of: (a) contact pressure and (b) the fretting wear parameter F_1 , at the rivet-panel interface of the lower panel (MODEL II).

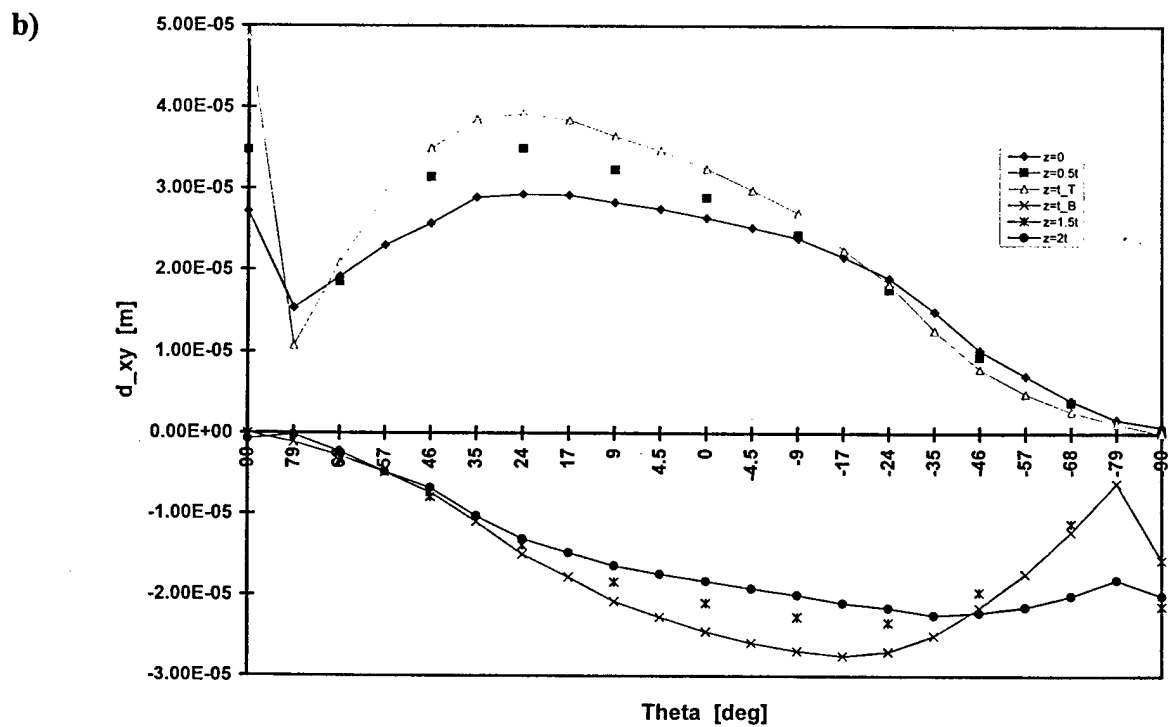
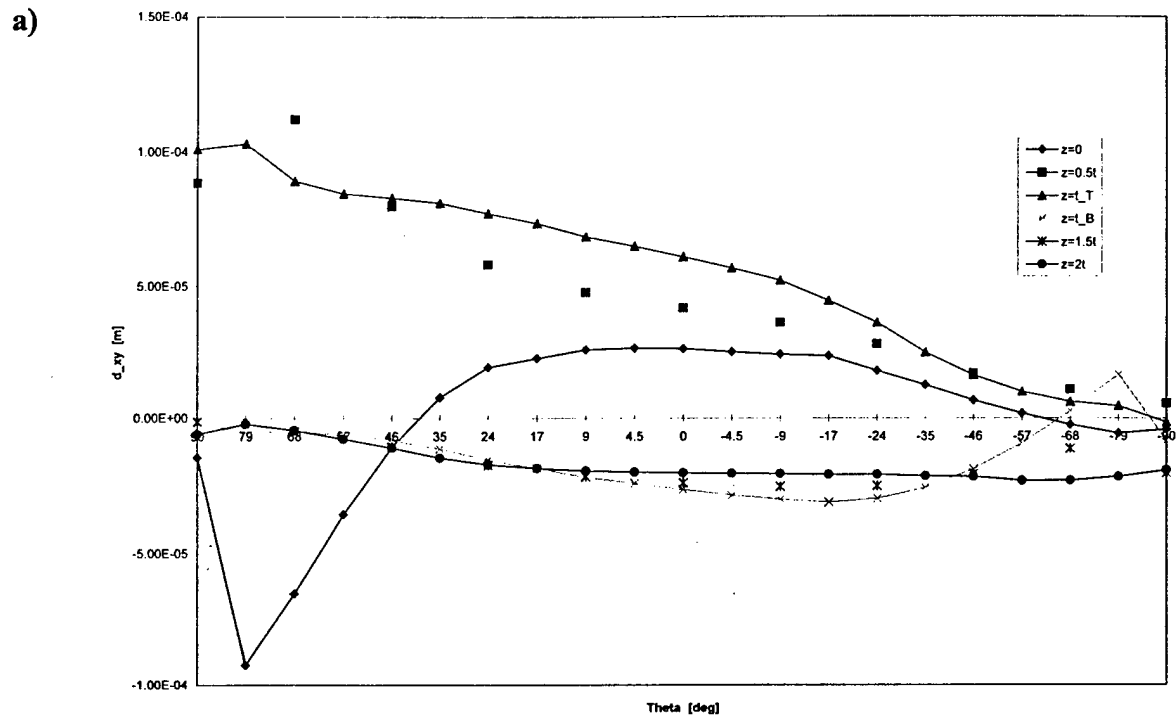


Figure 5.34. Computed, circumferential variation of in-plane slip amplitudes: (a) Model I and (b) Model II.

3-D finite element model (III)

More refined, 3-dimensional models of lap joints were devised and successfully analyzed. The analyses treat a single rivet-row and double rivet-row lap joint of two wide, partially overlapping panels fastened with multiple rivets. Figure 5.35a illustrates the model for a multi-riveted, *double* row joint extending in the positive and negative 2-direction which consists of one-half of the repeatable unit (by virtue of symmetry) and appropriate boundary conditions. Figure 5.35b identifies the convention for defining angular locations and depths in the 3-D models. Rivet and panel shapes and dimensions, and rivet spacings are patterned after those employed in airframes. The repeatable units of the *single* rivet-row models, which are not shown, have only one rivet. The repeat distance between successive units is 30.6 mm. The upper panel may possess a countersunk hole. Finite element analysis (FEA) was performed using the ABAQUS code; 27-noded brick elements were used to mesh the three bodies and single-noded slide surface elements were defined internally to solve the contact inequality constraints.

A nominal uniaxial tensile stress (monotonic or cyclic) is applied at the non-lapping end face of the upper sheet while the corresponding face belonging to the lower sheet is fixed along the 1-axis. Figure 5.35 shows the main features of the models. Symmetry planes are constrained against motion in the 2-direction. In addition, the extreme edges parallel to the 2-axis, at a depth of 1.53 mm and on 2-3 planes are fixed in the 3-direction to prevent unrestrained rotation of the body in space. All the boundary conditions are symmetric. Biaxial loading is simulated by displacing the long panel edge (the edge parallel to the 1-direction) uniformly by an amount corresponding with $\frac{1}{2}$ of the nominal σ_{11} -stress ($\sigma_{22} = 0.5 \sigma_{11}$). Calculations were performed for conventional and countersunk rivet geometries and three values of interfacial friction coefficient, μ . Interference fits are modeled by forcing radial conformity for rivets whose radii are initially greater than the hole radius. Clamping forces are generated by forcing the elongation of a rivet whose shank height is initially shorter than the combined thickness of the 2 panels. The material properties and types of calculations are shown in Table 5.10. M is the plastic modulus (2). In all cases, the panels were ascribed the material properties of 7075-T6 aluminum alloy. The rivet(s) possessed properties of the same aluminum alloy or of steel. All *elastic* calculations involved the application of a *monotonic* nominal tensile stress of 125 MPa. All *elastic-plastic* calculations involved the application of a nominal *cyclic* load defined by $\Delta\sigma = 90$ MPa and $R = 0.1$.

The single rivet-row finite element meshes typically consist of 3171 user defined nodes, 252 user defined elements and 609 internally generated contact elements. A typical figure for the total number of variables is 11,340. Elastic-plastic calculations consumed between 18,000s to 20,000s of CPU time on a SGI Power Challenge Array. The double rivet-row finite element meshes typically consist of 5832 user defined nodes, 472 user defined elements and 1213 internally generated contact elements. A typical figure for the total number of variables is 21,135 and elastic-plastic calculations consumed about 45,000s.

Stress Concentration Factor (SCF)³. Results of the analyses are illustrated in Figure 5.36 and Table 5.11 which summarizes the stress concentration factors (SCFs) and their angular locations. The analyses reveal that out-of-plane distortions are as influential as in-plane deformation. Figure 5.36 illustrates steep stress gradients in the out-of-plane direction; the peak stresses are generated at the depth of the interior panel interfaces as a result of out-of-plane bending. The SCF for a single row of countersunk rivets (SCF = 9.8 and 12.1 for 50% and 100% countersinking) are 60% and 100% higher than the factor for the single row of conventional rivets (SCF = 6.1). This is because the larger and stiffer rivet head reduces local panel bending (see Figure 5.36). The response of the rivet is a combination of shear and rotation. Rivet shear stresses are directly related to the extent of in-plane load transfer and the panel SCF, while the rivet axial stresses are related to rotation and the out-of-plane transfer which *reduce* the SCF. Both friction and the stiffer steel rivet promote rotation and out-of-plane load transfer thereby tending to reduce the panel SCF (compare entries 4 and 9 and also 12 and 13 in Table 5.11). The biaxial loading generated by a pressurized fuselage shifts the angular *locations* of the peak values of the fatigue and fretting drivers by about 10 degrees toward the 270° orientation (see Figure 5.35b) and reduces the SCF by about 15% (compare entries 15 and 16 for uniaxial loading with 17 and 18 for biaxial loading).

Multi Rivet-Rows. The main advantages of the double over the single rivet-row are: (1) the reduction in the load transmitted by each rivet, the resulting 30% to 40% reduction in the SCF, and corresponding ~30% to ~40% increase in load carrying capacity, and (2) the large decrease in the excess assembly compliance which drops from 27-35 m/GN for the single row to 7-10 m/GN for the double row. The full 50% reduction in SCF and corresponding 50% increase in load carrying capacity are not obtained because of subtle changes in the in-plane and out-of-plane load transfer. Load transfer in a *conventional*⁴, 3 rivet-row assembly is much more inefficient. Antisymmetric displacement gradients are generated in the top and bottom panel when a virtual load is transferred to the middle row. These gradients produce rivet displacements that cancel the rivet reaction forces. As a result, the middle rivet-row sheds its load and transfers it to the outer rows. For this reason, the load carrying capacity of a *conventional*, 3 rivet-row lap joint is comparable to that of a 2 rivet-row lap joint.

The Location of Fretting Fatigue Critical Regions. In addition to the stresses and strains, the calculations evaluate 2 quantities that approximate the drivers for fatigue crack initiation. One is the peak cyclic tensile stresses, $\Delta\sigma$, which promotes conventional fatigue. The other is the fretting fatigue parameter, $F_2 = \sigma_{\theta\theta} \mu p \delta$, where $\sigma_{\theta\theta}$ is the (cyclic) circumferential tensile stress, $\mu = 0.4$ is the coefficient of friction, p is the local contact pressure, and δ is the relative movement of the contacting interfaces or slip. The parameter F_2 correlates with the fretting fatigue life (Ruiz et al, 1984, Kuno et al, 1989). The variations of these quantities at the edge of the panel rivet hole with angular orientation and at the rivet shank-panel interface are illustrated in Figure 5.37. The peak

³The stress concentration factor (SCF) is the ratio of the peak tensile stress generated in the panel to the remote nominal stress.

⁴The term "conventional" is used here to denote an assembly in which the top and bottom panel rivet holes are in registry.

values identify the likely angular locations of the crack initiation sites. The relative magnitudes of $\Delta\sigma$ and F_2 determine whether initiation is dominated by ordinary or fretting fatigue processes. The calculations identify 2 general sites for fretting fatigue (see Figure 5.38a):

Location A: Between the rivet shank and the panel hole surface near the 0° - and 180° -orientations. Fretting fatigue arises in these locations from the conjunction of large values of in-plane slip, moderate contact pressure and large values of circumferential (cyclic) tensile stress. An example is shown in Figure 5.38b.

Location B: Between the 2 panels at the $\sim 185^\circ$ and $\sim 345^\circ$ -orientations. Fretting fatigue arises from large values of in-plane slip at the panel-panel interfaces and large values of out-of-plane contact pressure between the crimped edge of the lower panel hole and the upper panel where the tilted rivet head presses against the lower panel. This produces a crescent shaped fretted region centered on the 270° orientation (see Figure 5.38b). The superposition of large values of bulk circumferential (cyclic) tensile stress and superficial fretting stresses at the extreme edges of the crescent-shaped fretted region account for the initiation of fatigue cracks at the $\sim 185^\circ$ - and $\sim 345^\circ$ -orientations as shown in Figure 5.38b). Biaxial loading, which shifts the peak circumferential stresses toward 270° orientation favors the conjunction and is expected to promote fretting fatigue in this location.

Locations C and D at the interfaces are sites for fretting, but they do not spawn fatigue cracks because high levels of compressive stress are generated in the panel adjacent to the interface.

Effects of Interference and, Clamping. The present calculations reveal that the rivet shank interference varies along the rivet axis. The results in Table 5.12 show that interference is maximum at the rivet heads and not optimum at the depth $z = t$ (i.e., at the depth corresponding to the interior panel-panel interface). The variation in interference is a consequence of: (i) the nonlinear dependence of the circumferential stress on the amount of plastic deformation generated by the misfit and (ii) the constraining effect of the stiff rivet head. The dependence arises in spite of the fact that the finite element model rivet shank and panel hole radii are initially uniform along their entire length and depth. As a result, the circumferential residual stresses at the hole edge after installation (and before loading) may be compressive near the panel exterior surfaces are generally not compressive at the depth of the interior panel-panel interface where the cyclic stresses are maximum.

Interference between the countersunk head and shank promote clamping. The effects of interference and clamping on the SCFs are shown in Table 5.11 (see entries 5, 6 and 7, and also 13 and 14); the effects of interference and clamping on $\Delta\sigma$ and F_2 in Figure 3b and 3c. Interference shifts the angular location of the panel SCF, peak cyclic stress range and peak mean stress toward the loading end. Clamping does not alter the angular locations of the peak stress values. Interference and clamping also reduce the assembly compliance, rivet tilt and in-plane slips and the contact pressures under load; both increase out-of-plane slips. Qualitatively similar results are obtained for the 2 rivet-row joint. In spite of the fact that interference is not optimum at the panel-panel interface location, both interference and clamping dramatically reduce the drivers for in-plane fatigue and fretting fatigue (Figures 5.37a-d).

Analyses of Fretting Fatigue Lives. The present analyses, which allow the evaluation of peak values of F_2 , provide a rough measure of the fretting fatigue life. This is based on the findings of Novell and Hills (1990) who demonstrate the following relation between F_2 and the cyclic life, N for an aluminum alloy:

$$N > 10^7 \quad \text{when } F_2 < 4 \cdot 10^9 \text{ Pa}^2\text{m} \quad \text{and} \\ N << 10^7 \quad \text{when } F_2 > 4 \cdot 10^9 \text{ Pa}^2\text{m}.$$

Viewed in this light, the F_2 -values given in Table 13 for a nominal cyclic stress of 90 MPa provide rough estimates of the joint fretting fatigue lives of the various lap joints. These results indicate that only the double rivet-row joint with interference is likely to display a long life. In this case, the nominal cyclic stress must be reduced by more than 50% to compensate for the absence of interference because $F_2 \propto \Delta\sigma^3$. The lives of the single rivet-row joint at this stress will be very short even with interference. Consistent with this prediction, single row lap joint specimens with the same geometry as the finite element model and with interference, failed after as few as $N = 3 \cdot 10^3$ stress cycles at a nominal cyclic stress of 65 MPa.

Stresses Generated in the Rivet. The analyses also describe the stress distributions in the rivet. Distributions obtained for rivets of the 2 rivet-row joint are illustrated in Figure 5.39; peak stresses are summarized in Table 5.14. In-plane rivet shear is predominantly a direct consequence of in-plane load transfer to the rivet and these quantities are proportional to the in-plane compressive stresses generated in the shank at the 270° (upper panel hole) and 90° (lower panel hole) locations (see Figure 5.39a and b). The nonaligned in-plane loads induces a rotational moment which is resisted by the rivet head. The peak axial stress generated at the corner where the head extends from the shank is proportional to the bending moment. The peak tensile stresses generated in the panels are $2\times$ to $3\times$ larger than the peak axial stresses in the rivets.

Limitations of the Analyses. Several significant shortcomings of the finite element models should be noted. The elastic-linear-kinematic-plastic constitutive relations employed offer an approximate description of the steady state hysteresis loop observed after about 20 to 50 strain cycles. Consequently, they do not provide a very satisfying description of the cyclic plastic deformation during the initial stress cycles. The analyses of interference and clamping are also open to question since they are generated artificially in the models rather than by the plastic upsetting of the rivet which can affect the yield condition during the initial load cycles. However similar findings have been reported by Muller (1995), who has observed interference gradients in actual installations. Another difference is that the models simulate metal-to-metal contact while, in practice, joints are assembled with a thin coating of a corrosion inhibiting, polymeric sealant at the rivet-panel and panel-panel interfaces. Preliminary studies by the authors indicate that the pressure dependence of the shear resistance of the coatings can be approximated by a slip amplitude dependent friction coefficient that, on average, is less than the value for dry friction: $\mu = 0.4$. Finally, the authors recognize that the recent treatment of fretting fatigue by Szolwinski and Farris (1996) is sounder and potentially more reliable than the characterization provided by the fretting fatigue parameter, F_2 . However, finer meshes than can presently be accommodated by ABAQUS are needed to apply the analysis directly to a 3-D model of the joint. This problem may be overcome by the rezoning of small regions on either side of an interface where large values of the F_2 -parameter are encountered.

Opportunities for Fatigue Mitigation. The findings touched on here point to 9 strategies for mitigating fretting fatigue damage.

1. **Control of Interference.** Alterations in shank design -- both shape and material properties -- and in the upsetting procedure that enhance the interference at the panel-panel interface depth, $z = t$ (location 2 in Figure 6a) may produce further improvements joint performance.
2. **Promotion of Out-of-Plane Load Transfer.** Increases in the out-of-plane component of load transfer *reduce* the panel SCF and cyclic tensile stresses which promote fatigue and fretting damage. Out-of plane load transfer can be promoted by:
 - (i) Installing rivets with a "pre-tilt" of from $\theta = 5^\circ$ to 10° (see Figure 5.40c)
 - (ii) Increasing the clamping force by more forceful upsetting
 - (iii) Increasing the lateral reaction forces produced by interference in the countersink region by changing the countersink and or geometry
 - (iv) Applying stiffer adhesives or sealants at the panel-panel interfaces
3. **Modification of Rivet-Head Geometry to Reduce Panel Bending.** Changes in the size and shape of the countersunk rivet head that enhance its stiffness (Figure 5.40b) may reduce panel bending under the head and the SCF.
4. **Equilibration of Rivet Loads.** A more uniform load distribution and higher load carrying capacities can be obtained 3 rivet-row lap joints by offsetting the middle row rivet holes to produce disregistry of the holes in the top panel relative to the bottom. This is illustrated in Figure 6d. In this way, load is immediately transmitted to the middle rivet row until the precompression is eliminated. Subsequent load is transmitted to the outer rows.
5. **Equilibration of Panel SCFs.** In principle, the higher SCFs generated in the "top" panel of a single-row lap joint assembled with countersunk rivets ($SCF = 9.8$) can be reduced by increasing the thickness of the top panel. The additional weight may be offset by a corresponding reduction in the thickness of the lower panel. In this way, unequal panel thicknesses may offer improved joint performance.
6. **Control of Panel-Panel Fretting Fatigue.** Out-of-plane bending of the panel hole edge produces serious fretting damage at the panel-panel interface. There is evidence that fatigue cracks are nucleated when the fretted region around the lower half of the hole overlaps the region of high in-plane tensile stresses generated at the hole circumference. Biaxial loading of the connection promotes the conjunction of the 2 regions. The extent of the fretted region is directly related to the compliance of the panel hole edge, specifically, the hole diameter-to-panel thickness ratio. Reductions in this ratio can reduce and even eliminate the danger of fretting fatigue at this location.

7. **Control of Interface Shear Traction.** The surface shear tractions transmitted by polymer sealants and adhesives at the joint interfaces can affect fatigue and fretting. Low Traction can mitigate fretting fatigue in regions where high contact pressure and slip coincide with large tangential cyclic tension. Fatigue and fretting may also be reduced by high Traction at the panel-panel interface which promote out-of-plane load transfer and reduce the SCF.
8. **Optimizing Rivet-Panel Strength Combinations.** The load carrying capacity of the riveted joint is maximized by matching the rivet and panel strength-SCF-ratios. The ability to evaluate the stresses and stress concentrations in *both* the panel and the rivet makes it possible to identify optimum rivet-panel strength combinations for different joint geometries.
9. **Modulation of Crack Growth Trajectories.** The angular locations of the peak values of the fretting fatigue driver, F_2 , corresponds with the likely sites of fatigue cracks and, possibly, their initial growth trajectory. These locations are influenced by the amounts of interference and clamping (see Figure 5.37d). This raises the possibility that the sites and initial trajectories of fatigue cracks can be controlled and modulated (by changing interference and clamping along the rivet row) to reduce the interaction of cracks from neighboring rivets.

Conclusions

1. The out-of-plane distortions of a riveted lap joint are as influential as the in-plane deformation.
2. The stress concentration factor (SCF) for countersunk rivets are from 60% to 100% higher than the factor for conventional, 2-headed rivets because the larger, stiffer head reduces panel bending.
3. Rivet shear stresses are directly related to the extent of in-plane load transfer, while the rivet axial stresses are related to rotation and out-of-plane transfer which reduce the SCF.
4. Two rivet-rows reduce the load transmitted by each rivet resulting in a 30% to 40% increase in load carrying capacity of a lap joint. A third rivet-row does not increase the load carrying capacity significantly beyond that of the two rivet-row lap joint.
5. Two general sites for fretting fatigue are identified.
6. The rivet-shank interference produced by rivets with an initial uniform shank radius varies along the rivet axis and is not optimum at the depth of the interior panel-panel interface where the SCF is highest. Still, both interference and clamping reduce the drivers for in-plane fatigue and fretting fatigue. Locations of maximum damage are identified.

7. The peak tensile stresses generated in the panels are 2× to 3× larger than the peak axial stresses in the rivets.
8. The findings point to 9 possible strategies for mitigating fretting fatigue damage in riveted lap joints.

TABLE 5.10. SUMMARY OF TYPES OF CALCULATIONS ACCORDING TO MATERIAL PROPERTIES

#	Alloy	Calculation	E (GPa)	ν	σ_y or σ_k (MPa)	M	Hardening Approximation
1	7075-T6	Elastic	70	0.25	-	-	-
2	7075-T6	Elastic-plastic	69	0.3	530.75	0.7	Isotropic
3	7075-T6	Elastic-plastic	69	0.3	369.9	0.7	Elastic-linear-kinematic-plastic
4	Steel	Elastic	207	0.25	-	-	-

TABLE 5.11 SUMMARY OF PEAK STRESS CONCENTRATION FACTORS (SCF) AND THEIR ANGULAR LOCATIONS

#	Joint Type	μ	% Interference (I) and Clamping (C)	Tensile SCF	
				value	θ range, °
1	Single rivet-row with non-countersunk aluminum rivets	0.4	0 I, 0 C	5.3	-14.9° to 8.6°
2	Single rivet-row with non-countersunk aluminum rivets	0.4	1 I, 0 C	4.3	4.3° to 8.6°
3	Single rivet-row with non-countersunk aluminum rivets	0.4	1 I, 0.5 C	4.1	4.3° to 8.6°
4	Single rivet-row with countersunk (100°, 1/2 panel depth) steel rivets	0.2	0 I, 0 C	8.8*	-13.5° to 11.2°
5	Single rivet-row with countersunk (100°, 1/2 panel depth) aluminum rivets	0.4	0 I, 0 C	5.8	-11.4° to 5.4°
6	Single rivet-row with countersunk (100°, 1/2 panel depth) aluminum rivets	0.4	1 I, 0 C	5.0	8.7° to 22.5°
7	Single rivet-row with countersunk (100°, 1/2 panel depth) aluminum rivets	0.4	2 I, 0.5 C	4.3	15.6° to 22.5°
8	Single rivet-row with countersunk (61.6°, full panel depth) aluminum rivets	0.2	0 I, 0 C	10.5*	-17.4° to 5.4°
9	Single rivet-row with countersunk (100°, full panel depth) aluminum rivets	0.2	0 I, 0 C	12.1*	-12.7° to 0°
10	Double rivet-row with non-countersunk aluminum rivets	0.2	0 I, 0 C	4.4*	-10.9° to 6.2°
11	Double rivet-row with countersunk (100°, 1/2 panel depth) aluminum rivets	0.2	0 I, 0 C	6.1*	-15.6° to 9.8°
12	Double rivet-row with countersunk (100°, 1/2 panel depth) steel rivets	0.2	0 I, 0 C	5.9*	-13.2° to 10.7°
13	Double rivet-row with countersunk (100°, 1/2 panel depth) aluminum rivets	0.4	0 I, 0 C	5.6	-15.6° to -4.3°
14	Double rivet-row with countersunk (100°, 1/2 panel depth) aluminum rivets	0.4	1 I, 0 C	5.0	4.3° to 15.6°
15	Single rivet-row with non-countersunk aluminum rivets	0.2	0 I, 0 C	6.1*	-14.9° to 8.6°
16	Single rivet-row with countersunk (100°, 1/2 panel depth) aluminum rivets	0.2	0 I, 0 C	9.8*	-11.4° to 5.4°
Biaxial Loading					
17	Single rivet-row with non-countersunk aluminum rivets	0.2	0 I, 0 C	5.3*	-22.6° to -8.7°
18	Single rivet-row with countersunk (100°, 1/2 panel depth) aluminum rivets	0.2	0 I, 0 C	8.1*	-24.4° to 4.5°

* value obtained from an elastic calculation. The remaining values are obtained from elastic-plastic calculations

TABLE 5.12 THE VARIATION WITH DEPTH, z , OF THE PEAK VALUES OF THE CIRCUMFERENTIAL TENSILE STRESS, $\sigma_{\theta\theta}$, AND THE IN-PLANE SLIP, δ_{12} , GENERATED IN THE TOP PANEL BY COUNTERSUNK RIVETS INSTALLED WITH DIFFERENT AMOUNTS OF INTERFERENCE AND CLAMPING*.

Model		Installation $\sigma_{\theta\theta}$ (MPa)	Peak $\sigma_{\theta\theta}$ (MPa)	Peak δ_{12} (μm)
B0	$z=0$	0	199.3	51.5
	$z=0.5t$	0	726.1	47.0
	$z=t$	0	933.0	55.6
B1	$z=0$	159	198.7	4.3
	$z=0.5t$	102	336.9	7.6
	$z=t$	269	544.2	10.6
B2	$z=0$	281	303.4	2.1
	$z=0.5t$	-198	-65.7	2.3
	$z=t$	132	297.2	4.2
B3	$z=0$	1	202.8	39.1
	$z=0.5t$	-1	651.2	37.6
	$z=t$	29	848.8	45.2
B4	$z=0$	265	282.0	2.1
	$z=0.5t$	-200	-72.6	2.1
	$z=t$	179	346.8	4.2

* Results are for the "top" panel of a single rivet-row lap joint fastened by a rivet countersunk (100°) to half panel thickness with a standard head at the bottom panel.

B0 - 0% interference and 0% clamping
 B1 - 1% interference and 0% clamping
 B2 - 2% interference and 0% clamping
 B3 - 0% interference and 0.5% clamping
 B4 - 2% interference and 0.5% clamping

TABLE 5.13 PEAK F_2 -VALUES CALCULATED FOR DIFFERENT CONNECTIONS

Fretting Fatigue Driver	0% Interference		1% Interference	
	Single Rivet-Row	Double Rivet-Row	Single Rivet-Row	Double Rivet-Row
Peak F_2 , 10^{10} Pa ² .m	297.4	75.1	30.0	0.12

TABLE 5.14 PEAK STRESSES GENERATED IN THE RIVETS OF A TWO RIVET-ROW LAP JOINT UNDER A NOMINAL STRESS OF 125 MPa.

Model	Peak Shank-Hole Compressive Stress (σ_{11}), MPa		Peak Shear Stress (σ_{13}), MPa		Peak Axial Tensile Stress (σ_{33}), MPa		Peak Axial Compressive Stress (σ_{33}), MPa	
	rivet # 1	rivet # 2	rivet # 1	rivet # 2	rivet # 1	rivet # 2	rivet # 1	rivet # 2
A1	-240	-240	126	126	174	174	-95	-95
B1	-353	-321	175	143	160	224	-115	-164
B2	-338	-335	168	133	200	266	-116	-157

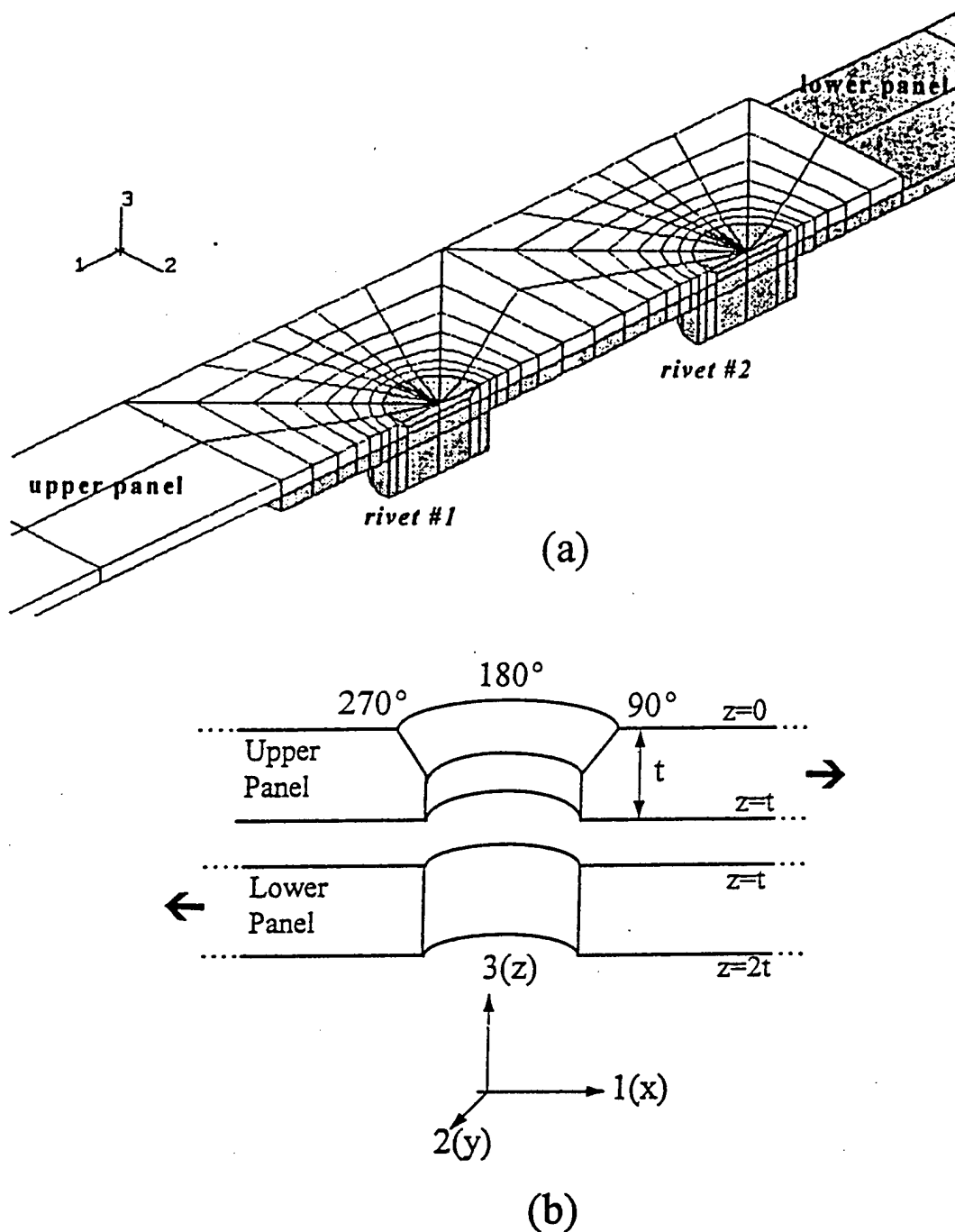
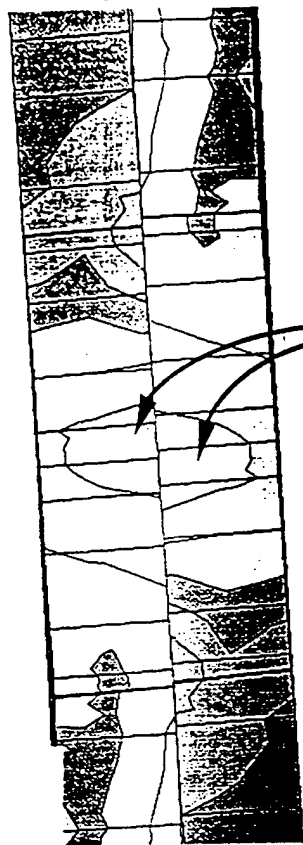
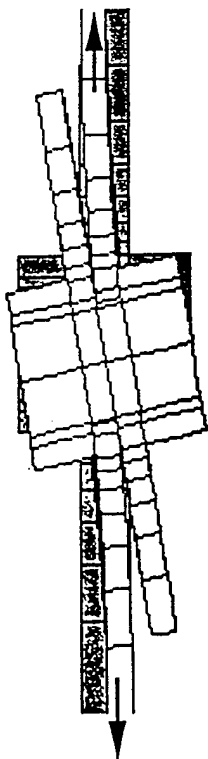


Figure 5.35. Description of model: (a) Wide multi-riveted, two rivet-row lap joint represented by 3-D, finite element model of one-half of the repeatable unit with symmetry and appropriate boundary conditions. The thickness of each panel is 1.53 mm, the non-countersunk rivet shank diameter is 6.12 mm and the countersunk rivet diameter 7.94 mm; the rivet head diameter is 9.792 mm, and its height 3.83 mm, the overall length of the assembly is 336.6 mm, the length of the overlap is 61.2 mm, and the half-repeat width is 15.3 mm. (b) Definition of axes, loading directions, depth and angular location in the 3-D models.

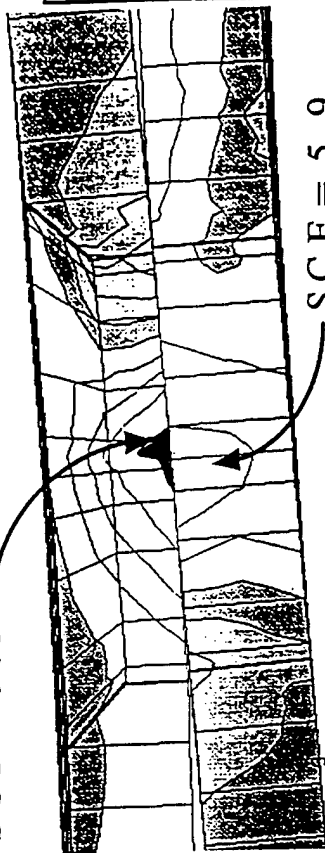


SCF = 6.1

(a)

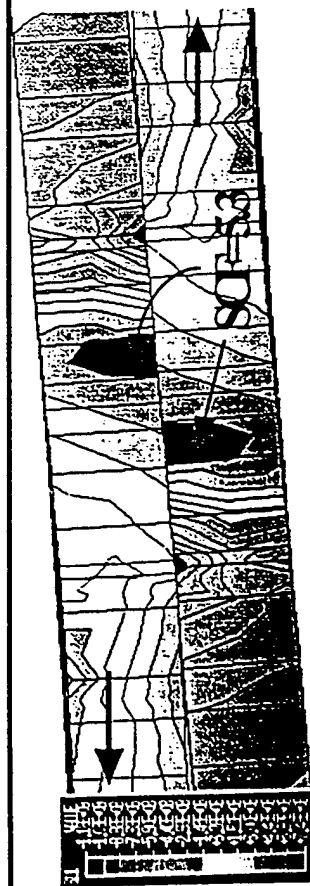
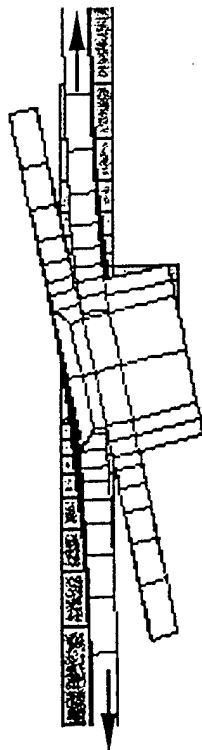


SCF = 9.8



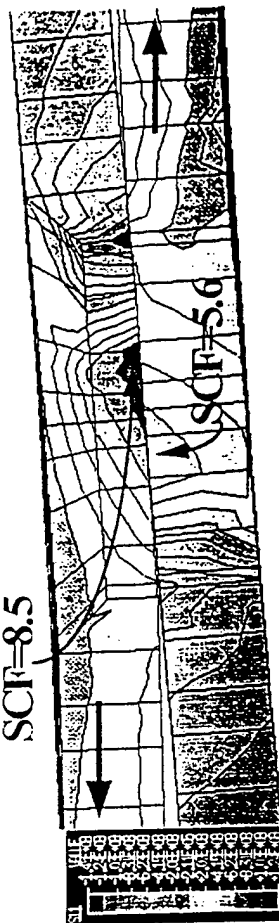
SCF = 5.9

(b)



(c)

SCF = 8.5



SCF = 5.6

Figure 5.36 Results of finite element calculations of the distortion and local panel stresses of riveted lap joints: (a) Single Rivet-row with conventional rivets under a uniaxial load, (b) Single rivet-row with countersunk rivets under a uniaxial load, c) Single rivet row cases under biaxial loading conditions. Displacements are magnified 3x. The contour plots describe the σ_{11} -stress field and identify the (peak) stress concentration factor (SCF) and its physical location.

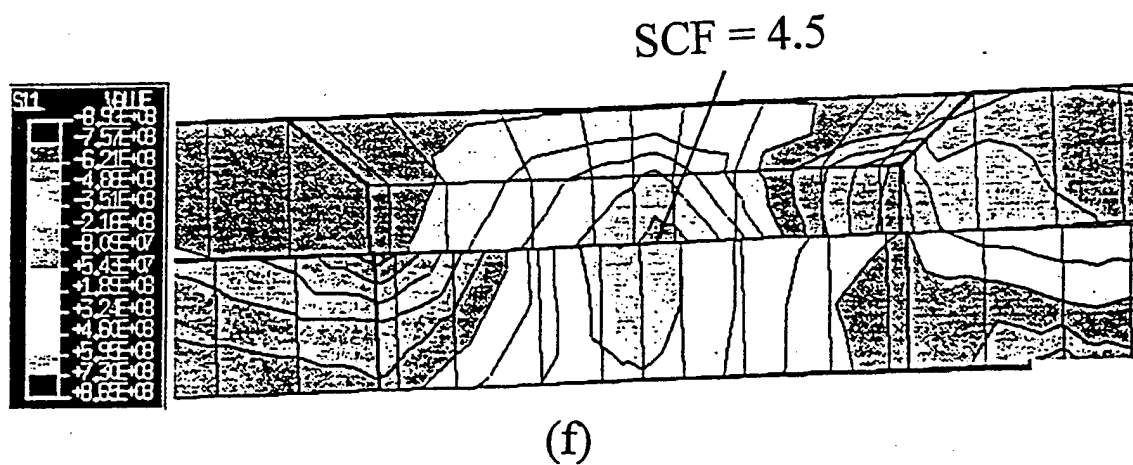
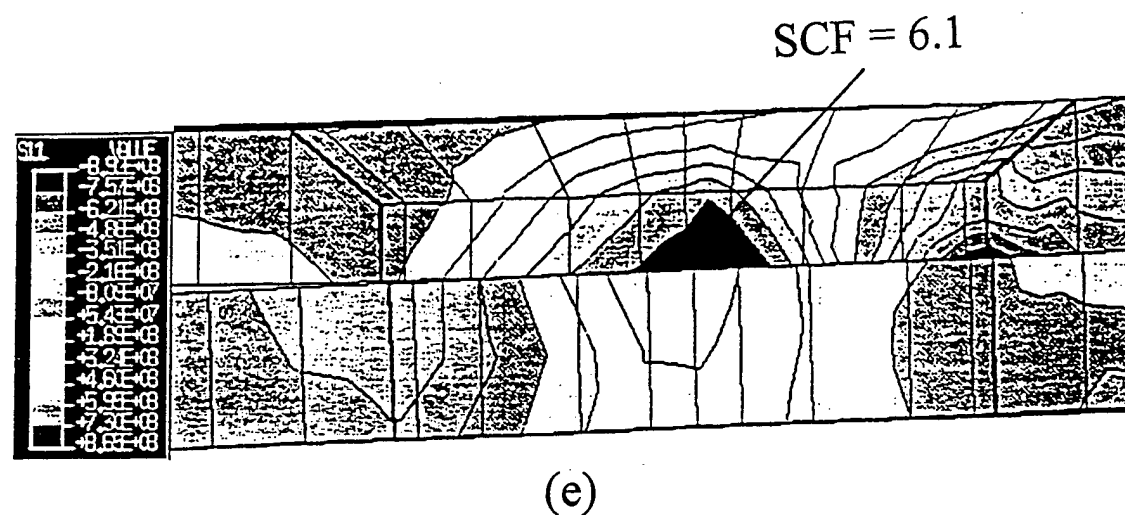
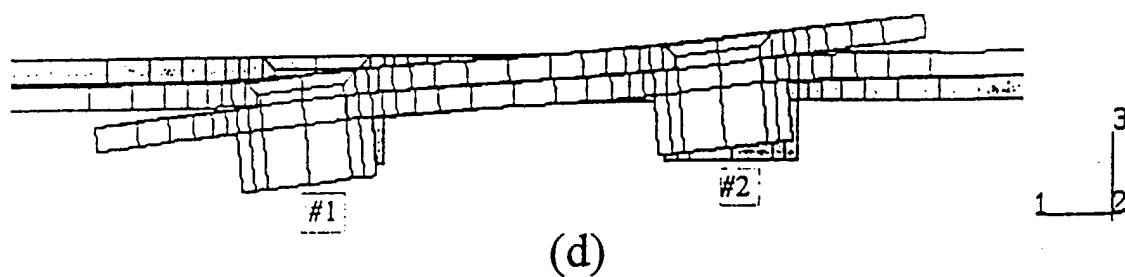


Figure 5.36 (Cont'd) (d) Two-rivet row with countersunk rivets #1 and #2, (e) Tensile stress field adjacent to rivet hole #1, (f) Tensile stress field adjacent to hole #2. Note: the results in (a) – (f) are for assemblies without interference and clamping.

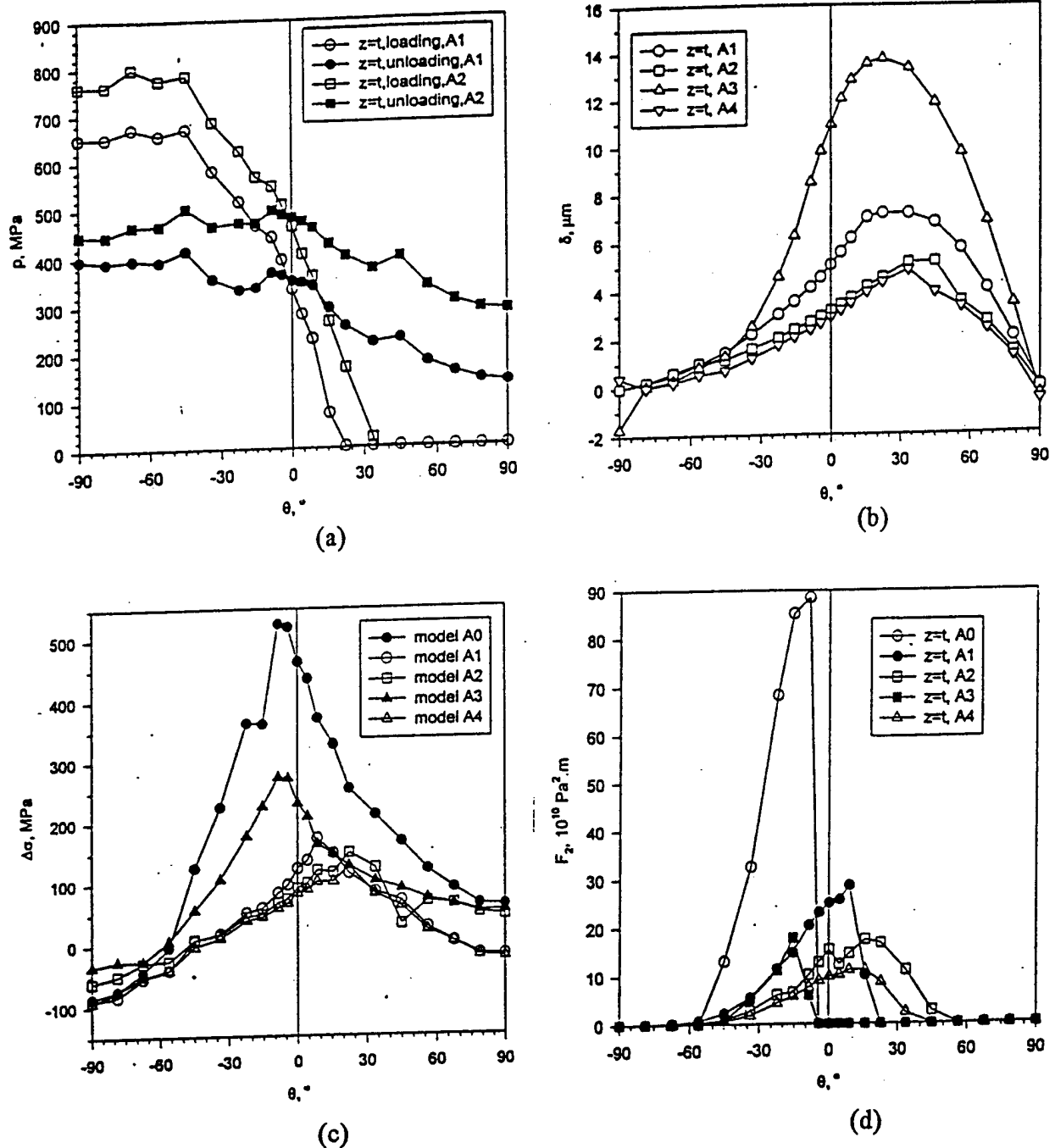


Figure 5.37 Effects of interference and clamping on the conditions at the rivet shank-panel interface of a single rivet-row lap joint with non-countersunk rivet heads. The graphs describe the angular-location dependence at the depth of the interior panel interface ($z = t$) of: (a) the contact pressure, (b) slip, (c) circumferential stress range, and (d) the fretting fatigue parameter F for the following combinations of present interference (I) and clamping (C): A0 – 0% I, 0% C, A1 – 1% I, 0% C, A2 – 2% I, 0% C, A3 – 0% I, 0.5% C, A4 – 1% I, 0.5% C.

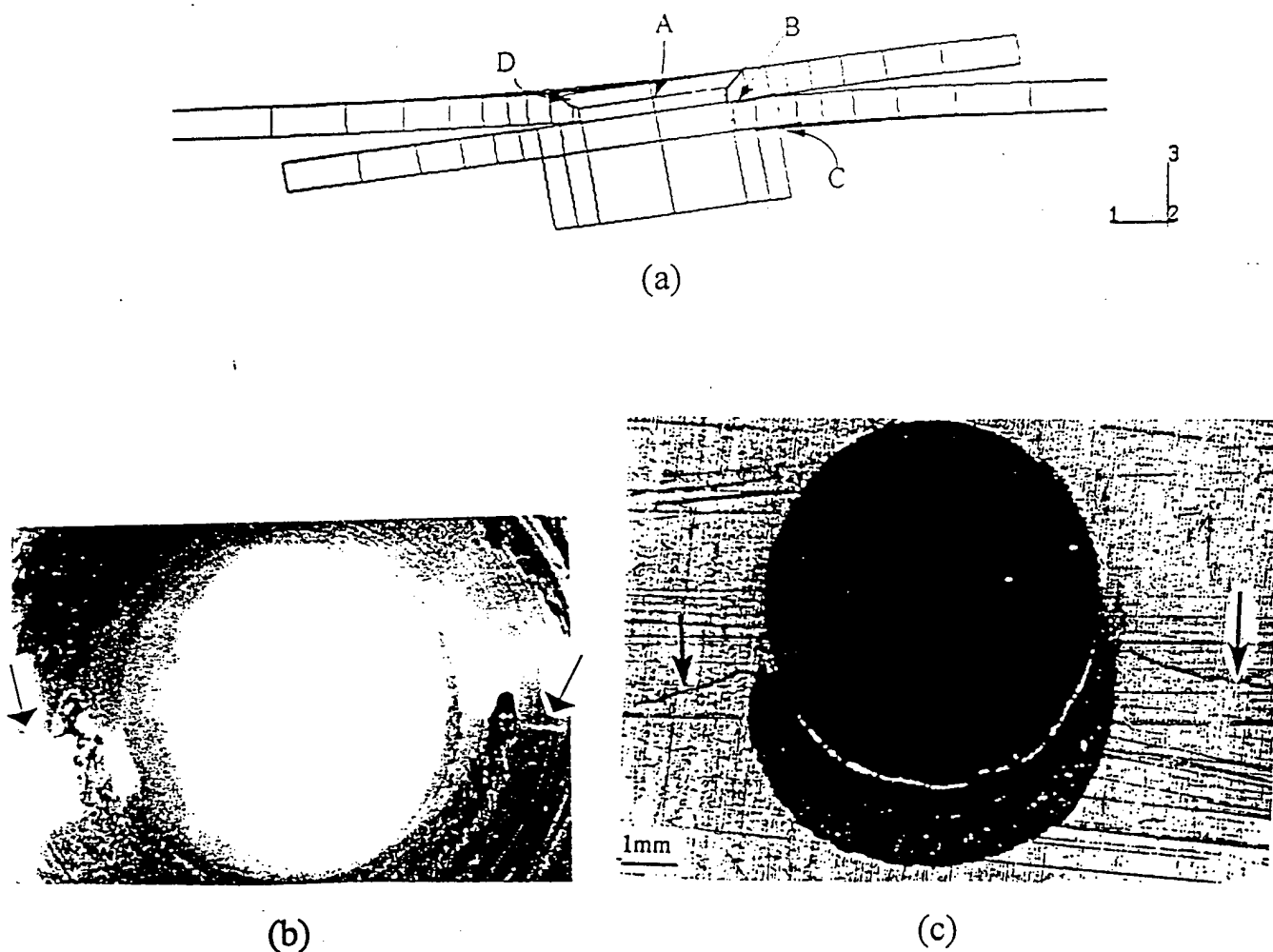


Figure 5.38 Location of fretting and fretting fatigue at the rivet shank-panel and panel-panel interfaces of a single rivet-row lap joint: (a) 4 locations A, B, C, and D. (b) Example of fretting-fatigue of the panel in location A where fretting is in conjunction with high cyclic tensile stress. (c) Example of fretting – the dark crescent region – and fretting fatigue cracks in the panel in location B at edge of crescent where fretting is in conjunction with high cyclic tensile stresses attending. Fretting does not spawn cracks in location C and D because of the attending compressive stresses.

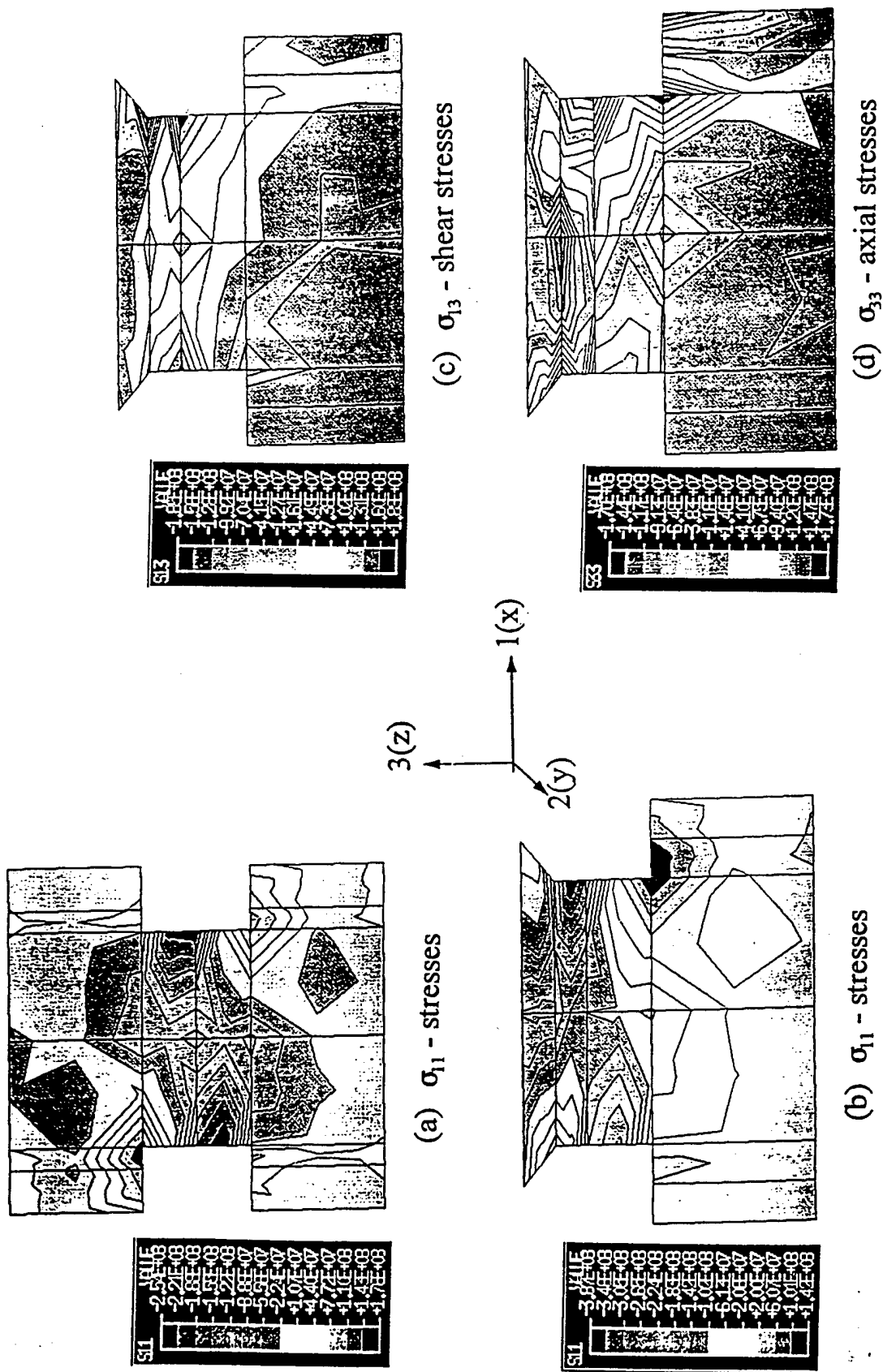


Figure 5.39. Stresses generated in rivet #1 of a two rivet-row lap joint: (a) the σ_{11} - stresses generated in a rivet with conventional heads, (b) the σ_{11} - stresses in a rivet with a countersunk head, (c) the σ_{13} - shear stresses generated in a rivet with a countersunk head and (d) the σ_{33} - axial stresses generated in a rivet with a countersunk head

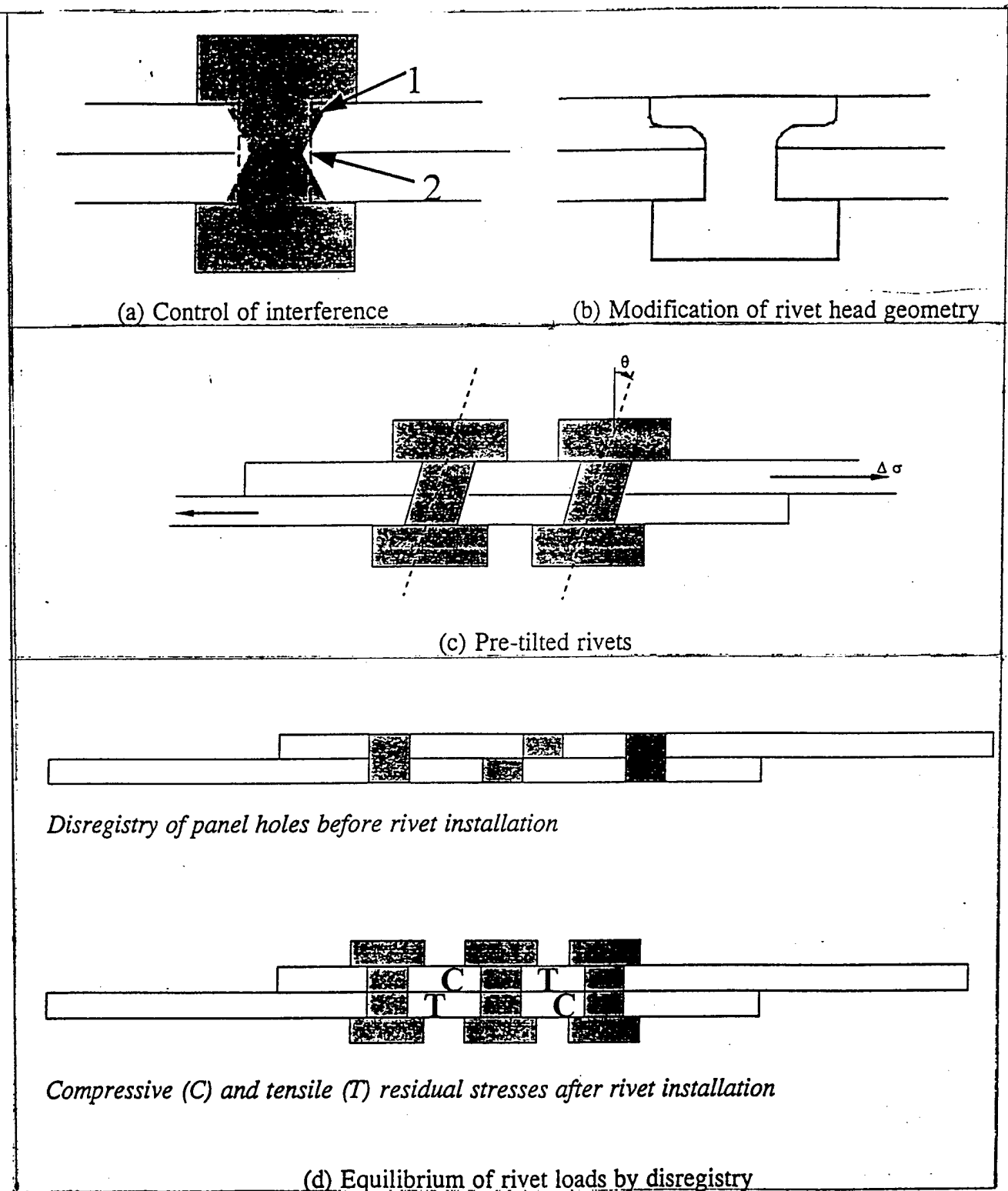


Figure 5.40 Schematic representation of fatigue mitigation strategies: (a) control of interference, (b) modification of rivet head geometry, (c) promotion of out-of-plane load transfer, (d) equilibration of rivet loads by disregistry.

3. Personnel Supported:

George T. Hahn, Professor, Mechanical and Materials Engineering
Carol A. Rubin, Professor, Mechanical Engineering
Pedro C. Bastias, Research Assistant Professor, Mechanical and Materials Engineering
K. Iyer, R. Kasinadhuni, and R. Turvaville, Graduate Research Assistants

4. Publications and Related Items:

Journal Articles

"Analysis of Fretting in Pinned Connections, " K. Iyer, G.T. Hahn, P.C. Bastias, and C.A. Rubin, Wear: 181-183: 524-530 (1995).

"Three-Dimensional Analyses of Single Rivet-Row Lap Joints; Part I: Elastic Response," K. Iyer, P.C. Bastias, C.A. Rubin, and G.T. Hahn, ASME J. App. Mechanics, 1997.

"Three-Dimensional Analyses of Single Rivet-Row Lap Joints; Part II: Elastic-Plastic Response," K. Iyer, P.C. Bastias, C.A. Rubin, and G.T. Hahn, ASME J. App. Mechanics, 1997.

"Three-Dimensional Analyses of Double Rivet-Row Lap Joints; Part I: Non-Countersunk Rivets," K. Iyer, P.C. Bastias, C.A. Rubin, and G.T. Hahn, J. of the AIAA, 1997.

"Three-Dimensional Analyses of Double Rivet-Row Lap Joints; Part II: Countersunk Rivets," K. Iyer, P.C. Bastias, C.A. Rubin, and G.T. Hahn, J. of the AIAA, 1997.

"Implications of Interference on the Residual Stresses in Single Row Lap Joints," K. Iyer, P.C. Bastias, C.A. Rubin, and G.T. Hahn, ASME J. App. Mechanics, 1997.

Conference Proceedings

"Contribution of Fretting to the Fatigue and Corrosive Deterioration of a Riveted Lap Joint," K. Iyer, M. Xue, R. Kasinadhuni, P.C. Bastias, C.A. Rubin, J.J. Wert, and G.T. Hahn, " Structural Integrity in Aging Aircraft, C.I. Chang and C.T. Sun, Eds., AD-Vol. 47, ASME, New York, pp. 35-62, 1995.

"Analyses of the Local Stress and Distortions of a 3-Dimensional, Cyclically Loaded, Riveted Lap Joint," K. Iyer, P.C. Bastias, C.A. Rubin, and G.T. Hahn, USAF Structural Integrity Conference, San Antonio, November 1995.

"Analyses of Fretting and Fretting Corrosion in Airframe Riveted Connections," K. Iyer, M. Xue, P.C. Bastias, C.A. Rubin, and G.T. Hahn, 1996 AGARD Specialists' Meeting on "Tribology for Aerospace Systems", Sesimbra, Portugal, May 1996.

"Local Stresses, Distortions, Interface Slip and the Potential for Fatigue and Fretting in Three Dimensional, 1-Rivet-Row and 2-Rivet-Row Lap Joints," K. Iyer, M. Xue, P.C. Bastias, C.A. Rubin, and G.T. Hahn, ICAF '97 Conference, Edinburgh, June 1997.

"Analysis of Fatigue and Fretting of Three-Dimensional, Single and Double Rivet-Row Lap Joints," K. Iyer, P.C. Bastias, C.A. Rubin, and G.T. Hahn, Proc. ICAF '97 Symposium on Fatigue in New and Aging Aircraft, June 16-20, 1997, Edinburgh, Scotland.

"Three Dimensional Analyses of Fatigue and Fretting Conditions in Aluminum Alloy Riveted Lap Joints," G.T. Hahn, K. Iyer, C.A. Rubin, and P.C. Bastias, Proc. First Joint DoD/FAA/NASA Conference on Aging Aircraft, July 1997, Ogden, Utah.

Theses/Dissertations

"Fretting Contribution to Crack Nucleation and Growth in 7075-T6 Al Sheet Riveted Connections," R. Kasinadhuni, M.S. Thesis, Vanderbilt University, December 1995.

"Three Dimensional Finite Element Analyses of the Local Mechanical Behavior of Riveted Lap Joints," K. Iyer, Ph.D Dissertation, Vanderbilt University, May 1997.

5. Interactions/Transitions:

a. Participation/presentations at meetings, conferences, seminars, etc.

The set of 39 riveted samples with hidden cracks will be available to John Wikswo at Vanderbilt, Jan Achenbach at Northwestern, and ultimately other groups interested in validating NDE procedures.

K. Iyer, P. C. Bastias, C. A. Rubin and G. T. Hahn, "Analyses of the Local Stresses and Distortions of a 3-Dimensional, Cyclically Loaded, Riveted, Lap Joint". Submitted for presentation at the 1995 USAF Structural Integrity Program Conference.

K. Iyer, M. Xue, R. Kasindhuni, P. C. Bastias, C. A. Rubin, J. J. Wert and G. T. Hahn, "Contribution of Fretting to the Fatigue and Corrosive Deterioration of a Riveted Lap Joint". To be presented at the Air Force 3rd Aging Aircraft Conference, WPAFB, 1995.

We have prepared a set of 39 riveted lap joints with different, documented amounts of fatigue damage (mainly small, under the rivet head cracks) which are being used to evaluate the sensitivity of advanced NDE techniques being developed by Professors John Wikswo and Jan Achenbach at Vanderbilt University and Northwestern University, respectively.

We are exploring a collaboration with Professor T.N. Farris, whose group is developing a detailed treatment of fretting fatigue crack nucleation. We intend to provide Professor Farris with the results of stress and fretting calculations for critical regions of the riveted lap joint with which he will predict fatigue life. His predictions will be compared with our experiments.

We are exploring a collaboration with Captain Scott Fawaz (USAF) whose Ph.D. dissertation at Delft University in the Netherlands is examining the fatigue life of riveted, aluminum lap joints. Captain Fawaz has concluded that 3-D, out-of-plane bending is an important feature of the failure process. We want to finite element model the test pieces Captain Fawaz is using and compare the calculations with his experiments.

We have obtained samples of advanced chromated and non-chromated sealants from Bill Keller of Courtaulds Aerospace, Sealants and Coatings Division, and are examining ways of evaluating the constitutive relations and their effects on joint performance.

b. Consultative and advisory functions to other laboratories and agencies

None

c. Transitions.

None

6. New discoveries, inventions, or patent disclosures:

In collaboration with Professor T. N. Farris of Purdue University, an effort to devise the means for coupling, 3-dimensional finite element analyses with the Purdue analysis of fretting fatigue has been proposed to the AFOSR.

Fatigued lap joints with characterized damage, produced as part of Task 5.2, are being used to evaluate NDI procedures at both Northwestern and Vanderbilt University.

The mechanical response of samples of advanced, chromated and non-chromated sealants obtained from Courtaulds Aerospace, Sealants and Coatings Division have been measured in an effort to include these effects in the finite element analyses of lap joints.

Nine different strategies for mitigating the fatigue and fretting fatigue damage of riveted lap joints have been identified. A study to evaluate the potential benefits of these strategies has been proposed to the AFOSR.

A methodology for incorporating the mechanical effects of thin, polymer sealant coatings in finite element analyses of riveted lap joints has been devised. A study of the effects of such coatings on the mechanical response of lap joints has been proposed to the AFOSR.

7. Honors/Awards:

George T. Hahn, Fellow of the ASM; ASM 1981 Edward deMille Campbell Memorial Lecturer, Chairman, Gordon Conference in Physical Metallurgy, 1980.

George T. Hahn, ASM 1981 Edward deMille Campbell Memorial Lecturer.

REFERENCES

- A. Kumar, A. M., Hahn, G. T., and C. A. Rubin, "A Study of Subsurface Crack Initiation Produced by Rolling Contact Fatigue," *Met. Trans. A*, 1993, Vol. 24A, pp. 351-359.
- Y. Furuya, and H. Shimada, "Fatigue Crack Initiation from Notch Root (Local-Strain Damage Accumulation Process on Crack Initiation)," *Eng. Fracture Mech.*, 1986, Vol. 23, pp. 983-989.
- Z. Yang, and Z. Wang, "Cyclic Deformation and Fracture Behavior of AL Alloy 6061 under the Action of the Mean Stresses," *Met. Trans. A*, 1993, Vol. 24A, pp. 2083-2093.
- M. O. Lai, J. T. Oh, and A. Y. C. Nee, "Fatigue Properties of Holes with Residual Stresses," *Eng. Fracture Mech.*, 1993, Vol. 45, pp. 551-557.
- Beuth, J. L., and Hutchinson, J.W., 1994, "Fracture Analysis of Multi-Site Cracking in Fuselage Lap Joints", *Computational Mechanics*, Vol. 13, pp. 315-331.
- Fongsamootr, T., Bastias, P. C., Rubin, C. A. and Hahn, G. T. (unpublished research)
- Fung, C.P. and Smart, J., 1994, "An Experimental and Numerical Analysis of Riveted Single Lap Joints", *Proc. Inst. Mechanical Engrs, Part G, J. Aerospace Engineering*, Vol. 208, pp. 79-90.
- Ganapathy, H. and Farris, 1997, T. N., "Modelling of Skin/Rivet Contact: Application to Fretting Fatigue", *Proc. AIAA/ASME Structures, Structural Dynamics and Materials Conference*, Kissimmee, FL., April, 1997.
- Iyer, K., Hahn, G. T., Bastias, P. C. and C. A. Rubin, 1995, "Analysis of Fretting in Pinned Connections", *Wear*, Vol. 181-183, pp. 524-530.
- Iyer, K., 1997, "Three Dimensional Finite Element Analyses of the Local Mechanical Behavior of Riveted Lap Joints", *Ph.D Dissertation*, Vanderbilt University, May 1997.
- Iyer, K., Bastias, P. C., Rubin, C. A. and Hahn, G. T., 1997A, "Three-Dimensional Analyses of Single Rivet-Row Lap Joints; Part I: Elastic Response", submitted to the *ASME J. App. Mechanics*.
- Iyer, K., Bastias, P. C., Rubin, C. A. and Hahn, G. T., 1997B, "Three-Dimensional Analyses of Single Rivet-Row Lap Joints; Part II: Elastic-Plastic Response", submitted to the *ASME J. App. Mechanics*.
- Iyer, K., Bastias, P. C., Rubin, C. A. and Hahn, G. T., 1997C, "Three-Dimensional Analyses of Double Rivet-Row Lap Joints; Part I: Non-Countersunk Rivets", submitted to the *J of the AIAA*.

Iyer, K., Bastias, P. C., Rubin, C. A. and Hahn, G. T., 1997D, "Three-Dimensional Analyses of Double Rivet-Row Lap Joints; Part II: Countersunk Rivets", submitted to the J. of the AIAA.

TASK 6. CORROSION

TASK 6. CORROSION

1. Objective

The objective of Task 6 is to develop a methodology for the detection, evaluation, and quantification of active corrosion on aircraft aluminum alloys. The focus is on developing a series of in-situ model-systems of active corrosion and measuring the magnetic field distribution due to corrosion activities active corrosion of aluminum alloys used in aircraft using Superconducting Quantum Interference Device (SQUID) magnetometry.

2. Accomplishments

A. Detection of in-situ active corrosion

The magnetic field distributions due to undergoing in-situ active corrosion on the surface of aircraft aluminum alloys were successfully detected non-invasively using SQUID imaging system. Two models of in-situ corrosion were designed and tested :

(a) Active Pitting Corrosion using 2024 and 7075 aluminum alloys in a solution of 3.5% NaCl + 5ppm Cu⁺⁺;

(b) Active Uniform Corrosion using a 1.5 mm thick 2024 aluminum alloy plate which was exposed in a solution of 2 ml HF, 3 ml HNO₃, 5 ml HCl, and 190 ml H₂O.

Figure 6-1a shows a schematic diagram of the SQUID imaging system for active corrosion measurements. Figures 6-2a and 6-2b are the typical magnetic field distributions on an active pitting corrosion sample. The maximum amplitude of magnetic signal was changing with time as shown in Fig. 6-3. It is considered to be characteristic of normal pitting initiation and pitting development processes.

Figure 6-4 and 6-5 show the magnetic images for pitting corrosion of aluminum 7075 alloy and 2024-T3 alloy, respectively. Figure 6-6 is the magnetic images for "uniform" corrosion of 2024-T3 aluminum alloy in a "acid" solution. All three figures show that the amplitude and polarity vary with time during the corrosion process.

B. Detection of hidden active corrosion

The magnetic field distributions due to hidden active corrosion on the bottom surface of aircraft aluminum alloy plate were detected using a SQUID magnetometer, without any electrical or mechanical connections intruding on the sample. The magnetic field strength decreases with thickness of the aluminum plate, distance between the SQUID and the top surface of the plate (lift-off distance), and increases with NaCl concentration of the solution.

Figure 6-7 is the schematic diagram of the SQUID experimental setup for the measuring. Figure 6-8 is the relation between the signal strength and the thickness of the plate when the

SQUID pick-up coils were located 2 mm away from the top-surface of the sample. From Fig. 6-8 we may conclude that the hidden corrosion occurring on the lower surface of a 10.2 mm thick stack of aluminum alloy plates in 3.5% NaCl solution may be detected.

The magnetic field strength *versus* distance between the SQUID pick-up coils and the top-surface of the sample was measured for a hidden corrosion occurring on the bottom surface of a 3 mm 2024-T3 aluminum alloy plate in 3.5% NaCl solution as shown in Fig. 6-9. The results showed that the magnetic field strength decreases with increasing distance, and the hidden corrosion at the bottom surface of a 3 mm thick can be detected at distances as far as 13 mm.

Figure 6-10 is the magnetic field strength *versus* NaCl concentration of the solution. The signal due to hidden corrosion occurs on the lower surface of a 3 mm 2024-T3 aluminum alloy plate in the solutions containing different concentrations of Cl⁻ were measured when the SQUID pick-up coils were located 2 mm away from the top-surface of the sample. The results showed that the measured magnetic field strength decreases with decreasing NaCl concentration. The SQUID is able to detect corrosion signals for solutions containing only 1 ppm NaCl, a dilution 1/35000 that of sea water.

The originally-proposed effort for this task was completed. This effort has been transferred to NCI, Inc., working with the Air Force Corrosion Program Office at Warner Robins Air Force Base.

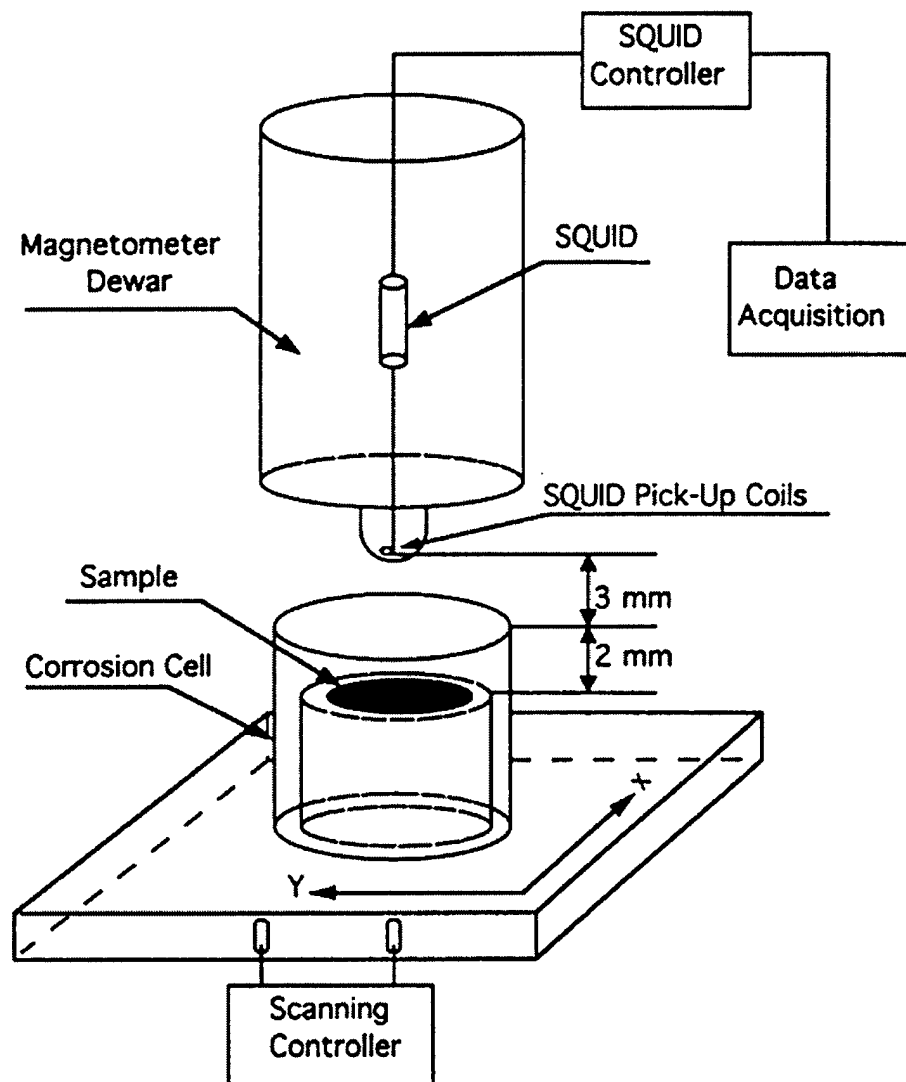


Figure 6.1. Schematic diagrams of the test systems for detection of active corrosion. The sample is placed in a corrosion cell so that the top surface is 2 mm below the solution surface.

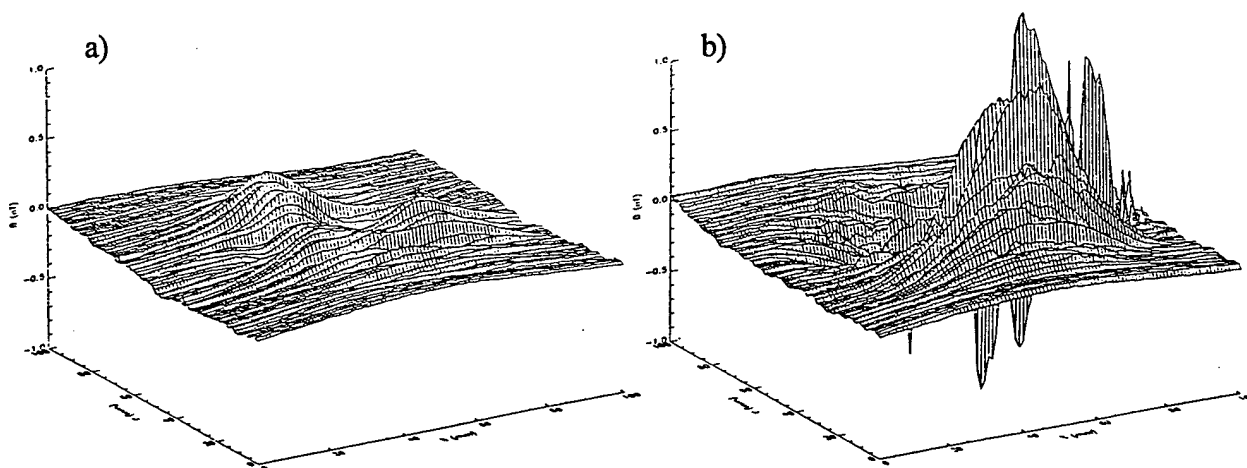


Figure 6.2 Typical magnetic field distributions on an active corrosion 7075 aluminum alloy sample in a solution of 3.5% NaCl + 5ppm Cu^{++} . Data was obtained (a) in the period of 25 to 43 minutes after the sample was placed in the solution, (b) in the period of 276 to 294 minutes.

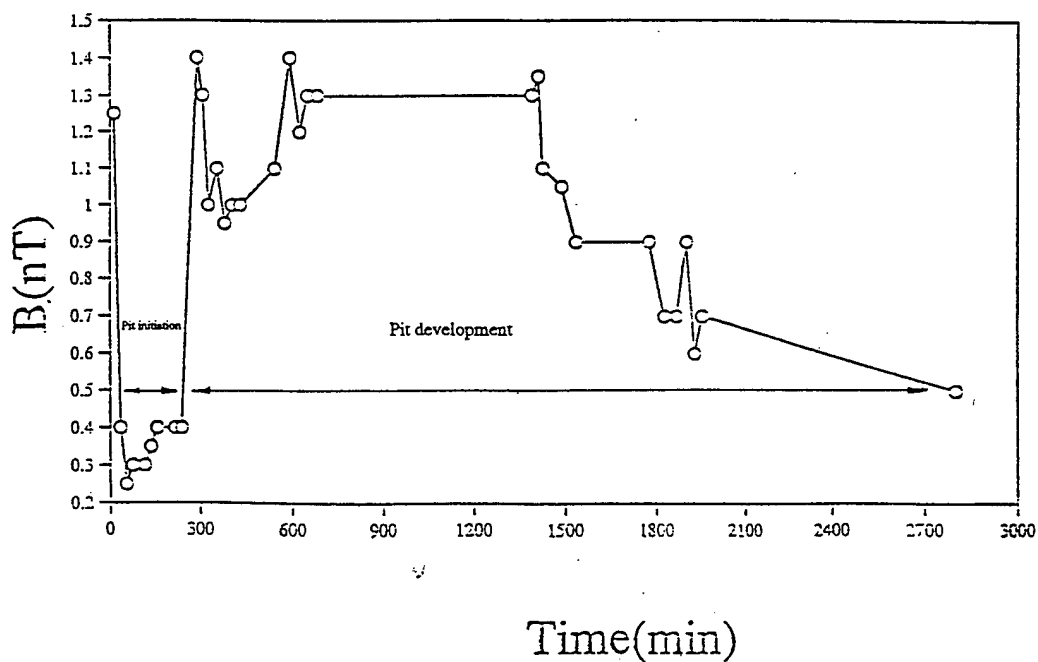


Figure 6.3 The maximum amplitude of the magnetic signal as a function of time during pitting corrosion. The first 300 minutes represents pit initiation followed by an increase in magnetic field signifying the onset of the pit development phase.

ACTIVE CORROSION
(7075 Aluminum Alloy in 3.5% NaCl + 5 ppm Cu⁺⁺ Solution)

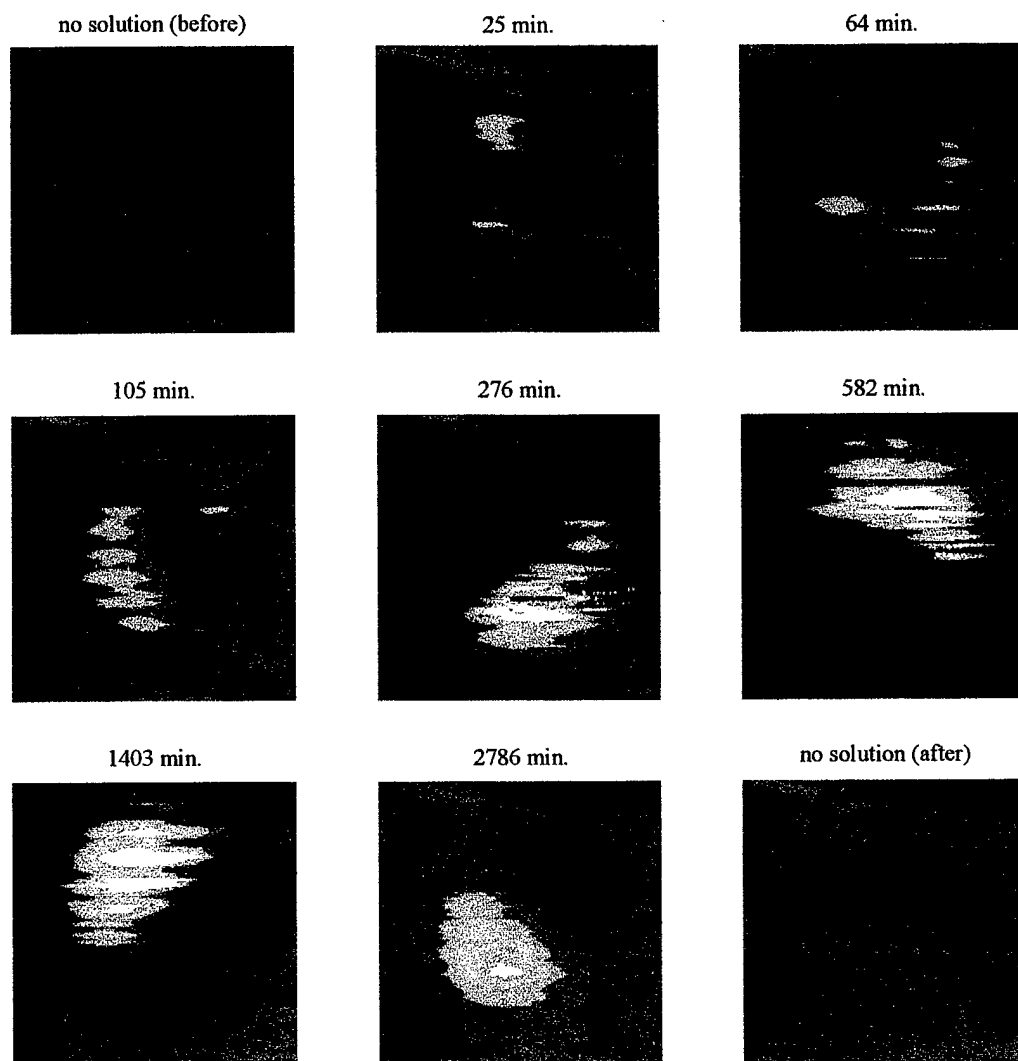


Figure 6.4. Magnetic field as a function of time during pitting corrosion of 7075 aluminum alloy in a solution of 3.5% NaCl + 5 ppm Cu⁺⁺.

ACTIVE CORROSION
(2024 Aluminum Alloy in 3.5% NaCl + 5 ppm Cu⁺⁺ Solution)

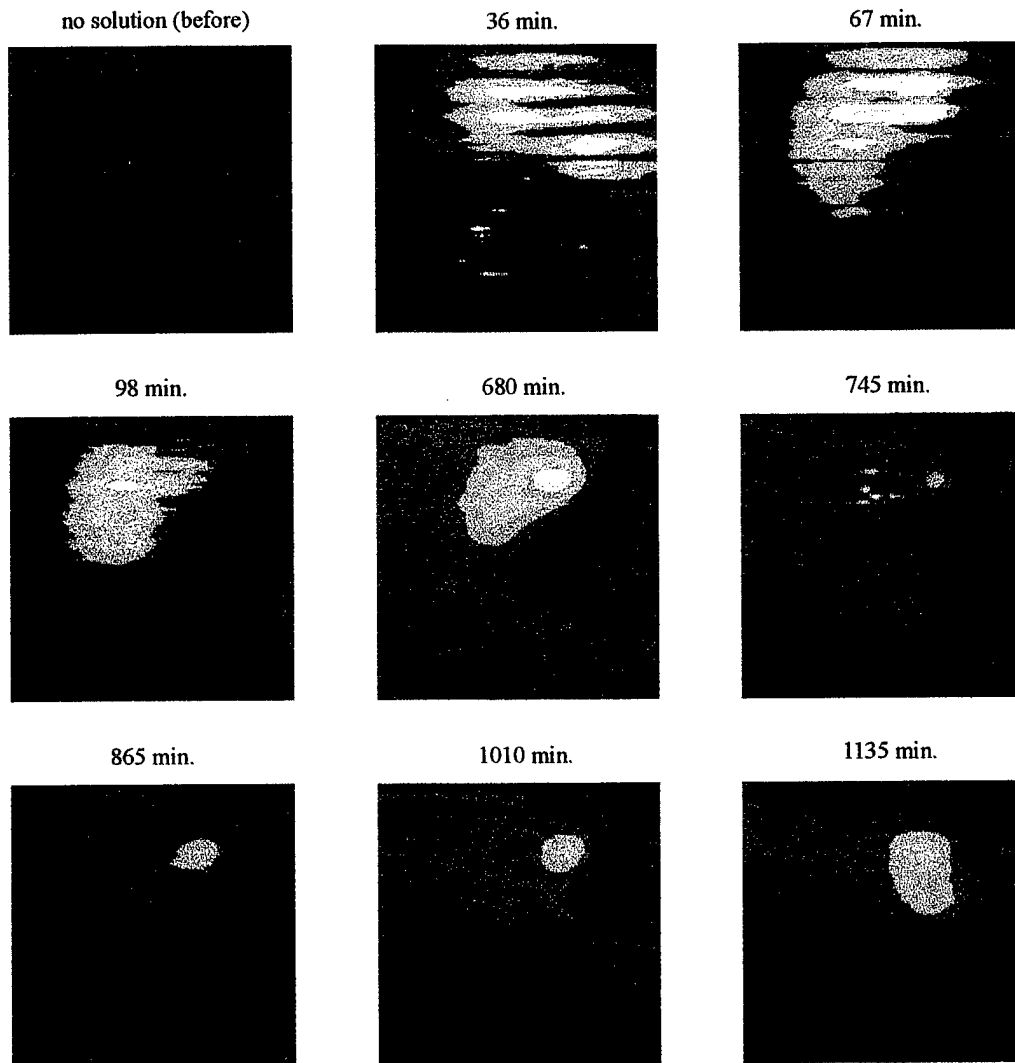


Figure 6.5. Magnetic field as a function of time during pitting corrosion of 2024-T3 aluminum alloy in a solution of 3.5% NaCl + 5 ppm Cu⁺⁺.

ACTIVE UNIFORM CORROSION

(2024-T3 Aluminum Alloy in 58% HF, 3 ml 71% HNO₃, 5ml 36.5% HCl, and 590 ml H₂O)

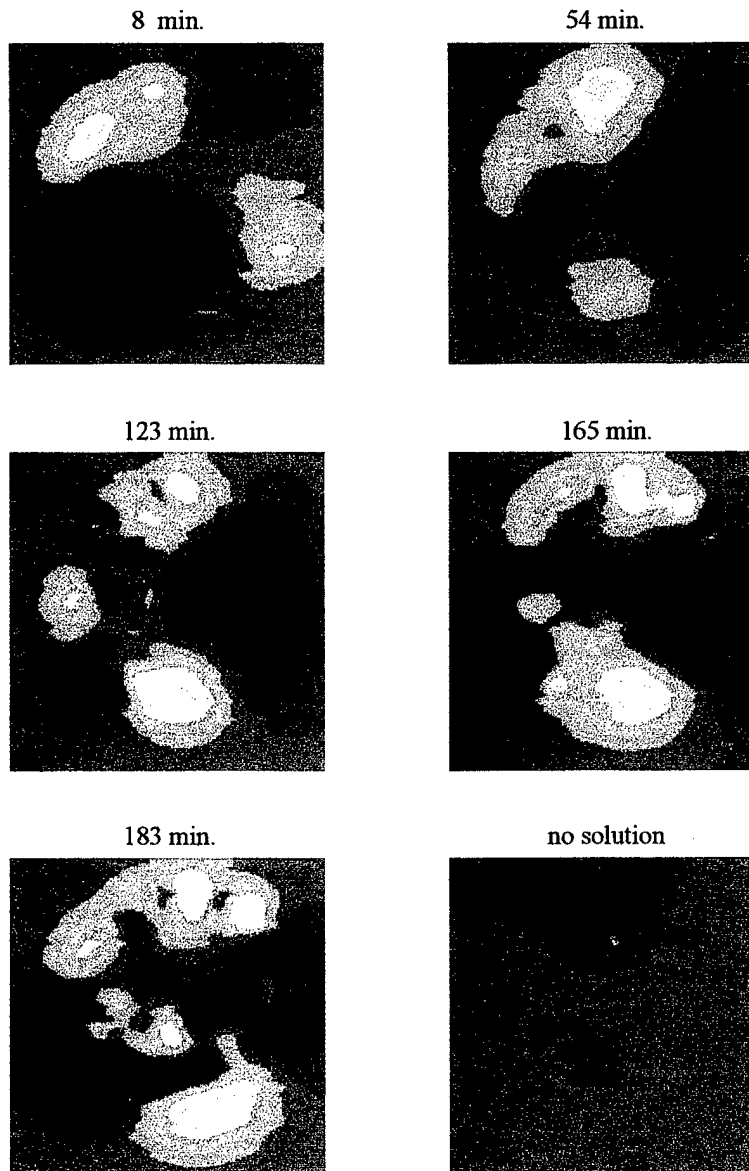


Figure 6.6. Magnetic field as a function of time during uniform corrosion of 2024-T3 aluminum alloy in a solution of 2 ml 58% HF, 3ml 71% HNO₃, 5ml 36.5% HCl, and 590 ml H₂O.

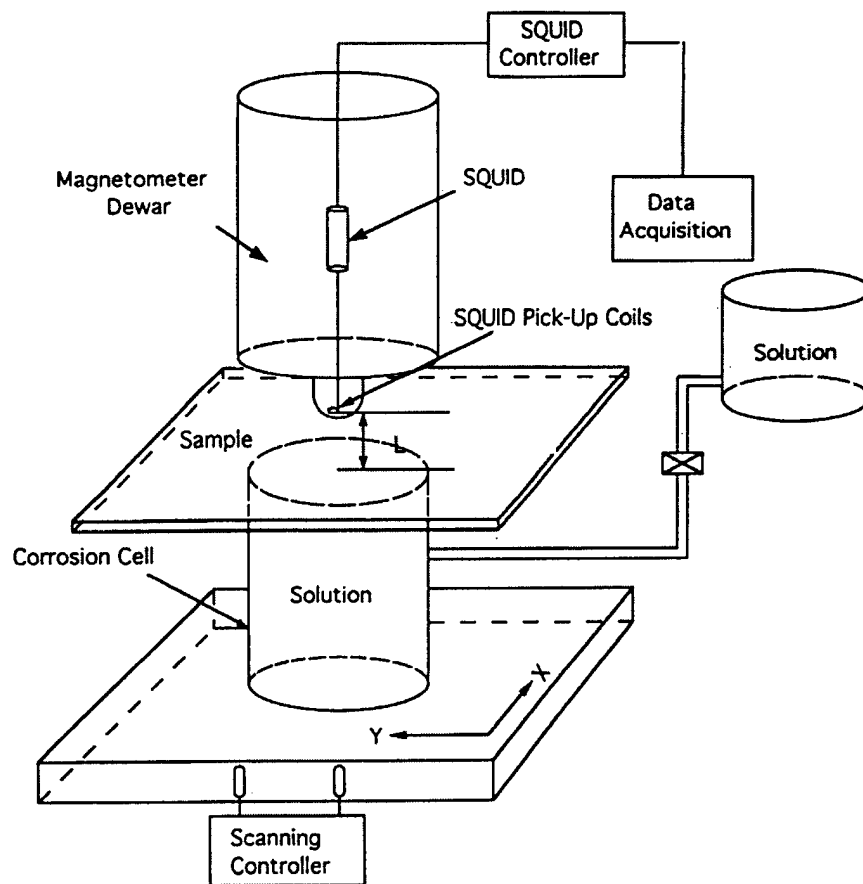


Figure 6.7. Schematic diagrams of the test systems for detection of active hidden corrosion. A 150 mm by 150 mm 2024-T3 aluminum plate is placed on a 45 mm diameter cylindrical corrosion cell such that only a 45 mm diameter area on the lower surface of the plate is exposed to the solution.

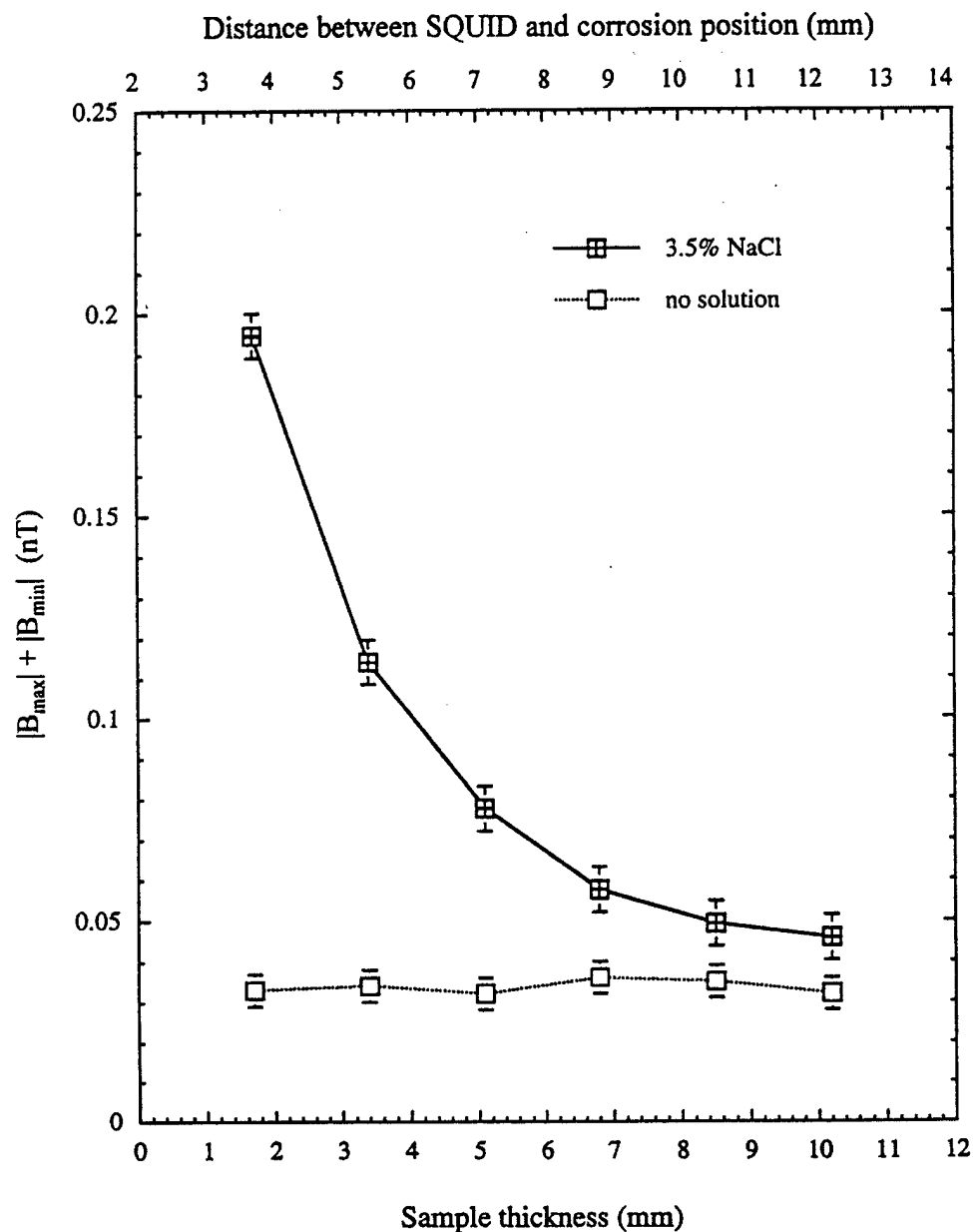


Figure 6.8. Magnetic field strength *versus* sample thickness detected using the SQUID from 2 mm above the top-surface of the 150×150 mm, stack of aluminum alloy plates which has a 45 mm diameter area to exposed to a 3.5% NaCl solution in the bottom surface of the plates, on the side away from the SQUID magnetometer.

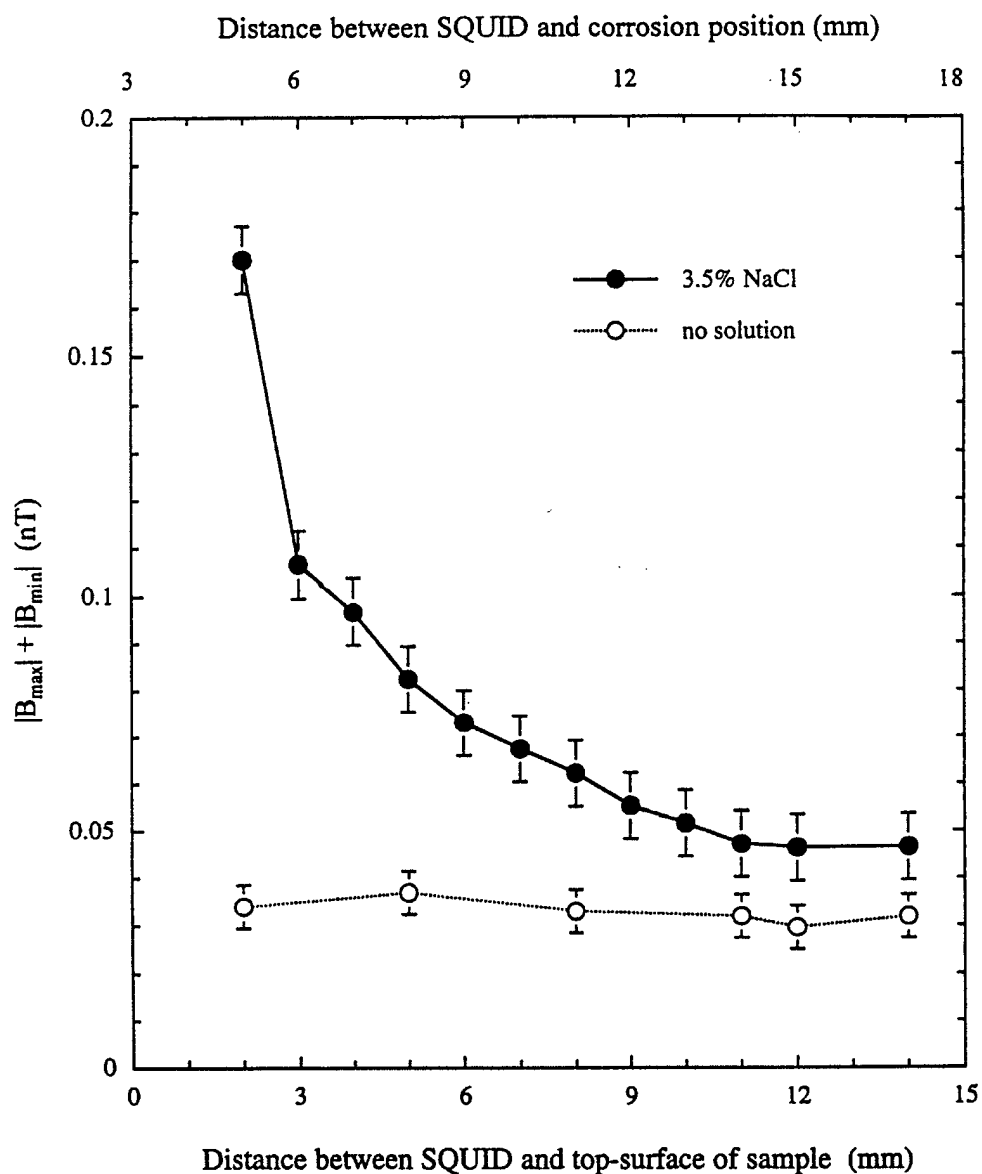


Figure 6.9. Magnetic field strength *versus* the distance between the SQUID pick-up coils and the top-surface of a 150×150 mm, 3 mm thick aluminum alloy plate which has a 45 mm diameter area to exposed to a 3.5% NaCl solution in the bottom surface, on the side away from the SQUID magnetometer.

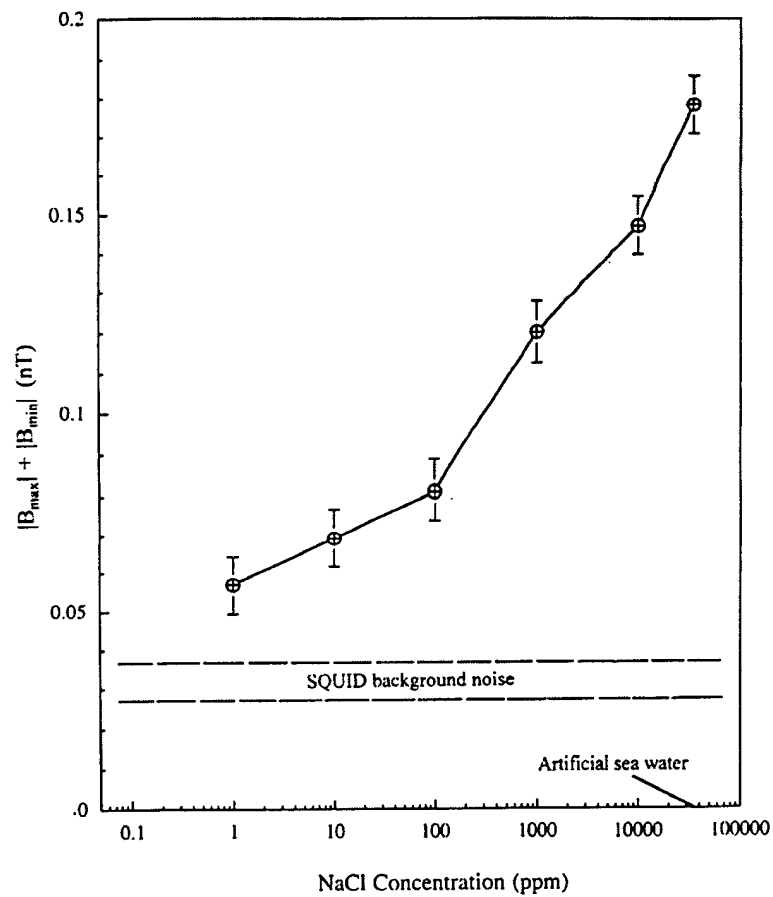


Figure 6.10. Magnetic field strength *versus* NaCl concentration detected using the SQUID from 2 mm above the top-surface of a 150×150 mm, 3 mm thick 2024-T3 aluminum alloy plate which has a 45 mm diameter area to exposed to the solutions containing different NaCl in the lower surface of the plate.

3. Personnel Supported :

William F. Flanagan, Professor, Mechanical and Materials Engineering
Barry D. Lichter, Professor, Mechanical and Materials Engineering
Delin Li, Research Associate
Yu Pei Ma, Research Assistant Professor of Physics
John P. Wikswo, Jr., Professor of Physics

4. Publications and Related Items:

Journal Articles

"Detecting In-Situ Active Corrosion by a SQUID Magnetometer," D. Li, Y.P. Ma, W.F. Flanagan, B.D. Lichter, and J.P. Wikswo, Jr., Journal of Minerals, Metals & Materials, 47(9): 36-39 (1995).

"Application of Superconducting Magnetometry in the Study of Aircraft Aluminum Alloy Corrosion," D. Li, Y.P. Ma, W.F. Flanagan, B.D. Lichter, and J.P. Wikswo, Jr., Corrosion, 52(3): 219-231 (1996).

"Detection of Hidden Corrosion of Aircraft Aluminum Alloys by Magnetometry Using a Superconducting Quantum Interference Device," D. Li, Y.P. Ma, W.F. Flanagan, B.D. Lichter, and J.P. Wikswo, Jr., Corrosion, 53(2): 93-98 (1997).

Conference Proceedings

"The Use of Superconducting Magnetometry to Detect Corrosion in Aircraft Alloys," D. Li, Y. Ma, W.F. Flanagan, B.D. Lichter, and J.P. Wikswo, Jr., Proc. of the Tri-Service Conference on Corrosion, Orlando, FL, pp. 335-346, June 1994.

"SQUID Magnetometers for Studying Corrosion and Corrosion Protection in Aircraft Aluminum," J.P. Wikswo, Jr., NACE International, Paper No. 293, pp. 1-17 (1997).

5. Interactions/Transitions:

a. Participation/presentations at meetings, conferences, seminars, etc.

John P. Wikswo and Delin Li attended the Tri-Service Conference on Corrosion, Orlando, FL, June 1994.

On November 22, 1995, Barry Lichter presented a seminar on "Detection of Corrosion by SQUID Magnetometry" at the Corrosion Colloquium of the

Laboratory for Materials Science at Delft University of Technology, Delft, The Netherlands.

On November 29, 1995, Barry Lichter gave an invited lecture on "Remote Sensing of Aluminum Alloy Corrosion by Superconducting Magnetometry" to the Corrosion Studiekern (an organization of industrial and university personnel concerned with corrosion engineering) at Arnhem, The Netherlands.

John Wikswo attended the AFOSR/NDE Program Review Meeting at Warner Robins, Air Force Base, GA on April 2, 1996.

John Wikswo attended the QNDE Conference held on July 28 - August 2, 1996 in Brunswick, Maine.

John Wikswo attended the Corrosion '97 Conference held on March 9 - 14 1997 in New Orleans, LA.

John Wikswo attended the NATO ASI Conference held on June 1 - 20, 1997 in Loen, Norway.

John Wikswo and Yu Pei Ma attended the QNDE Conference held on July 27 - August 1, 1997 in San Diego, CA.

b. Consultative and advisory functions to other laboratories and agencies

John Wikswo met with NCI Information Systems and staff from Warner Robins Air Logistics Center on March 5 - 6, 1996 and August 5 - 6, 1996 to discuss corrosion and the Air Force aging aircraft problem.

We received a contract from NCI, Inc. to integrate a high-resolution SQUID magnetometer, a magnetic shield, and a scanning stage into a laboratory corrosion measurement system. The design and fabrication of this system are based directly upon the findings from the research supported by this URI. Particular attention has been paid to sample registration for repeated measurements over long periods of time, ease of use, the limits for spatial and temporal sampling of rates, drift suppression, and noise reduction. This system is capable of detecting hidden, localized corrosion in aircraft within less than one-half hour of the application of a sodium chloride solution to the metal. It will be utilized to monitor the time and temperature dependence of hidden corrosion in aircraft lap joints and the ability of sealant techniques and corrosion prevention compounds to reduce this corrosion. For the past six months, we have been working closely with the engineering staff of NCI to train them in the use of the SQUID system, and to guide the development of calibration, image processing, and data analysis software required for the project. The system should be delivered to NCI's facility at WR-ALC in

September 1997. The significance of this instrumentation and our measurement techniques is that we know of no other approach that can provide real-time, totally non-invasive detection of hidden corrosion activity in aircraft lap joints. The potential for this technique to improve our understanding of corrosion in aircraft is excellent.

c. Transitions.

We have initiated discussions with Alcoa on the study of corrosion of aircraft aluminum. Alcoa is now providing large amount of sample material for the SQUID studies.

Discussions with and demonstrations to numerous visitors to our labs.

3. New discoveries, inventions, or patent disclosures:

"Method and Apparatus for Detecting Flaws Below the Surface of an Electrically Conductive Object," Y.P. Ma and J.P. Wikswo, Jr., United States Patent 5,610,517 (March 11, 1997).

4. Honors/Awards:

None

TASK 7. EVALUATION OF NDE CAPABILITIES

TASK 7. EVALUATION OF NDE CAPABILITIES

1. Objective

The objective is to develop systems models to predict the reliability of the proposed NDE methods. A probability of detection (POD) analysis is being used to evaluate NDE reliability consistent with damage tolerant design philosophies used in aerospace to make life predictions. Measurement models combined with experimental data are being used to conduct this probabilistic analysis and will result in a quantitative representation (e.g., a set of POD curves) of the capability of SQUID NDE techniques. From these curves, the minimum detectable flaw size at 90% probability of detection and 95% confidence can be determined for a variety of conditions.

2. Accomplishments

Overview

As the commercial and military aircraft fleets age, additional resources are required to ensure their airworthiness. As the aircraft become older, the more likely they are to develop structural damage that may lead to unscheduled repairs or, in the worst case, accidents. Fatigue and corrosion are the two main causes of structural damage in aging aircraft and this research examines the use of a Superconducting QUantum Interference Device (SQUID) magnetometer as a tool for Nondestructive Evaluation (NDE) to detect and characterize these aging aircraft problems. The primary advantage of using SQUIDS in NDE over other techniques is the ability to detect second layer cracks and corrosion commonly found in aircraft structures.

In general, verification of a NDE method means demonstrating, through experiment and/or calculations, the ability to distinguish signal from noise for the flaw types and sizes and instrument/flaw configurations expected in the actual inspection. A common approach to quantify and validate the capabilities of an inspection technique is to conduct a probability of detection (POD) analysis. There are basically two ways to conduct this type of analysis. The first is, experimentally, which requires a large number of samples with ranging flaw characteristics being examined by several inspectors. The second is, analytically, which requires a model simulating the inspection process for a range of samples and testing conditions.

A POD analysis has been done using the analytical approach, combined with experimental information, to evaluate SQUID NDE reliability consistent with damage tolerant design philosophies used in aerospace to make life predictions. A minimum detectable crack length at 90% probability of detection and 95% confidence was used as the reliability criteria.

Fatigue Cracks – a Problem Requiring NDE

Fatigue cracking in aircraft is primarily due to cyclic stress loading. For example, internal pressurization during flight creates stresses on the fuselage longitudinal skin splices. The two basic splice designs used are shown in Figure 7.1.

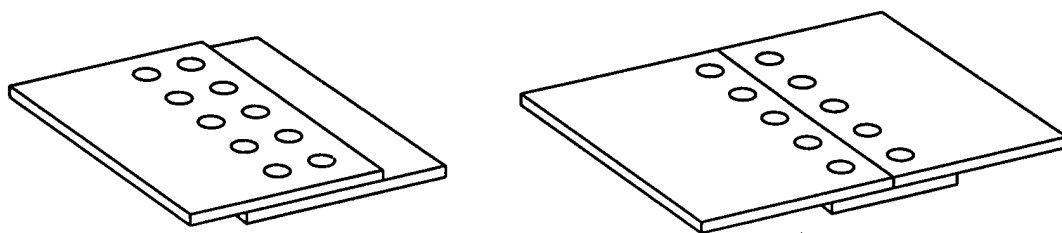


Figure 7.1 Fuselage skin splices: a) lap splice and b) butt splice

Fatigue cracks are most likely to develop along the direction of the fastener row since the primary stress direction is transverse to the row (see Figure 7.2). Usually, the cracks start at the fastener hole and propagate radially and, if there is multiple site damage (MSD), the structural strength is greatly reduced even for small crack lengths.

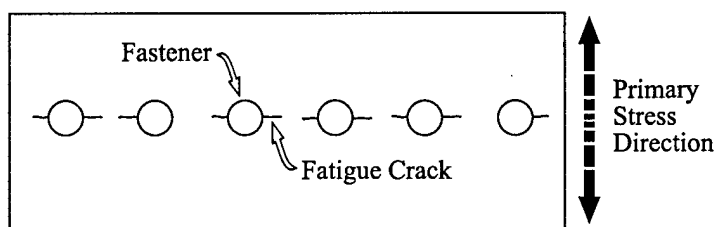


Figure 7.2 Fatigue crack development along direction of fastener row

Aircraft are designed to meet damage tolerant requirements and nondestructive evaluation/inspection (NDE/I) techniques are needed to efficiently and reliably detect and characterize damage, if it occurs, so that repairs can be made. Damage tolerant design basically involves fatigue crack growth predictions starting from some assumed crack length, a_0 , due to possible manufacturing defects. For aircraft structures, damage tolerance specifications require a 90% detection probability and 95% confidence level for detecting a specified crack length, a_{th} (threshold crack length), at a particular location. The dependence of a_{th} on the inspection process and the uncertainties associated with the detection of a crack lead to the statistical problem that can be addressed by POD analyses. Earlier NDE work established POD as a way in which NDE process performance could be quantified and incorporated into specifications, standards and design documents. By quantifying the procedure to measure the performance capability of a NDE system, objective comparison could be done for different NDE systems and NDE performance requirements could be defined for development of new techniques.

Probability of Detection (POD)

Probability of detection can be defined as the probability that a specific crack length can be detected with a particular inspection system under known conditions. POD combines characteristics of the measurement system, including noise, with statistical information pertinent to the cracks being examined. The schematic POD curve in Figure 7.3 shows the probability of detection as a function of crack length. The probability of detecting a small crack is low whereas, the probability of detecting larger cracks approaches unity.

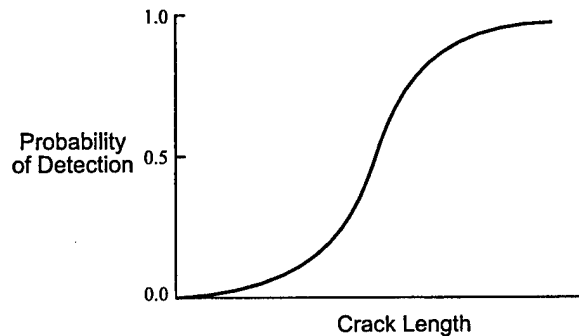


Figure 7.3 Probability of detection as a function of crack length

The POD function serves as a basis to evaluate the capability of an NDE system. For these analyses, POD is a function of crack length to be consistent with life prediction calculations that are based on crack length. The POD then is a measure of how well cracks of all sizes can be found. This capability cannot be determined exactly but, through the use of confidence bounds that account for the random errors of the NDE process, can be estimated. For example, the Air Force uses a 95% lower confidence bound that provides a risk factor that the true probability of detection is better than this bound 95% of the time.

Use of SQUID's in NDE

A superconducting quantum interference device (SQUID) magnetometer is the world's most sensitive detector of magnetic fields. The potential advantage that a SQUID has over other techniques is its ability to detect second layer flaws by using low frequency excitation.

A SQUID NDE technique is not only defined by the SQUID instrument characteristics but also by nature of the current distributions used to probe the flaws. When the current passing through the sample is affected by inhomogenieties, voids, cracks, and edges, the magnetic field is perturbed and can be sensed by the pickup coil of the SQUID. This work focuses on the dc-current injection technique. Injecting or inducing a uniform current distribution in the specimen causes the current to be parallel to the specimen surface under the pickup coil. For example, a large, uniform plate would have a magnetic field from this that encircles the specimen. This magnetic field would primarily be parallel to the specimen surface for scans centrally located and for small liftoff distances. The pickup coils measure only the perpendicular component (or gradient of this) of the magnetic field. A flaw in the specimen will perturb the parallel field and produce a perpendicular component which can then be detected (pickup coils measure only B_z). Figure 7.4 illustrates the SQUID pickup coil being scanned over the sample containing a flaw and the typical magnetic map produced revealing a signature that commonly has a dipolar shape. The trough and ridge at the ends of the map are due to the edge effects of the plate.

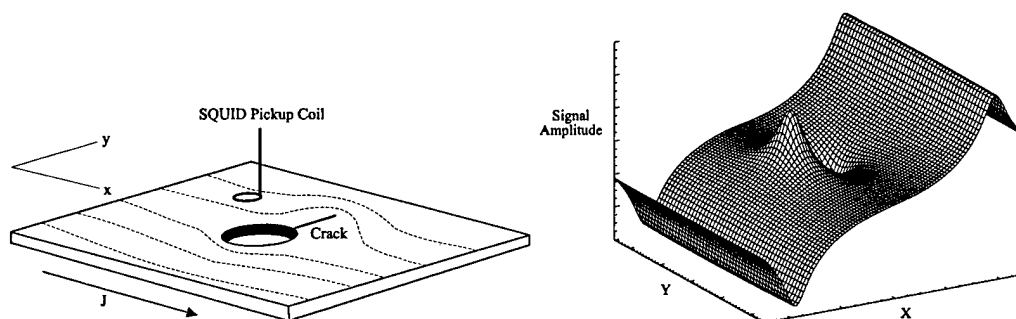


Figure 7.4 DC-current injection: (a) scan over sample (b) resulting B_z magnetic map

Although this technique is not likely to be used in a field instrument, the current distributions produced are similar to the planar ac eddy currents produced by sheet inducers, which *are* proposed for a field instrument. Also, since existing boundary element methods can be used to model dc-current injection, the analytical approach to a POD analysis can be taken.

Measurement Model

A measurement model using boundary element methods has been constructed simulating a SQUID magnetometer being scanned over a dc-current injected, finite plate containing an ideal (*i.e.*, straight, infinitely thin, and perfectly insulated) crack. The model was used to examine the effect of system parameter variability on flaw detectability. The results of this sensitivity analysis was then combined with empirical noise distributions to determine probability of detection. A goal in this research was to develop a method where simulation represents the experimental approach, is cheaper and faster, and identifies sources of unreliability in SQUID NDE.

The objective of the SQUID measurement model, which solves the forward problem of calculating the magnetic field from a known current distribution, is to simulate what the instrument may see in a test environment on an unknown sample. A SQUID gradiometer measures the vertical component of magnetic field, which is the result of currents flowing in the sample. A flaw will perturb these currents and, if the perturbation is large enough (*e.g.*, signal/noise > 1), show up as an anomaly in the magnetic field map. The specific aging aircraft problem being addressed is the modeling of a fatigue crack emanating radially from a fastener hole (schematically shown in Fig. 7.5) as discussed previously regarding fuselage skin splices.

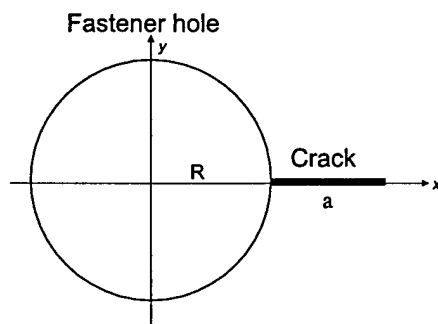


Figure 7.5 Schematic of a fastener hole with crack

For the interested reader, the details of the mathematical development of this can be found in Chapter II of the associated dissertation from which this summary is written.

POD Curves from Simulated Experimental Data

Figure 7.6 shows the centerline profiles of the magnetic maps resulting from simulated scans over a hole with crack for four different crack lengths while keeping the hole diameter constant. As can be seen, for increasing crack length, the signal amplitude increases. Also, the asymmetry increases, pulling the crack side of the dipolar signal to the right while the hole side remains relatively fixed. The important characteristic for POD is the increasing peak-to-peak value as a function of crack length, which is the "signal" used in the POD analysis.

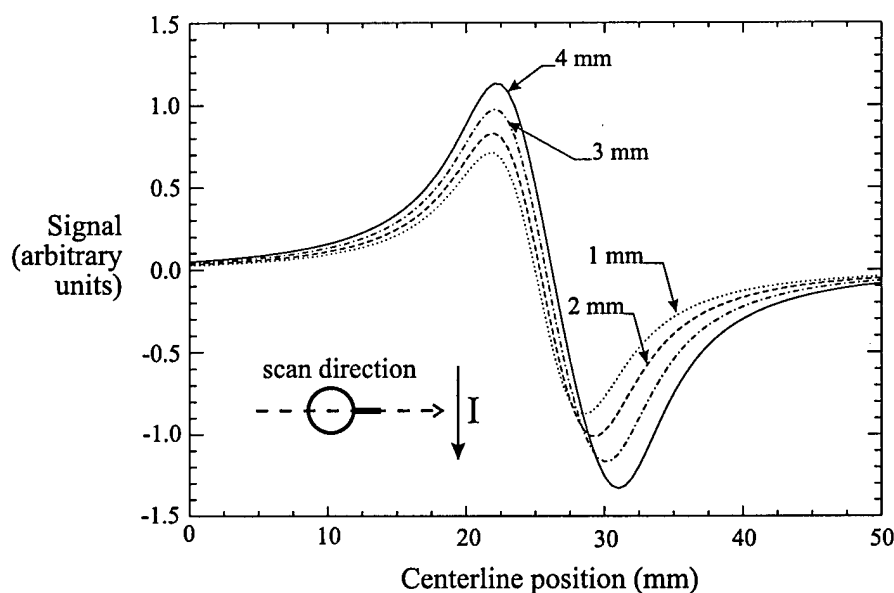


Figure 7.6 Scan centerline profiles for various crack lengths (with hole)

Sensitivity analyses were done on the system parameters of scan resolution, plate thickness, pick-up coil liftoff, and pick-up coil tilt angle to determine how they affect the overall signal distribution. Monte Carlo simulations used this signal distribution along with experimental noise distributions to generate realistic POD curves.

Noise distributions must be characterized in order to determine POD and POFA. Several noise distributions have been extracted from existing experimental data for different SQUID systems and measurement techniques. The measurement model simulates dc-current injection and experiments using direct dc-current injection have large noise distributions since they use the entire bandwidth of the SQUID (dc to ~10kHz) and therefore, include noise over these frequencies as well. Noise conditions associated with other experimental techniques are more representative of what SQUID's will be operated in. Techniques based upon eddy current inducers use lock-in amplifiers at a particular frequency and greatly reduce the noise. The dc-measurement data shows approximately 400 pT peak-to-peak noise while the lock-in measurement data shows about 2 pT, a noise reduction

factor of 200! POD values determined using noise from lock-in measurements represent present SQUID capability.

Monte Carlo simulation, utilizing the results from the BEM measurement model, was used to sample from the uncertainty distributions of scan resolution, plate thickness, pick-up coil liftoff and pick-up coil tilt angle to generate an overall signal distribution. The resulting signal distribution was then compared with the noise distributions associated with ac and dc measurements to determine POD. A 95% lower confidence bound was then generated by iterative generation of multiple signal distributions at each crack length. Figure 7.7 is the dc-measurement POD curve resulting from generating similar distributions at each crack length. The abruptness of the POD curve near the origin is due to a combination of the relative sharpness of the signal distribution with respect to the noise distribution and the one-sidedness of the noise distribution. The 95% lower confidence limit applies more to experimentally based POD curves that are usually generated from a relatively small number of data points. For simulated data, the lower confidence bound can be made to basically lie on the POD curve if enough runs are made and is not as useful a concept as for the experimentally derived POD curve.

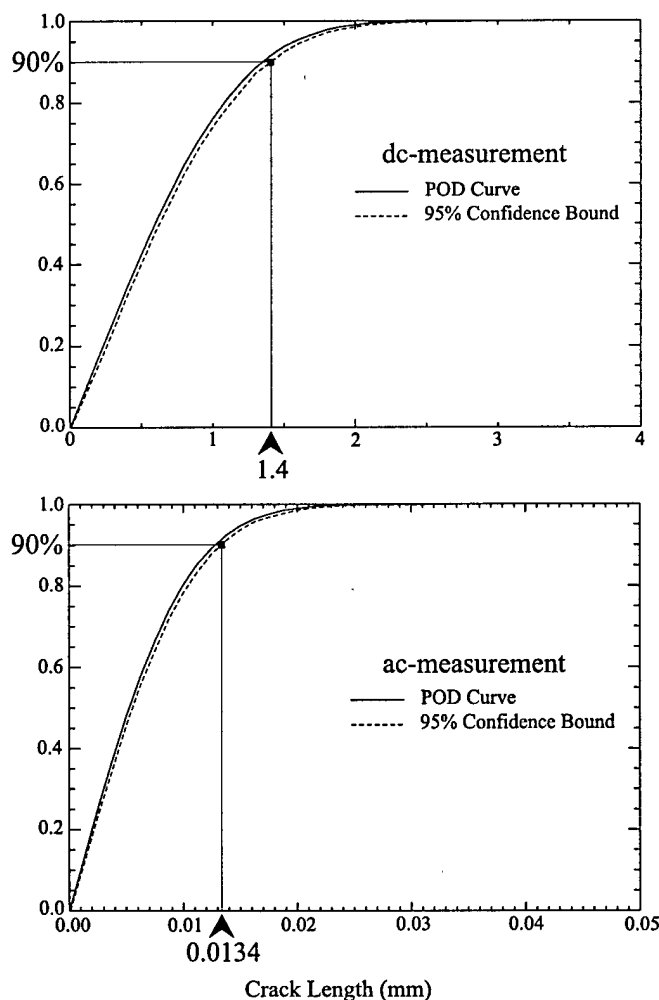


Figure 7.7 Ac/dc-measurement POD curves showing 90/95 crack lengths

The minimum detectable crack lengths corresponding to 90% probability of detection at 95% confidence are 1.4 mm for the dc-measurement and 0.0134 mm for the ac-measurement. The very small minimum detectable crack length determined for the ac-measurement is due to the large noise reduction through use of the lock-in amplifier in this type of measurement.

In the Monte Carlo simulations, the signal distribution was compared directly with the noise distribution to determine POD. For direct sampling from distributions, the signal-to-noise ratio set the threshold (\hat{a}_h), which set the detection criteria. To examine the tradeoff between the probability of detection (POD) and the probability of false alarm (POFA) when setting \hat{a}_h , the signal and noise distribution data generated by the Monte Carlo simulations can be presented in a different format. The SNR requirements determine where \hat{a}_h is to be placed, thus affecting POD (larger SNR requirements correspond to larger minimum detectable crack lengths).

Figure 7.8 displays the dc-measurement POFA and POD curves for three crack lengths, including the minimum detectable crack length, as a function of threshold. By setting a threshold, a value for POFA and POD for all crack lengths is determined. As can be seen, for a crack length of 0.5 mm, the 90% probability of detection point corresponds to a 28% POFA (*i.e.*, there is a 28% chance that noise will be mistaken for a signal). There is only a single POFA curve since probability of false alarm is determined from the noise distribution, which for these simulations is constant. Figure 7.9 shows the ac-measurement POFA and POD as a function of threshold for the previously determined minimum detectable crack length of 0.0134 mm. In both the dc and ac measurement cases, the POFA corresponding to the minimum detectable crack length is approximately zero.

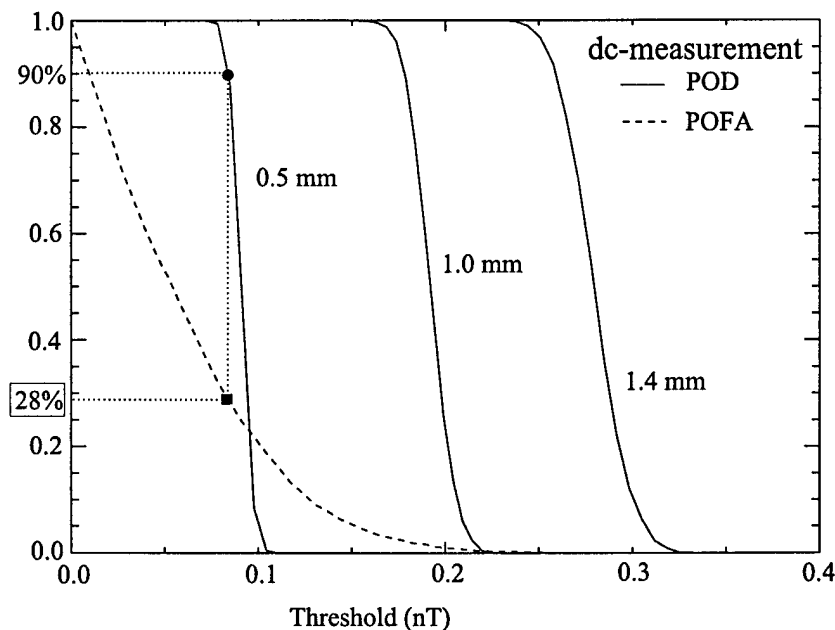


Figure 7.8 Dc-measurement POFA and POD as a function of threshold for three values of crack length

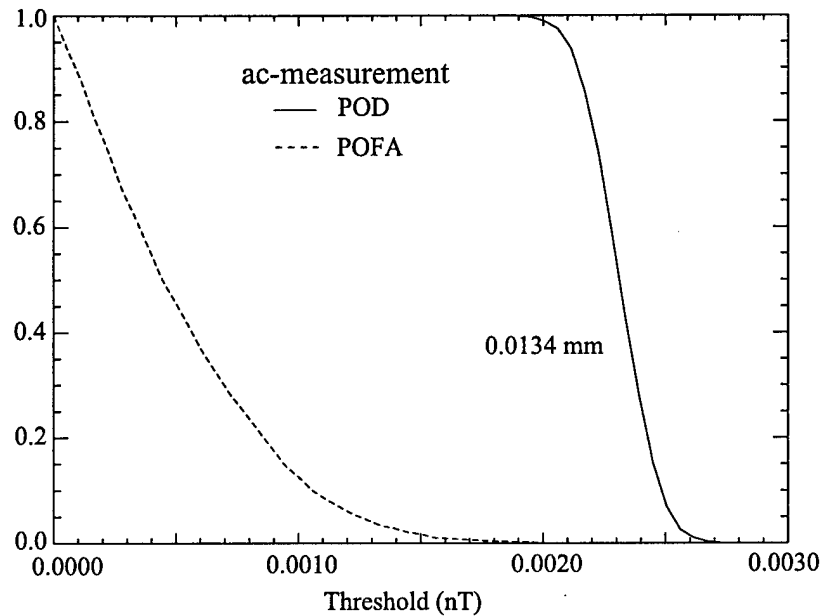


Figure 7.9 Ac-measurement POFA and POD as a function of threshold for the minimum detectable crack length

Factors That May Decrease POD Capability

The relatively small values of minimum detectable crack length determined from this analysis prompts discussion on whether this reflects the true capability of SQUIDs in the detection of real cracks near fasteners in aircraft lap joints. Experimental measurements using SQUIDs on fatigue cracks in lap joints have demonstrated the difficulty in finding cracks, adjacent to fasteners, on the order several millimeters in length. For the POD analysis done here, only four system parameters (scan resolution, plate thickness, pickup coil liftoff and tilt angle) and their associated uncertainties were considered. Since it is these parameter uncertainties that determine the overall signal distribution, and therefore POD, it is apparent that significant parameters have been left out of this analysis. More than likely, these stem from sample-related noise associated with real measurements, which have not been represented in either the measurement model itself or through the parameter uncertainty distributions. Sample-related noise results from the geometry of the sample or, more specifically, how that geometry affects the current flow used to probe the sample. Figure 7.10 shows how some of these current paths can go under and/or through the crack and the fastener, further complicating the detection and characterization of the crack. Some of these issues are discussed in the following sections.

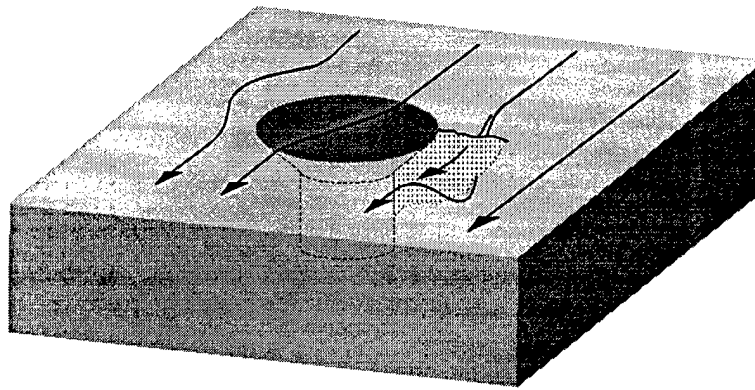


Figure 7.10 Additional current paths complicating crack detection

Crack shape - Probability of detection is traditionally stated as a function of crack length to be consistent with damage tolerant requirements, which are stated in terms of crack length. However, crack shape is an important issue to discuss briefly since cracks of the same "length" but different shape could result in different signals. Currently, the BEM measurement model simulates a straight-through crack (the same length through the entire thickness of the plate) but it is possible to use the model to simulate "3-D" cracks to examine the effect of crack "shape" on magnetic field. By creating slices of varying shapes and depths (see Fig. 7.11), a pseudo-3D crack can be modeled.

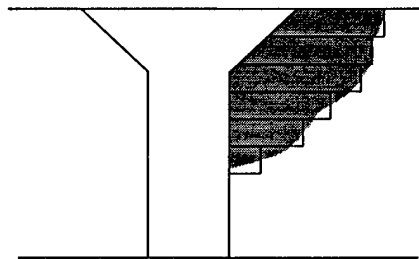


Figure 7.11 Pseudo 3-D modeling of a crack using slices

Since crack shape affects both the amplitude and the shape of the magnetic field, then this pseudo 3-D approach would be a better approximation to a real crack that has shape that varies with depth.

Ideal cracks versus real cracks and slots - The BEM measurement model assumes an ideal, perfectly insulating, and infinitely thin crack. This assumption will lead to differences between the model and measurements made on samples containing either wide cracks (slots) or real fatigue cracks. Most fabricated test samples used in our laboratory use slots, made by a saw or electrodischarge machining (EDM), to simulate cracks. A combination of a drilled hole with an EDM slot is an approximation to a crack emanating from an aircraft fastener hole. This is useful in preliminary analyses, especially for development of NDE techniques. Fabrication of test samples made this way is simple and controllable, making it easy to build a test set representing the range of conditions that are of interest. But, measurements with NDE instruments have shown that the instrument response from a slot is not necessarily the same as that from a fatigue crack of the same

size and geometry. Figure 7.12 schematically shows some of the possible variations, each possibly resulting in a different instrument response.

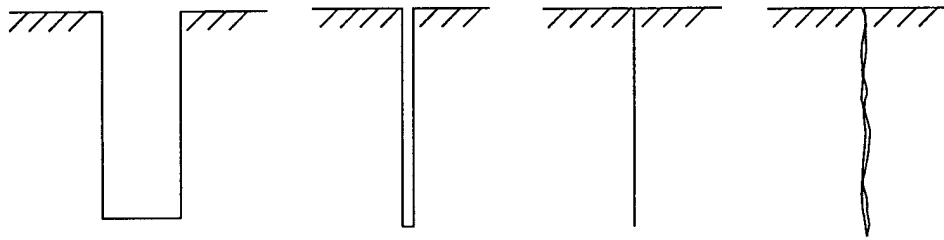


Figure 7.12 Slot profiles: (a) wide slot (b) narrow slot (c) ideal crack (d) real crack

The BEM measurement model simulates a closed crack that is electrically insulated along the entire length. We have shown that it provides a reasonable approximation to a thin slot for liftoffs appropriate for SQUIDs commonly used in the laboratory (> 3 mm). However, for real fatigue cracks, it is possible that crack closure may cause electrical conductivity across parts of the crack. Probability of detection will be strongly dependent on the effects of crack closure since, if current is flowing through the crack instead of around it, the signal (which is proportional to the perturbation of the current) will be greatly reduced. It is not yet understood how much crack closure effects current flow since it is likely that the oxide layers that form on the crack surfaces will act as an electrical insulator and so, only those contact points where the oxide layer is not present will provide conductive paths.

Additional current paths - The POD analysis has been based on simulated measurements of a crack emanating from a fastener *hole* and has completely ignored the effects of the fastener itself. This is most likely one of the larger sources of discrepancy present between the model and real measurement. Since most fatigue cracks start under the fastener head, early detection is difficult and usually the crack has to propagate beyond the fastener head before detection occurs. Another critical issue is that of contact between the fastener and the hole sides, which can create numerous current flow paths across and through the fastener. These currents may be too difficult to model directly and their associated uncertainty might have to be represented through a sample-related noise distribution. This will probably have to be determined experimentally by examining samples with holes alone and with fasteners inserted to quantify the effect on the magnetic signal.

Geometry factors - Current can also be greatly affected by the geometry of the surrounding structure, particularly edges such as lap joint seams. Figure 7.13 shows that edges can produce a large signal amplitude that can make flaw detection difficult, especially if the flaw is located near an edge. Image processing techniques can partially remove the background slope due to these edges but it is still difficult to extract the signal from a flaw that is near an edge. Edges and other geometrical factors (e.g., structural support members) affect the ability of the SQUID to detect a crack and these have not been taken into account in this POD analysis.

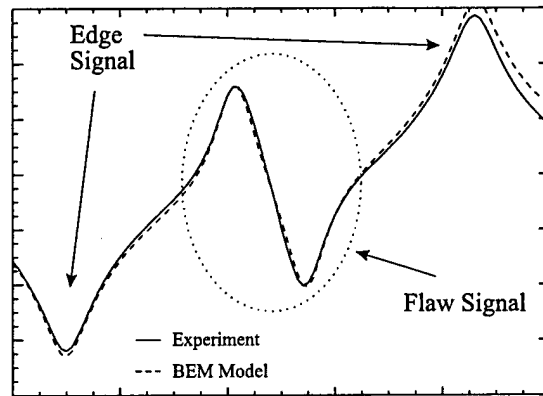


Figure 7.13 Magnetic map centerline profile pointing out edge and flaw signals.

Factors That May Increase POD Capability

Signal definition - The peak-to-peak value of the magnetic dipolar map is the present definition of “signal” used in these analyses. Peak-to-peak amplitude is a very limited use of the information available in the mapping since it reduces the entire 2-D image to a single value. It is the opinion of the author that image features (*e.g.*, shape and asymmetry) of the 2-D magnetic field map are just as important as the peak-to-peak signal amplitude in the detection and characterization of cracks, especially near fastener holes. For example, if we look at the magnetic map centerline profiles for various ideal geometries that have the same “cross sectional length” perpendicular to the current injection direction, we can see that using only peak-to-peak information for current perpendicular to the crack can lead to detection problems. The left-hand side of Fig. 7.14 shows the profiles for the current transverse to the crack at three different liftoffs for a 9 mm diameter hole, a 5 mm hole with a 4 mm crack, and a 9 mm crack. The signal values for each of the traces are plotted on the same scale and represent a SQUID system using 3 mm pickup/balance coils with a 3 cm baseline. From this information, all the profiles look the same in that they are dipolar with a mostly symmetrical shape. Based on peak-to-peak amplitude in a single direction, we can not distinguish between a crack alone, hole alone, or a hole-with-crack combination unless a baseline signal amplitude can be established as was done earlier in this POD analysis using the signal associated with a 5 mm hole alone. However, this approach would not work here since the 5 mm hole is not a constant feature in all three geometries.

The rotating current schemes take advantage of the differing two-dimensional structure of these three geometries. By rotating the current direction, the signals associated with a crack will go through a maximum (when the current is perpendicular to the crack) and a minimum (when the current is parallel to the crack). A hole alone will not show this cyclic behavior (unless it is out-of-round). On the right-hand side of Fig. 7.14 are the corresponding profiles when the current is parallel to the crack showing the 9 mm crack having a flatline (zero signal) and the 5 mm hole with a 4 mm crack having a signal corresponding to a 5 mm hole alone and the 9 mm hole is unchanged. In this way, the three geometries could be distinguished by a measure of their peak-to-peak difference at the two current injection directions, with the crack alone being the largest, the hole-with-crack combination the next largest, and the hole alone having no difference. Real fatigue cracks will have some small signal for current injected parallel to the crack (versus zero signal for the ideal cracks of Fig. 7.14) but will still show the same maximum/minimum behavior as a

function of current injection direction (the signal difference will just be smaller than the ideal crack case).

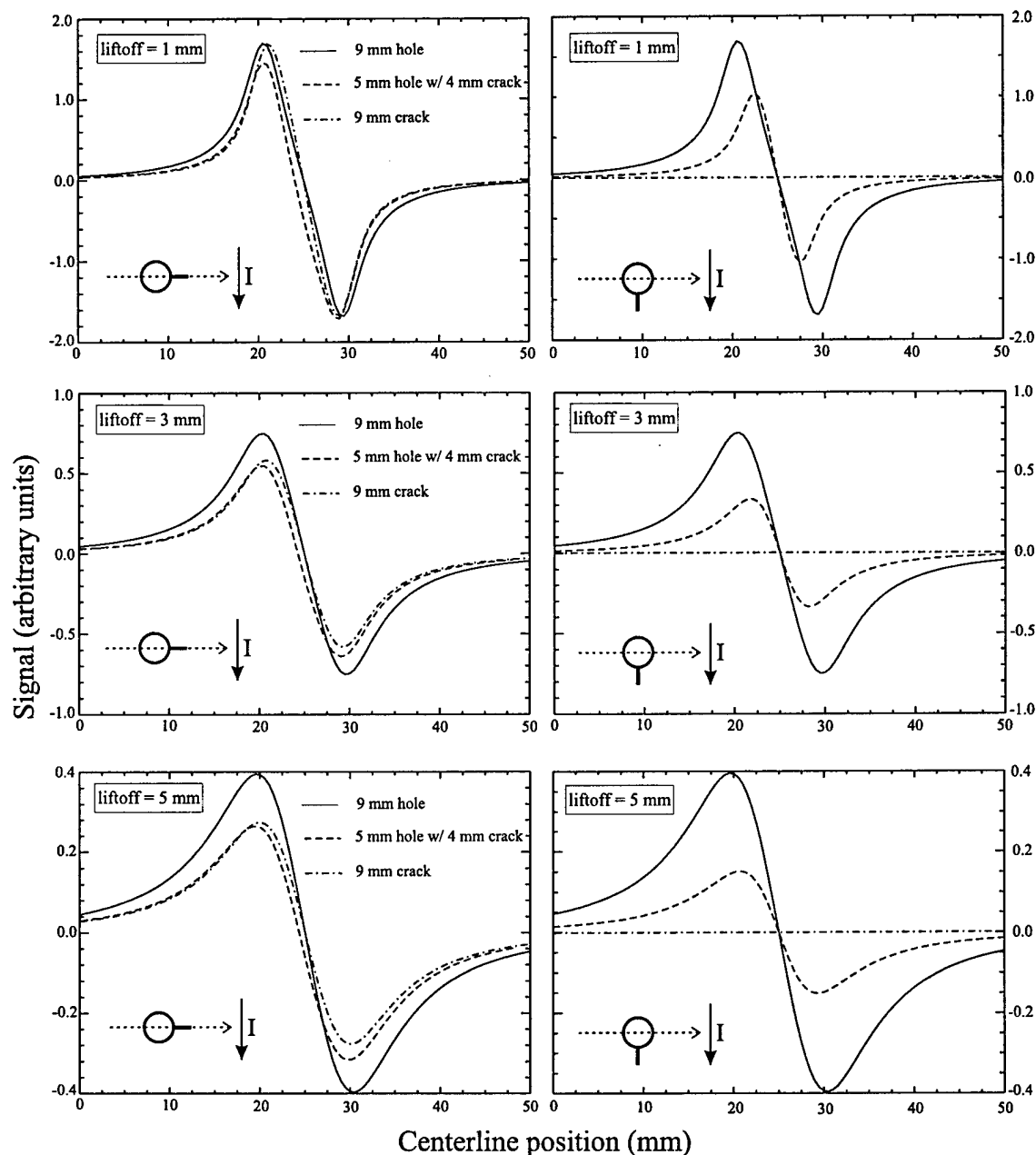


Figure 7.14 Profiles for three 9-mm "cross section" geometries at varying liftoffs (Note: all profile traces are on the same scale).

SQUID NDE systems will have to use asymmetry measures (which includes the rotating current direction technique) for crack detection, especially for cracks originating from fastener holes. If the asymmetry technique is used only to find the maximum and minimum of the signal, then POD may still be determined primarily from peak-to-peak amplitudes. However, if additional measures of asymmetry (*e.g.*, eccentricity or other shape factors) are to be used, then POD analyses must

incorporate these measures into the standard peak-to-peak analysis to reflect the true capability of the system. This is an important topic to be addressed for future development of SQUID POD methodologies.

Conclusions

A measurement model using boundary element methods has been constructed simulating a SQUID magnetometer being scanned over a dc-current injected, finite plate containing an ideal (*i.e.*, straight, infinitely thin, and perfectly insulated) crack. The model was used to examine the effect of system parameter (scan resolution, plate thickness, pick-up coil liftoff, and pick-up coil tilt angle) variability on flaw detection. The results of this sensitivity analysis were then combined with empirical noise distributions to determine probability of detection. A goal in this research was to develop a method where simulation represents the experimental approach, is cheaper and faster, and identifies sources of unreliability in SQUID NDE.

This POD analysis resulted in minimum detectable crack lengths corresponding to 90% probability of detection at 95% confidence of 1.4 mm for the dc-measurement and 0.0134 mm for the ac-measurement. The very small minimum detectable crack length determined for the ac-measurement is due to the large noise reduction through use of the lock-in amplifier in this type of measurement. . However, there is a large discrepancy between experimental measurements on real fatigue cracks and the results of this analysis. If the model is to be used to calculate realistic probability of detection values for SQUID systems, more work has to be done to quantify additional sources of noise to be incorporated into the analysis. Some of the possible sources of this noise have been discussed but no work has been done as of yet to quantify their effects.

The BEM measurement model has already been used in other experimental work involving validation and calibration techniques. The model is just now beginning to be used for POD work, which was what it was originally designed for, and continued development will improve the model as a tool for SQUID NDE development and capability measurement.

3. Personnel Supported:

Thomas A. Cruse, H. Fort Flowers Professor of Mechanical Engineering

Anthony Ewing, Graduate Student, Mechanical Engineering

John P. Wikswo, A.B. Learned Professor of Living State Physics, Professor of Physics

4. Publications and Related Items:

Journal Articles

"Imaging of Small Defects in Nonmagnetic Tubing Using a SQUID Magnetometer," D.C. Hurley, Y.P. Ma, S. Tan, and J.P. Wikswo, Jr., Research in Nondestructive Evaluation, 5: 1-29 (1993).

"An Improved Method for Magnetic Identification and Localization of Cracks in Conductors," J.P. Wikswo, Jr., D.B. Crum, W.P. Henry, Y.P. Ma, N.G. Sepulveda, and D.J. Staton, Journal of Nondestructive Evaluation, 12(2): 109-119 (1993).

Conference Proceedings:

"Imaging Subsurface Defects Using SQUID Magnetometers," Y.P. Ma and J.P. Wikswo, Jr., Review of Progress in QNDE, 12: 1137-1143 (1993).

"Superconducting Magnetometry: A Possible Technique for Aircraft NDE," J.P. Wikswo, Jr., Y.P. Ma, N.G. Sepulveda, D.J. Staton, S. Tan, and I.M. Thomas, Nondestructive Inspection of Aging Aircraft, M.T. Valley, N.K. Grande, and A.S. Kobayashi, Eds., SPIE Proceedings, Vol. 2001, pp. 164-190 (1993) (invited).

"Detection of Subsurface Flaws Using SQUID Eddy Current Technique," Y.P. Ma and J.P. Wikswo, Jr., Nondestructive Inspection of Aging Aircraft, M.T. Valley, N.K. Grande, and A.S. Kobayashi, Eds., SPIE Proceedings, Vol. 2001, pp. 191-199 (1993).

"Design Considerations For Magnetic Imaging with SQUID Microscopes and Arrays," J.P. Wikswo, Jr., International Superconductive Electronics Conference, pp. 189-190 (1993).

"SQUID Eddy Current Techniques for Detection of Second Layer Flaws," Y.P. Ma and J.P. Wikswo, Jr., Review of Progress in QNDE, 13: 303-309 (1994).

"A SQUID NDE Measurement Model Using BEM," A.P. Ewing, T.A. Cruse, and J.P. Wikswo, Jr., Review of Progress in QNDE, 17A: 1083-1090 (1998).

"Boundary Integral Equations for Modeling Arbitrary Flaw Geometries in Electric Current Injection NDE," A.P. Ewing, C. Hall Barbosa, T.A. Cruse, A.C. Bruno, and J.P. Wikswo, Jr., Review of Progress in QNDE, 17A: 1011-1015 (1998).

"Measurements of Surface-Breaking Flaws in Steel Pipes Using a SQUID Susceptometer in an Unshielded Environment," C. Hall Barbosa, A.C. Bruno, G.S. Kühner, J.P. Wikswo, Jr., A.P. Ewing, Y.P. Ma, and C.S. Camerini, Review of Progress in QNDE, 17A: 1091-1097 (1998).

"SQUID Magnetometers for Depth-Selective, Oriented Eddy Current Imaging," Y.P. Ma and J.P. Wikswo, Jr., Review of Progress in QNDE, 17A: 1067-1074 (1998).

Theses/Dissertations

"SQUID NDE and POD Using a BEM Measurement Model," Anthony Ewing, Ph.D., Mechanical Engineering, 1997.

5. Interactions/Transitions:

None

6. New discoveries, inventions, or patent disclosures:

None

7. Honors/Awards:

None

APPENDIX 1

Techniques for Depth-Selective, Low-Frequency Eddy Current Analysis for SQUID-Based Nondestructive Testing

Yu Pei Ma¹ and John P. Wikswa, Jr.¹

Received April 30, 1995; revised August 13, 1995

Conventional eddy current techniques are widely used for detection of surface-breaking cracks in metal structures. These techniques have limited success in the detection of deep, nonsurface-breaking flaws that require low frequency eddy currents, for which inductive pick-up probes have drastically reduced sensitivity. High resolution, Superconducting QUantum Interference Device (SQUID) magnetometers, which are very sensitive to dc or low frequency magnetic fields, have been developed for detection of subsurface flaws. We have now extended SQUID NDE by utilizing a sheet inducer to produce an extended eddy current parallel to the surface in a conducting plate. The magnitude of the induced current density inside the plate reduces with the depth; however, the current component at a certain phase angle may increase with the depth. At a particular phase angle, the current density on the surface becomes zero, while the current inside the plate is large, so that the magnetic signal at that phase angle due to the surface structures can be minimized. With this method, we have detected simulated cracks in the sides of plugged holes in a thick plate, a hidden corrosion area in a specimen which consisted of two painted aluminum plates joined with sealant, as well as crack defects adjacent to fasteners in the second layer of lap-joined aluminum plates. We present a theoretical model for simulation of the phase-related magnetic signal due to a flaw, which shows the relation between the phase angle and the depth of the flaw. The theoretical phase analysis is compared with the experimental results.

KEY WORDS: Eddy current; SQUID magnetometer; phase analysis; sheet inducers; deep flaws.

1. INTRODUCTION

Conventional eddy current techniques, which are very sensitive for detecting surface-breaking cracks in metal structures, have been studied and developed extensively for many years. Because of the frequency-dependent penetration depth of eddy currents, the detection of deep, nonsurface-breaking flaws requires very low frequency eddy currents. However, the key parameters measured by eddy current probes, typically the secondary voltage induced in the pick-up coil or the impedance change of the probe that result from eddy currents in-

duced in the conductor by the primary coil, are proportional to the frequency of the magnetic field to be measured. Hence the sensitivity and the signal-to-noise ratio are suppressed drastically at the low frequencies that are required for detection of subsurface cracks.

As an alternative electromagnetic approach, ac field techniques have been developed during the past decade.⁽¹⁾ Instead of inductively coupling the electromagnetic field above the metal surface as in eddy current methods, the differences in surface electric potential due to a current injected or induced inside the metal are measured by using two electrodes in direct contact with the metal surface.⁽²⁾ Because the current disturbed by the flaw is constrained largely within a region of dimensions comparable to those of the flaw, the flaw may not disturb the surface potential significantly, even at a low enough

¹ Electromagnetics Laboratory, Department of Physics and Astronomy, Vanderbilt University, Box 1807 Station B, Nashville, Tennessee 37235.

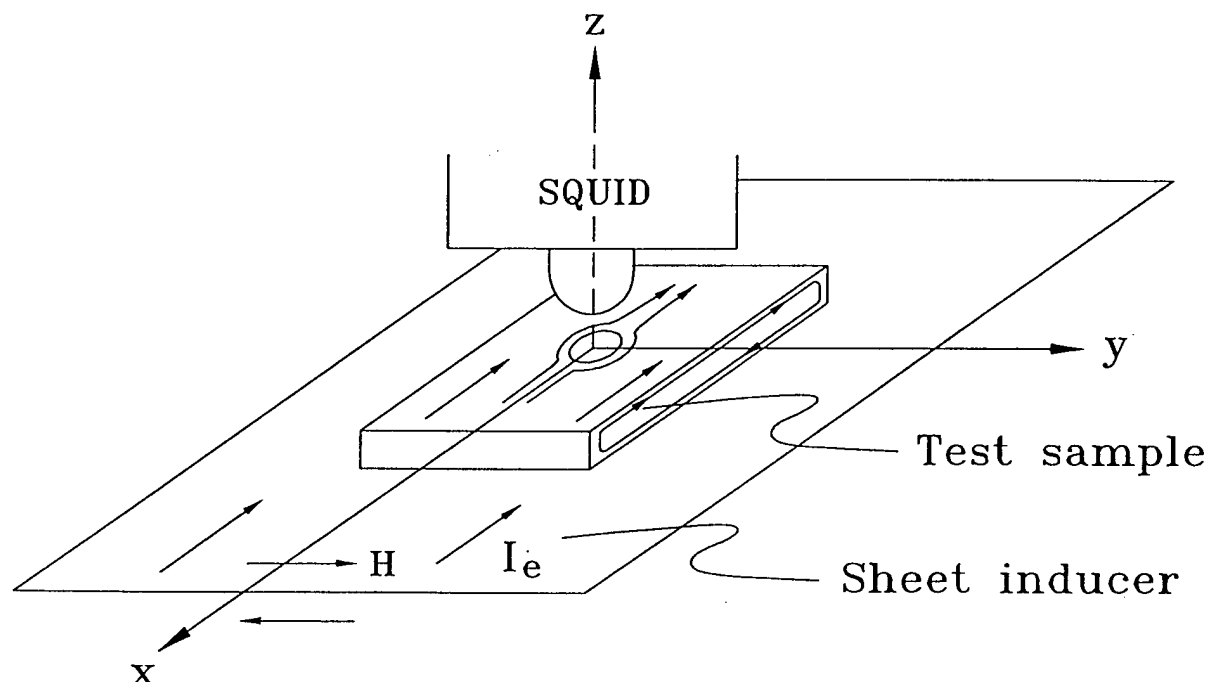


Fig. 1. A sheet inducer, carrying an excitation current along the x direction, is placed beneath a test plate with a flaw at the center. The induced eddy current disturbed by a flaw produces a magnetic signal which is detected by the SQUID magnetometer located above the sample.

frequency, if the distance between the flaw and the surface is larger than the dimensions of the flaw. Thus, the detectability of subsurface flaws is limited. This technique is only suitable for a conducting object with a smooth conducting surface.⁽²⁾

A modified inducing mechanism for the eddy current technique, which consists of two parallel U-shaped wires, has been devised to simplify the complicated calibration procedure in the ordinary eddy current method,⁽³⁾ but this inductive approach is as yet limited to surface-breaking cracks in ferromagnetic materials.

High resolution SQUID (Superconducting QUantum Interference Device) magnetometers, which are very sensitive to dc and low frequency magnetic fields, have been developed and used for the detection of flaws in nonferromagnetic conductors.⁽⁴⁻⁷⁾ By injecting a spatially uniform current (dc or low frequency ac) into a conductor, and measuring the magnetic field normal to the surface, subsurface flaws can be detected.⁽⁸⁾ The magnetic field near the surface due to a subsurface flaw is dependent not only on the surface current distribution, as is the case in ac field measurements, but also on the total current disturbed by the flaw inside the conductor.

In several circumstances, such as a conductor covered by an insulation layer, it is difficult to inject current.

In these cases, induced eddy currents may be used instead of injected current for SQUID NDE. In contrast to the conventional eddy current probe, the amplitude of the output signal of the SQUID is independent of the frequency of the field measured, so extremely low frequency (ELF) eddy current measurements are feasible.

The small, coil-like surface probes used in most eddy current techniques induce localized eddy currents circulating inside the extended conductors, for which the effective penetration length may be less than the standard penetration depth. While increasing the diameter of the probe coil may improve the penetration, it also reduces the spatial resolution and hence complicates the detection of small cracks. In addition, the coil-like surface probe produces a large magnetic field in the direction normal to the surface. This type of excitation coil is disadvantageous for a SQUID magnetometer, whose pick-up coil is typically sensitive to the field component normal to the surface, since the magnetic signals due to the current disturbed by flaws in a conductor are difficult to distinguish from the large field background resulting from the large eddy currents circulating beneath the excitation coil.

We have now extended SQUID NDE by utilizing a sheet inducer, as shown schematically in Fig. 1, to

produce an extended eddy current parallel to the surface of a conducting plate, which is similar to the method used with the Magneto-Optic/eddy current Imager (MOI).⁽⁹⁾ In this paper, we present the theoretical calculation of the eddy current density inside a plate with finite thickness induced by a sheet inducer. The induced current distribution inside the plate depends on the frequency, the thickness of the plate and the phase relative to the excitation current. The magnetic signal due to the eddy current disturbed by a flaw in the plate depends upon the depth of the flaw, the phase angle and the frequency. At certain phase angles, the current density below the surface is much larger than that at the surface, so that the magnetic signal due to the surface structures can be reduced and the signal due to the subsurface flaw enhanced by choosing an appropriate frequency and phase angle.

For a SQUID that measures the vertical component of the magnetic field, we need consider only the horizontal components of the current in the test plate. As shown in Fig. 1, the horizontal currents induced in the plate flow in opposite directions at the upper and lower surfaces; by symmetry, the horizontal currents must be zero in the plane midway between these two surfaces, regardless of phase angle. As we will show in this paper, at certain phase angles there can be two additional horizontal planes for which the horizontal currents are zero. This in turn implies that at these phase angles there will be four depth zones for which the induced currents flow in a direction opposite to that in the adjacent zones. As a result, the magnetic signals from two flaws in adjacent zones will have opposite signs, and hence the sign of the signal at particular phase angles conveys depth information.

For flaws located at depths near the transition regions, where the magnetic signal changes its polarity, the dipolar signal typical of planar dc current being deflected by a flaw^(5,10) becomes quadrupolar, and is hence noticeably different. The phase-related amplitude and the separation between the maximum and the minimum of the signal provide important information about the location and the depth of the flaw.

To verify the phase analysis, we measured the magnetic signal due to the slots inside a thick aluminum plate and compared our results with the theoretical calculation. With this method, we have detected both hidden corrosion damage in a specimen which consists of two heavily painted aluminum plates, and crack defects adjacent to fasteners in the bottom layer of lap-joined aluminum plates.

2. THEORY

2.1. The Eddy Current Distribution in a Conducting Plate

For a homogeneous extended conductor placed in a time-varying external magnetic field, with a frequency that is low enough that displacement currents and finite propagation velocity effects can be neglected, the induced magnetic field \vec{H} inside the conductor is given by⁽¹¹⁾

$$\nabla^2 \vec{H} - \mu\sigma \frac{\partial \vec{H}}{\partial t} = 0 \quad (1)$$

where μ is magnetic permeability and σ is electric conductivity of the conductor, both of which are uniform and constant. At the boundary surface of the conductor, the tangential component of \vec{H} and the normal component of \vec{B} are continuous, where $\vec{B} = \mu\vec{H}$. The solution to Eq. (1) depends upon the geometry of the boundary of the conductor.

We will first consider the simple example of a conductor that is of infinite extent in the xy direction with its boundary surface in the xy -plane. External to the sample, we apply a magnetic field, H_y , that is uniform, harmonically varying, parallel to the boundary, and in the y direction,

$$H_y = H_0 e^{i\omega t} \quad (2)$$

where H_0 is the magnitude of the external field and $\omega = 2\pi f$ is the angular frequency. For linear media, the magnetic field, H_y , inside the conductor is only in the y direction, and Eq. (1) becomes

$$\frac{\partial^2 H_y}{\partial z^2} - i\omega\mu\sigma H_y = 0 \quad (3)$$

where H_y is the induced field.

If the conductor is also of infinite extent in the positive z direction, as shown in Fig. 2a, the solution of Eq. (3) is well known⁽¹¹⁾

$$H_y = H_0 e^{-z/\delta} e^{i(\omega t - \frac{z}{\delta})} \quad (4)$$

where

$$\delta = \sqrt{\frac{2}{\omega\mu\sigma}} \quad (5)$$

is termed the skin depth or the standard depth of penetration, which depends on the frequency of the external field and the electric and magnetic properties of the con-

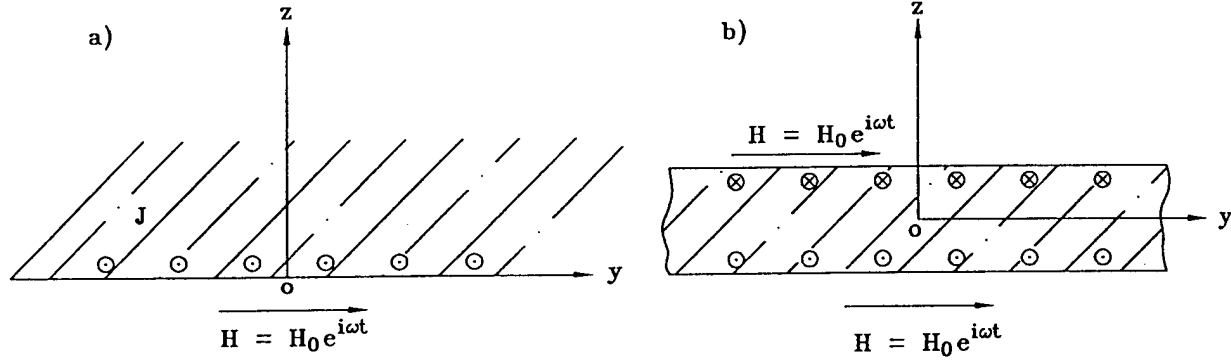


Fig. 2. The coordinate system for (a) a semi-infinite extended conductor, and (b) an infinite extended conducting plate with a finite thickness in a uniform external magnetic field. The circles with a central dot represent induced current coming out of the pages, while those with a cross represent current entering the page.

ductor. The amplitude of the magnetic field within the conductor decreases exponentially with (z/δ) . By using Ampere's law in differential form,

$$\vec{J} = \nabla \times \vec{H} \quad (6)$$

we can write the induced eddy current as

$$J_x = -\frac{\partial H_y}{\partial z} = \frac{\sqrt{2}H_0}{\delta} e^{-z/\delta} e^{i(\omega t + \frac{\pi}{4} - \frac{z}{\delta})} \quad (7)$$

which is in the x direction and is uniform in the xy plane. The amplitude of the current density decreases exponentially with (z/δ) , as does the magnetic field within the conductor. At the surface of the conductor, i.e., $z = 0$, the phase of the current density leads the external field by $\pi/4$, and decreases as (z/δ) .

If instead the conductor is a plate with finite thickness, as in Fig. 2b, the magnetic field inside the plate can be derived from Eq. (3) by using the symmetry with respect to z

$$H_y = H_0 \frac{e^{(1+i)z/\delta} + e^{-(1+i)z/\delta}}{e^{(1+i)d/\delta} + e^{-(1+i)d/\delta}} e^{i\omega t} \quad (8)$$

where $2d$ is the thickness of the plate.

Substituting Eq. (8) into Eq. (6), we find that the induced eddy current inside the plate is

$$J = J_x e^{i\omega t} \quad (9)$$

where

$$J_x = \frac{H_0}{\delta} \frac{e^{(1+i)z/\delta} - e^{-(1+i)z/\delta}}{e^{(1+i)d/\delta} + e^{-(1+i)d/\delta}} (1+i) \quad (10)$$

Then the real and imaginary parts of J_x may be obtained from Eq. (10) as

$$J_{\text{real}} = \frac{H_0}{\delta} (R_e - I_m) \quad (11)$$

$$J_{\text{imag}} = \frac{H_0}{\delta} (R_e + I_m) \quad (12)$$

where

$$R_e = \frac{\cos\left(\frac{d-z}{\delta}\right) \sinh\left(\frac{d+z}{\delta}\right) - \cos\left(\frac{d+z}{\delta}\right) \sinh\left(\frac{d-z}{\delta}\right)}{\cos\left(\frac{2d}{\delta}\right) + \cosh\left(\frac{2d}{\delta}\right)} \quad (13)$$

$$I_m = \frac{\sin\left(\frac{d-z}{\delta}\right) \cosh\left(\frac{d+z}{\delta}\right) - \sin\left(\frac{d+z}{\delta}\right) \cosh\left(\frac{d-z}{\delta}\right)}{\cos\left(\frac{2d}{\delta}\right) + \cosh\left(\frac{2d}{\delta}\right)} \quad (14)$$

The eddy current density depends not only on the depth in the plate and the frequency of the external field, but also upon the thickness of the plate, or the ratio of the thickness to the penetration depth $(2d/\delta)$. As we stated earlier, its distribution is antisymmetric about the center plane of the plate ($z = 0$) so that \vec{J} is zero for $z = 0$.

2.2. Sheet Inducer

In principle, a current sheet of infinite extent produces a spatially uniform magnetic field, which will induce an eddy current with a well-defined direction inside a conducting plate that is parallel to the current sheet. As shown in Fig. 1, a conducting sheet in the xy plane

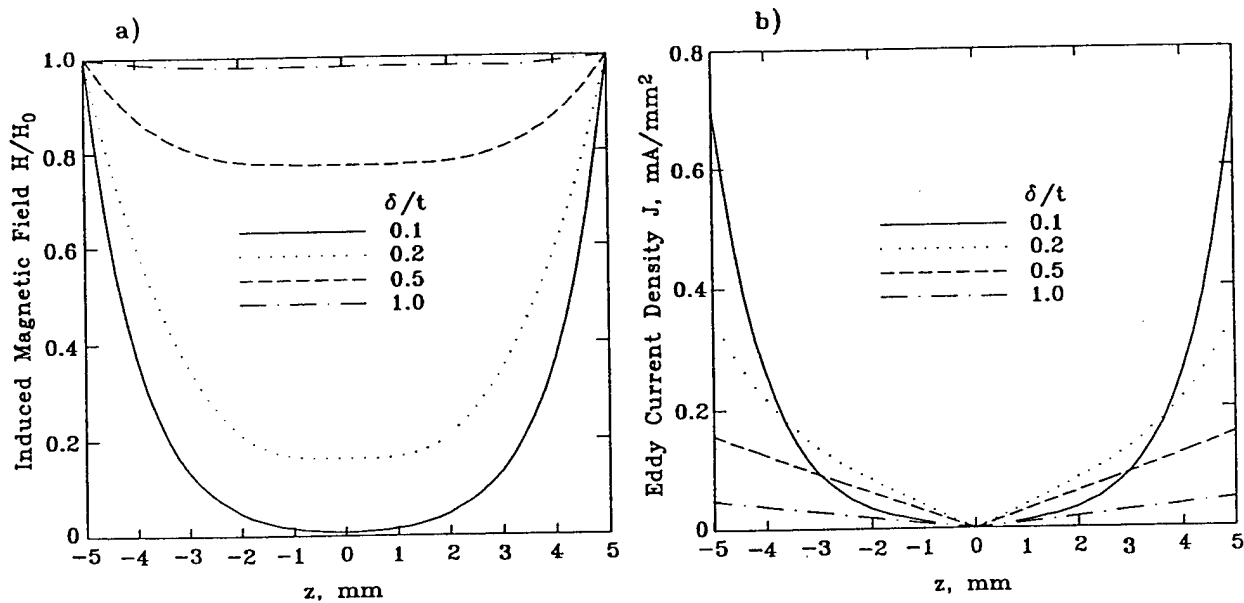


Fig. 3. The magnitude of the magnetic field and current density inside a 10-mm thick conducting plate for the ratio of skin depth to sample thickness δ/t of 0.1, 0.2, 0.5, and 1.0 and a sheet-inducer excitation current of 1.0 mA/mm. (a) The magnitude of the induced magnetic field distribution, normalized by the external field H_0 . (b) The magnitude of the induced eddy current density distribution.

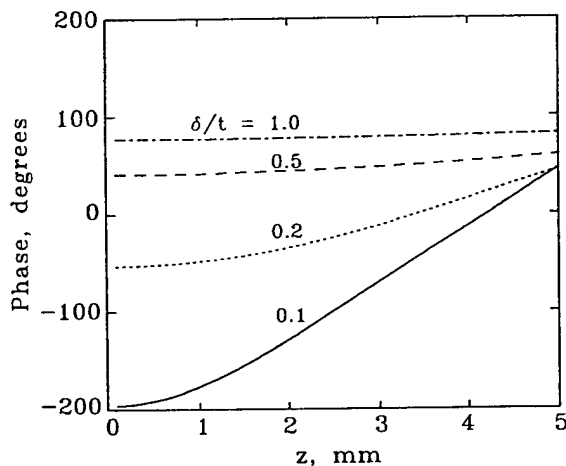


Fig. 4. The phase of the eddy current with respect to the excitation current (see Fig. 2) inside a 10-mm thick conducting plate for the ratio of skin depth to the thickness δ/t of 0.1, 0.2, 0.5, and 1.0. The origin $z = 0$ is at the center of the plate and $z = 5$ is the top surface of the plate. For $z < 0$, the phase is shifted by 180° with respect to the phase at $z > 0$.

that carries a uniform current along the $-x$ direction produces a magnetic field along the y direction if the edge effect is neglected. In the limit of a sheet inducer of infinite extent in the xy plane, the magnetic field strength is independent of z . The magnitude of the field

is $H_0 = I/2$, where I is the excitation current per unit width.

Figure 3 shows the magnitudes of the magnetic field and the induced eddy current density as a function of z inside the plate, calculated from Eqs. (8) and (10) for $\delta/t = 0.1, 0.2, 0.5$, and 1.0 , where δ is the standard penetration depth given in Eq. (5), and $t = 2d = 10$ mm is the thickness of the plate. In Fig. 3a, the magnetic fields have been normalized by the external field H_0 . Figure 3b shows the magnitude of the current densities calculated when the excitation current density per unit width of plate, I_{exc} , is 1.0 A/m. The origin is taken at the center plane of the plate, as shown in Fig. 2b.

At higher frequencies, where $\delta \leq 0.1t$, the current density reduces to $1/e$ of surface current density at the depth δ (see the solid line in Fig. 3b), which is similar to the case of the semi-infinite extended conductor. At lower frequencies, where $\delta \geq 0.5t$, the induced eddy current density reduces linearly with the depth. In this case, the actual penetration length is larger than the standard penetration depth δ . In fact, increasing δ/t , i.e., reducing the frequency, beyond this point would not increase the actual penetration length of the induced current into the plate but would simply reduce the magnitude of the eddy current density. At the center plane of the plate, $z = 0$, the current density vanishes, while the magnetic field remains nonzero. The phase of the induced current den-

sity relative to the excitation current depends on the depth and (δ/t) , as shown in Fig. 4, which is for the upper half plate ($z > 0$) only. At $z < 0$, the phase changes by π with respect to the phase at $z > 0$.

In practice, the dimensions of the conducting plate being tested (the test plate) and the conducting sheet carrying the current for exciting the eddy current (the sheet inducer) are both finite. If it is desired to reduce the effect of the edge of the inducer, the width of the sheet inducer should be much larger than both the distance between the inducer and the test sample, and the width of the region of test object being examined.

It should be noted that there is a mutual inductance between the sheet inducer and the test sample. The disturbance in the eddy current arising from a flaw or other inhomogeneity in the test sample may induce a secondary eddy current inside the sheet inducer, and thereby distort the excitation current. When the thickness of the sheet inducer is very thin as compared to the penetration depth in the sheet inducer, the secondary eddy current should be very small and may be neglected.

2.3. The Magnetic Field Due to a Flaw in a Plate

A large sheet carrying a uniform excitation current produces a magnetic field that is parallel to the surface, except near the edges of the sheet. Inside a large, homogeneous unflawed test plate far away from the edges, the induced eddy current is uniform in any plane that is parallel to the surface.

In our previous work, we calculated and measured the normal component of the magnetic fields due to a uniform dc current injected into a two- or three-dimensional conductor that contains flaws.^(5,8,10) (Our SQUID magnetometer⁽¹²⁾ measures the normal component, i.e., B_z , and hence we will limit our discussion to B_z .) All the dc magnetic signals shown in xy maps of B_z have a bi-phasic shape, i.e., one maximum and one minimum on a line that passes above the flaw and is perpendicular to the direction of the applied current. For small insulating, cylindrical or spherical flaws, the field pattern is the same as that of a current dipole antiparallel to the injected current, and will hereafter be referred to as a dipolar field pattern.

For dc currents in conductors with a homogeneous conductivity, the volume integral in the law of Biot and Savart that is used to calculate the magnetic field can be replaced by an integral over all surfaces s' , including that of the flaw^(5,10)

$$\vec{B}(\vec{r}) = \frac{\bar{\mu}_0}{4\pi} \int_{s'} \frac{\vec{J}(\vec{r}') \times \hat{n}}{|\vec{r} - \vec{r}'|} ds' \quad (15)$$

where $\bar{\mu}_0 = 4\pi \times 10^{-7} \text{H/m}$, \hat{n} is a unit vector normal to the bounding surface and in the outward direction from the region occupied by the current density. For a conducting plate with a flaw, the surfaces s' include not only the top and bottom surfaces of the plate, but also the surface of the flaw. Because the normal vector, \hat{n} , for the plate surfaces is in the z direction, these surfaces do not contribute to B_z , and the measured magnetic signal arises only from the current at the flaw surface. Either analytic or numerical methods can be used to calculate this current and the resulting magnetic field.^(5,10)

In contrast to the dc current, which is uniform through the plate, the amplitude and the phase of the eddy current density disturbed by the flaw vary with the depth of the flaw, and thus the expressions for the magnetic field due to eddy currents that have been disturbed by a flaw are more complicated. When the geometry of the flaw is not the function of z , such as a cylinder or a slot with a flat bottom, the currents at the surface of the flaw flow primarily within the xy plane. We may then utilize our solution for an elliptic cylinder in a plate carrying a dc current⁽¹³⁾ to simulate the magnetic field due to a similar flaw in a plate carrying an eddy current. Instead of the uniform dc current, we use the local, instantaneous eddy current density given by Eqs. (11–14), which is a function of depth and phase. We neglect the skin-depth effect at the surface of the flaw, and any curl in the eddy currents other than that at the flaw surface.

2.4. Phase Analysis

It is well known that the magnitude of the eddy current density reduces monotonically with depth toward the center of the plate, as shown in Fig. 3b. However, the current density at a specific phase angle with respect to the excitation current will exhibit a more complicated behavior. For example, the calculated eddy currents at phase angles ϕ of 0° , 45° , 85° , and 135° inside a 12.6-mm thick aluminum plate without a flaw are shown in Figs. 5a–d, where the excitation current density is 0.1 mA/mm. A skin depth δ of 2.4 mm was used for this calculation, which implies that the frequency of the excitation current is about 2.5 kHz for 7075 aluminum alloy. The vertical axis is the induced eddy current density with units of mA/mm².

Figure 5a shows that the in-phase component is positive on the upper surface of the plate ($z = 6.3$ mm), with an amplitude that reduces to zero at the center of

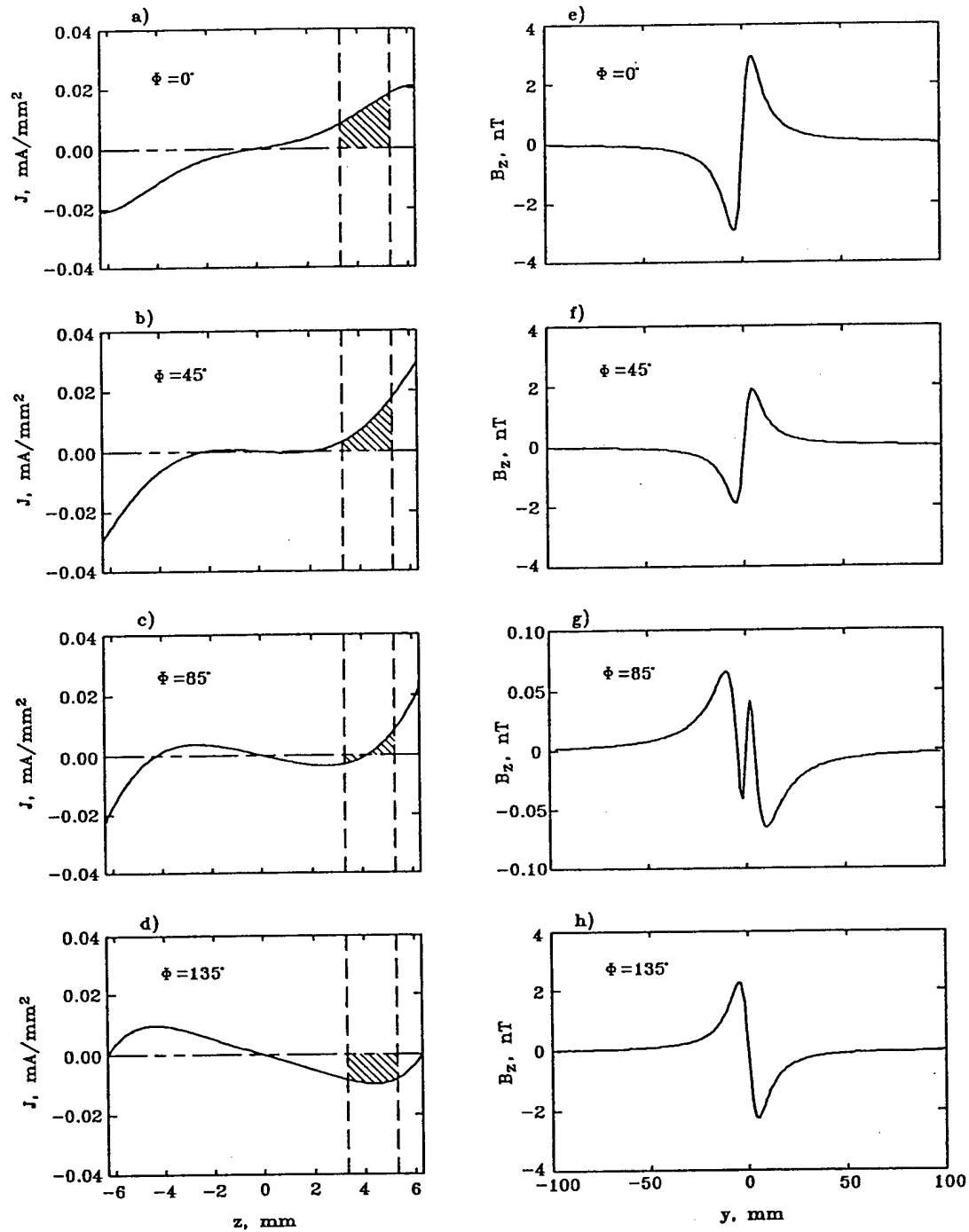


Fig. 5. The calculated eddy current at several phase angles: (a) $\phi = 0^\circ$, (b) $\phi = 45^\circ$, (c) $\phi = 85^\circ$, and (d) $\phi = 135^\circ$ inside a 12.6-mm thick aluminum plate without a flaw, and the simulated magnetic signal at the same phase angles: (e) $\phi = 0^\circ$, (f) $\phi = 45^\circ$, (g) $\phi = 85^\circ$, and (h) $\phi = 135^\circ$ due to an 8-mm diameter void with a vertical extent of 3 mm whose upper surface is located 1 mm below the surface of the plate. The excitation current density is 0.1 mA/mm . The standard penetration depth $\delta = 2.4$ mm was used for this calculation, which implies that the frequency of the excitation current is about 2.5 kHz for 7075 aluminum alloy. The vertical axis is the induced eddy current density with units of mA/mm^2 . The current densities disturbed by the hole are shown by the shaded areas in (a)–(d), where the dashed vertical lines indicate the upper and lower ends of the hole.

the plate, and then changes polarity. At $\phi = 45^\circ$ in Fig. 5b, the value of induced current density at the surface becomes larger, and then reduces to zero at 4 mm below the surface. At $\phi = 85^\circ$ in Fig. 5c, the positive current density at the surface becomes smaller, while the negative current density beneath the surface becomes larger, and reaches a maximum value at 3 mm below the surface. At $\phi = 135^\circ$, as shown as in Fig. 5d, the current density at the surface of the plate becomes zero, while the current beneath the surface essentially penetrates through the whole plate with a local null at the center plane of the plate. The ability to control the depth at which the current density becomes relatively larger is a potentially useful means to adjust depth sensitivity and to search preferentially for nonsurface-breaking flaws.

To examine how the depth dependence of the current at a particular phase angle affects the magnetic signature of a flaw, we will first consider a cylindrical void (i.e., zero conductivity) that is 8 mm in diameter and 3 mm tall, and whose upper end is 1 mm below the surface of the plate. The current densities disturbed by the void are shown by the shaded areas in Figs. 5a–d, where the dashed vertical lines indicate the location of the cylinder ends. Figures 5e–f show the simulated magnetic signal at 3 mm above the surface of the plate due to the void at the phase angles $\phi = 0^\circ, 45^\circ, 85^\circ$, and 135° as determined by the current densities shown in Figs. 5a–d, respectively. The dipolar signals in Figs. 5a and b are primarily the result of the large positive current near the surface. Figure 5c, where $\phi = 85^\circ$, shows that the negative subsurface current within the depth of the void becomes comparable with the positive current near the surface, which produces an additional biphasic signal with opposite polarity but with a different peak-to-peak spacing. Thus the dipolar signal splits to one with four extrema (quadrupolar), as shown in Fig. 5g, that is noticeably different from the simple biphasic signal obtained by injecting a dc current. Obviously, the sharper peak is due to the positive current near the surface. At $\phi = 135^\circ$, the quadrupolar signal becomes a dipolar signal again (Fig. 5f), with reversed polarity due to the negative current density below the surface (see Fig. 5d).

For the qualitative analysis of flaw signals, there are two important parameters: the amplitude of the signal and the separation between its minimum and the maximum. In the case of an injected dc current, the amplitude of the magnetic signal, which is proportional to the current density, increases with the size of the flaw and depends on the orientation of the flaw respect to the current.^(10,13) The separation between the maximum and minimum of the dipole signal is equal to $\sqrt{2}z_0$, where z_0 is the distance between the flaw and the sensor, which

is valid only if the linear dimensions of the flaw are much smaller than z_0 .⁽¹⁰⁾ When one or more dimensions of the flaw are much larger than z_0 , the separation of the two peaks can also depend on the shape and dimensions of the flaw, as has been discussed elsewhere.⁽¹³⁾

In the case of an induced eddy current, the current density distribution is a function of both depth and phase, so that the qualitative analysis of the magnetic signal becomes more complicated. The amplitude of the dipolar signals in Figs. 5e–h changes with the phase, and depends on the value of the shaded area in Figs. 5a–d, respectively. As a consequence, the phase at which the quadrupolar signal appears and disappears (transition region) for a fixed frequency depends upon the depth and geometry of the flaw. In addition, the separation between the maximum and the minimum varies with the phase.

As an example, we have calculated the phase-related amplitude (taken from the larger peak for the quadrupolar signal) and the separation between the maximum and minimum of the magnetic signals from slots with various dimensions at several locations in a 12.6-mm thick aluminum plate. We chose an excitation current density of 0.1 A/m, and a standard penetration depth of 2.4 mm, which implies a frequency of 2.5 kHz for 7075 aluminum alloy. The dimensions and the locations of the slots used for calculation are listed in Table I (for Fig. 6) and Table II (for Fig. 7), where a , b , and h are the length, width, and height of the slot, respectively. As shown in Fig. 6a, the depth D is taken as the distance between the top surface of the plate and the top of the slot. Figure 6b shows the amplitude of the signal for the slots at $D = 0$ (solid line), $D = 1$ mm (dotted line), and $D = 2$ mm (dashed line). The amplitude is minimum at a phase angle (ϕ_{\min}) of 121° for the slot at $D = 0$, 99° for the slot at $D = 1$ mm, and 75° for the slot at $D = 2$ mm. At most phase angles, the amplitude of the signal due to the surface breaking slot ($D = 0$ mm) is larger than those due to the subsurface slots. However, between $\phi = 115^\circ$ and 140° , the subsurface slots produce larger signals than does the surface slot, demonstrating that this technique is useful for enhancing the signal due to subsurface flaws and reducing the background signal due to surface structures.

The baseline value of the separation between the maximum and the minimum of the signal (S_{pp}), as shown in Fig. 6c, is 5.4 mm, 6.8 mm, and 8 mm for the slots at $D = 0$ mm, 1 mm, and 2 mm, respectively (see Table I). At the transition region, within which the quadrupolar signal appears and disappears, the separation between the maximum and the minimum decreases and then rapidly increases to the largest value. The width of the transition region (W_{tr}) is less than 1° for all three slots, and

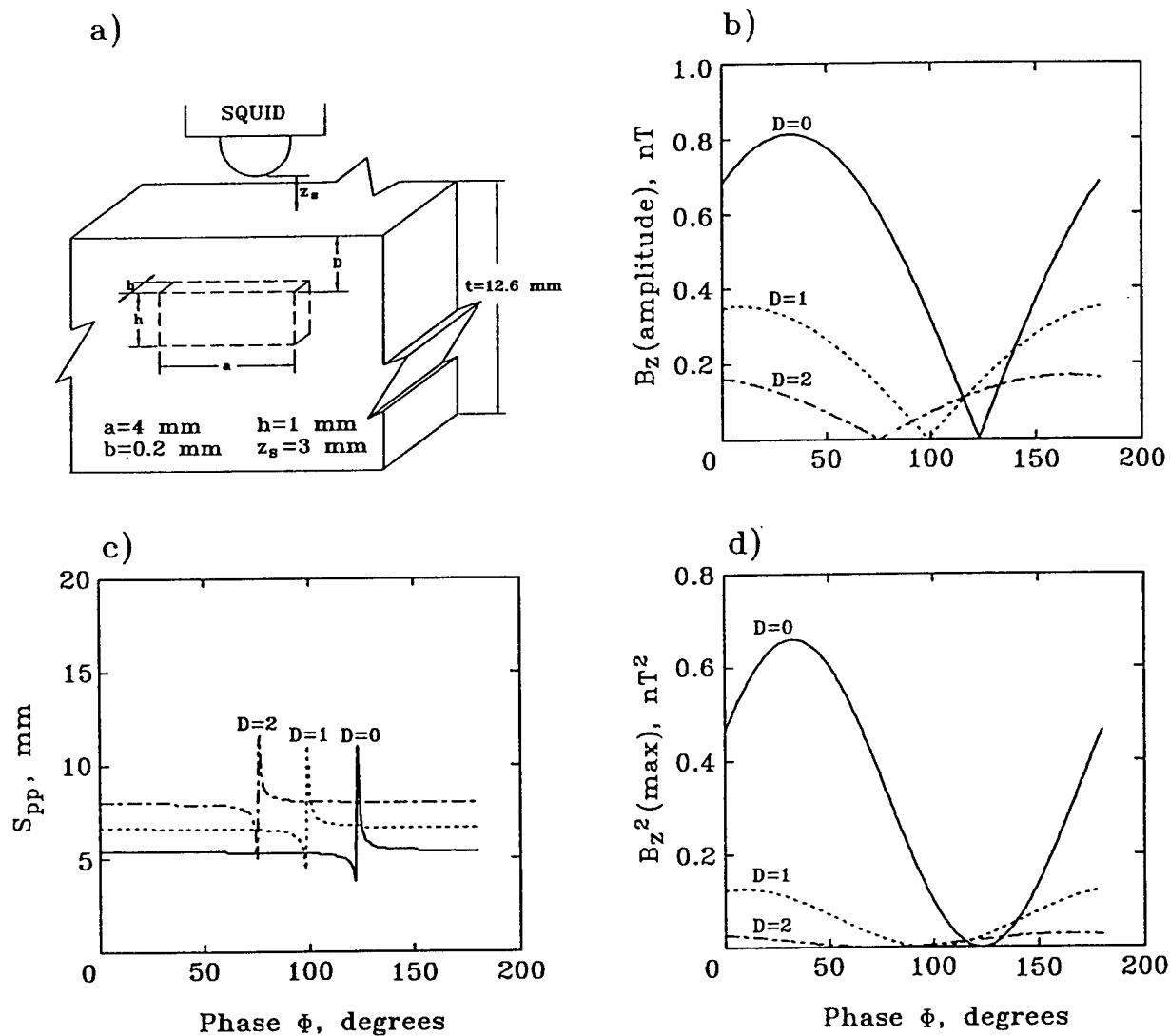


Fig. 6. (a) The dimensions of the slots for the calculations, where $a = 4$ mm, $b = 0.2$ mm, and $h = 1$ mm. (b) The calculated amplitude of the magnetic signal due to the slot inside a 12.6-mm thick aluminum plate located at $D = 0$ mm (solid line), $D = 1$ mm (dotted line) and $D = 2$ mm (dashed line) between the phase angle ϕ of 0° to 180° . (c) The separation between the maximum and the minimum for the slot at $D = 0$ mm (solid line), $D = 1$ mm (dotted line), and $D = 2$ mm (dashed line), respectively. (d) The maximum of the squared magnitude $B_z^2(max)$, which is a sine (or cosine) function of phase ϕ . The standard penetration depth is 2.4 mm, which corresponds to a frequency of 2.5 kHz.

Table I. The Values of Various Parameters in Fig. 6: Slot Dimensions, (a , b , h); the Phase Angle for Minimum Signal, ϕ_{min} ; the Peak-to-Peak Separation, S_{pp} ; and the Width of the Transition Region, W_τ

Line	a (mm)	b (mm)	h (mm)	D (mm)	ϕ_{min}	S_{pp} (mm)	W_τ (mm)
Solid	4	0.2	1	0	121°	5.4	$< 1^\circ$
Dotted	4	0.2	1	1	99°	6.8	$< 1^\circ$
Dashed	4	0.2	1	2	75°	8.0	$< 1^\circ$

hence is not strongly dependent upon the location of the flaw below the surface (see Fig. 6c). Figure 6d shows the maximum of squared magnitude $B_z^2(max)$, which is a sine (or cosine) function of phase ϕ .

Figure 7b shows the amplitude, 7d the amplitude of the squared signal, and 7c the separation between the maximum and the minimum for the surface breaking slots with $h = 1$ mm (solid line), 2 mm (dotted line), and 3 mm (dashed line) (see Fig. 7a). The phase at which the

amplitude becomes minimum (ϕ_{\min}) is 121° , 115° , and 110° for the slots with vertical height, h , of 1 mm, 2 mm and 3 mm, respectively (see Fig. 7b). It is clear that the transition region is much wider for the slots with greater vertical height, shown as in Fig. 7c, where the transition region is $<1^\circ$, 6° , and 10° for the slots with $h = 1$ mm, 2 mm, and 3 mm, respectively (see Table II).

Comparing Table I with Table II, we see that the phase at which the amplitude becomes minimum (or maximum) (ϕ_{\min}) is determined by the depth of the flaw below the surface (D), while the width of the transition region (W_{tr}) is determined by the vertical height of the flaw (h). Both of them depend on the parameter δ/t , which is the function of frequency for a particular material. These phase-related features provide a potential method to determine the depth and the extent of the flaw.

Because the phase of the eddy current changes more at higher frequencies, shown as in Fig. 4, it is better to use as high a frequency as possible for the phase analysis. Since the amplitude of the signal for the deeper flaw is reduced more at higher frequencies, it is necessary to determine an optimum frequency for a particular measurement or to use multiple frequencies. In general, the optimum value for δ/t is between 0.1 and 0.5.

3. EXPERIMENTAL RESULTS

3.1. Sheet Inducer

We used a 300 mm \times 300 mm and 0.3-mm thick copper sheet as a sheet inducer to induce the eddy current in a conducting plate. The test sample was a 121 mm \times 254 mm and 12.6-mm thick aluminum plate with several 8 mm diameter holes through the plate. The SQUID sensing coil was located at 3 mm above the plate. The output signal of the SQUID magnetometer was sent to a two-phase lock-in amplifier, so that both the in-phase and quadrature signals could be recorded,

Table II. The Values of Various Parameters in Fig. 7: Slot Dimensions, (a , b , h); the Phase Angle for Minimum Signal, ϕ_{\min} ; the Peak-to-Peak Separation, S_{pp} ; and the Width of the Transition Region, W_{tr}

Line	a (mm)	b (mm)	h (mm)	D (mm)	ϕ_{\min}	S_{pp} (mm)	W_{tr} (mm)
Solid	4	0.2	1	0	121°	5.4	$< 1^\circ$
Dotted	4	0.2	2	0	115°	5.8	6°
Dashed	4	0.2	3	0	110°	6.0	10°

referenced to the phase of the source voltage of the excitation current.

When the frequency of the excitation current was 500 Hz, ($\delta \approx 5$ mm), the magnetic signal due to the hole showed the quadrupolar signature at the phase $\phi = 123^\circ$, in good agreement with the calculated value of 124° .

3.2. Subsurface Slots

To simulate subsurface flaws, six 8-mm diameter holes were drilled through a 12.6-mm thick aluminum plate. A 3-mm long ($a = 3$ mm) EDM slot was cut through the wall of each hole, as shown in Fig. 8, where A is a surface-breaking slot with a vertical extent $h = 3$ mm, B is a slot at $D = 1$ mm below the surface with $h = 4.8$ mm, and C is a slot at $D = 2.3$ mm below the surface with $h = 4.4$ mm. Each hole was then plugged with an aluminum cylinder. However, the contact between the cylinder and the wall surface of the hole was not perfect, so that the plugged hole without the slot also produced a magnetic signal which was superimposed upon the signal due to the slot. A sheet inducer carrying a 2.5 kHz ($\delta = 2.4$ mm) current, in the direction perpendicular to the orientation of the slot, was placed below the test sample.

The measured fields maps have been processed by fitting the background to a polynomial and subtracting the result from the raw data. To examine the phase-analysis technique discussed in Sec. 2.4, we show in the left column of Fig. 9 one-half of the maximum-to-minimum amplitude of the field map as a function of phase angle. The middle column in Fig. 9 shows the maximum values of the map of the field strength squared, $B_z^2(max)$, where the solid lines are the data and the dotted lines are the fitted function of $P\cos(2\phi - \phi_0) + P$, where P is a constant. The right column in Fig. 9 gives the spatial separation between the maximum and the minimum S_{pp} of the field map as a function of phase angle. The first row (Fig. 9a) is for the calculated field map due to an 8-mm diameter hole in a 12.6-mm thick plate, and serves as a comparison with the measured signals. Figure 9b is for the plugged hole without a slot, and Figs. 9c-e are for the plugged holes with slots A, B, and C, respectively. The amplitude of the magnetic signal due to a hole that is imperfectly plugged (Fig. 9b) is similar to that predicted for an unplugged hole (Fig. 9a), for which $B_z^2(max)$ are well fitted by a cosine function. The separation of the maximum and the minimum S_{pp} in Fig. 9b is also similar to that in Fig. 9a.

Comparing Figs. 9c and d with Fig. 9b, we find several differences. First, the phase dependence of the

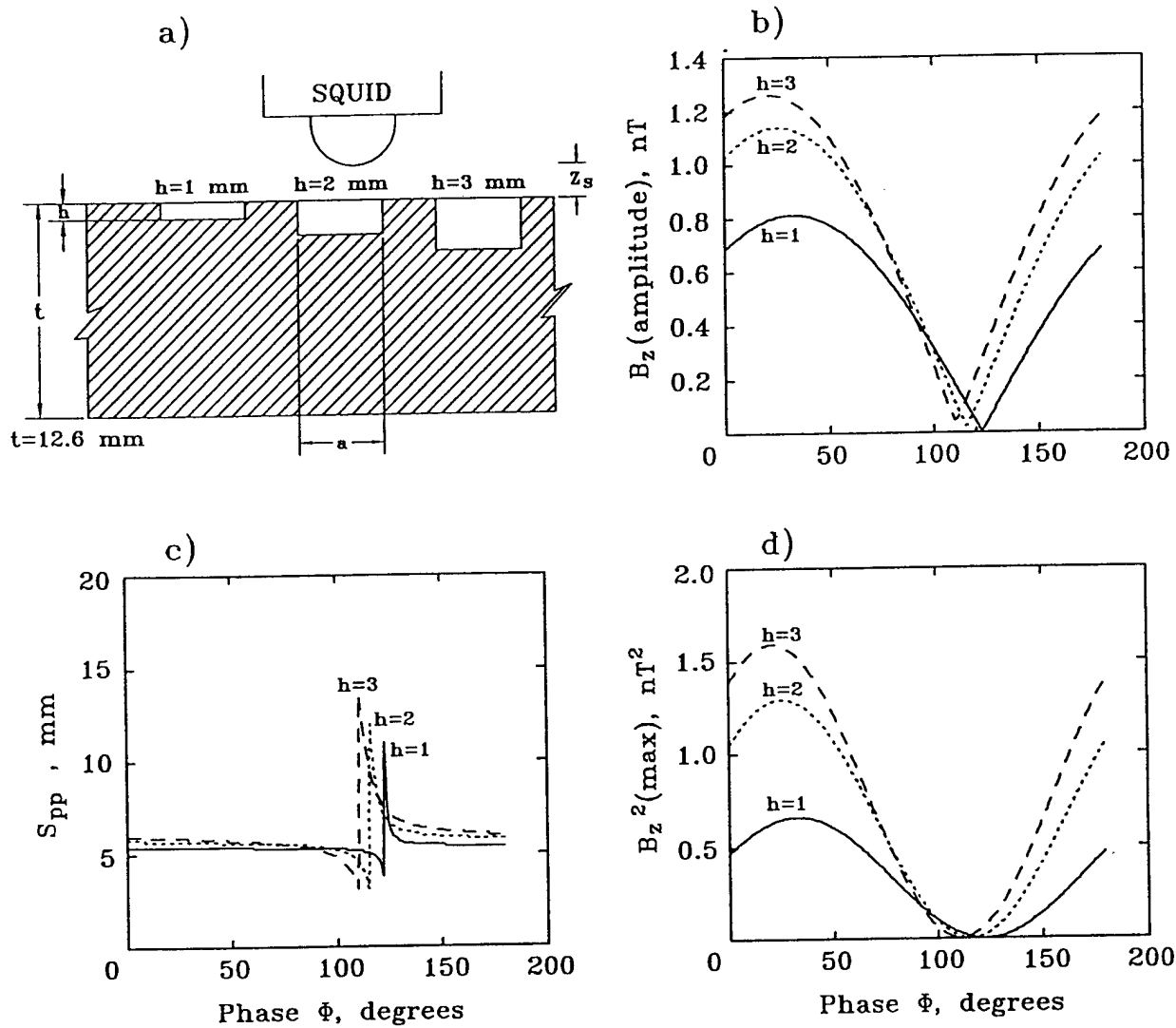
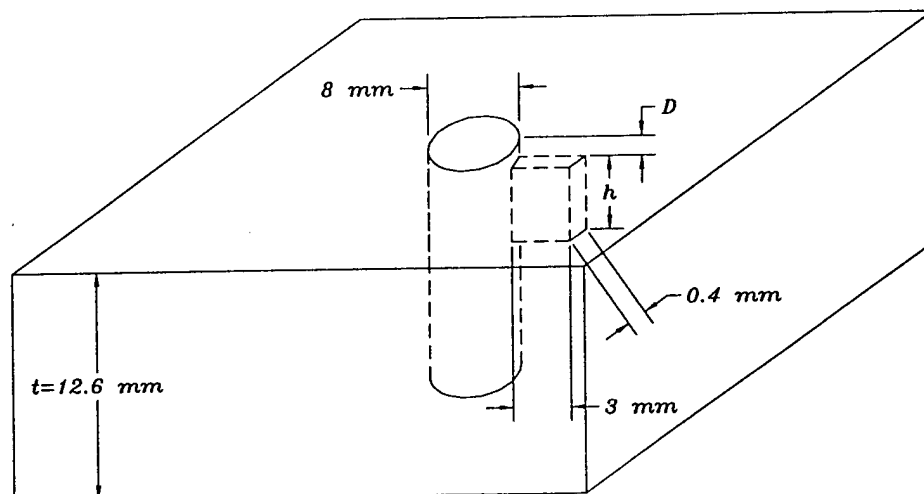


Fig. 7. (a) The dimensions of the slots for the calculations, where $a = 4$ mm, $b = 0.2$ mm, and $D = 0$ mm. (b) The calculated amplitude of the magnetic signal due to the slot with the vertical extent $h = 1$ mm (solid line), 2 mm (dotted line), and 3 mm (dashed line) inside a 12.6-thick aluminum plate located at the surface between the phase angle of 0° to 180° . (c) The separation between the maximum and the minimum for the slot with the vertical extent $h = 1$ mm (solid line), 2 mm (dotted line), and 3 mm (dashed line) at the surface. The standard penetration depth is 2.4 mm, which corresponds to a frequency of 2.5 kHz. (d) The maximum of the squared magnitude $B_z^2(max)$, which is a sine (or cosine) function of phase ϕ .

$B_z^2(max)$ (the middle column in Fig. 9) deviates from the cosine function (dotted lines) within the transition region, because of the broken symmetry due to the slot adjacent to the hole. Second, the phase dependence of S_{pp} (the right column in Fig. 9) due to the plugged hole with the slot shows a wider transition region, and its shape is different from that due to the plugged hole without the slot. In addition, the baselines of S_{pp} are 8 mm and 10 mm for the signal due to the plugged hole without slot and the plugged hole with a slot, respectively.

Third, the phase at which the amplitude of the signal is minimum (or maximum), ϕ_{min} , for the hole with the slots A and B (Figs. 9c and d) shifts with respect to the ϕ_{min} for the hole without the slot in Fig. 9b. It shifts slightly for the hole with the surface-breaking slot A (Fig. 9c), while it shifts by 30° for the slot B at 1 mm below the surface (Fig. 9d), which is consistent with the calculated phase shift in Fig. 6.

Since the imperfectly plugged hole through the plate produces a signal which may be larger than the



A	$D=0$ mm	$h=3$ mm
B	$D=1$ mm	$h=4.8$ mm
C	$D=2.3$ mm	$h=4.4$ mm

Fig. 8. The geometry of simulated subsurface slots in an aluminum test sample.

signal due to the slot alone, it is difficult to distinguish the field pattern due to the hole with deeper slot C from the signal due to the hole without the slot. However, the phase analysis, as in Fig. 9e for the plugged hole with slot C at 2.3 mm below the surface, shows a wider transition region as compared to that for the plugged hole without the slot (Fig. 9b), indicating that the phase analysis provides additional information which may not be visible in the field map.

In general, the amplitude of the signal increases with the dimension of the flaw and decreases with the depth of the flaw, which provides important information for quantitative analysis of the flaw detection. However, the amplitude of the signal is also dependent on the "lift-off" (the distance between the surface and the sensor) although this dependence is much less than for measurements with a conventional eddy current probe. Because the measurements on each of the holes were performed sequentially after repositioning the sample underneath the SQUID magnetometer, the position of the SQUID pickup coils within the dewar relative to the sample was changed, and the lift-off distance was slightly different for each measurement. This may lead to variations in signal amplitude that are dependent upon the depth or size of the slot, but which can be avoided by careful calibration for each measurement. The advantage of the phase information is that it is much less de-

pendent on the lift-off distance, and it can be used readily for quantitative analysis of the magnetic signal due to the flaw, especially when the position of the sensor is not calibrated.

3.3. Hidden Corrosion

We have used this approach to detect hidden corrosion in the second layer of a simulated aircraft lap joint. The sample consisted of two 100×125 mm by 4.1-mm thick 7075-T6 aluminum panels bonded together with sealant. The exterior surfaces were painted with epoxy and polyurethane enamel. The hidden corrosion area, 9.5 mm in diameter, was in one of the surfaces between two panels, as shown as in Figs. 10b and e, and the corrosion depth was measured as 7% of the thickness of one panel of the sample. Because the exterior surface was not conducting, it was not possible to inject current into the sample. The sheet inducer carrying a 7.7 mA, 5 kHz ($\delta \approx 1.7$ mm) current was placed beneath the sample to induce an eddy current in the x direction (see Fig. 10a).

Figure 10c is the field contour map when the corroded area was in the upper surface of the lower plate (see Fig. 10b), while Fig. 10f is the contour map for the corroded area in the lower surface of the upper plate and closer to the SQUID (see Fig. 10e). Both contour maps

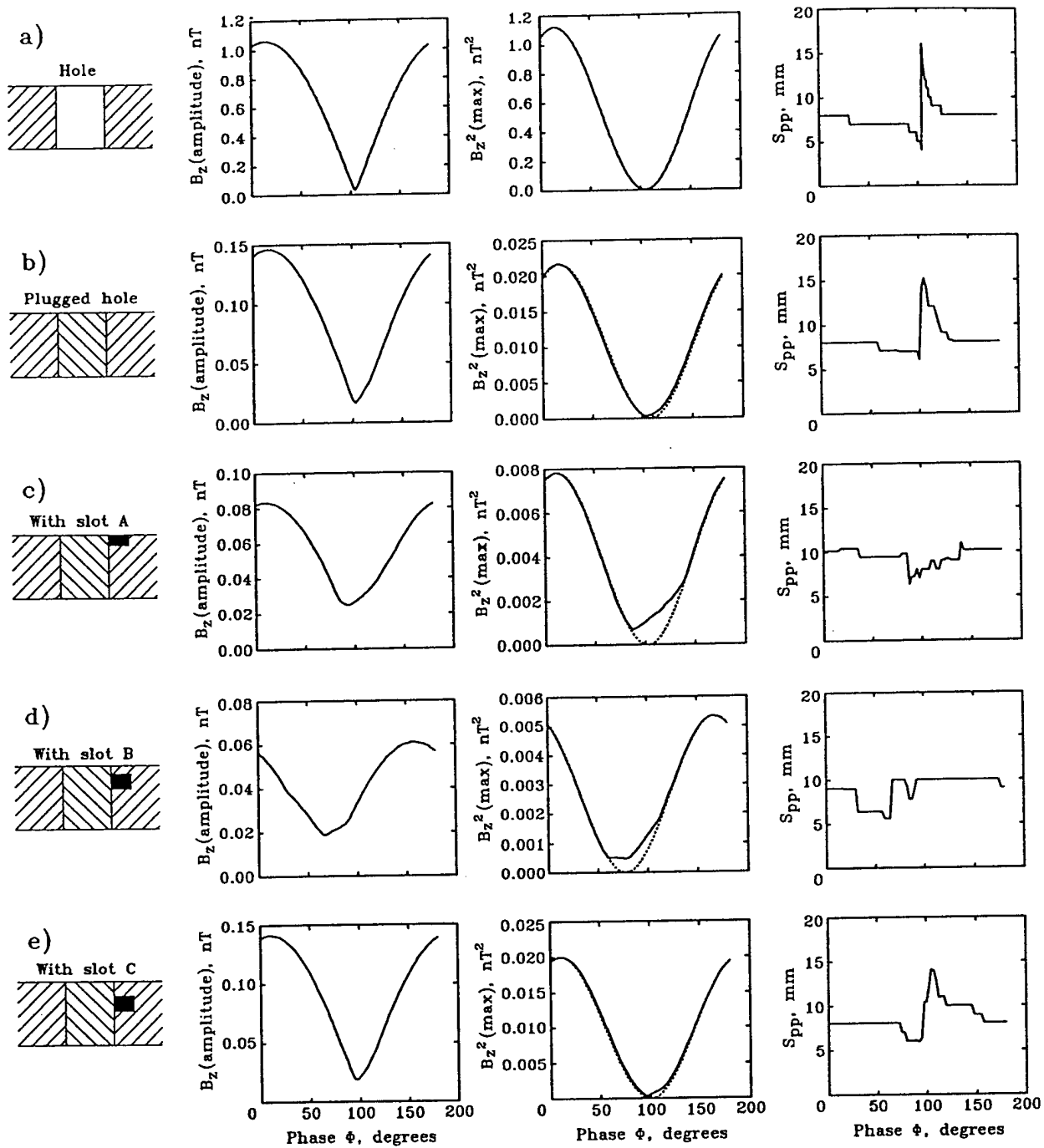


Fig. 9. Phase analysis for the calculated signal (a) and the measured signal for the sample in Fig. 8. The left column is the amplitude of the magnetic signal, the middle is the maximum value of the squared signal where the solid line is the data, and the dotted line is the fitted cosine function; and the right column is the separation between the maximum and the minimum of the signal. (a) The calculated magnetic signal due to a 8-mm diameter hole through a 12.6-mm thick plate. (b) The plugged hole without slot. (c) The plugged hole with the surface-breaking slot A. (d) The plugged hole with the subsurface slot B. (e) The plugged hole with the subsurface slot C.

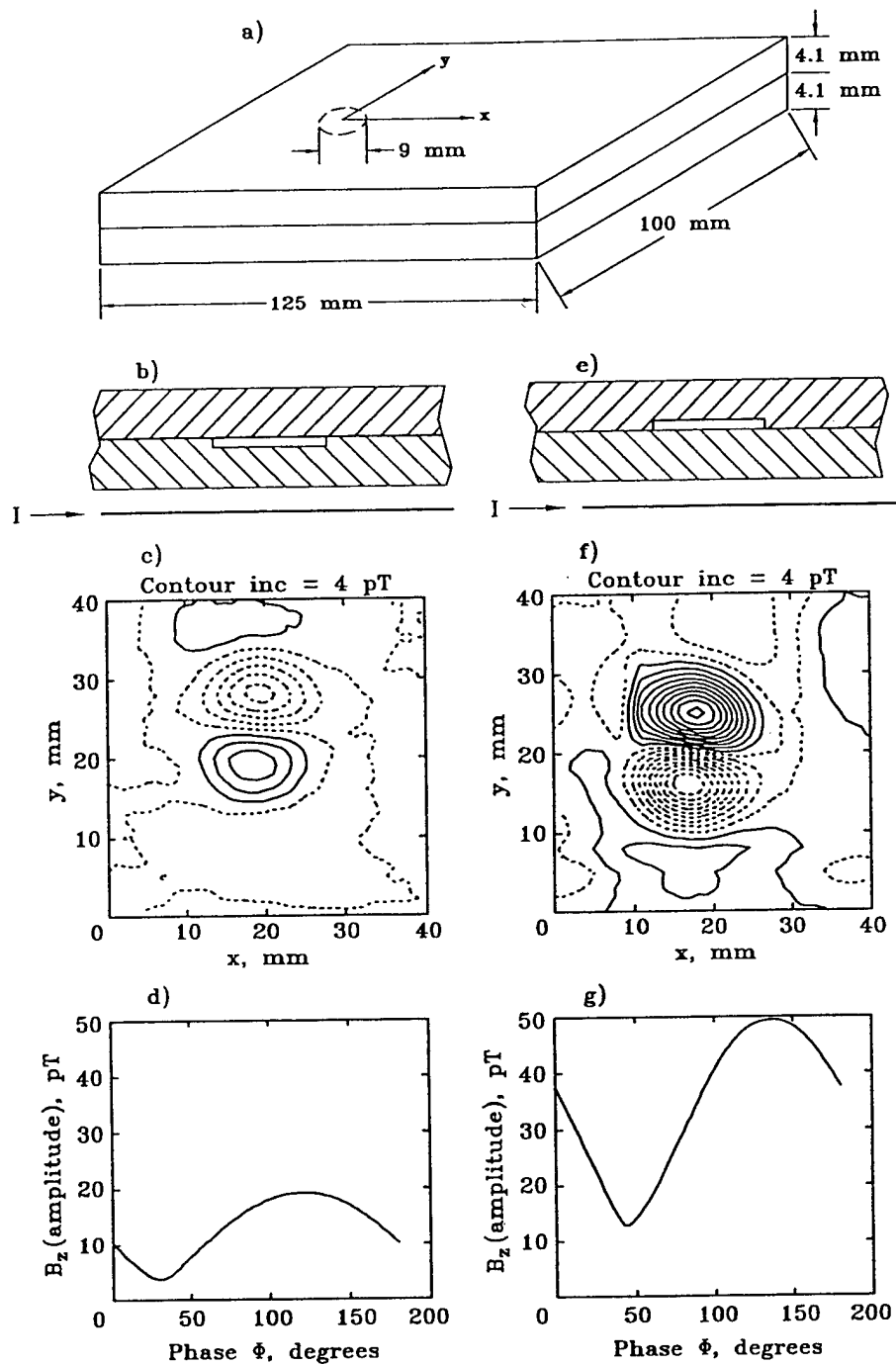


Fig. 10. The detection of hidden corrosion. (a) A schematic drawing of the test sample, which consists of two 4.1-mm thick 7075-T6 aluminum panels bonded together with sealant. The exterior surface is painted with epoxy and polyurethane enamel. The corrosion depth was measured as 7% of the thickness of one panel of the sample. (b) The corroded area is in the lower panel, further from the SQUID sensor. (c) The field contour map for the sample in (b). (d) The phase dependence of the amplitude taken from the data in (c). (e) The corrosion depth is in the upper panel, closer to the SQUID. (f) The contour map for the sample in (e). (g) The phase dependence of the amplitude taken from the data in (f). The excitation current is 5 kHz ($\delta \approx 1.7$ mm). Both contour maps are at phase $\phi = 100^\circ$ and have contour intervals of 4 pT. The dotted lines indicate negative values.

were taken at a phase of 100° , where the dotted lines indicate negative values, and the contour interval is 4 pT. Figures 10c and 10f show the amplitude of the signal as a function of phase angle for sample orientations (b) and (e), respectively.

The amplitude of the signal in Fig. 10d is less than one half of that in Fig. 10g. The corrosion in the lower panel is approximately 1 mm deeper than the corrosion in the upper panel, which would result in the signal from lower panel being reduced by a factor of 0.85 relative to the upper one, rather than the observed factor of 0.5. The other contribution to the reduction of the signal is believed due to the mutual inductance between two panels which are insulated from each other: the magnetic field due to the corrosion in the lower panel was partially shielded by the upper, unflawed panel.

There is an approximately 10° phase shift between the signal due to the lower-layer corrosion and the signal due to the upper layer corrosion. Obviously, the polarity of the signal in Fig. 10c is opposite to that of the signal in Fig. 10f, because one is in the upper surface of the lower panel (Fig. 10c) and the other is in the lower surface of the upper panel (Fig. 10f), for which the eddy currents flow in the opposite direction.

3.4. Second Layer Crack

The test sample shown in Fig. 11a was made of two aluminum panels bolted together by six aluminum pins and nuts. Each panel was 250mm \times 100 mm and 2.4-mm thick. The crack-like defects beneath the surface are simulated by saw cut slots through the lower layer adjacent to the pins A, B, and C. Pins D, E, and F are without cracks, and are for reference only. The slots beneath pins A and C are 12-mm long, with two different orientations. The slot beneath pin B is 6-mm long and is oriented longitudinally. The width of all slots is less than 0.4 mm.

In order to detect cracks with an unknown orientation in the sample, it is convenient if the current can be injected or induced in two orthogonal directions. For a sample with rectangular geometry, it is easier to inject a uniform current longitudinally than transversely. Field maps with injected current in the longitudinal direction are presented elsewhere.⁽¹⁴⁾ Here we discuss the results obtained when a transverse current is induced in the test sample by a sheet inducer, carrying a 45 mA 340 Hz current, that was located 12 mm below the test sample. The SQUID sensor is located at 3 mm above the head of the pins.

Figure 11b shows the field maps for each of the six pins at $\phi = 30^\circ$. The contour interval is 0.3 nT. Both

the pins and the slots disturb the eddy current distribution and produce signals in the field map. At the phase $\phi = 30^\circ$, it is easy to distinguish the signal from a pin with a slot from the signal for a pin without a slot. The map for pin A shows the smallest signal because the eddy current was parallel to the slot. The cross-section plots in Figure 11c, which are taken at the center of the pins, indicate the differences between the pins with slots and those without.

4. DISCUSSION: EDDY CURRENT TOMOGRAPHY

The analysis we have presented so far assumes that the induced currents flow in a single direction in the inducer, and that the analysis of the data will be performed at only a single frequency. If we relax these assumptions, it is possible to extend this approach to allow three-dimensional tomographic reconstruction of the conducting object. We have shown before that the magnetic signature of an elliptical flaw depends upon the direction of the applied current relative to the axis of the flaw.^(10,13) However, the current can be applied from multiple directions, to allow determination of the shape of the flaw. This can be done by either rotating the inducer, or by using a circular inducer with multiple wires, each of which carries a current given by $I_n = I_0 \cos(\theta_0 - \theta_n)$, where θ is the desired angle of the uniform current in the inducer and θ_n is the angle of the n th wire, as shown in Fig. 12. Sequential measurements would simply be made with different values of θ_0 . Other current distributions could also be produced if desired. In electrical impedance tomography, this approach is used, but instead of imaging the current distribution between various combinations of electrodes, only the potential drops between all electrode pairs are recorded.⁽¹⁵⁾ With SQUID current tomography, the magnetic field from each current configuration would be imaged over the entire surface of the object. While this problem is ill-conditioned, it should be more stable than the electric tomography: for a two-dimensional current distribution, the magnetic problem has a unique solution that provides an image of the currents in the plane,⁽¹⁶⁾ rather than requiring a self-consistent calculation of the overall current distribution throughout the plate given only the potentials at the edge.

In the case of thick samples, the magnetic and electric tomography problems become more complex, but the eddy current/phase shift technique should provide a new approach. As we described in detail above, the choice of phase angle in the image determines the depth

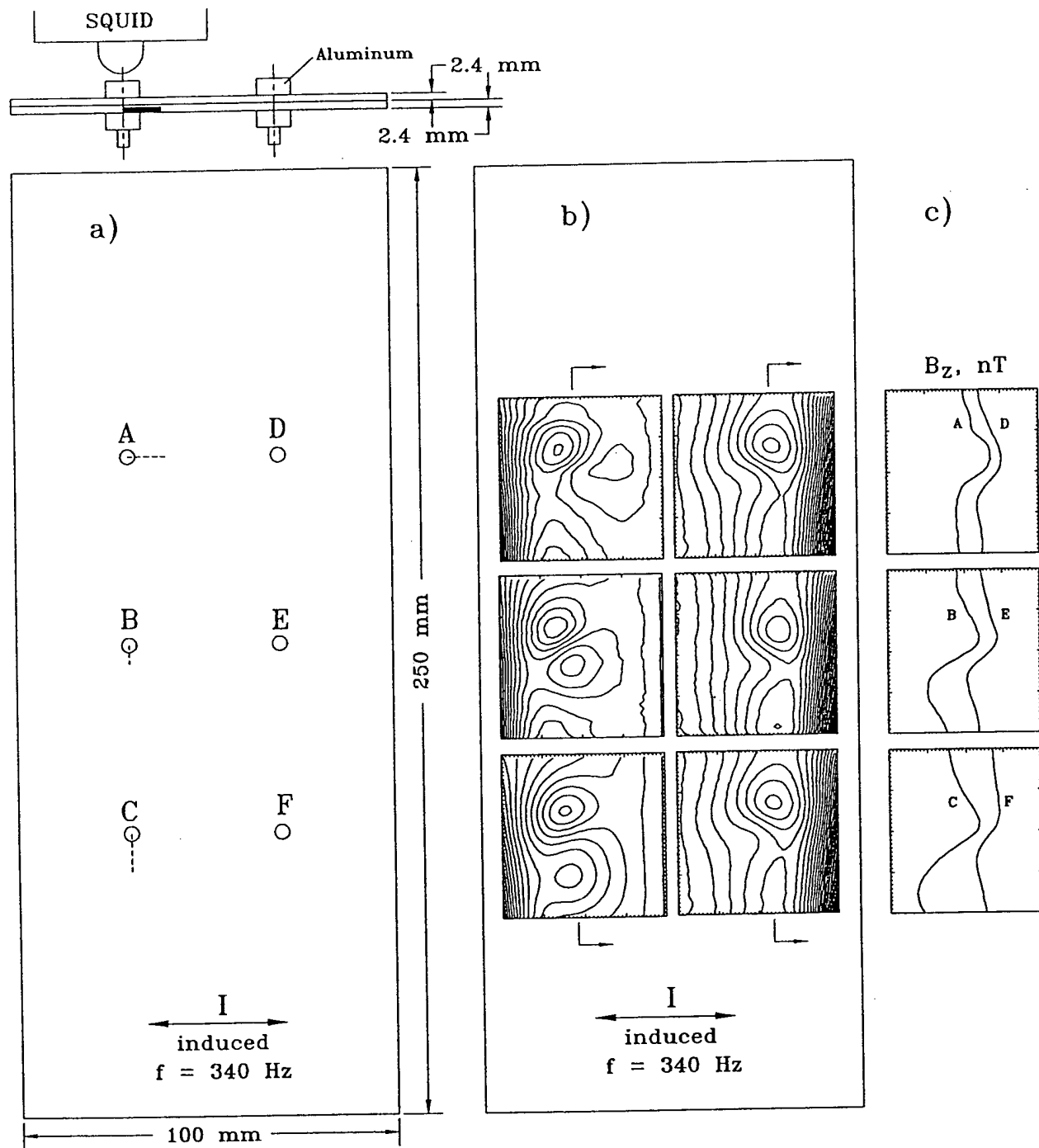


Fig. 11. Detection of second-layer cracks using a sheet inducer. (a) A test sample of two 7075-T6 aluminum panels bolted together by six aluminum pins and nuts. For pins A, B, and C, second layer cracks are simulated by slots through the bottom layer adjacent to the pins. Slots at pins A and C are 12-mm long and the slot at pin B is 6-mm long. A sheet inducer, carrying a 45 mA, 340 Hz current in a transverse direction, was located 12 mm below the sample. (b) The measured field contour maps at $\phi = 30^\circ$ with contour interval of 0.3 nT. (c) Plots of the cross-sections taken from the contour maps in (b).

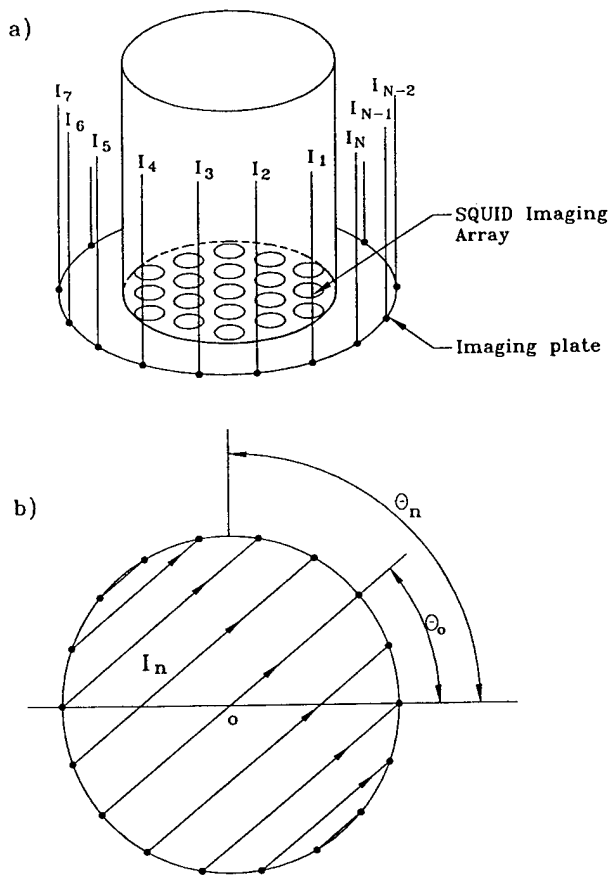


Fig. 12. Schematic representations of a SQUID array (a) and a multiwire, circular inducing plate (b) suitable for eddy current tomography.

at which the zero-current plane occurs. While one might think that it would be possible to sweep the phase angle so as to obtain an image across the depth, it is important to realize that at each measurement point only two numbers are recorded: the in-phase and quadrature components of the magnetic field. Thus, in an overly simplistic way, it follows that the sample could at most be divided vertically into only two zones—one above a chosen zero crossing and one below, so that if the image had N pixels, the three-dimensional current reconstruction might have $2N$ voxels, although it may be prudent to use singular value decomposition and obtain a more stable inverse with fewer than $2N$ voxels. However, because the eddy current approach could be used at M different frequencies, it may be possible, if adequate frequency separation is achieved to make $2M$ vertical separations, or a three-dimensional current reconstruction with $2M \cdot N$ voxels. Of course, more sophisticated analysis of the

magnetic images could also contribute depth information in a model-dependent inverse solution.

5. CONCLUSIONS

We have developed techniques to induce extended eddy currents in metallic structures, such as a conducting plate, that allow us to detect subsurface flaws using a SQUID magnetometer.

The eddy current distributions inside a plate induced by a sheet inducer have been calculated. Inside a plate, the magnitude of the eddy current density decays exponentially if $\delta/t \leq 0.1$, or linearly if $\delta/t \geq 0.5$. At the center of the plate, the induced current density is zero, as expected from symmetry. However, the component of the induced current at a particular phase may not decay with the depth, so that the subsurface current density may be much larger than the surface current density at certain phase angles. Because the magnetic signal detected by the SQUID magnetometer depends on the current density disturbed by flaws, this type of current distribution provides a potential application for discrimination of a subsurface flaw from a surface structure that may not be achieved by a conventional eddy current surface probe.

In addition, the sheet inducer may induce the same amount of current in a surface away from the inducer as at the surface near the inducer. Thus two possible measurement configurations may be utilized, as shown in Fig. 13. The sheet inducer can be placed on the same side of the sample as the sensor (Fig. 13a), or on the opposite side (Fig. 13b). Compared with the conventional eddy current probe coil, a larger diameter coil is required for better field penetration and less lift-off effect, which may reduce the sensitivity for detection of the smaller defects.

Recently, the sheet inducer has been replaced by multiple wire segments connected in series to reduce the distortion due to the secondary eddy currents in the inducer. Alternatively, a patterned, thin metallic film could be used.

The analysis of the phase of the magnetic signal obtained by using the sheet inducer has demonstrated a phase dependence of the amplitude and the separation between the maximum and the minimum of the magnetic signal that is almost independent of the lift-off distance and provides useful information about the depth of the flaw.

With the phase analysis, we have shown that we can distinguish between measured signals due to holes with a surface-breaking or subsurface slot from holes without a slot. In comparison with the impedance-plane

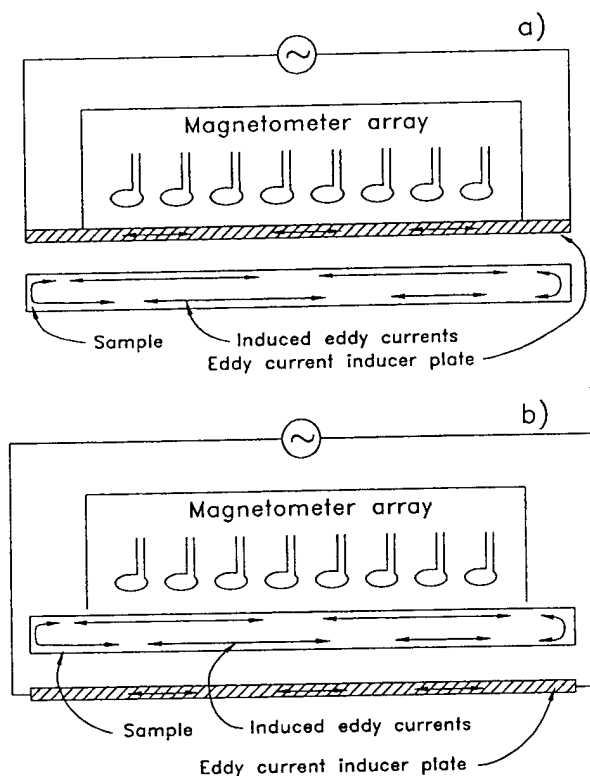


Fig. 13. Two configurations of a sheet inducer and a SQUID array to allow imaging of flaws with extended currents induced in the test specimen.

display used with conventional eddy current techniques, which is affected by many parameters such as lift-off, sample thickness, edges, and properties of the materials, and which requires the complicated calibration procedure, our phase analysis is simpler, because the background from both the inducer and the induced eddy current may be minimized before applying the phase analysis. This method is well suited for quantitative flaw characterization.

With this technique, we have readily detected a hidden corrosion area which was measured as a 7% mass loss at the bottom layer of a specimen that consisted of two bonded 4.1-mm thick aluminum panels with a heavy insulated coating on their surfaces. We have also detected flaws, located immediately adjacent to 4-mm diameter bolts, in the second layer of a lap-joint aluminum plate. These experimental results demonstrate the potential applications of SQUIDs for the detection of second layer-flaws. This approach is especially suitable for a SQUID with a pick-up coil measuring the field component perpendicular to the sample surface.

The thin sheet inducer may also be used with conventional eddy current pick-up sensors because the pen-

etration of the eddy current is deeper than that for surface probe excitation coils.

ACKNOWLEDGMENTS

We are indebted to Steve R. Baughman of Lockheed for providing all of the plate samples. We thank Licheng Li for preparing the illustrations and Leonora Wikswo for her comments on the manuscript. This work was supported in part by grants from the Air Force Office of Scientific Research, the Electric Power Research Institute, and Lockheed.

REFERENCES

1. R. Collins, W. D. Dover, and D. H. Michael, The use of a.c. field measurements in nondestructive testing, in *Research Techniques in Non-Destructive Testing*, Vol. VIII, R. S. Sharpe, ed. (Academic Press, London, 1985).
2. D. Mirshekar-Syahkal, R. Collins, and D. H. Michael, Developments in surface crack detection by the a.c. field technique, in *Review of Progress in QNDE*, Vol. 4A, D. O. Thompson and D. E. Chimenti, eds. (Plenum Press, New York, 1985), pp. 349-357.
3. S. H. H. Sadeghi and D. Mirshekar-Syahkal, A new technique for sizing cracks in metals, utilizing an induced surface magnetic field, in *Review of Progress in QNDE*, Vol. 9A, D. O. Thompson and D. E. Chimenti, eds. (Plenum Press, New York, 1990), pp. 351-358.
4. J. P. Wikswo, Jr., J. M. van Egeraat, Y. P. Ma, N. G. Sepulveda, D. J. Staton, S. Tan, and R. S. Wijesinghe, Instrumentation and techniques for high-resolution magnetic imaging, in *Digital Image Synthesis and Inverse Optics*, Vol. 1351, A. F. Gmitro, P. S. Idell, and I. J. LaHaie, eds. (SPIE Proceedings, 1990), pp. 438-470.
5. Y. P. Ma, D. J. Staton, N. G. Sepulveda, and J. P. Wikswo, Jr., Imaging flaws with a SQUID magnetometer array, in *Review of Progress in QNDE*, Vol. 10A, D. O. Thompson and D. E. Chimenti, eds. (Plenum Press, New York, 1991), pp. 979-986.
6. D. J. Staton, Y. P. Ma, N. G. Sepulveda, and J. P. Wikswo, Jr., High resolution magnetic mapping using a SQUID magnetometer array, *IEEE Trans. Mag.* 27(2):3237-3240 (1991).
7. J. P. Wikswo, Jr., D. B. Crum, W. P. Henry, Y. P. Ma, N. G. Sepulveda, and D. J. Staton, An improved method for magnetic identification and localization of cracks in conductors, *J. Nondestr. Eval.* 12(2):109-119 (1993).
8. Y. P. Ma and J. P. Wikswo, Jr., Detection of deep flaw inside a conductor using a SQUID magnetometer, in *Review of Progress in QNDE*, Vol. 11A, D. O. Thompson and D. E. Chimenti, eds. (Plenum Press, New York, 1992), pp. 1153-1159.
9. G. L. Fitzpatrick, D. K. Thome, R. L. Skaugset, and E. Y. C. Shih, The present status of magneto-optic eddy current imaging technology, in *Review of Progress in QNDE*, Vol. 12, D. O. Thompson and D. E. Chimenti, eds. (Plenum Press, New York, 1993), pp. 617-624.
10. N. G. Sepulveda, D. J. Staton, and J. P. Wikswo, Jr., A mathematical analysis of the magnetic field produced by flaws in two-dimensional current-carrying conductors, *J. Nondestr. Eval.* 11(2): 89-101 (1992).
11. W. R. Smythe, ed., *Static and Dynamic Electricity* (McGraw-Hill, New York, 1950), p. 390.
12. D. S. Buchanan, D. B. Crum, D. Cox, and J. P. Wikswo, Jr., MicroSQUID: A close-spaced four channel magnetometer, in *Ad-*

- vances in Biomagnetism*, S. J. Williamson, M. Hoke, G. Stroink, and M. Kotani, eds. (Plenum Press, New York, 1990), pp. 677–679.
13. Y. P. Ma and J. P. Wikswo, Jr., A solution for the magnetic field produced by a elliptic cylinder in a current-carrying plate and its application for flaw detection (in preparation).
 14. Y. P. Ma and J. P. Wikswo, Jr., Imaging subsurface defects using SQUID magnetometers, in *Review of Progress in QNDE*, Vol. 12, D. O. Thompson and D. E. Chimenti, eds. (Plenum Press, New York, 1993), pp. 1137–1143.
 15. R. Henderson and J. Webster, An impedance camera for spatially specific measurements of the thorax, *IEEE Trans. Biomech. Eng.* 25:250 (1978).
 16. B. J. Roth, N. G. Sepulveda, and J. P. Wikswo, Jr., Using a magnetometer to image a two-dimensional current distribution, *J. Appl. Phys.* 65:361–372 (1989).

APPENDIX 2

Analytical Solution of the Magnetic Field Above a Current-Carrying Conducting Plate Containing a Spherical Inclusion

Yu Pei Ma and John P. Wikswo, Jr.

Electromagnetics Laboratory
Department of Physics and Astronomy
Vanderbilt University, Nashville, TN 37235

Abstract

Electromagnetic techniques are widely used for Non-Destructive evaluation (NDE) materials and their defects. For quantitative analyses, models can compliment experimental results providing physical insight and allowing simulations to relieve the time and resource requirements of experimental data collection. Analytical models provide advantages over numerical models both in computational speed and accuracy but are usually limited to simple geometries. This paper presents an analytical solution of the magnetic field associated with a spherical inclusion embedded in a current-carrying conducting plate. The method of images was used for the determination of the current distribution. The result was compared to experimental data taken with a Superconducting Quantum Interference Device (SQUID) magnetometer. The analytical model can be used to determine the location and dimension of a spherically shaped inclusion in metallic structures.

I. Introduction

For characterization of conducting materials, electromagnetic tests have been widely used for Nondestructive Evaluation (NDE)[1]. Conventional eddy current techniques have dramatically suppressed sensitivity at low frequencies due to the frequency dependence of the pickup coil impedance. For high sensitivity measurements at low frequencies, several new techniques, such as the Superconducting QUantum Interference Device (SQUID)[2], Magneto-Optical Image (MOI) system, and the magneto-resistance detector, have been introduced for NDE applications because their sensitivity is frequency independent.

For quantitative NDE, models can compliment experimental results providing physical insight and allowing simulations to relieve the time and resource requirements of experimental data collection. Most of the modeling for NDE are involved

in the impedance calculations for high frequency eddy current probes [3 eddy current calculation? too many, do I have to?]. At low frequencies, which electromagnetic field is quasi-static, and the magnetic field may be calculated as a dc current around the flaw.

Commonly the numerical methods can be used for modeling, however, the results published by one author may not be able to be adapted by someone who is not familiar with the method used. Analytical models provide advantages over numerical model in accuracy, simplicity and computationally efficient. Then the analytic solutions are most desired if they are available.

This paper presents an analytical solution of the magnetic field due to the current perturbed by a spherical inclusion embedded in a thick conducting plate. The electrical potential perturbed by both the sphere and the surface of the plate is calculated by using the method of images. Then the magnetic signal due to the perturbed current around the sphere is calculated by the Law of Biot- Savart.

II. Electrical Potential

In principle, a three-dimensional static electric potential distribution may be found by solving Laplace's equation. The Laplacian operator is separable in eleven different coordinate systems [4], however, it is difficult to utilize the method of separation of variables for problems with Neumann boundary conditions at both the spherical surface and the plane surface. In this case, the method of images is appropriate. The Green's function for a sphere placed in an initially uniform electric field can be found easily [5]. When a surface is introduced, the additional terms need to be added to correct the Green's function.

We assumed that the conducting volume is an infinite extended plate with uniform conductivity σ . The current density, J_0 , is originally uniform and parallel to the surfaces of the plate. A spherical inclusion F , with radius a and zero conductivity, is located beneath the top surface of the conductor (see Fig. 1). The distance between its center O and the surface is d . The plate is thick enough that the influence of the bottom surface may be neglected.

At $r \gg a$, the current density $J_0 = \sigma E_0$ is constant and along the z direction, where σ is the conductivity of the conductor and E_0 is electrical field. The potential Ψ at the point p , which is inside the conductor but outside the sphere F , can be written as

$$\Psi = -E_0 r \cos \theta + \psi(r, \theta) , \quad (1)$$

where $\psi(r, \theta)$ is the potential perturbation due to both the sphere F and the planar boundary at $x = d$. Because of $\nabla^2 \Psi = 0$ So that ψ satisfies Laplace's equation $\nabla^2 \psi = 0$.

The boundary conditions for Ψ are

$$\frac{\partial \Psi}{\partial r} \Big|_{r=a} = 0, \quad (2)$$

$$\frac{\partial \Psi}{\partial x} \Big|_{x=d} = 0, \quad (3)$$

$$\Psi \Big|_{r \rightarrow \infty} = -E_0 r \cos \theta. \quad (4)$$

Then, the boundary conditions for ψ are found from Eq.(1)

$$\frac{\partial \psi}{\partial r} \Big|_{r=a} = E_0 \cos \theta, \quad (5)$$

$$\frac{\partial \psi}{\partial x} \Big|_{x=d} = 0, \quad (6)$$

$$\psi \Big|_{r \rightarrow \infty} = 0. \quad (7)$$

An image sphere F' , with the same radius a , and center O' at $x = 2d$, is introduced. Similar to the velocity potential of fluid flow discussed by Milne-Thomson [6], the potential ψ at the point p due to both the spheres F and F' can be written as the sum of two parts

$$\psi = \psi_1 + \psi_2, \quad (8)$$

where ψ_1 is the potential corresponding to the sphere F , and ψ_2 , that corresponding to the image sphere F' .

It is assumed that the spheres F and F' are separated far enough so that the sphere F (or F') is unaffected by the presence of F' (or F). From Eq.(5), the boundary conditions at the surface, $r = a$, of sphere F become

$$\frac{\partial \psi_1}{\partial r} \Big|_{r=a} = E_0 \cos \theta, \quad (9)$$

$$\frac{\partial \psi_2}{\partial r} \Big|_{r=a} = 0, \quad (10)$$

and the boundary conditions at the surface, $r' = a$, of sphere F' are

$$\frac{\partial \psi_1}{\partial r'} \Big|_{r'=a} = 0, \quad (11)$$

$$\frac{\partial \psi_2}{\partial r'} \Big|_{r'=a} = E_0 \cos \theta', \quad (12)$$

where r and r' are shown in Fig. 1, and are related through

$$r \cos \theta = r' \cos \theta' . \quad (13)$$

The zero order approximation of ψ , $\psi^{(0)}$ is the solution for a sphere without the planar boundary, which satisfies only the first boundary condition, Eq. (9), at the surface of the sphere F ,

$$\psi^0 = \psi_1^{(0)} = -\frac{E_0 a^3 \cos \theta}{2 r^2} . \quad (14)$$

Then Ψ is

$$\Psi^{(0)} = -E_0 r \cos \theta \left(1 + \frac{a^3}{2r^3} \right) . \quad (15)$$

Equation 15 is valid in the special case, $a/d \ll 1$, the surface of the plate does not affect the potential due to the sphere.

Since Eq. 14 does not satisfy the corresponding boundary condition, Eq.(11) at the surface of the image sphere F' , an additional term, $V_1^{(1)}$, is required. Then the first order approximation of the potential ψ_1 , corresponding to F , becomes

$$\psi_1^{(1)} = \psi_1^{(0)} + V_1^{(1)} . \quad (16)$$

To find $V_1^{(1)}$, it is recalled that the spheres F and F' are separated sufficiently that the radius a is much smaller than the separation between F and F' , $2d$. Since only the potential at the vicinity of the surface of the sphere F' ($r' \sim a$) is of concern, the approximation of $r \approx 2d$ at $r' \sim a$ is suggested. Substituting Eqs. (14) and (16) into Eqs. (9) and (11) and using Eq. (13), the first order correction term $V_1^{(1)}$ should satisfy the following conditions on the surfaces of spheres F and F' ,

$$\frac{\partial V_1^{(1)}}{\partial r} \Big|_{r=a} = 0 , \quad (17)$$

$$\frac{\partial V_1^{(1)}}{\partial r'} \Big|_{r'=a} = \frac{E_0 a^3 \cos \theta'}{16d^3} . \quad (18)$$

A solution which satisfies these boundary conditions is

$$V_1^{(1)} = -\frac{E_0 a^6 \cos \theta'}{32d^3 r'^2} . \quad (19)$$

Then, the first order approximation of ψ_1 becomes

$$\psi_1^{(1)} = -\frac{E_0 a^3 \cos \theta}{2 r^2} - \frac{E_0 a^6 \cos \theta'}{32d^3 r'^2} . \quad (20)$$

Similarly, the first order approximation of ψ_2 is

$$\psi_2^{(1)} = -\frac{E_0 a^3 \cos \theta'}{2} \frac{1}{r'^2} - \frac{E_0 a^6 \cos \theta}{32 d^3} \frac{1}{r^2}. \quad (21)$$

From Eq. (8) the first order approximation of the perturbed potential is

$$\psi^{(1)} = \psi_1^{(1)} + \psi_2^{(1)}. \quad (22)$$

Substituting Eqs. (20) and (21) into Eq. (22), and then re-examining the boundary conditions at the surface of the sphere F , Eq. (5), the second order correction term of ψ_1 , $V_1^{(2)}$, is found to be

$$V_1^{(2)} = -\frac{E_0 a^6 \cos \theta'}{32 d^3} \frac{1}{r'^2} \left(\frac{3a}{d} \sin \theta' \cos \phi' + \frac{9a^2}{2d^2} \right). \quad (23)$$

Therefore, the second order approximation of ψ_1 is

$$\psi_1^{(2)} = \psi_1^{(0)} + V_1^{(1)} + V_1^{(2)}. \quad (24)$$

Using the symmetry between F and F' , $\psi_2^{(2)}$ should be similar to $\psi_1^{(2)}$. Substituting $\psi_1^{(2)}$ and $\psi_2^{(2)}$ into Eq. (8) and using Eq. (13), the potential due to both the spherical and the planar surfaces, $\psi^{(2)}$, becomes

$$\begin{aligned} \psi^{(2)} = & -E_0 r \cos \theta \left\{ \frac{a^3}{2r^3} \left[1 + \frac{a^3}{16d^3} \left(1 + \frac{3a}{d} \sin \theta \cos \phi + \frac{9a^2}{2d^2} \right) \right] \right. \\ & \left. + \frac{a^3}{2r'^3} \left[1 + \frac{a^3}{16d^3} \left(1 + \frac{3a}{d} \sin \theta' \cos \phi' + \frac{9a^2}{2d^2} \right) \right] \right\}, \end{aligned} \quad (25)$$

which satisfies the planar surface boundary condition, Eq. (6). It is necessary to examine the accuracy of Eq. (25) by substituting it into Eq. (5), the boundary condition for $\psi^{(2)}$ at the surface of the sphere F ($r \rightarrow a$). The error is on the order of $(a/d)^6$. So, the Eq. (25) is valid if the condition of $(a/d)^6 \ll 0$ is satisfied.

Since only the current density at the surface of the sphere is used for the calculation of the magnetic field, Eq. (25) may be simplified. In the vicinity of the sphere F , $r \approx a$ and $r' > d$, and by neglecting the terms with an order of $(a/d)^6$ or higher, the second order approximation of Ψ can be written as

$$\Psi^{(2)} = -E_0 r \cos \theta \left\{ 1 + \frac{a^3}{2} \left[\frac{1}{r^3} + \frac{a^3}{16d^3} \frac{1}{r^3} \left(1 + \frac{3a}{d} \sin \theta \cos \phi + \frac{9a^2}{2d^2} \right) + \frac{1}{r'^3} \right] \right\} + \dots, \quad (26)$$

where

$$r' = (r^2 + 4d^2 - 4dr \sin \theta \cos \phi)^{\frac{1}{2}}. \quad (27)$$

Equation (26) is valid in the vicinity of the sphere F if $(a/d)^6 \ll 1$ is satisfied.

III. Magnetic Field

Figure 2 shows the coordinate system for the calculation of the magnetic field, where $p(x, y, z)$ is the source point and $P(X, Y, Z)$ is the field point. The magnetic field at the point P outside the conductor produced by the source current \vec{J} at the point p inside the conductor can be calculated using the law of Biot and Savart [7]

$$\vec{B}(\vec{R}) = \frac{\mu_0}{4\pi} \iint_s \frac{\vec{J} \times \vec{n}}{|\vec{R} - \vec{r}|} ds, \quad (28)$$

where s is the bounding surface of the region occupied by the current, in this case, the surface of the sphere $r = a$ and the surface of the plate $x = d$ (see Fig. 2), \vec{J} is the current density on the bounding surface, and \vec{n} is an outward unit vector from the region occupied by current and normal to the surface s . Because most SQUID magnetometers used for NDE applications measure the magnetic field normal to the surface of the conductor [2], only the field component in the X direction, B_x is calculated in this paper.

From Fig. 2, the current at the surface $x = d$ does not contribute to the X component of the magnetic field since $\vec{J} \times \vec{n} = 0$. Only the current density at the spherical surface $r = a$, where \vec{n} is in the $-\vec{r}$ direction, contributes to the B_x .

1. Current density at the surface of the sphere

The current density at the surface of the sphere $r = a$ is derived from the potential in the vicinity of the sphere, Eq. (26), by using Ohm's law

$$\vec{J} = -\sigma \nabla \Psi. \quad (29)$$

Under the condition of $(a/d)^6 \ll 1$, the second order approximation of Ψ in Eq. (25) is used. At the surface $r = a$, the components of the current density expressed in spherical coordinates (r, θ, ϕ) are

$$J_\theta = -J_0 \left[\left(\frac{3}{2} + \frac{1}{32} \left(\frac{a}{d} \right)^3 + \frac{9}{64} \left(\frac{a}{d} \right)^5 + \frac{a^3}{2r^3} \Big|_{r=a} \right) \sin \theta - \frac{3a^4 d \cos^2 \theta \cos \phi}{r^{15}} \Big|_{r=a} \right]$$

$$- \frac{3}{32} \left(\frac{a}{d} \right)^4 (\cos^2 \theta - \sin^2 \theta) \cos \phi \Big] \quad (30)$$

$$J_\phi = -J_0 \left[\frac{3a^4 d \cos \theta \sin \theta \sin \phi}{r^{15} \Big|_{r=a}} + \frac{3}{32} \left(\frac{a}{d} \right)^4 \cos \theta \sin \phi \right] \quad (31)$$

$$J_r = 0, \quad (32)$$

where $J_0 = \sigma E_0$ is the current density at $r \gg a$ and is along the z direction.

We have calculated J_θ and J_ϕ at the surface of the spheres with different radii, $a = 1$ mm and $a = 7$ mm, both with centers located at $d = 10$ mm below the surface. Figure 3 shows the isocontour of the current. The point at $\theta = 90^\circ$ and $\phi = 0^\circ$ is nearest to the surface, while the point at $\theta = 90^\circ$ and $\phi = 180^\circ$ is farthest from the surface (see Fig. 2). For $a = 1$ mm, $a/d = 0.1$ is small, and J_θ is almost independent of ϕ , as shown by the straight lines in Fig. 3a. While at $a/d = 0.7$, J_θ is distorted by the top planar surface and is dependent on ϕ , as shown as in Fig. 3b. From Fig. 3c and 3d, J_ϕ for $a = 1$ mm is three orders of the magnitude smaller than J_ϕ for $a = 7$ mm, and it is negligible.

In the limiting case of $(a/d) \ll 1$, the current distribution is disturbed by the sphere only and the effect due to the top surface of the conductor may be neglected. At the surface $r = a$, the current density can be derived from Eqs. (15) and (29):

$$J_\theta = -\frac{3}{2} J_0 \sin \theta \quad (33)$$

$$J_\phi = 0 \quad (34)$$

$$J_r = 0. \quad (35)$$

Equation (34) shows that there is no current flowing in the ϕ direction at the surface of the sphere.

2. Magnetic field

In spherical coordinates, the Green's function in Eq. (28) may be expanded in terms of the Legendre polynomials of the order l [8]:

$$\frac{1}{|\vec{R} - \vec{r}|_{r=a}} = \sum_{l=0}^{\infty} \frac{a^l}{R^{l+1}} P_l(\cos \gamma), \quad (36)$$

where

$$R = [X^2 + Y^2 + Z^2]^{\frac{1}{2}}, \quad (37)$$

$X = d + d_0$, d_0 is the distance from the point $P(X, Y, Z)$ to the surface of the conductor, and γ is the angle between \vec{R} and \vec{r} . For the convenience of integration, $P_l(\cos \gamma)$ is expressed as a function of the spherical coordinates, θ, ϕ and Θ, Φ , as shown in Fig. 2:

$$P_l(\cos \gamma) = P_l(\cos \Theta)P_l(\cos \theta) + 2 \sum_{m=1}^l \frac{(l-m)!}{(l+m)!} P_l^m(\cos \Theta)P_l^m(\cos \theta) \cos[m(\Phi - \phi)], \quad (38)$$

where $P_l^m(\cos \theta)$ is the associated Legendre function.

The second order approximation is under the condition of $(a/d)^6 \ll 1$. The normal component of the magnetic field is determined from the normal component of $(\vec{J} \times \vec{n})$ at the surface $r = a$, using Eqs. (30) - (32)

$$(\vec{J} \times \vec{n})_x = J_0 \left[\frac{3}{2} + \frac{1}{32} \left(\frac{a}{d} \right)^3 + \frac{9}{64} \left(\frac{a}{d} \right)^5 + \frac{a^3}{2r'^3} \Big|_{r=a} \right] \sin \theta \sin \phi - J_0 \left(\frac{3}{32} \right) \left(\frac{a}{d} \right)^4 \sin^2 \theta \sin \phi \cos \phi, \quad (39)$$

where

$$r' \Big|_{r=a} = (a^2 + 4d^2 - 4ad \sin \theta \cos \phi)^{\frac{1}{2}}. \quad (40)$$

It is difficult to evaluate the integral in Eq. (28) if the parameter r' is expressed in the form of Eq. (40). Therefore, by using the binomial theorem, a new parameter β is introduced,

$$\beta = \frac{4ad}{a^2 + 4d^2}, \quad (41)$$

and the term of $1/r'^3$ can be expanded as a series in terms of β

$$\frac{1}{r'^3} \Big|_{r=a} = (a^2 + 4d^2)^{-\frac{3}{2}} \times \sum_{n=0}^{\infty} b_n \beta^n \sin^n \theta \cos^n \phi, \quad (42)$$

where b_n are the binomial coefficients

$$b_n = \frac{\frac{3}{2} \times \frac{5}{2} \times \cdots \times (\frac{3}{2} + n - 1)}{n!}. \quad (43)$$

Because a is always less than d , then $\beta < 1$ is valid, the series in Eq. (42) is convergent.

Combining Eqs. (36)-(38) and Eqs. (42)-(46) with Eq. (28), using orthogonality of triangle functions and Legendre functions, neglecting the terms which are equivalent or higher than the order of $(a/d)^6$, and taking l and m up to 3, the expression

for the normal component of the magnetic field at the point $P(X, Y, Z)$ expressed in Cartesian coordinates is

$$B_X(X, Y, Z) = \frac{\mu_0 J_0 a^3 Y}{R^3} \left[\frac{1}{2} + \frac{a^3}{96d^3} + \frac{9a^5}{192d^5} + \frac{a^3}{8(a^2 + 4d^2)^{3/2}} \left(A_1 + A_2 \frac{3aX}{R^2} - A_3 \frac{3a^2}{2R^2} + A_3 \frac{15a^2 X^2}{2R^4} \right) \right], \quad (44)$$

where

$$\begin{aligned} A_1 &= \frac{4}{3} + \frac{1}{2}\beta^2 + \frac{9}{32}\beta^4, \\ A_2 &= \frac{2}{5}\beta + \frac{1}{4}\beta^3 + \frac{11}{64}\beta^5, \\ A_3 &= \frac{1}{7}\beta^2 + \frac{1}{8}\beta^4, \\ R &= [X^2 + Y^2 + Z^2]^{\frac{1}{2}}, \end{aligned}$$

In the limiting case of $(a/d) \ll 1$, the x component of $(\vec{J} \times \vec{n})$ is derived from Eq. (33) directly,

$$\vec{J} \times \vec{n} |_x = \frac{3}{2} J_0 \sin \theta \sin \phi. \quad (45)$$

Substituting Eqs. (36)-(38) and (45) into Eq. (28), using orthogonality of triangle functions and Legendre functions, the integral is nonvanishing only if $m = 1$. Then using the following integral

$$\int_0^\pi \sin^2 \theta P_l^1(\cos \theta) d\theta = \begin{cases} -\frac{4}{3} & l = 1 \\ 0 & l \neq 1 \end{cases}, \quad (46)$$

the magnetic field at the point P is

$$B_X = \frac{\mu_0 J_0 a^3}{2} \frac{\sin \Theta \sin \Phi}{R^2} = \frac{\mu_0 J_0 a^3}{2} \frac{Y}{R^3}. \quad (47)$$

The field component in Eq. (47) is equivalent to the field component produced by a current dipole, $\vec{dI} = -2\pi a^3 \vec{J}_0$, located at the center of the sphere. Then the dipole approximation Eq. (47) is valid under the condition of $(a/d) \ll 1$.

IV. Applications to NDE

The results obtained in the above section may be applied to quantitative non-destructive evaluation of flaws embedded inside a conductor. The magnetic field due to the sphere is dipolar in shape as shown as in Fig. 4a. There are two parameters that are associated with these types of signals, and are useful for quantitative analysis in NDE: the peak-to-peak amplitude, B_{pp} , and the spatial separation between the extrema, S_{pp} , of the magnetic signal.

Figure 4a is the calculated magnetic field at 1 mm above the surface of the conductor, containing a 8 mm radius sphere centered 10 mm below the surface. The solid line is calculated from the second order approximation, Eq. (44), and the dashed line is calculated from the dipole approximation, Eq. (47). The error due to the simplified dipole approximation is calculated as the difference of the amplitude of the magnetic signal between the solid line and the dashed line shown in Fig. 4a. Figure 4b shows the percentage error, which is the error divided by the amplitude of the signal, for the spheres with various radii (1-8 mm) at the same location (centered 10 mm below the surface). The error is 7% for the large sphere with $a/d = 0.8$.

Figures 5a and 6a are the calculated B_{pp} and S_{pp} as a function of sphere radius at constant depth, $d = 10$ mm. Figure 5b and 6b are the calculated B_{pp} and S_{pp} as a function of sphere depth at constant radius, $a = 8$ mm. In both Fig. 5 and 6, the solid lines show the two parameters obtained from the second order approximation, Eq. (44), and the dashed lines are obtained from the dipole approximation, Eq. (47). And the magnetic fields are calculated at $d_0 = 1$ mm above the surface by using $J_0 = 30$ A/m².

The analytical expressions of B_{pp} and S_{pp} for dipole approximation can be derived from Eq. (47) directly. The maximum and the minimum of the magnetic signal occur at $Z = 0$ and $Y = \pm (d + d_0)/\sqrt{2}$, leading to the amplitude

$$B_{pp} = 2\mu_0 J_0 a^3 \frac{1}{3\sqrt{3}(d + d_0)^2}, \quad (48)$$

and the separation between the two extrema of

$$S_{pp} = \sqrt{2}(d + d_0), \quad (49)$$

It can be seen that B_{pp} is directly proportional to the volume of the sphere a^3 , and inversely proportional to the square of the distance to the center of the sphere $(d + d_0)^2$. And S_{pp} is proportional to the distance to the center of the sphere $d + d_0$, and is independent of the radius of the sphere.

Equation (49) is very useful, in that it provides the most convenient method to estimate the depth of the spherical flaw directly from the spacing between the two extrema of the field map. It is then possible to determine the dimension of the flaw if the applied current density is known by looking at the amplitude of the extrema (see Eq. (48)).

There is no simple analytical expressions for the second order approximation. In Figs. 5, there is only slight difference between the solid lines and the dashed lines for B_{pp} because of the logarithmic scale. The maximum difference for B_{pp} has been calculated as 7% for $(a/d) < 0.8$ (see Fig. 4b). In Fig. 6a the solid line deviate from the dashed line with increasing sphere radius. However, in Fig. 6b there is no difference between the solid line and the dashed line, which means that it is possible to use the simple dipole approximation, Eq. (49), to determine the depth of the sphere regardless the size of the sphere.

From Fig. 3, the percentage change of the current density disturbed by the planar surface is obvious larger than that of magnetic field disturbed. The reason is that the X component of magnetic field due to the perturbed J_θ is partially canceled by the field due to the perturbed J_ϕ .

Comparisons have been made with experimental data [9]. The test sample, as shown in Fig. 7a, is a rectangular brass bar containing a 4.7 mm radius spherical cavity, whose center is located 7.9 mm below the top surface. The SQUID sensor was at 2.8 mm above the surface of the bar.

The current distortion due to the bottom and side surfaces may be considered negligible, since the distance between the cavity and the bottom or side surfaces of the bar (> 17 mm) was much larger than the radius of the flaw. However, the discontinuities of the conductivity at edges do produce an additional background signal and, in order to compare with our present calculation which is for an infinite extent conductor, the background signal must be subtracted.

Figure 7b shows the experimental results after subtraction of the background signal. The small irregular shape, indicated by an arrow, in Fig. 7b may be caused by the solder leakage at the joint of the two halves during sample fabrication. Figure 7c is the magnetic field calculated from Eq. (47) using the same current density as in the experiment and fitting the parameters a and d . Figure 7d shows a cross-section comparison of the contour maps in Figs. 7b and 7c, with fit parameters of $a = 4.5$ mm and depth $d = 7.9$ mm, which are in good agreement with the actual values of $a = 4.7$ mm and $d = 7.9$ mm.

The results discussed above can be used for estimating the minimum size of a detectable flaw for various detectors. For example, from Fig. 5a, a SQUID magnetometer with a noise level of $100 \text{ fT}/\sqrt{\text{Hz}}$, (2 pT noise in 400 Hz bandwidth), can detect a 1 mm diameter sphere located 10 mm below the surface. Since the deeper flaw produces a signal with a broader peak and smaller amplitude, the detectability of a flaw is also limited by the noise other than the instrument, and the variations in the background due to the imperfect geometry of the test object.

IV. Conclusions

An analytic expression for the normal component of the magnetic signal due to a spherical inclusion embedded in a conducting plate carrying an static uniform current has been derived. The expression for second order approximation is valid under the condition of $(a/d)^6 \ll 1$, and the dipole approximation is valid if $(a/d) \ll 1$.

The results can be applied for quantitative non-destructive evaluation of subsurface flaws in a conductor. The simple dipole approximation may be used for determining the location and the dimension of the flaw within 7% of error. Although the actual geometry of flaws in general are not perfect spheres, the analytic expression of the solution provides a simple method to estimate the depth and dimensions of the flaw.

The results have been compared to experimental data recorded by a SQUID magnetometer, and the predictions of the model are in good agreement with experimental data.

Acknowledgements

We are grateful to Dr. Anthony P. Ewing for his valuable comments to the manuscript. This research has been supported by Air Force Office of Scientific Research Grant 87 0337 and by the Electric Power Research Institute. Tony

REFERENCES

1. "Nondestructive Testing Handbook", Vol 4, Electromagnetic Testing, R.C.McMaster, P. McIntire, and M. L. Mester, second edition, 1986.
2. W.G.Jenks, S.S.H.Sadeghi, and J.P. Wikswo,Jr., "SQUIDS for Non-Destructive Evaluation", *J. of Physics D: Applied Physics*, 30(3): 293-323, (1997).

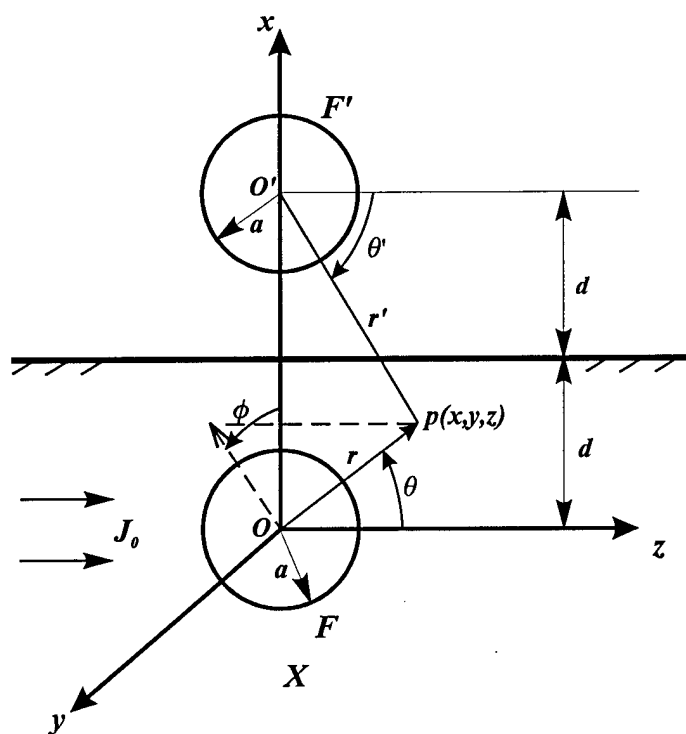


Figure 1. Illustration of the coordinate system for potential distribution.

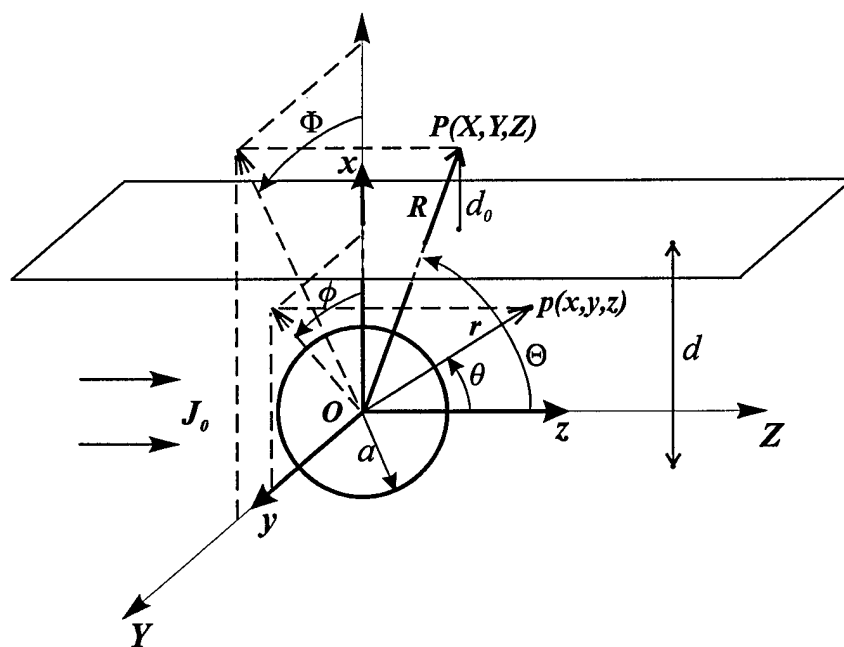


Figure 2. The coordinate system for the calculation of magnetic field.

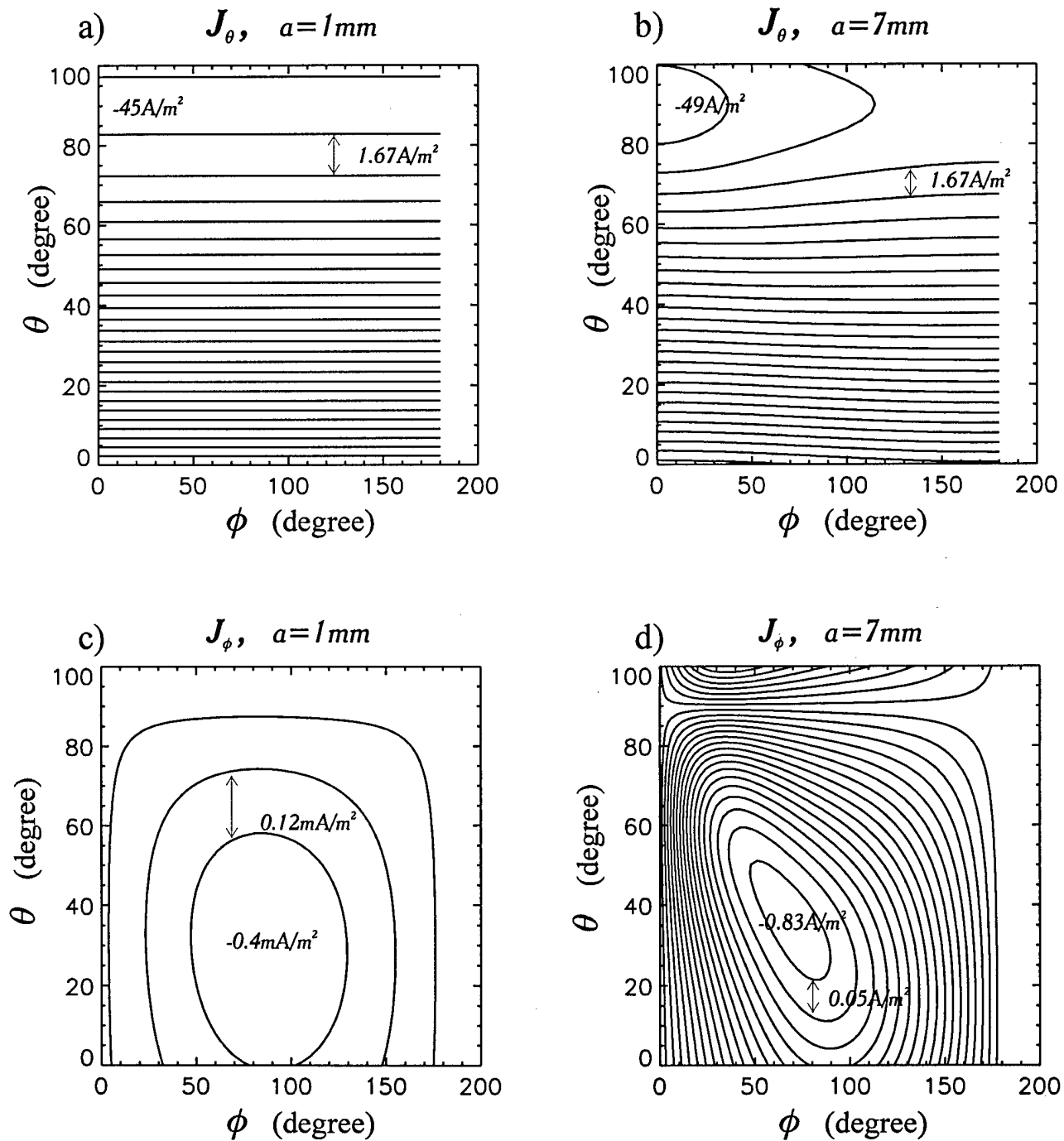


Figure 3. Calculated isocontour of the current distribution.

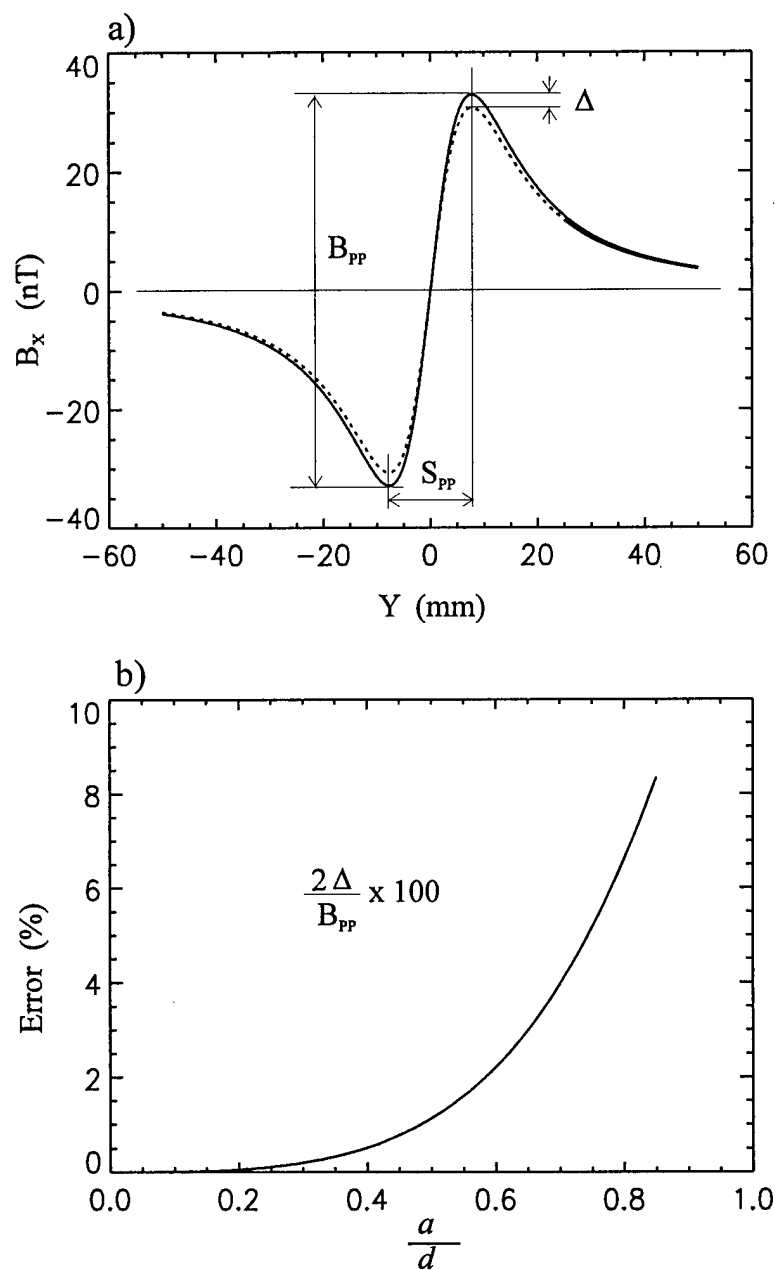


Figure 4. (a) Calculated magnetic field from a 8 mm radius sphere centers 10 mm below the surface. (b) The percentage error due to the far field approximation.

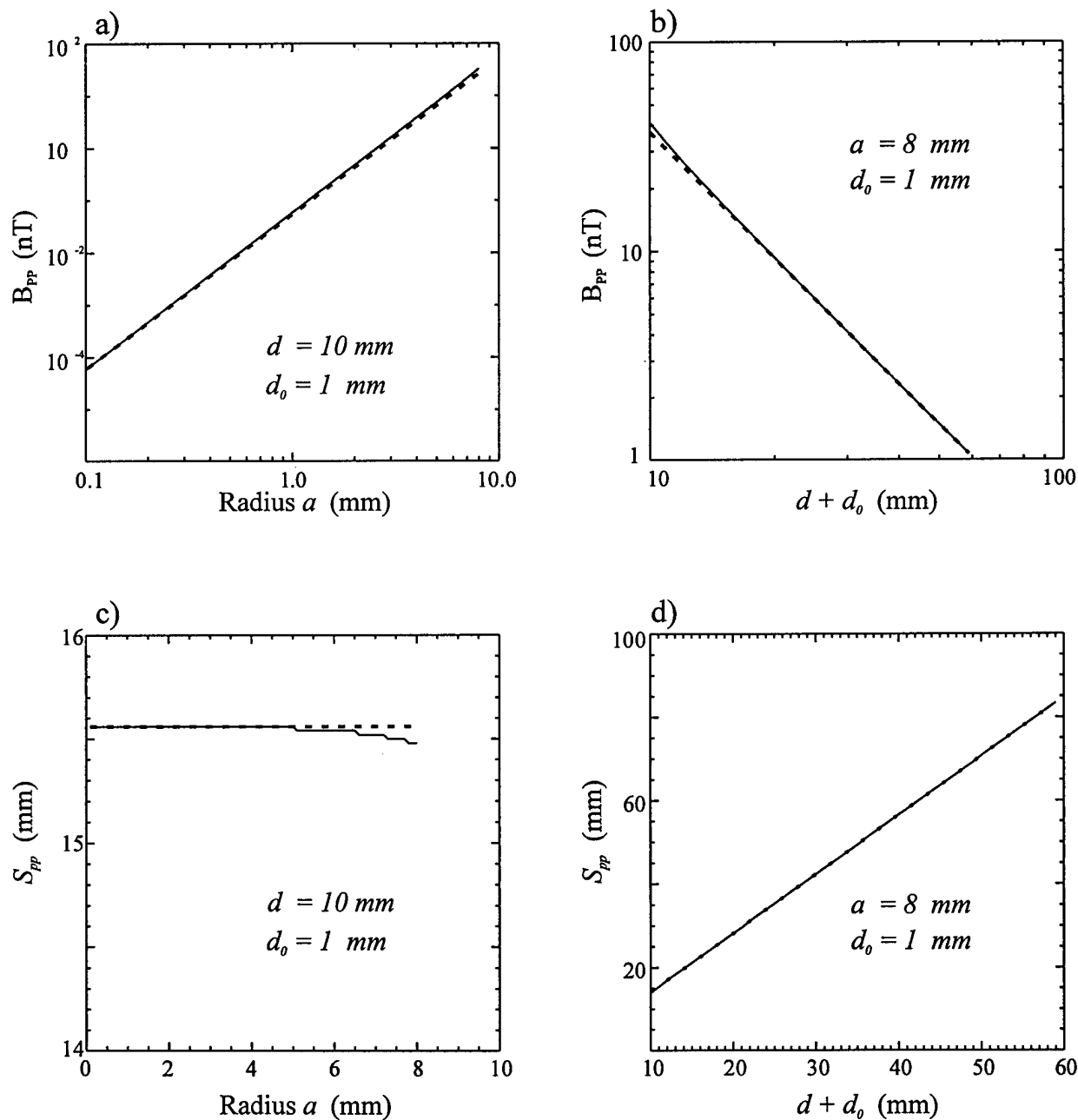


Figure 5. (a) and (b) Calculated parameters as function of radius of sphere. (c) and (d) Calculated parameters as function of the depth of the sphere.

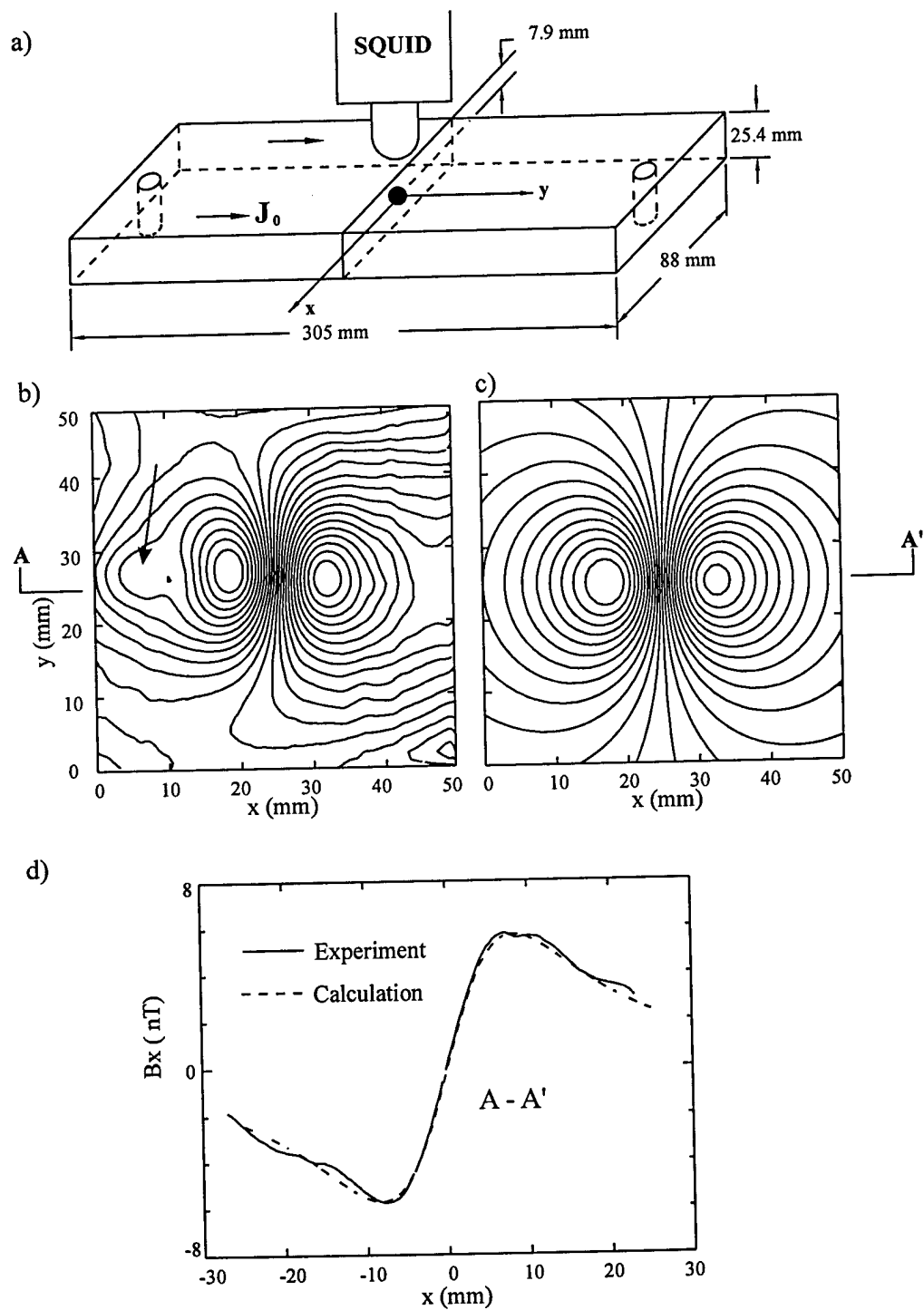


Figure 6. (a) Sketch of the sample. (b) Experimental data.. (c) Simulated map. (d) A cross section comparison.

APPENDIX 3

Magnetic Field Produced by a Plate With a Elliptic inclusion carrying a dc Current — Application for Flaw Detection

Yu Pei Ma and John P. Wikswo, Jr.

Electromagnetics Laboratory
Department of Physics and Astronomy
Vanderbilt University, Box 1807, Station B
Nashville, TN 37235

Abstract

The detection of a crack in a metal structure by electromagnetic method, mostly involved in the eddy current techniques, has been studied intensively. Recently developed high spatial resolution SQUID magnetometers are capable to measure the weak DC magnetic field, and have been used for detection of the flaw in a conductor. This paper is subject to find an analytic solution for the magnetic field due to an elliptic hole inside a conducting plate carrying a dc current. Then the magnetic field due to a slot is obtained by reducing the length of the minor-axis of the ellips, which overcomes the difficulty caused by the infinite current density at the ends of the slot. The solution may be used for quantitatively non-destructive evaluation of the cracks and inclusions, and may be applied for the low frequency ac magnetic field.

I. Introduction

The high spatial resolution SQUID magnetometers, which are able to detect the weak DC magnetic field, have been used for detection of the flaws in a conductor carrying a dc current. [1, Wikswo et al] For quantitatively evaluation of the dimension and the location of the flaw, the magnetic field produced by the disturbed dc current due to the flaws inside a conductor may be calculated either numerically or analitically.

II. Current Distribution

A. Electric Potential

For a homogenous, infinitely extended conducting plate, carrying a uniform current J_0 which is in the direction with an angle α respect to the x direction (see Fig. 1), the potential V_0 is

$$V_0 = -E_0(x \cos \alpha + y \sin \alpha), \quad (1)$$

where $E_0 = J_0/\sigma$ is the electrical field inside the conducting plate, and σ is the conductivity of the conductor.

When an elliptic cylindrical inclusion with the major axis $2a$ and minor axis $2b$ is located at the center and through the plate, the potential V near the inclusion is disturbed and it satisfies the Laplace's equation

$$\nabla^2 V = 0 . \quad (2)$$

In general the solutions of the Laplace's equation differ from each other in the nature of the boundary conditions applied. In the case of the elliptic boundary, the cartesian coordinates are not separable for the Laplace's equation. However, any coordinates obtained by conformal transformation from the rectangular coordinates (x, y) are separable coordinates for the Laplace's equation [1- Feshbach V1. 499]. The conformal transformation $z = c \cosh w$, where $z = x + iy$ and $w = \mu + i\theta$, gives rise of the elliptic coordinates, [2- Feshbach V2. 1195],

$$\begin{aligned} x &= c \cosh \mu \cos \theta \\ y &= c \sinh \mu \sin \theta , \end{aligned} \quad (3)$$

where $c = \sqrt{a^2 - b^2}$, $a = c \cosh \mu_0$ (major semi-axis) and $b = c \sinh \mu_0$ (minor semi-axis). Figure 2 shows the elliptic coordinates (μ and θ). The curves corresponding to $\mu = \text{constant}$ are ellipses. The ellipse for $\mu = 0$ becomes a straight line with a length of $2c$. The curves corresponding to $\theta = \text{constant}$ are hyperbolas with foci at $x = \pm c$.

Using elliptic coordinates, the Laplace's equation Eq. 2 becomes

$$\frac{\partial^2 V}{\partial \mu^2} + \frac{\partial^2 V}{\partial \theta^2} + \frac{\partial^2 V}{\partial z^2} = 0 , \quad (4)$$

and V can be separated as

$$V(\mu, \theta, z) = M(\mu)\Theta(\theta)Z(z) \quad (5)$$

The potential at infinity satisfies Eq. 1 which can be represented in the elliptic coordinate

$$V(\mu \rightarrow \infty) = -E_0(c \cosh \mu \cos \theta \cos \alpha + c \sinh \mu \sin \theta \sin \alpha) . \quad (6)$$

It is suggested that the conductivity of the inclusion cylinder $\mu = \mu_0$, the boundary conditions are

$$V_{out}(\mu, \theta) = V_{in}(\mu, \theta) \quad \mu = \mu_0 \quad (7)$$

$$\sigma \frac{\partial V_{out}(\mu, \theta)}{\partial \mu} = 0 \quad \mu = \mu_0, \quad (8)$$

where V_{out} and V_{in} are the potential outside and inside the cylinder, respectively. Because the boundary conditions Eqs. 6, 7 and 8 do not vary with the z , the potential V should be independent of the z . The equation becomes two-dimensional. Using conformal transformation, the potential outside the inclusion may be found. If the potential inside the inclusion is also desired, which is useful for a conducting inclusion with different conductivity with the plate, the method of separation should be used.

Using the method of separation, the solutions of Eq. 4, satisfying the boundary condition 6, 7 and 8 are:

$$V_{in}(\mu, \theta) = -E_0(a + b) \left(\frac{\cosh \mu}{\cosh \mu_0} \cos \theta \cos \alpha + \frac{\sinh \mu}{\sinh \mu_0} \sin \theta \sin \alpha \right) \quad \mu < \mu_0 \quad (9)$$

$$V_{out}(\mu, \theta) = -E_0(a + b) \cosh(\mu - \mu_0) \cos(\theta - \alpha) \quad \mu \geq \mu_0. \quad (10)$$

The potential V_{out} may be also found by conformal transformation.

B. Current distribution

In elliptic coordinates, the gradient of a scalar $V(\mu, \theta)$ is

$$\nabla V = \frac{1}{c} \frac{1}{\sqrt{\cosh^2 \mu - \cos^2 \theta}} \left[\frac{\partial V}{\partial \mu} \hat{e}_\mu + \frac{\partial V}{\partial \theta} \hat{e}_\theta \right], \quad (11)$$

where \hat{e}_μ and \hat{e}_θ are the unit vectors in the μ and θ direction, respectively. Then the electric field and the current density may be derived from

$$\vec{E} = -\nabla V, \quad (12)$$

$$\vec{J} = \sigma \vec{E}. \quad (13)$$

Because V_{in} may be written as

$$V_{in} = -E_0 e^{\mu_0} \left[\frac{x \cos \alpha}{\cosh \mu_0} + \frac{y \sin \alpha}{\sinh \mu_0} \right], \quad (14)$$

the electrical field inside the elliptic cylinder can be represented in the cartesian coordinate

$$\vec{E}_{in} = E_0(a+b) \left[\frac{\cos \alpha}{a} \hat{e}_x + \frac{\sin \alpha}{b} \hat{e}_y \right], \quad (15)$$

which is uniform with a different magnitude and direction from the applied field.

For the convenience of further calculations, the electric field outside the cylinder is represented in the elliptic coordinates

$$\vec{E}_{out} = \frac{E_0(a+b)}{c\sqrt{\cosh^2 \mu - \cos^2 \theta}} [\sinh(\mu - \mu_0) \cos(\theta - \alpha) \hat{e}_\mu - \cosh(\mu - \mu_0) \sin(\theta - \alpha) \hat{e}_\theta]. \quad (16)$$

Because the conductivity inside the cylinder is zero, the current at the boundary surface $\mu = \mu_0$ may be obtained from Eqs. 13 and 16,

$$\vec{J}(\mu, \theta)|_{\mu=\mu_0} = -J_0(a+b) \frac{\sin(\theta - \alpha)}{c\sqrt{\cosh^2 \mu_0 - \cos^2 \theta}} \hat{e}_\theta, \quad (17)$$

where $J_0 = \sigma E_0$ is the magnitude of the current density at infinity. The current is flowing only in the direction of \hat{e}_θ , i.e. tangential direction around the boundary of the ellips.

When $b \rightarrow 0$, $\mu_0 = 0$, the ellips becomes a thin slot with length $2a$ (see Fig.2). The current density is divergent at the two ends of the slot, $\theta = 0$, and $\theta = \pi$.

III. Magnetic field

The magnetic field produced by a current source $\vec{J}(\vec{r}')$ is given by the law of Biot-Savart, which can be written in the form [3- wikswol]

$$\vec{B}(\vec{r}) = \frac{\bar{\mu}_0}{4\pi} \int_{v'} \frac{\nabla' \times \vec{J}(\vec{r}')}{|\vec{r} - \vec{r}'|} dv' + \frac{\bar{\mu}_0}{4\pi} \int_{s'} \frac{\vec{J}(\vec{r}') \times \vec{n}}{|\vec{r} - \vec{r}'|} ds', \quad (18)$$

where $\bar{\mu}_0 = 4\pi \times 10^{-7} \text{H/m}$, \vec{n} is a unit vector normal to the bounding surface and in the outward direction from the region occupied by the current density. When the current is in the steady state, and the conductivity in the region of current flowing is a constant, $\nabla' \times \vec{J}(\vec{r}') = 0$, then the Eq. 17 becomes

$$\vec{B}(\vec{r}) = \frac{\bar{\mu}_0}{4\pi} \int_{s'} \frac{\vec{J}(\vec{r}') \times \vec{n}}{|\vec{r} - \vec{r}'|} ds'. \quad (19)$$

The surfaces s' include the top and bottom surfaces of the plate, $z = 0$ and $z = -h$, and the surface of the elliptic cylinder, $\mu = \mu_0$. In this paper, we are interested in the field component in the direction normal to the surface of the plate B_z only. At the top and bottom surface, $\vec{J}(\vec{r}') \times \vec{n}$ is in the $x - y$ plane, which do not contribute to the field component in the z direction. So that only the integral over the elliptic cylindrical surface should be calculated.

At the surface $\mu = \mu_0$, $\vec{n} = -\hat{e}_\mu$. From Eq. 16 and 18 the z component of the magnetic field is

$$\vec{B}_z(\vec{r}) = \frac{\bar{\mu}_0}{4\pi} \int_{s'} \frac{J_\theta(\mu_0, \theta)}{|\vec{r} - \vec{r}'|} ds' , \quad (20)$$

where s' is the elliptic cylindrical surface, and

$$ds' = c \sqrt{\cosh^2 \mu_0 - \cos^2 \theta} d\theta dz' . \quad (21)$$

The coordinate of a point on the elliptic surface s' is

$$\begin{aligned} x' &= c \cosh \mu_0 \cos \theta = a \cos \theta \\ y' &= c \sinh \mu_0 \sin \theta = b \sin \theta \\ z' &= z' . \end{aligned} \quad (22)$$

It is more convenient to use the Cartesian coordinate for the point outside the plate $\vec{r}(x, y, z)$,

$$|\vec{r} - \vec{r}'| = [\gamma + (z - z')^2 - \beta \sin^2 \theta - \eta \cos \theta - \xi \sin \theta]^{\frac{1}{2}} , \quad (23)$$

where

$$\begin{aligned} \gamma &= x^2 + y^2 + a^2 \\ \beta &= a^2 - b^2 \\ \eta &= 2ax \\ \xi &= 2by . \end{aligned}$$

Substituting Eq.16 and 22 into Eq.19, the z component of the magnetic field is

$$B_z(x, y, z) = \frac{\bar{\mu}_0 J_0(a + b)}{4\pi} \int_{-h}^0 (I_1 \sin \alpha - I_2 \cos \alpha) dz , \quad (24)$$

where

$$I_1 = \int_0^{2\pi} \frac{\cos \theta d\theta}{[\gamma + (z - z')^2 - \beta \sin^2 \theta - \eta \cos \theta - \xi \sin \theta]^{\frac{1}{2}}}, \quad (25)$$

$$I_2 = \int_0^{2\pi} \frac{\sin \theta d\theta}{[\gamma + (z - z')^2 - \beta \sin^2 \theta - \eta \cos \theta - \xi \sin \theta]^{\frac{1}{2}}}. \quad (26)$$

The integral I_1 and I_2 are the elliptic integrals involving trigonometric integrals. In principle, they may be expressed in terms of three basic elliptic functions and elementary functions [ref. handbook p242]. However, the calculations of the integrals I_1 and I_2 by using elliptic functions are extremely laborious and difficult. Our approach is to find a suitable series expansion that their approximation may fit the requirement of our application.

First we found that

$$\gamma - \beta \sin^2 \theta - \eta \cos \theta - \xi \sin \theta = (x - a \cos \theta)^2 + (y - b \sin \theta)^2 \geq 0. \quad (27)$$

We are interested in the magnetic field above the conducting plate, where $|z - z'| > 0$, we have

$$R^2 > \beta \sin^2 \theta + \eta \cos \theta + \xi \sin \theta, \quad (28)$$

where

$$R^2 = \gamma + (z - z')^2 = x^2 + y^2 + a^2 + (z - z')^2. \quad (29)$$

By introducing a parameter p which is always less than 1,

$$P = \frac{\beta \sin^2 \theta + \eta \cos \theta + \xi \sin \theta}{R^2}, \quad (30)$$

the denominator of the integral Eqs. 24 and 25 becomes $R(1 - p)^{\frac{1}{2}}$. Then it can be expanded in the binomial series of p

$$\frac{1}{R(1 - p)^{\frac{1}{2}}} = \frac{1}{R} \left[1 + \frac{1}{2}P + \frac{\frac{1}{2} \cdot \frac{3}{2}}{2!}P^2 + \dots + \frac{\frac{1}{2} \cdot \frac{3}{2} \cdots (\frac{1}{2} + n + 1)}{n!}P^n + \dots \right]. \quad (31)$$

The maximum of $|p|$ is found if $y = 0$, $x = \pm a^2 + (z - z')^2^{\frac{1}{2}}$ and $\theta = 0, \pi$, which is a function of $(z - z')/a$.

Substituting Eq. 28-30 to Eq.24 and 25, and integrating over θ , the I_1 and I_2 can be evaluated to the desired accuracy. Here we present the results up to the order of

P^3 :

$$I_1 = \frac{\pi ax}{R^3} + \frac{3\pi(a^2 - b^2)}{8} \frac{ax}{R^5} + \frac{15\pi}{64} [(a^2 - b^2)^2 + 8(a^2x^2 + b^2y^2)] \frac{ax}{R^7} + \dots, \quad (32)$$

$$I_2 = \frac{\pi by}{R^3} + \frac{9\pi(a^2 - b^2)}{8} \frac{by}{R^5} + \frac{15\pi}{64} [5(a^2 - b^2)^2 + 8(a^2x^2 + b^2y^2)] \frac{by}{R^7} + \dots, \quad (33)$$

Substituting Eq.31 and 32 to Eq.23 and then integrating over z' , the z component of the magnetic field can be evaluate by the formular

$$B_z = \frac{\bar{\mu}_0}{4} J_0(a+b) \times \left\{ \frac{ax}{R_0^2} \left[\Delta_1 + \frac{3(a^2 - b^2)}{8} G_1 + \frac{15}{64} [(a^2 - b^2)^2 + 8(a^2x^2 + b^2y^2)] G_2 + \dots \right] \sin \alpha - \frac{by}{R_0^2} \left[\Delta_1 + \frac{9(a^2 - b^2)}{8} G_1 + \frac{15}{64} [5(a^2 - b^2)^2 + 8(a^2x^2 + b^2y^2)] G_2 + \dots \right] \cos \alpha \right\} \quad (34)$$

where

$$\Delta_1 = \frac{z+h}{R_{z+h}} - \frac{z}{R_z}, \quad (35)$$

$$G_1 = \frac{1}{3} \Delta_3 + \frac{2}{3} \frac{1}{R_0^2} \Delta_1, \quad (36)$$

$$G_2 = \frac{1}{5} \Delta_5 + \frac{4}{15} \frac{1}{R_0^2} \Delta_3 + \frac{8}{15} \frac{1}{R_0^4} \Delta_1, \quad (37)$$

$$\Delta_3 = \frac{z+h}{R_{z+h}^3} - \frac{z}{R_z^3}, \quad (38)$$

$$\Delta_5 = \frac{z+h}{R_{z+h}^5} - \frac{z}{R_z^5}, \quad (39)$$

$$R_{z+h} = [x^2 + y^2 + a^2 + (z+h)^2]^{\frac{1}{2}}, \quad (40)$$

$$R_z = [x^2 + y^2 + a^2 + z^2]^{\frac{1}{2}}, \quad (41)$$

$$R_0 = [x^2 + y^2 + a^2]^{\frac{1}{2}}, \quad (42)$$

α is the angle of the current respected to the x axis.

There are three special cases:

(1) $a = b$, the elliptic cylinder becomes a circular cylinder. the Eq. 33 becomes

$$B_z(x, y, z) = \frac{\bar{\mu}_0 J_0 a^2}{2R_0^2} \left[\Delta_1 + \frac{15a^2}{8} (x^2 + y^2) G_2 + \dots \right] (x \sin \alpha - y \cos \alpha). \quad (43)$$

If the orientation of the current is choosen along the y axis, *i.e.* $\alpha = 90^\circ$, the magnetic field for the circular cylinder in Eq. is consistant with the expression derived by solving the Bessel equation. [ref. cylinder paper]

(2) $b \rightarrow 0$, the ellips degenerate to a very thin slot with length of $2a$. At the end of the slot, $\mu = 0$, $\theta = 0$ or $\theta = \pi$, the electric field in Eq.14 or the current density in Eq. 15 are divergent, which causes the difficulty when a numerical integration is used for evaluating the magnetic field. The analytical solution is useful because the divergence can be avoid. Let $b \rightarrow 0$ in Eq. 33, then we have

$$B_z(x, y, z) = \frac{\bar{\mu}_0 J_0 a^2}{4} \frac{x}{R_0^2} \left[\Delta_1 + \frac{3a^2}{8} G_1 + \frac{15a^2}{64} (a^2 + 8x^2) G_2 + \dots \right] \sin \alpha. \quad (44)$$

The magnetic field depends on the current component perpendicular to the slot only.

(3) $h/z \rightarrow 0$, the solution becomes two-dimensional. The terms Δ in Eq. can be written as

$$\Delta_1 = \frac{z+h}{R_{z+h}} - \frac{z}{R_z} = \left(\frac{1}{R_z} - \frac{z^2}{R_z^3} \right) h, \quad (45)$$

$$\Delta_3 = \frac{z+h}{R_{z+h}^3} - \frac{z}{R_z^3} = \left(\frac{1}{R_z^3} - \frac{3z^2}{R_z^5} \right) h, \quad (46)$$

$$\Delta_5 = \frac{z+h}{R_{z+h}^5} - \frac{z}{R_z^5} = \left(\frac{1}{R_z^5} - \frac{5z^2}{R_z^7} \right) h. \quad (47)$$

$$(48)$$

Then hJ_0 becomes the surface current density.

Application for Non-destructive Evaluation

The analytical solution of the magnetic field has been applied for non-destructive evaluation of the flaws in conducting material. Figures 3 shows the calculated magnetic field contour maps for four current orientations, $\alpha = 0^\circ, 30^\circ, 60^\circ, \text{and } 90^\circ$, indicated by arrows. In Fig. 3, column (a) is for a circular cylinder with $a = b = 4\text{mm}$, column (b) is for a elliptical cylinder with $a = 4\text{mm}$ and $b = 4\text{mm}$, and column (c) is for a very thin elliptic cylinder with $a = 4\text{mm}$ and $b = 0.1\text{mm}$. For each column, the contour intevels for the maps with different current orientations are the same. The thickness of the plate $h = 3\text{mm}$ and the lift-off distance $z = 3\text{mm}$ are used for all the calculations.

For a circular cylinder, as shown in Fig. 3a, the amplitude of the signal is independent of the current orientation, while the rotation of the dipole follows the

rotation of the current. The maps in column (b) of Fig. 3 shows that both the amplitude and orientation of the dipole are vary with the rotation of the current if $b < a$, however, the rotation of the dipole does not consistant with the current. When $b \ll a$, as shown in column (c), the amplitude of the dipole is almost zero if the current is along the major axis, while the dipoles do not rotate with the current at all.

The amplitude variations with the current orientation in Fig. 3 are plotted in Fig. 4. The solid line (a) is obtained from the data in Fig. 4a, which is for a circular cylinder ($b = a$). The lines (b) and (c) are related to the data in Figs. 4b and 4c, which are for elliptical cylinders ($b/a = 0.5$) and ($b/a = 0.1$), respectively. The variation of the amplitude is a measure of the axial symmetry. Then we define an assymmetric factor:

$$S = \frac{A_{max} - A_{min}}{A_{max} + A_{min}}, \quad (49)$$

where A_{max} and A_{min} are the maximum value and minimum value of the amplitude, as shown in Fig. 4. For a circular cylinder $a = b$, $S = 0$, while for a very thin elliptical cylinder $b \rightarrow 0$, $S = 1$. The relation between S and b is shown in Fig. 5a, which is non-linear. However, the relation between b and $1/(a + b)$ is almost linear, as shown as in Fig. 5b. The assymmetric factor has been used for the Self-referencing technique which was developed for detection of a crack beneath a fastener in aging aircraft NDE.

For quantatively evaluation of the location and dimension of the flaw, there are two useful parameters: amplitude of the signal A and the spacing between the maxima and the minima, ΔX_p . Figure 6 shows the calculated magnetic field signal for the ellips with $a = 0.5, 1, 5, 3.0, 4.5$ and 6.0 mm, where $b = 0.2$ mm, $h = 1.0$ mm, $z = 3.0$ mm, and $J_0 = 1.0$ A/m². The current is in the direction perpendicular to the major axis. Both the amplitude A and the spacing between the two extrema ΔX_p increases with the dimension of the ellips a .

If the dimension of the flaw is much less than the distance between the flaw and the detection coil, $a/z \ll 1$, Eq. 33 becomes

$$B_z = \frac{\mu_0}{4} \frac{J_0(a+b)}{(x^2 + y^2 + a^2)} \times \Delta_1 \times (ax \sin \alpha - by \cos \alpha). \quad (50)$$

Figure 7 shows the difference between the Eq. 34 (solid lines) and the far field approximation Eq. 50 (dotted lines), where $z = 3.0$ mm. When $a = 0.5$ mm, there is no difference between the two lines, which imply that the far field approximation can be used. For $a = z = 3.0$ mm, the difference is obvious. The relation between the signal

and the dimension a and location z are plotted in Fig. 8. Figure 8a and 8b are the parameters versus a , and Figs. 8c and 8d are parameters versus z . The solid lines are calculated from Eq. 34 and the dashed lines are from far field approximation. When $2a/z < 1$, the far field can be used that the amplitude of the field signal is proportional to the dimension a , and inversely proportional to the lift-off z .

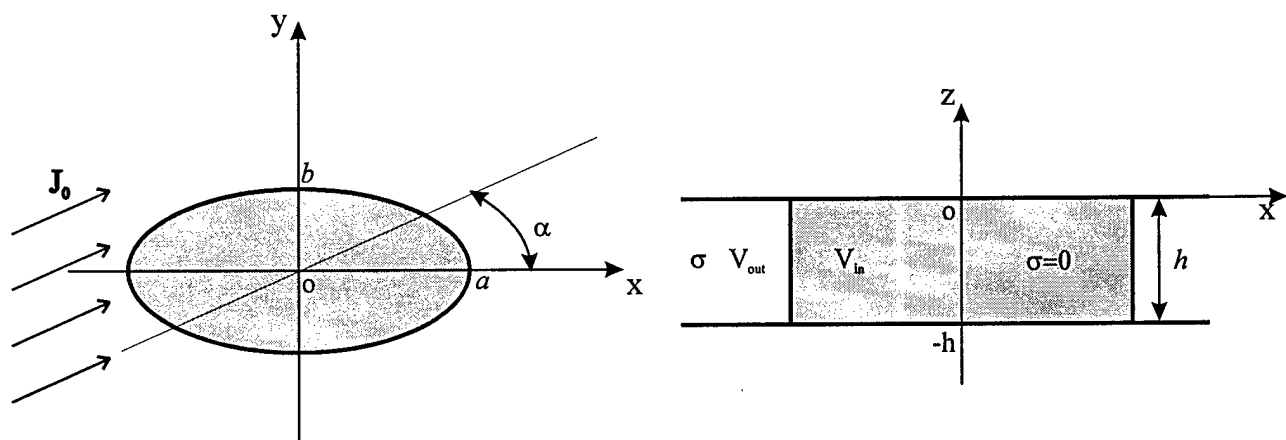


Figure 1. Illustration of coordinates.

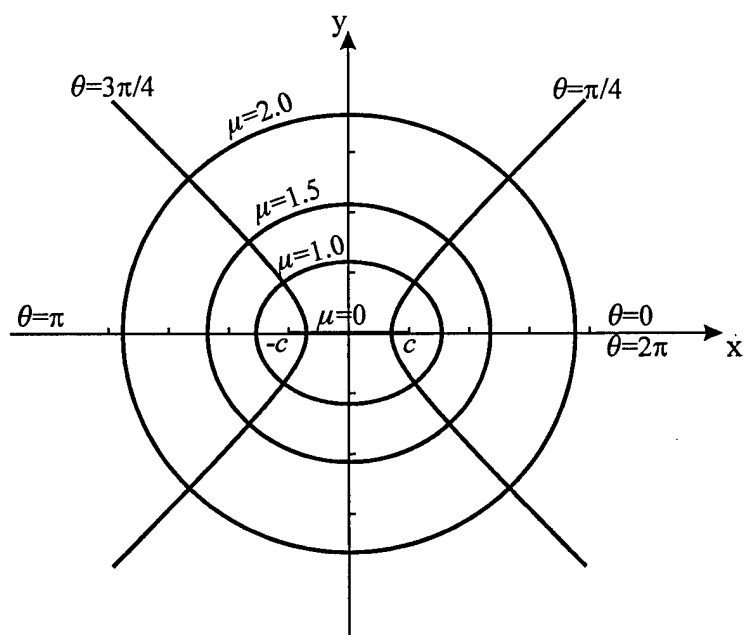


Figure 2. Elliptic coordinates used for calculation

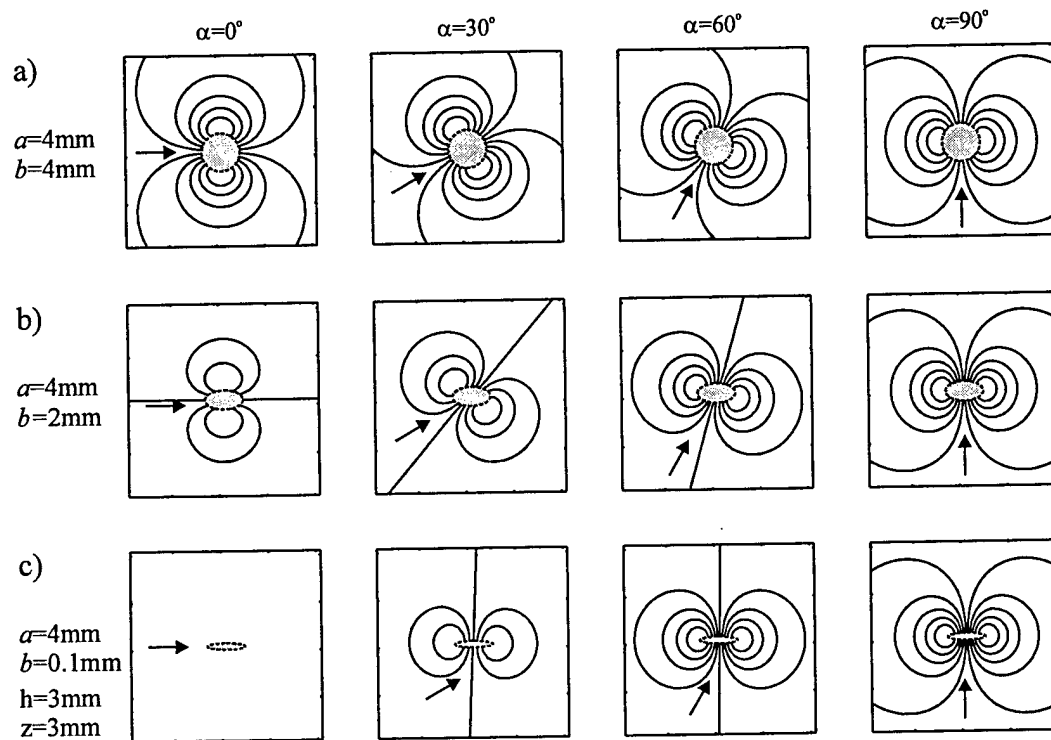


Figure 3. Calculated magnetic field contour maps for four current orientations.

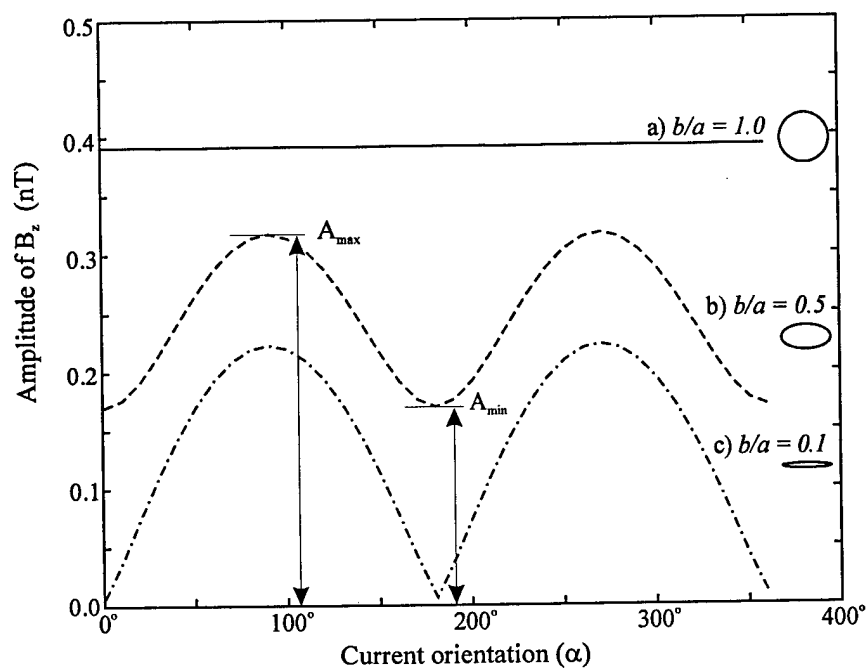


Figure 4. Amplitude of the signal as a function of current orientations

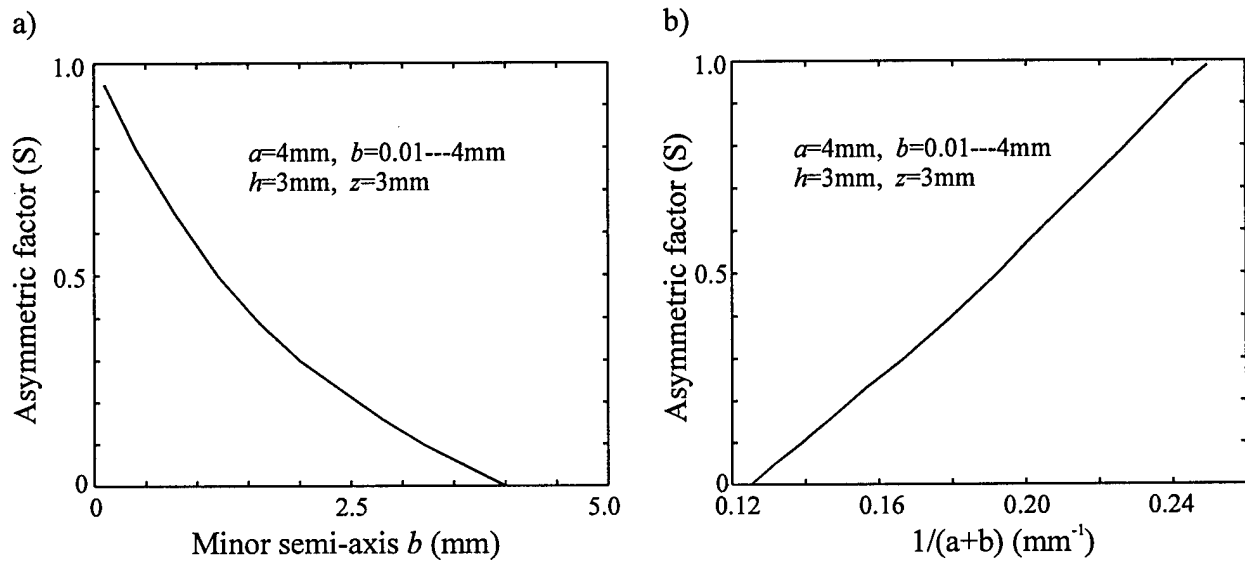


Figure 5. Asymmetric factor as a function of minor semi-axis b .

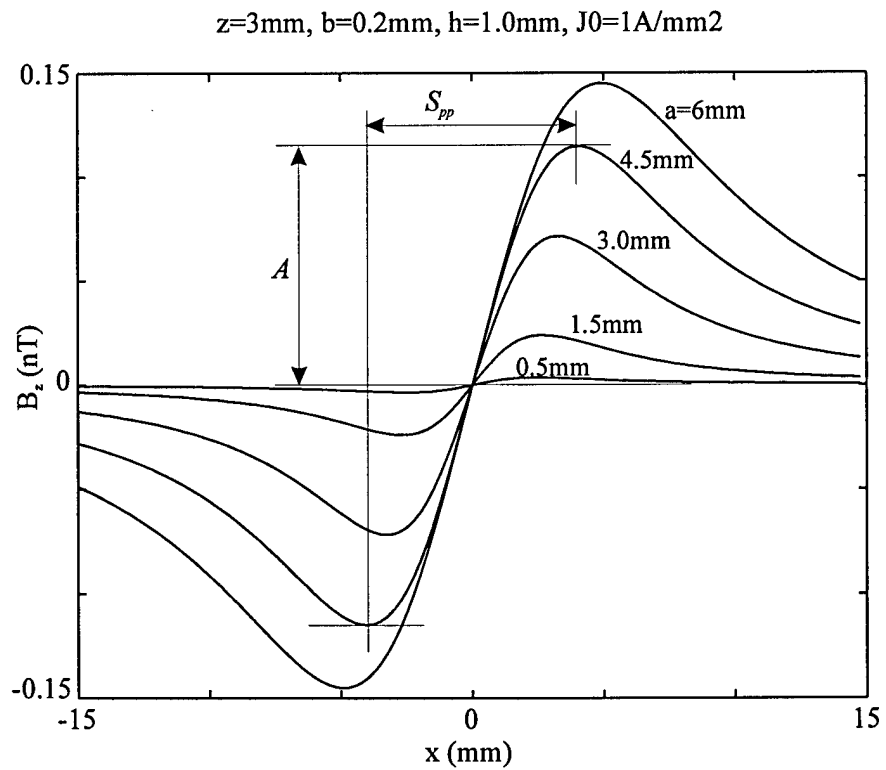


Figure 6. Calculated magnetic signal for the ellipse with $a = 0.5, 1.5, 3.0, 4.5$ and 6.0 mm

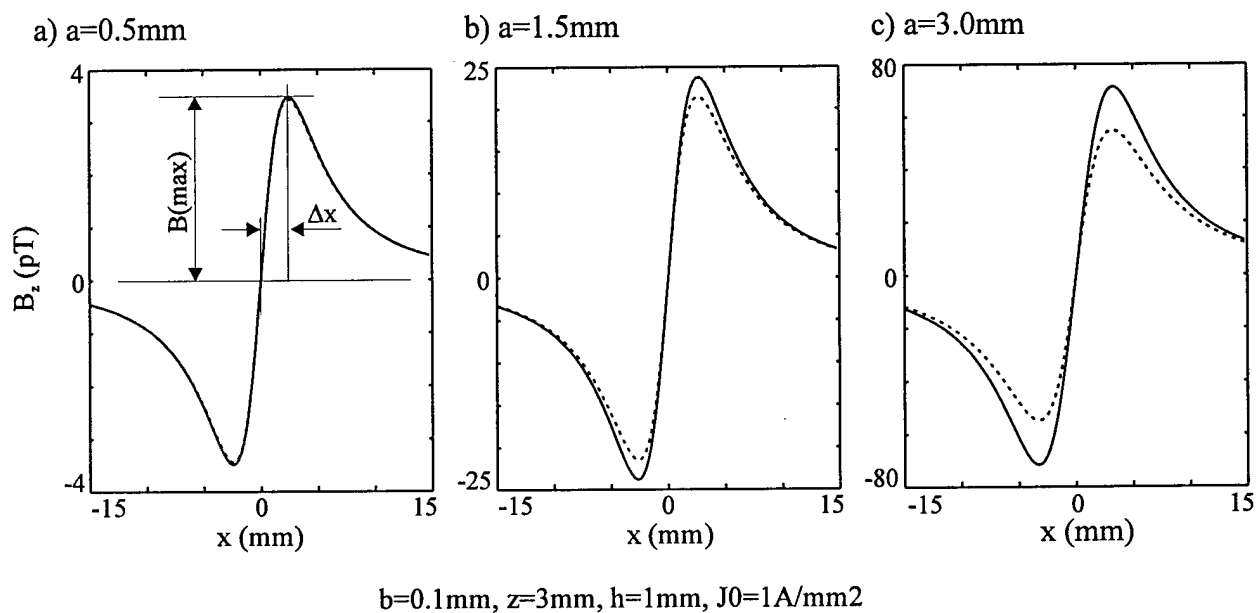


Figure 7. The amplitude difference between Eq. 34 (solid lines) and the far field approximation Eq. 50 (dotted lines).

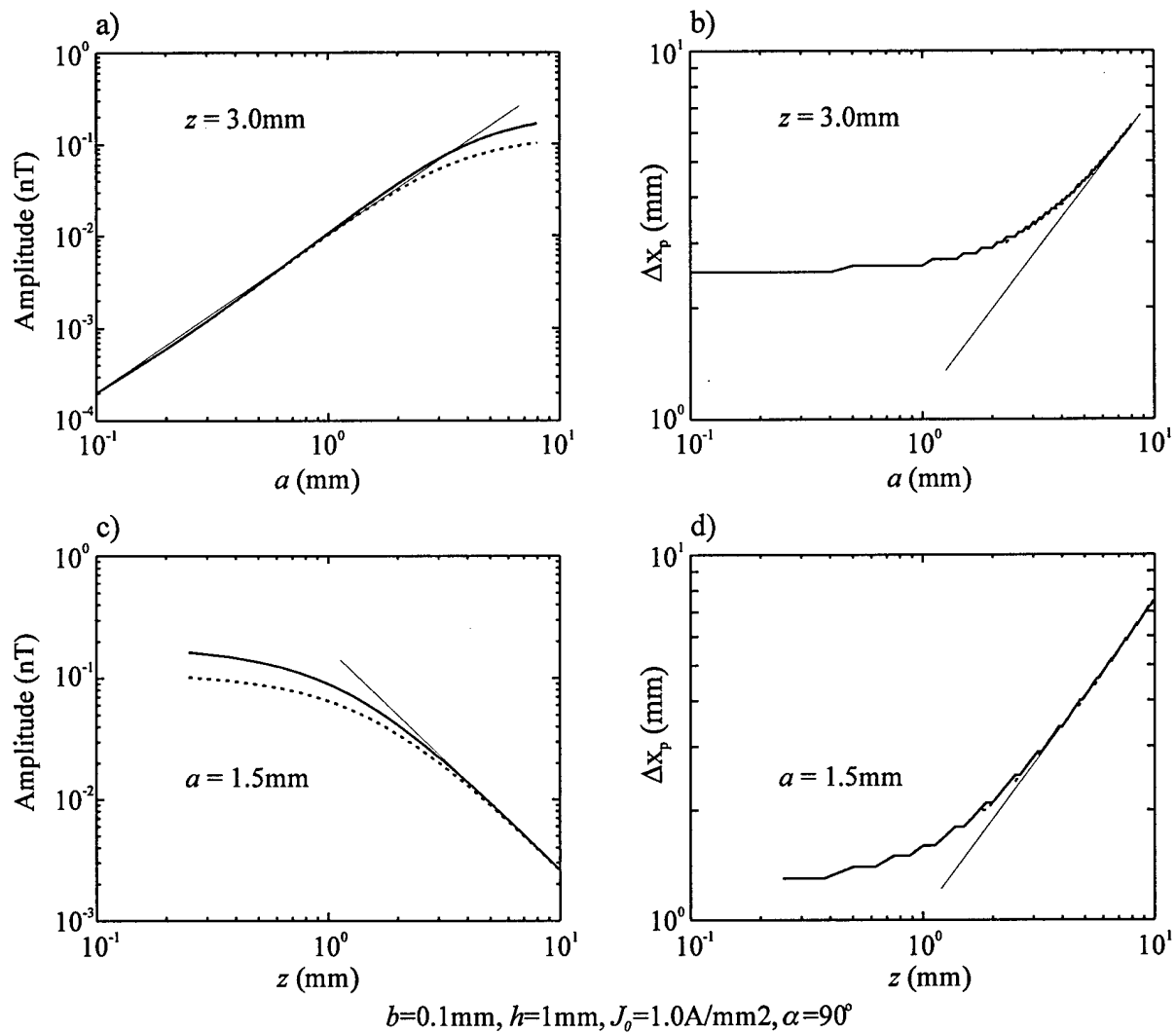


Figure 8. (a) and (b) The calculated parameters as a function of a . (c) and (d) The calculated parameters as function of z .

APPENDIX 4

Magnetic Field from a Cylindrical Flaw with Finite Length in a Conducting Plate Carrying a DC Current

Yu Pei Ma

Electromagnetics Laboratory

Department of Physics and Astronomy

Vanderbilt University, Nashville, TN 37235

Abstract

Recently developed high spatial resolution SQUID magnetometer is available to scan weak magnetic field close to the room temperature sample surface, It has been used for detection of the flaw in the conducting structure. This paper is subject to find an analytical expression of the magnetic field related to a flaw with a cylindrical geometry. By using a generalization of the Hankel integral transformation and constructing a suitable test function, the three dimensional electrical potential distribution disturbed by the flaw in a thick conducting plate has been solved exactly. Then the magnetic field profile due to such disturbed current has been calculated. The results would be useful for characterizing the flaw in the conductor.

1 Introduction

Recently developed high spatial resolution SQUID magnetometers are able to detect weak DC magnetic field, and they have been used for detection of the flaws in the metal structure. [1, Wikswo et al] For quantitatively evaluating the dimensions and the location of the flaw, the magnetic field produced by the disturbed current due to the flaws inside a conductor may be calculated either numerically or analytically. [ref. 2 nestors paper, 3 QNDE paper] For the convenience of the application, an analytic solution is always desirable if it is available.

In general the boundary-value problems in electric potential for a homogeneous media with cylindrical boundary may be solved using Hankel integral transformation. In the case of that the current flowing in an inhomogeneous media, such as a conducting plate with a flaw which conductivity is different from the plate, the solution must satisfy the boundary conditions which are involving in both Dirichlet and Neumann type at the surface between the plate and the flaw. For such special case, A. A. Inayat-Hussain

has found a set of quasiorthogonal eigenfunctions associated with the Bessel equation, which yields a new generalization of the Hankel integral transformation. [ref. 4 math] He has calculated the normal component of the magnetic field due to a dc current flowing through a semi-infinite cylinder inbedded in a half space beneath a conductive surface layer. (ref. 5 appli) The singular integral equation associated with the coefficient of the expressions of the electric potential has been solved exactly for a special case of an outcropping cylinder with no surface layer.

This work is subject to find an analytic solution of the magnetic field due to the dc current disturbed by a cylindrical flaw with finite depth in a thick conducting plate. It is assumed that the conducting plate is infinitely extended in the x-y direction, and the current density is uniformly distributed except the region near the flaw. The flaw has cylindrical geometry open at the surface and its length is finite. Using the mathematical technique developed by A. A. Inayat-Hussan, the solutions associated with the Bessel equation within the inhomogeneous region is expanded as a set of generalized eigenfunctions subject to the two coupled integral equations at the boundary between the homogeneous and inhomogeneous regions may be reduced to a single Cauchy singular integral equation. However, it is difficult to be solved in this case. This approaching is to introduce a suitable test function which satisfies the one of the dual integral equation, and then the exactly solutions of the coupled integral equation are achieved. The analytical expression of the magnetic field in the vertical direction is derived, which is easy to be evaluated numerically. The result provides an analytical method to estimate the dimension of a flaw inside the conductor.

2 Potential distribution

Figure 1 is the illustration of the cylindrical coordinates used for the calculation of the potential distribution. It is assumed that the conducting plate with thickness h and constant conductivity σ_1 is infinitely extended, a flaw which conductivity is σ_2 is cylindrical with radius a and depth d . The current is flowing uniformly along the x direction except the region near the flaw.

The electrical potential V satisfies the Laplace's equation:

$$\frac{\partial^2 V}{\partial \rho^2} + \frac{1}{\rho} \frac{\partial V}{\partial \rho} + \frac{1}{\rho^2} \frac{\partial^2 V}{\partial \theta^2} + \frac{\partial^2 V}{\partial z^2} = 0, \quad (1)$$

By separating variables, the solution of Eq.(1) may be written as

$$V_1(\rho, \theta, z) = R_1(\rho)Q(\theta)Z_1(z), \quad (2)$$

$$V_2(\rho, \theta, z) = R_2(\rho)Q(\theta)Z_2(z), \quad (3)$$

where V_1 is the potential at $h > z > d$ and V_2 is the potential at $d > z > 0$ as shown as in Fig. 1.

The current density in the conductor is given by

$$\vec{J}(\rho, \theta, z) = -\sigma \nabla V(\rho, \theta, z). \quad (4)$$

where σ is conductivity. At the boundary between two conducting mediums, both the potential and the normal component of the current density should be continual. At the bottom surface of the cylinder, $z = d$, the boundary conditions are

$$V_1|_{z=d} = V_2|_{z=d}, \quad (5)$$

$$\sigma_2 \frac{\partial V_2}{\partial z} \Big|_{z=d} = \sigma_1 \frac{\partial V_1}{\partial z} \Big|_{z=d} \quad a > \rho > 0, \quad (6)$$

$$\sigma_1 \frac{\partial V_2}{\partial z} \Big|_{z=d} = \sigma_1 \frac{\partial V_1}{\partial z} \Big|_{z=d} \quad \rho > a, \quad (7)$$

where σ_1 is the conductivity of conducting plate and σ_2 is the conductivity of the cylinder. At the cylindrical surface, $\rho = a$, the boundary conditions are

$$\lim_{\rho \rightarrow a^-} V_2 = \lim_{\rho \rightarrow a^+} V_2 \quad (8)$$

$$\lim_{\rho \rightarrow a^-} \sigma_2 \frac{\partial V_2}{\partial \rho} = \lim_{\rho \rightarrow a^+} \sigma_1 \frac{\partial V_2}{\partial \rho}. \quad (9)$$

At the top and bottom surface of the plate, $z = 0$ and $z = h$, there is no current flow in the z direction, the boundary conditions are

$$\frac{\partial V_1}{\partial z} \Big|_{z=h} = \frac{\partial V_2}{\partial z} \Big|_{z=0} = 0. \quad (10)$$

At $\rho \rightarrow \infty$ and $h \geq z \geq 0$

$$V \rightarrow -E_0 \rho \cos \theta, \quad (11)$$

It is well known that the eigenfunctions of $Q(\theta)$ are $\sin n\theta$ and $\cos n\theta$, and the eigenfunctions of $Z(z)$ are $e^{\lambda z}$ and $e^{-\lambda z}$. The function $R(\rho)$ is associated with Bessel equation

$$\frac{1}{\rho} \frac{d}{d\rho} \left[\rho \frac{d}{d\rho} R(\rho) \right] + \left(\lambda^2 - \frac{n^2}{\rho^2} \right) R(\rho) = 0, \quad (12)$$

where n is integer and $\lambda \geq 0$. At $\rho = 0$, $R(\rho)$ must be finite. The eigenfunctions of R_1 are Bessel function of the first kind $J_n(\lambda\rho)$. $R_2(\rho)$ must satisfy the boundary condition at $\rho = a$ from Eq. (9) and (10):

$$\lim_{\rho \rightarrow a^-} R_2(\rho) = \lim_{\rho \rightarrow a^+} R_2(\rho), \quad (13)$$

$$\lim_{\rho \rightarrow a^-} \sigma \frac{dR_2(\rho)}{d\rho} = \lim_{\rho \rightarrow a^+} \frac{dR_2(\rho)}{d\rho}, \quad (14)$$

where $\sigma = \sigma_2/\sigma_1$. The eigenfunctions of $R_2(\rho)$ subject the conditions above are given by [A.A.Inayat-Hussain math]

$$\Psi_n(\rho, \lambda; a, \sigma) = \begin{cases} J_n(\lambda\rho) & 0 < \rho < a \\ (\pi\lambda a/2)[M(\lambda a)J_n(\lambda\rho) - N(\lambda a)Y_n(\lambda\rho)] & \rho > a \end{cases} \quad (15)$$

where

$$M(\lambda a) = J_n(\lambda a)Y_n'(\lambda a) - \sigma J_n'(\lambda a)Y_n(\lambda a), \quad (16)$$

$$N(\lambda a) = (1 - \sigma)J_n(\lambda a)J_n'(\lambda a), \quad (17)$$

where $J_n(x)$ is the Bessel function of the first kind, $Y_n(x)$ is the Weber function (or Neumann function) of order n , $J_n'(\lambda a)$ and $Y_n'(\lambda a)$ are $(d/dx)J_n(x)$ and $(d/dx)Y_n(x)$ at $x = \lambda a$, respectively. The functions Ψ_n are quasiorthogonal with a discontinuous weight function $\omega(\rho)$ [A.A.]:

$$\lambda[\Omega_n(\lambda)]^{-1} \int_0^\infty d\rho \omega(\rho) \Psi_n(\rho, \lambda; a, \sigma) \Psi_n(\rho, \mu; a, \sigma) = \delta(\lambda - \mu), \quad (18)$$

where

$$\omega(\rho) = \begin{cases} \sigma\rho, & 0 < \rho < a \\ \rho, & \rho > a \end{cases} \quad (19)$$

and $\Omega_n(\lambda)$ is a positive definite function:

$$\begin{aligned} \Omega_n(\lambda) = & (\pi\lambda a/2)^2 \{ J_n^2(\lambda a)[J_n'^2(\lambda a) + Y_n'^2(\lambda a)] - \\ & 2\sigma J_n(\lambda a)J_n'(\lambda a)[J_n(\lambda a)J_n'(\lambda a) + Y_n(\lambda a)Y_n'(\lambda a)] + \\ & \sigma^2 J_n'^2(\lambda a)[J_n^2(\lambda a) + Y_n^2(\lambda a)] \}. \end{aligned} \quad (20)$$

And then Ψ_n in Eq.(15) can be used as a basis for the expansion of $R_2(\rho)$. The general solution of the Laplace's equation (1) subject to the boundary conditions (6) (7) (11) and (12) may be written as

$$V_1 = -E_0\rho \cos \theta +$$

$$\begin{aligned}
& \frac{1}{2\pi} \sum_{n=0}^{\infty} (2 - \delta_{n,0}) \cos n\theta \int_0^{\infty} d\lambda B_n(\lambda) \lambda J_n(\lambda\rho) [e^{\lambda(z-h)} + e^{-\lambda(z-h)}], \quad (21) \\
V_2 &= -E_0 \xi(\rho) \cos \theta + \\
& \frac{1}{2\pi} \sum_{n=0}^{\infty} (2 - \delta_{n,0}) \cos n\theta \int_0^{\infty} d\lambda A_n(\lambda) [\Omega_n(\lambda)]^{-1} \lambda \Psi_n(\rho, \lambda; a, \sigma) [e^{\lambda z} + e^{-\lambda z}], \quad (22)
\end{aligned}$$

where $\delta_{n,0}$ is Kronecker delta and

$$\xi(\rho) = \begin{cases} (\frac{2}{\sigma+1})\rho, & 0 \leq \rho < a \\ \rho - (\frac{\sigma-1}{\sigma+1})\frac{a^2}{\rho}, & \rho > a \end{cases}. \quad (23)$$

It is noticed that $E_0 \rho \cos \theta$ is the potential in the region I (without the cylinder) if region II does not exist, while $E_0 \xi(\rho) \cos \theta$ is the potential in the region II (with cylinder) if the region I does not exist, and they are the source of the current.

The coefficients $A_n(\lambda)$ and $B_n(\lambda)$ in (21) and (22) can be determined uniquely by the boundary conditions at $z = d$. Substituting V_1 and V_2 , Eq. (21) and (22), into Eq. (7),

$$\begin{aligned}
E_0[\rho - \xi(\rho)]\delta_{n1} &+ \frac{1}{\pi} \int_0^{\infty} d\lambda A_n(\lambda) [\Omega_n(\lambda)]^{-1} \lambda \Psi_n(\rho, \lambda; a, \sigma) [e^{\lambda d} + e^{-\lambda d}] = \\
& \frac{1}{\pi} \int_0^{\infty} d\lambda B_n(\lambda) \lambda J_n(\lambda\rho) [e^{\lambda(d-h)} - e^{-\lambda(d-h)}]. \quad (24)
\end{aligned}$$

Substituting Eqs.(21) and (22) into Eqs.(8) and (9),

$$\begin{aligned}
& \frac{\omega(\rho)}{\rho} \int_0^{\infty} d\lambda A_n(\lambda) [\Omega_n(\lambda)]^{-1} \lambda^2 \Psi_n(\rho, \lambda; a, \sigma) (e^{\lambda d} - e^{-\lambda d}) = \\
& \int_0^{\infty} d\lambda B_n(\lambda) \lambda^2 J_n(\lambda\rho) [e^{\lambda(d-h)} - e^{-\lambda(d-h)}]. \quad (25)
\end{aligned}$$

When $n \neq 1$, the first term in the left of the Eq. (24) becomes zero. Then the coupled integral equation (24) and (25) can be satisfied only if $A_n(\lambda) = B_n(\lambda) = 0$. The coefficient $A_n(\lambda)$ and $B_n(\lambda)$ have non-zero solution only when $n = 1$.

Using the standard integrals involving in Ψ_1 and $J_1(\mu\rho)$: [Hussain Phys.]

$$\begin{aligned}
\int_0^{\infty} d\rho \rho J_1(\mu\rho) \Psi_1(\rho, \lambda; a, \sigma) &= (1 - \sigma)(\mu^2 - \lambda^2)^{-1} \lambda a J_1(\mu a) J_1'(\lambda a) + \\
& \frac{\pi a}{2} [J_1(\mu a) Y_1'(\mu a) - \sigma J_1'(\mu a) Y_1(\mu a)] \times \delta(\mu - \lambda), \quad (26)
\end{aligned}$$

and

$$\int_0^\infty d\rho \omega(\rho) J_1(\mu\rho) \Psi_1(\rho, \lambda; a, \sigma) = (1 - \sigma)(\mu^2 - \lambda^2)^{-1} \mu a J_1'(\mu a) J_1(\lambda a) + \frac{\pi a}{2} [J_1(\mu a) Y_1'(\mu a) - \sigma J_1'(\mu a) Y_1(\mu a)] \times \delta(\mu - \lambda) \quad (27)$$

applying Hankel operator $\int_0^\infty \rho J_1(\mu\rho) d\rho$ to both side of (24) and (25), taking $n = 1$, the equation (24) and (25) may be reduced to a single Cauchy singular integral equation of $A_1(\lambda)$. However, the exactly solution of this singular integral equation is difficult to be achieved especially in the case of that the cylindrical boundary has finite length and the conductivities of the plate and the flaw are visible different.

Our approaching is to find a test function which satisfies the one of the boundary conditions at $z = d$. We assume that the conductivity of the flaw $\sigma_2 = 0$, and the depth of the flaw is much less than the thickness of the plate $d \ll h$. In the case of $n = 1$ and $\sigma = 0$ the function Ψ_n in (15) becomes

$$\Psi_1(\rho, \lambda; a, 0) = \begin{cases} J_1(\lambda\rho) & 0 < \rho < a \\ (\pi\lambda a/2) J_1(\lambda a) \Phi_1(\rho, \lambda; a) & \rho > a \end{cases} \quad (28)$$

where

$$\Phi_1(\rho, \lambda; a) = Y_1'(\lambda a) J_1(\lambda\rho) - J_1'(\lambda a) Y_1(\lambda\rho). \quad (29)$$

Then (25) reduced to a dual integral equation:

$$\int_0^\infty d\lambda B_1(\lambda) \lambda^2 J_1(\lambda\rho) [e^{\lambda(d-h)} - e^{-\lambda(d-h)}] = \begin{cases} 0 & 0 < \rho < a \\ I & \rho > a \end{cases} \quad (30)$$

where

$$I = \int_0^\infty d\lambda A_1(\lambda) [\Omega_1(\lambda)]^{-1} \lambda^2 (\pi\lambda a/2) J_1(\lambda a) \Phi_1(\rho, \lambda; a) [e^{\lambda d} - e^{-\lambda d}] \quad (31)$$

Then we introduce a test function into (35) as following:

$$B_1(\lambda) = \frac{\sin \lambda a}{\lambda^2} [e^{\lambda(d-h)} - e^{-\lambda(d-h)}] \times f(h, E_0, a) \quad (32)$$

where $f(h, E_0, a)$ is an unknown function needed to be determined. Substituting (32) to (30), we noted that the dual integral equation (30) is satisfied automatically if $\rho < a$. When $\rho > a$, it becomes

$$\frac{a}{\rho\sqrt{\rho^2 - a^2}} \times f(h, E_0, a) = I \quad (33)$$

Applying an integral operator $\int_a^\infty \Phi_1(\rho, \lambda; a) \rho d\rho$ to both side of (33) and using the integral representations of the Dirac δ function[A-A, J.math.phys. 30, 1989, p.41]:

$$\delta(\lambda - \mu) = \lambda [J_\nu'^2(\lambda a) + Y_\nu'^2(\lambda a)]^{-1} \int_a^\infty d\rho \rho \Phi_\nu(\rho, \lambda; a) \Phi_\nu(\rho, \mu; a) \quad (34)$$

we obtain

$$A_1(\mu) = \frac{\pi a J_1(\mu a) [Y_1'(\mu a) \sin(\mu a) + J_1'(\mu a) \cos(\mu a)]}{2\mu [e^{\mu d} - e^{-\mu d}]} \times f \quad (35)$$

To determine the function $f(h, E_0, a)$ and A_1 , the coupled integral equation (24) must be satisfied. Substituting the test function (32) to (24), taking $n = 1$ and $\sigma_2 = \sigma = 0$, applying the integral operator $\int_a^\infty \Phi_1(\rho, \mu; a) \rho d\rho$ to both side of (24), using the formula (34), and making an approximation if $d \ll h$

$$\frac{e^{\lambda(d-h)} + e^{-\lambda(d-h)}}{e^{\lambda(d-h)} - e^{-\lambda(d-h)}} \approx -1 \quad (36)$$

we obtain

$$A_1(\mu) = (-f + E_0 \pi a) \frac{J_1(\mu a)}{\mu^2 (e^{\mu d} + e^{-\mu d})} \quad (37)$$

Then the function $f(h, E_0, a)$ can be determined by (35) and (37)

$$f(h, E_0, a) = \frac{2E_0 L_-}{\mu [Y_1'(\mu a) \sin(\mu a) + J_1'(\mu a) \cos(\mu a) + (2/\pi \mu a) L_-]} \quad (38)$$

where

$$L_- = \frac{e^{\mu d} - e^{-\mu d}}{e^{\mu d} + e^{-\mu d}} \quad (39)$$

The coefficient $A_1(\mu)$ and $B_1(\mu)$ can be determined from (32), (35) or (37) straightforward, and the potential distribution can be solved exactly for the thick plate.

3 Magnetic Field

The magnetic field for a current density $\vec{J}(\vec{r}')$ is given by Biot-Savart Law. In our case, the conductivity σ_1 of the plate is constant except the hole region, the current is steady flow and no charge is accumulated in the conducting region, the magnetic field can be written as a surface integral [Wikswow, Biot-Savart ref]

$$B(\vec{R}) = \frac{\mu_0}{4\pi} \iint_S \frac{\vec{J}(\vec{r}) \times \vec{n}}{|\vec{R} - \vec{r}|} dS \quad (40)$$

where S is the boundary surface of the region occupied by current, i.e. the interface between the conducting and the insulating region. $\vec{J}(\vec{r})$ is the current density on the

bounding surface S , and \vec{n} is the unit vector normal to the surface S and points the insulating region. At the top and bottom surface of the plate, the currents are flowing in the x, y plane and the normal unit vector \vec{n} are in the $\pm z$ direction. It does not produce the magnetic field in the z direction. At the bounding surface of the cylindrical flaw the \vec{J} at the bottom surface of the flaw does not contribute to B_z same as in the top and bottom surface of the plate. The only non-zero contribution is from the current flowing at side surface of the flaw. At $\rho = a$ the normal unit vector $\vec{n} = -\hat{e}_\rho$ and the current density is $\vec{J}(\vec{r})' = -\sigma_1 \nabla V_2|_{\rho=a}$. The only current J_o , which is the component in the direction of \hat{e}_o , produces the field in the z direction. At $\rho = a$ the function $\phi_1(a\lambda; a) = \frac{2}{\pi\lambda a}$. Substitute the current $J_o = -\frac{\sigma_1}{a} \frac{\partial V_2}{\partial o}|_{\rho=a}$ into eq. (38). We have

$$B_z(R, \theta, Z) = -\frac{\mu_o \sigma_1 Z_o a}{2\pi} \int_0^d d\delta \int_0^{2\pi} \frac{\sin\sigma d\sigma}{[a^2 + R^2 - 2aR \cos(\sigma - \theta) + (Z - \delta)^2]^{1/2}} + \frac{1}{\pi} \int_0^d d\delta \int_0^{2\pi} \frac{\sin\theta d\sigma \int_0^\infty d\gamma A_1 \gamma [\Omega_1(\gamma)]^{-1} \gamma J_1(\gamma a) (e^{\gamma\delta} - e^{-\pi\delta})}{[a^2 + R^2 - 2aR \cos(\sigma - \theta) + (Z - \delta)^2]^{1/2}} \quad (41)$$

By substituting the expansion of Green's function for the $e^{-p/Z - \delta dP}$ case of no boundary surfaces:

$$\frac{1}{|\vec{R} - \gamma'|} = \int_0^\infty \sum_{n=0}^\infty (2 - \delta o n) [\cos n(y - y_1)] J_n(PR) J_n(pa) [a^2 + R^2 - 2aR \cos\theta + (Z - \theta)^2]^{1/2} = \int_0^\infty dp \sum_{n=0}^\infty (2 - \delta n, o) \cos n\theta J_n(ap) J_n(Rp) e^{-/Z - \theta/p} \quad (42)$$

where $\sigma = \sigma - \theta$, we obtain

$$\int_0^{2\pi} \frac{\sin\sigma d\sigma}{[a^2 + R^2 - 2aR \cos(\sigma - \theta) + (Z - \delta)^2]^{1/2}} = 2\pi \sin\sigma \int_0^\infty dp J_1(ap) J_1(Rp) e^{-/Z - \delta'/p} \quad (43)$$

The integral of the Bessel function in eq. (41) can be expressed by the hypergeometric function:

$$\int_0^\infty dP J_1(ap) J_1(RP) e^{/Z - \delta'/p} = \frac{aR}{2[a^2 + R^2 + (Z - \delta)^2]^{3/2}} F\left(\frac{5}{4}, \frac{3}{4}, 2, \chi\right)$$

where

$$\chi = \left[\frac{2aR}{a^2 + R^2 + (Z - \delta)^2} \right]^2, < 1 \quad (44)$$

when $Z - \delta \neq 0$. Substituting (41) and () to (39) we get the magnetic field in the z direction

$$\begin{aligned}
B_z(R, \theta, Z) = & -\frac{\mu_o}{2} J_o a^2 R \sin \theta \int_0^d \frac{dz}{[a^2 + R^2 + (Z - \delta)^2]^{3/2}} F\left(\frac{5}{4}, \frac{3}{4}, 2, \chi\right) \\
& + \frac{\mu_o a R}{4\pi} \sin \Phi \int_0^\infty d\gamma A_1(\gamma) [\Omega_1(\gamma)]^{-1} \gamma J_1(\gamma a) \\
& \times \int_0^d \frac{dz(e^{\gamma\delta} + e^{-\gamma\delta})}{[a^2 + R^2 + (Z - \delta)^2]^{3/2}} F\left(\frac{5}{4}, \frac{3}{4}, 2, \chi\right) \quad (45)
\end{aligned}$$

$A_1(\gamma)$ is shown in eq. (35)-(37), where

$$\chi = \left[\frac{2aR}{a^2 + R^2 + (Z - \delta)^2} \right]^2$$

and function $F\left(\frac{5}{4}, \frac{3}{4}, 2; \chi\right)$ can be expanded as a series of polynomial to any order of χ .

4 Discussions

The magnetic field as shown in eq. (43) has two terms. The first term is related to a cylindrical flaw through the conducting plate, i.e. the thickness of the plate is the same as the depth of the hole $h = d$. It is easy to write the field when the flaw is conducting material with conductivity $\sigma \pm o$ by multiplying a factor of $\left(\frac{1-\sigma}{1+\sigma}\right)$, where $\sigma = \frac{\sigma_2}{\sigma_1}$. If the diameter of the hole is smaller than the distance from the top of the plate, i.e. $a \ll |Z_o|$, the function $F\left(\frac{5}{4}, \frac{3}{4}, 2; \chi\right)$ eq. (43) can be expanded to the order of $O(x^3)$ then integrating it over z , we obtain

$$\begin{aligned}
B_z(R, \theta, Z_o) = & -\frac{\mu_o}{2} \left(\frac{1-\sigma}{1+\sigma}\right) \frac{J_o a^2 R \sin \theta}{R_o^2} \left\{ \left[\frac{Z}{R_z} - \frac{Z-h}{R_{z-h}} \right] \right. \\
& + \frac{3a^2 R^2}{8} \left[\left(\frac{Z}{R_z} - \frac{Z-h}{R_z^5} \right) + \frac{4}{3R_o^2} \left(\frac{Z}{R_z^3} - \frac{Z-h}{R_{z-h}^3} \right) \right]
\end{aligned}$$

$$+ \frac{8}{3R_o^4} \left(\frac{Z}{R_z} - \frac{Z-h}{R_{z-h}} \right) \Big] + \dots \Big\} \quad (46)$$

where

$$\begin{aligned} R_o^2 &= a^2 + R^2 \\ R_z^2 &= a^2 + R^2 + Z_o^2 \\ R_{z-h} &= a^2 + R^2 + (Z_o - h)^2 \end{aligned}$$

In the case of $h \approx a \ll Z$, the current distribution may be treated as two dimensional and eq. (44) becomes

$$\begin{aligned} B_z(R, \theta, Z_o) &= -\frac{\mu_o}{2} \frac{1-\sigma}{1+\sigma} Joha^2 R \sin \theta \left\{ +\frac{1}{R_{z^3}} + \frac{3(a^2 R^2)}{8} \right. \\ &\quad \left. \left(\frac{1}{R_z^5} + \frac{4}{3R_z^5} + \frac{8}{3R_z^5} \right) \right\} \\ &= -\frac{m\mu_o}{2} \left(\frac{1-\sigma}{1+\sigma} \right) Joha^2 R \sin \theta \left\{ \frac{1}{r_z^3} + \frac{15a^2 R^2}{8R_z^5} \right\} \\ B_z(R, \theta, Z_o) &= -\frac{\mu_o Joh}{2} \left(\frac{1-\sigma}{1+\sigma} \right) \frac{a^2 R \sin \theta}{R_z^3} \left(1 + \frac{15a^2 R^2}{8R_z^2} \right) \end{aligned}$$

The first term is related to a current dipole and the second term is related to octapole. There is no quadrupole. The second term is the disturbing hole to the finite length of the flaw. The current has the component in the z direction. This solution is obtained when the depth of the flaw much smaller than the thickness of the plate, and then the boundary at the bottom plates does not effect to the current distribution.

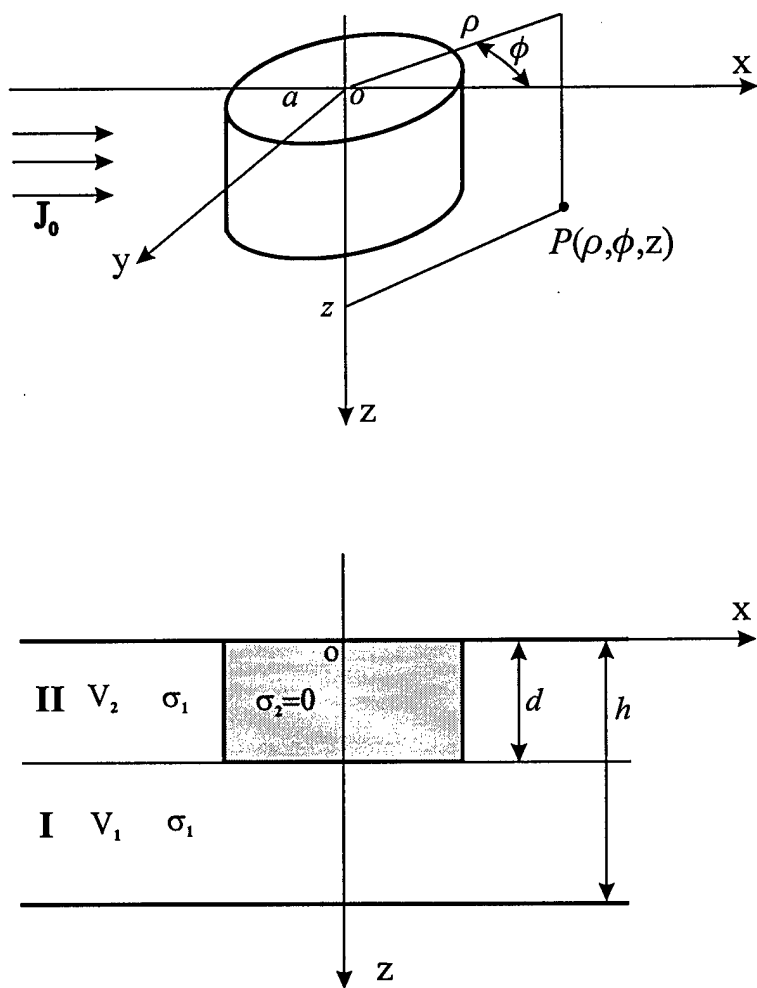


Figure 1. Illustration of the cylindrical coordinates used for calculation.